Detailed Two-Phase Modelling of Film Condensation on a Horizontal Tube

by

Esam Ahmad Saleh

A Thesis submitted to the Faculty of Graduate Studies of
The University of Manitoba
in partial fulfilment of the requirements for the degree of

Doctor of Philosophy

Department of Mechanical Engineering
University of Manitoba
Winnipeg, Manitoba, Canada

Abstract

A complete two-phase numerical model of film condensation from a mixture of a vapour and a non-condensing gas that is based on the two-dimensional elliptic governing equations with variable physical properties is presented. The model predicts the full viscous flow and heat and mass transfer for the mixture around the tube and in the entire liquid film from the top of the tube to the falling film below the tube. A finite volume method is used with a segregated solution approach and a dynamically moving computational grid that tracks the phase interface sharply. Fundamental balances of mass, energy, and force are enforced accurately at the phase interface.

The model was developed in steps and validated against various experimental and theoretical works in the literature for different two-phase flows. The validation tests included stratified flow of liquid and gas in a horizontal channel, falling liquid film over a vertical wall, and condensation of steam from a steam-air mixture in a vertical channel.

The model was used to simulate laminar film condensation from a downward flowing steam-air mixture over an isothermal horizontal tube. The validity of this new model is demonstrated by comparisons with previous theoretical and experimental studies. New results are presented on the effects of free-stream-to-tube temperature difference, upstream Reynolds number, free-stream gas mass fraction, and free-stream pressure on the condensate film development, the local and average heat transfer coefficients, and the total condensate mass flow rate.

It was found that the temperature difference had the greatest effect on the condensation rate and film thickness. The presence of non-condensing gas in the vapour has a strong negative impact on the condensation process. For the pure steam case, moderate changes in the upstream Reynolds number showed slight increases in condensate mass flow rate with increased Reynolds number. For the mixture case, however, moderate increase in upstream Reynolds number increases significantly the condensate mass flow rate and film thickness.

This trend becomes more noticeable as the free-steam gas mass fraction increases. Changing the free-stream pressure demonstrated that property variation had a relatively smaller effect than temperature difference and gas mass fraction changes.

Acknowledgements

My sincere thanks and appreciation to Dr. S. J. Ormiston, for his help and advice during the preparation of this thesis.

I would like also to extend my thanks to the staff of Mechanical Engineering Department, those who helped me throughout the graduate program.

Finally, I would like to extend my thanks to my family for their help and assistance during my academic study.

Dedication

This thesis is dedicated to my family.

Contents

Abstract ii

Acknowledgements iv

Dedication v

Dedication v

List of Tables xi

List of Figures xii

Nomenclature xviii

1 Introduction 1

1.1 Industrial Significance of this Work 1

1.2 Problem Statement 2

1.3 Literature Review of Condensation over Horizontal Tubes and Tube Banks 4

1.3.1 Introduction 4

1.3.2 Review of Previous Theoretical Work 4

1.3.3 Summary of Previous Theoretical Work 20

1.3.4 Review of Previous Experimental Work 21

1.3.5 Summary of Previous Experimental Work 26

1.4 Two Phase Flow Interface Modelling 26

1.4.1 Problem of the Interface 26

1.4.2 Interface Tracking Methods 27
1.4.3 Interface Capturing Methods 28
1.5 Objectives 29

2 Mathematical Model **31**
2.1 Assumptions 31
2.2 Governing Equations 31
2.2.1 Liquid Region 31
2.2.2 Mixture Region 32
2.3 Model Domain and Boundary Conditions 34
2.4 Balance Conditions at the Interface 36
2.5 Property Evaluation 38
2.5.1 Summary of the Governing Equations 39

3 Grid Generation **40**
3.1 Introduction 40
3.2 Grid Generation method 40
3.2.1 Grid geometry 41
3.2.2 Grid expansion factor 48
3.3 Grid Assembly (Paneling) 49
3.4 Grid Configuration in the Liquid Film 51

4 Discretisation of the Governing Equations **54**

4.1 Introduction . . . 54

4.2 Finite Volume Method . . . 54

4.3 Algebraic Transport Equations . . . 55

4.3.1 The Continuity Equation . . . 55

4.3.2 x-Momentum Conservation Equation . . . 57

4.3.3 y-Momentum Conservation Equation . . . 64

4.3.4 Energy Conservation Equation . . . 66

4.3.5 Gas mass conservation equation . . . 69

4.4 Algebraic Interface Equations . . . 71

4.4.1 Derivation of the Equations . . . 71

4.4.2 Modified Assignment of the Interface Algebraic Equations . . . 82

4.5 Boundary Condition Equation Implementation . . . 84

4.5.1 Dirichlet . . . 84

4.5.2 Neumann . . . 85

4.5.3 Absorption of the Boundary Conditions . . . 90

4.5.4 Face Velocity Boundary Conditions . . . 92

4.5.5 Face Value of a Property . . . 94

4.6 E-factor Formulation . . . 95

5 The Numerical Solution Method **97**

5.1 Pressure Velocity Coupling . . . 97

5.1.1 Pressure Weight Interpolation Method . . . 98
5.1.2 Velocity Corrections . . . 102
5.1.3 The SIMPLEC Algorithm . . . 104
5.1.4 Formulation of the Pressure Correction Equation . . . 106
5.1.5 Boundary Conditions for the Pressure Correction Equation . . . 115
5.2 Interface Moving Strategies . . . 121
5.2.1 Integral liquid mass balance (ILMB) . . . 121
5.3 Velocity Fields Initial Guess . . . 123
5.4 Velocity Coupling at the Interface . . . 124
5.5 Solution Algorithm . . . 126
5.6 Solving the Linearized Elliptic Equations . . . 127
5.7 Convergence Criteria . . . 128
5.7.1 Linearized Equations Convergence . . . 128
5.7.2 Global Steady State Convergence . . . 128

6 Comparison with Previous Work 130

6.1 Introduction . . . 130
6.2 Development of the Code . . . 130
6.3 Domain size Selection . . . 138
6.4 Grid Selection . . . 138
6.5 Model Validation . . . 148
6.5.1 Validation Tests for Pure Vapour Condensation . . . 148
6.5.2 Validation Tests for Condensation with a Vapour-Gas Mixture . . . 152

7 Results and Discussion **160**

7.1 Heat Transfer at the Tube wall 160

7.2 Pure Vapour Condensation 161

7.2.1 Detailed Examination of Sample Results 162

7.2.2 Effect of Changing ΔT 167

7.2.3 Effect of Changing Re_d 170

7.2.4 Effect of Changing P_∞ 174

7.3 Mixture of Vapour and Non-condensable Gas Condensation 177

7.3.1 Detailed Examination of Sample Results 177

7.3.2 Effect of Changing W_∞ 185

7.3.3 Effect of Changing ΔT 195

7.3.4 Effect of Changing Re_d 199

7.3.5 Effect of Changing P_∞ 205

8 Summary, Conclusions, and Recommendations **210**

8.1 Summary and Conclusions 210

8.2 Recommendations for Further work 211

A The Mass-Weighted Upwind Scheme (MAW) **222**

A.1 Introduction 222

A.2 Discretisation of the Advection Term 222

List of Tables

6.1 Effect of grid size on heat transfer characteristics and computational time. 141

7.1 Average Nusselt number and film Reynolds number variation with ΔT and Re_d for $P_\infty = 1$ atm. 167

7.2 Average Nusselt number and film Reynolds number variation with P_∞ and ΔT for $\mathrm{Re}_d = 50$. 176

7.3 Average Nusselt number and Re_L variation with W_∞, ΔT, and Re_d for $P_\infty =$ 1 atm. 192

7.4 Average Nusselt number and Re_L variation with W_∞ and ΔT for $P_\infty =$ 0.5 and 2 atm and $\mathrm{Re}_d = 50$. 208

List of Figures

1.1 Condensation on a horizontal tube. 3

2.1 Domain definition. 35

3.1 Computational molecule: indexing and notation. 41

3.2 Sample grid showing nomenclature used. The spacing between the nodes at the interface is exaggerated for illustration purposes. 43

3.3 Coordinates of control volume points and quadrant notation. 44

3.4 Distances, areas and volumes of a control volume. 45

3.5 Grid directional unit vectors. 46

3.6 Clarification of common distances. 48

3.7 Example of grid assembly: condensation over a horizontal tube. The size of the liquid region is exaggerated for clarity. 51

3.8 Grid configuration in the liquid film. 53

4.1 Co-located variable storage scheme. 55

4.2 South Boundary Computational Molecule. 85

5.1 Nomenclature used in the ILMB method. The interface node spacing is exaggerated for illustration purposes. 122

6.1 Laminar Film condensation in a vertical channel: Domain definition. . . . 132

6.2 Comparison with Siow's model: effect of ΔT on film thickness (δ). 133

6.3 Comparison with Siow's model: gas mass fraction along the interface (W_{int}). 134

6.4 Comparison with Siow's model: the U velocity profiles in the liquid film at different axial locations for $\Delta T = 20$ K. 135

6.5 Comparison with Siow's model: the U velocity profiles in the mixture at different axial locations for $\Delta T = 20$ K. 135

6.6 Comparison with Siow's model: temperature profiles at different axial locations for $\Delta T = 20$ K. 136

6.7 Comparison with Siow's model: gas mass fraction profiles at different axial locations for $\Delta T = 20$ K. 136

6.8 Comparison with Siow's model: pressure profiles at different axial locations for $\Delta T = 20$ K. 137

6.9 Sample coarse grid 140

6.10 Condensate film thickness along the tube. 142

6.11 Condensate film at the tube bottom. 142

6.12 Condensate U velocity profiles near $\theta = 90°$. 143

6.13 The U velocity profiles in the vapour region near $\theta = 90°$. 144

6.14 Details of the U velocity profiles in the vapour near the interface near $\theta = 90°$. 144

6.15 The V velocity profiles near $\theta = 90°$ in the liquid region. 146

6.16 The V velocity profiles near $\theta = 90°$ in the vapour region. 146

6.17 Details of the V velocity profiles in the vapour near $\theta = 90°$. 147

6.18 Condensate film thickness along the tube: comparison with [14] and [19]. 149

6.19 Sample grid showing details: (a) around the tube, (b) at the top of the tube, and (c) at the bottom of the tube. 150

6.20 Comparison with theoretical and experimental correlation equations. . . . 151

6.21 Condensate film thickness along the tube: comparison with [23] for $\mathrm{Re}_d = 68.5$. . . . 153

6.22 Local Nusselt number along the tube surface: comparison with [23] for $\mathrm{Re}_d = 68.5$. . . . 154

6.23 Condensate mass flux along the tube surface: comparison with [23] for $\mathrm{Re}_d = 68.5$. . . . 154

6.24 Interface temperature T_{int} along the tube surface: comparison with [23] for $\mathrm{Re}_d = 68.5$. . . . 155

6.25 Condensate film thickness along the tube: comparison with [19] for $P_\infty = 1$ atm. . . . 157

6.26 Local Nusselt number along the tube surface: comparison with [19] for $P_\infty = 1$ atm. . . . 158

7.1 The condensate film thickness for $P_\infty = 1$ atm, $\mathrm{Re}_d = 100$, and $\Delta T = 20$ K. 163

7.2 U velocity profiles in the liquid film at different locations for $P_\infty = 1$ atm, $\mathrm{Re}_d = 100$, and $\Delta T = 20$ K. . . . 164

7.3 U velocity profiles in the vapour at different locations for $P_\infty = 1$ atm, $\mathrm{Re}_d = 100$, and $\Delta T = 20$ K. . . . 164

7.4 Relative pressure distribution around the tube for $P_\infty = 1$ atm, $\mathrm{Re}_d = 100$, and $\Delta T = 20$ K. . . . 165

7.5 Temperature profiles in the liquid film at different locations for $P_\infty = 1$ atm, $\mathrm{Re}_d = 100$, and $\Delta T = 20$ K. . . . 166

7.6 Details of the flow pattern for $\mathrm{Re}_d = 100$ and $\Delta T = 20$ K at: (a) around the tube, (b) at the top of the tube, and (c) at the bottom of the tube. . . . 168

7.7 Effect of temperature difference for $\mathrm{Re}_d = 50$ and $P_\infty = 1$ atm. 169

7.8 Effect of temperature difference on Nu_s for $\mathrm{Re}_d = 50$ and $P_\infty = 1$ atm. . . 169

7.9 Effect of ΔT on the reverse flow region for $\mathrm{Re}_d = 50$ ($U_\infty = 7.3\times10^{-2}$ m/s). 171

7.10 Effect of Re_d on the condensate thickness for $P_\infty = 1$ atm. 172

7.11 Effect of Re_d on the local Nusselt number for $P_\infty = 1$ atm. 172

7.12 Effect of Re_d on the reverse flow region for $\Delta T = 20$ K. 173

7.13 Effect of pressure on the condensate thickness for $\mathrm{Re}_d = 50$. 175

7.14 Effect of pressure on the local Nusselt number for $\mathrm{Re}_d = 50$. 175

7.15 The condensate film thickness for $P_\infty = 1$ atm, $\mathrm{Re}_d = 100$, $W_\infty = 0.05$, and $\Delta T = 20$ K. 178

7.16 U velocity profiles in the liquid film at different locations for $P_\infty = 1$ atm, $\mathrm{Re}_d = 100$, $W_\infty = 0.05$, and $\Delta T = 20$ K. 179

7.17 U velocity profiles in the mixture at different locations for $P_\infty = 1$ atm, $\mathrm{Re}_d = 100$, $W_\infty = 0.05$, and $\Delta T = 20$ K. 179

7.18 Relative pressure distribution arount the tube for $P_\infty = 1$ atm, $\mathrm{Re}_d = 100$, $W_\infty = 0.05$, and $\Delta T = 20$ K. 180

7.19 Temperature profiles in the liquid film at different locations for $P_\infty = 1$ atm, $\mathrm{Re}_d = 100$, $W_\infty = 0.05$, and $\Delta T = 20$ K. 181

7.20 Temperature profiles in the mixture at different locations for $P_\infty = 1$ atm, $\mathrm{Re}_d = 100$, $W_\infty = 0.05$, and $\Delta T = 20$ K. 182

7.21 Gas mass fraction profiles in the mixture at different locations for $P_\infty = 1$ atm, $\mathrm{Re}_d = 100$, $W_\infty = 0.05$, and $\Delta T = 20$ K. 183

7.22 Details of the flow pattern for $\mathrm{Re}_d = 100$, W_∞ =0.05 and $\Delta T = 20$ K at: (a) around the tube, (b) at the top of the tube, and (c) at the bottom of the tube. 184

7.23 Effect of W_∞ on condensate height for $\mathrm{Re}_d = 50$, $P_\infty = 1$ atm and $\Delta T = 5$K. 185

7.24 Effect of W_∞ on condensate height for $\mathrm{Re}_d = 50$, $P_\infty = 1$ atm and $\Delta T =$ 10K. 186

7.25 Effect of W_∞ on condensate height for $\mathrm{Re}_d = 50$, $P_\infty = 1$ atm and $\Delta T =$ 20K. 186

7.26 Effect of W_∞ on Nu_s for $\mathrm{Re}_d = 50$, $P_\infty = 1$ atm and $\Delta T = 5$K. 187

7.27 Effect of W_∞ on Nu_s for $\mathrm{Re}_d = 50$, $P_\infty = 1$ atm and $\Delta T = 10$K. 188

7.28 Effect of W_∞ on Nu_s for $\mathrm{Re}_d = 50$, $P_\infty = 1$ atm and $\Delta T = 20$K. 188

7.29 Effect of W_∞ on W_{int} at the interface for $\mathrm{Re}_d = 50$, $P_\infty = 1$ atm and $\Delta T = 5$K. 189

7.30 Effect of W_∞ on W_{int} at the interface for $\mathrm{Re}_d = 50$, $P_\infty = 1$ atm and $\Delta T = 5$K. 190

7.31 Effect of W_∞ on W_{int} at the interface for $\mathrm{Re}_d = 50$, $P_\infty = 1$ atm and $\Delta T = 10$K. 190

7.32 Effect of W_∞ on W_{int} at the interface for $\mathrm{Re}_d = 50$, $P_\infty = 1$ atm and $\Delta T = 20$K. 191

7.33 Effect of W_∞ on condensate mass flow rate, Re_L, for $P_\infty = 1$ atm and $\mathrm{Re}_d = 50$. 193

7.34 Effect of W_∞ on the average Nusselt number, $\overline{\mathrm{Nu}}$, for $P_\infty = 1$ atm and $\mathrm{Re}_d = 50$. 193

7.35 Effect of W_∞ on the reverse flow region below the tube for $\mathrm{Re}_d = 50$ ($U_\infty = 7.3\times10^{-2}$ m/s) and $\Delta T = 20$ K. 194

7.36 Effect of ΔT on condensate height for $\mathrm{Re}_d = 50$ and $P_\infty = 1$ atm. 195

7.37 Effect of ΔT on Nu_s for $\mathrm{Re}_d = 50$ and $P_\infty = 1$ atm. 196

7.38 Change of interface shape with ΔT at the tube bottom for $P_\infty = 1$ atm, $\mathrm{Re}_d = 50$, and $W_\infty = 0.01$. 197

7.39 Effect of ΔT on the reverse flow region for $\mathrm{Re}_d = 50$ ($U_\infty = 7.3 \times 10^{-2}$ m/s) and W_∞ =0.001. 198

7.40 Effect of Re_d on condensate height for $\Delta T = 5$ K and $P_\infty = 1$ atm. 199

7.41 Effect of Re_d on condensate height for $\Delta T = 20$ K and $P_\infty = 1$ atm. . . . 200

7.42 Effect of Re_d on W_{int} for $W_\infty = 0.05$, $P_\infty = 1$ atm, and $\Delta T = 5$ and 20 K. 200

7.43 Effect of Re_d on Nu_s for $\Delta T = 5$ K and $P_\infty = 1$ atm. 201

7.44 Effect of Re_d on Nu_s for $\Delta T = 20$ K and $P_\infty = 1$ atm. 202

7.45 Effect of Re_d on condensate mass flow rate, Re_L, at $\Delta T = 20$K. 203

7.46 Effect of Re_d on $\overline{\mathrm{Nu}}$ for $P_\infty = 1$ atm and $\Delta T = 20$ K. 203

7.47 Effect of Re_d on the gas mass fraction boundary layer for W_∞ =0.05 and $\Delta T = 20$ K. 204

7.48 Effect of Re_d on the reverse flow region for $\Delta T = 20$ K and W_∞ =0.001. . 206

7.49 Effect of pressure on the condensate thickness for $\mathrm{Re}_d = 50$ and $W_\infty = 0.001$ and 0.05. 207

7.50 Effect of pressure on the local Nusselt number for $\mathrm{Re}_d = 50$ and $W_\infty = 0.001$ and 0.05. 207

A.1 Typical control element and control volume. 224

A.2 Associated control elements with control volume P. 228

Nomenclature

A	area, $[m^2]$
b	source term in algebraic equations
C_p	specific heat, $[\mathrm{J\,kg^{-1}\,K^{-1}}]$
D	diffusion coefficient of a transport equation
D^{ab}	binary diffusion coefficient, $[\mathrm{m^2\,s^{-1}}]$
d	tube diameter, [m]
ds	distance along $\hat{s}$ vector for a single control volume, [m]
dt	distance along $\hat{t}$ vector for a single control volume, [m]
f	interpolation coefficient
F	dimensionless parameter, $\dfrac{\mathrm{Pr}_L}{(\mathrm{Fr}\,\mathrm{Ja})}$
Fr	Froude number, $U_\infty^2/\left(d\,g\right)$
G	dimensionless parameter, $\left(\rho_L\mu_L/\rho_M\mu_M\right)^{1/2}\,\left(\mathrm{Ja}/\mathrm{Pr}_L\right)$
g	acceleration due to gravity, $[\mathrm{m\,s^{-2}}]$
h_s	local heat transfer coefficient, $(q''_{\mathrm{wall}}/\Delta T)$ $[\mathrm{W\,m^{-2}\,K^{-1}}]$
$\overline{h}$	average heat transfer coefficient, $\left(\,(\pi R)^{-1}\int_0^{\pi R} h\,ds\right)$ $[\mathrm{W\,m^{-2}\,K^{-1}}]$
h_{fg}	latent heat of vapourisation, $[\mathrm{J\,kg^{-1}}]$
h_L	interface height measured along the east face of each liquid column, [m]
H	domain height, [m]
i_B	first control volume on the west side of the domain
i_E	last control volume on the east side of the domain
Ja	Jakob number, $C_{p_L}\dfrac{(T_{sat}-T_w)}{h_{fg}}$
j_B	first control volume on the south side of the domain
j_E	last control volume on the north side of the domain
j_{BM}	first control volume index in the j-direction in the mixture region
j_{EM}	last control volume index in the j-direction in the mixture region
j_{BL}	first control volume index in the j-direction in the liquid region

j_{EL}	last control volume index in the j-direction in the liquid region
k	thermal conductivity, $[\mathrm{W\,m^{-1}\,K^{-1}}]$
L	domain length,[m]
L_s	coordinate along the tube surface and then below the tube along x, [m]
M	molecular weight
$\dot{m}$	mass flow rate, $[\mathrm{kg\,s^{-1}}]$
N_x	number of nodes along the i index
N_y	number of nodes along the j index
$N_{y,L}$	number of nodes along the j index in the liquid region
$N_{y,M}$	number of nodes along the j index in the mixture region
$\hat{n}$	normal unit vector, $n_x\,\hat{\imath} + n_y\,\hat{\jmath}$
Nu_s	local Nusselt number, $\frac{h_s\,d}{k_L}$
$\overline{\mathrm{Nu}}$	average Nusselt number, $\frac{\overline{h}\,d}{k_L}$
P	pressure, $[\mathrm{N\,m^{-2}}]$
$\tilde{P}$	dimensionless parameter, $\rho_g\,h_{fg}\,\nu_L/\left(\Delta T\,k_L\right)$
Pe	Peclet number
Pr	Prandtl number, $C_p\,\mu/k_L$
Q	lagged part of linearised source term
q''	heat flux, $[\mathrm{W\,m^{-2}}]$
R	tube radius
Re_d	mixture free stream Reynolds number, $\rho_M\,U_\infty\,d/\mu_M$
Re_L	liquid film Reynolds number , $4\,\dot{m}_L/\mu_L$
Re	two-phase Reynolds number, $\rho_L\,U_\infty\,d/\mu_L$
r_x	grid geometric expansion factor in the x direction
S	linearised source term
s	distance along the tube surface, [m]
$\hat{s}$	west to east geometric grid unit vector, $s_x\,\hat{\imath} + s_y\,\hat{\jmath}$

T	temperature, [K]
ΔT	free stream to tube wall temperature difference, [K]
t	time, [s]
$\boldsymbol{T}$	stress tensor, $[\mathrm{N\,m^{-2}}]$
$\hat{t}$	south to north geometric grid unit vector, $t_x\,\hat{\imath} + t_y\,\hat{\jmath}$
U	velocity in the Cartesian x direction, $[\mathrm{m\,s^{-1}}]$
V	velocity in the Cartesian y direction, $[\mathrm{m\,s^{-1}}]$
$\overrightarrow{V}$	velocity vector, $[\mathrm{m\,s^{-1}}]$, $U\,\hat{\imath} + V\,\hat{\jmath}$
$\forall$	volume, $[\mathrm{m^3}]$
W	gas mass fraction, $m_G/(m_V + m_G)$
x	Cartesian coordinate direction, [m]
y	Cartesian coordinate direction, [m]

Greek Letters

α	convective weighting coefficient for upwind differencing
β	diffusive weighting coefficient for upwind differencing
η	transformed coordinate in the j direction
γ	relaxation factor
δ	interface height normal to the tube wall
θ	tube central angle, [rad]
κ	curvature of the interface, $[\mathrm{m^{-1}}]$
μ	molecular dynamic viscosity, $[\mathrm{kg\,m^{-1}\,s^{-1}}]$
ξ	local grid unit vector
ρ	density, $[\mathrm{kg\,m^{-3}}]$
ϕ	general variable (referring to U, V , T, P' or W)

Subscripts

bnd	referring to boundary
cond	referring to condensation
d	referring to diameter
E, W, N, S	referring to nodal quantities to the east, west, north, and south of the present control volume
e, w, n, s	referring to face quantities to the east, west, north and south of the present control volume
f	referring to a face quantity
G	referring to gas
i	west to east control volume index
∞	referring to free stream
int	referring to the interface
j	south to north control volume index
L	referring to liquid
M	referring to mixture
NB	referring to the neighbouring nodal points of a standard control volume
nb	referring to the neighbouring points of a shifted control volume centred at a face of a control volume.
NE, NW	referring to nodal quantities to the northeast and northwest of the typical control volume
SE, SW	referring to nodal quantities to the southeast and southwest of the typical control volume
ne, nw	referring to corner quantities to the northeast and northwest

	of the typical control volume
s	referring to the distance along the tube surface or local quantity
sat	referring to saturation condition
se, sw	referring to corner quantities to the southeast and southwest
	of the present control volume
P	referring to the typical control volume
tot	referring to total
V	referring to vapour
wall	referring to tube wall
x	referring to the x horizontal direction
y	referring to the y vertical direction

Superscripts

o	referring to the previous time step or iteration
u, v, c, t, w	referring to U, V, continuity, temperature,
	and gas mass fraction equations
ϕ	referring to the general (ϕ) equation
$\star$	referring to calculated value from the solver
$'$	referring to the correction value
$\sim$	referring to a group of terms (eg. $\widetilde{\Phi}$ refers to a group of Φ terms)
$\cdot$	rate
$\oplus$	refers to a modified coefficient
$''$	per unit area
$'''$	per unit volume

Acronyms

ADI	Alternating-Direction Implicit
CDS	Central Differencing Scheme
I.D.	Inside Diameter
EDS	Exponential Differencing Scheme
FVM	Finite Volume Method
MAW	The MAss-Weighted upwind scheme
MSI	Modified Strongly Implicit procedure
MSI92D	Schneider and Zedan nine-point two dimensional solver
O.D.	Outside Diameter
ODE	Ordinary Differential Equation
PDE	Partial Differential Equation
PLR92D	Perić's nine-point Left to Right two dimensional solver
PWIM	Pressure-Weighted Interpolation Method
RHS	Right-Hand Side notation
SIMPLE	Semi-Implicit Method for Pressure-Linked Equations
SIMPLEC	SIMPLE-Consistent
SIP	Strongly Implicit Procedure
TDMA	Tri-Diagonal Matrix Algorithm
UDS	Upwind Differencing Scheme

Chapter 1

Introduction

1.1 Industrial Significance of this Work

Condensation is the process that involves changing of fluid state from a vapour to a liquid when the temperature goes below the saturation temperature of the vapour at a certain pressure. When condensation take places, vapour releases the latent heat of vapourisation to a cool surface by thermal conduction and forms either a film or droplets of condensate on the surface, depending on the characteristics of the surface. Film condensation is the common form in which a film of liquid condensate covers the entire surface and flows downward due to gravity. The condensate film provides additional thermal resistance between the vapour and the surface resulting in a decrease in the heat transfer rate as the film thickens.

There are many industries that use heat exchangers in which film condensation takes place. Thermal power plants, chemical processing units, desalination units, refrigeration and air conditioning industries are examples. Therefore, many investigators have studied film condensation experimentally and theoretically in order to improve designing those heat exchangers.

Condensers are large heat exchangers that are designed with various configurations and flow modes. In thermal power plants, cross flow shell-and-tube condensers are usually used. In this type of condenser, the expanded steam from a turbine is directed to a condenser which recovers the steam through a cooling process in contact with a bank of water-cooled horizontal tubes. These tubes are usually made with metals that have high thermal conduc-

tivity and corrosion resistance such as copper, copper alloys and stainless steel. The tube bundle has a large number of closely packed tubes in either staggered or in-line arrangements. Steam condenses over the outer surface of the tubes by rejecting heat to the cooling fluid through tubes wall. Condensate is collected in a hotwell to be pumped to a steam generator. Because condensers operate under a vacuum, leakage permits infiltration of air. The presence of the non-condensable gas significantly degrades the condenser performance.

To optimize the design of condensers, experiments or sophisticated numerical CFD models have to be developed to determine the influence of various parameters on the performance. Experimental studies require relatively large cost in setting the experiments for specific condenser design. Changing any parameter such as tube diameter, material, or configuration requires expensive changes in the setup. On the other hand, numerical simulations have many advantages over the experimental research such as less cost and ability to examine effects of each operating parameter with less cost. Also, they can be modified easily to study different designs, flow patterns, tube diameters, tube configurations and materials. The first step in modeling condensers is to model condensation process over a single horizontal tube. Then, banks of tubes can be considered with various configurations.

1.2 Problem Statement

The problem under consideration is shown schematically in Figure 1.1. A vertically downward uniform flow of mixture (vapour and non-condensing gas) is flowing over an isothermal horizontal tube. The temperature of the tube, T_w , is held below the saturation temperature of the vapour, T_{sat}. Thus, vapour starts condensing over the tube wall, forming a thin film of condensate of thickness, δ , that flows over the wall under the effects of gravity, shear stress at the interface and the pressure gradient that results from both fluid flow and surface tension effects. The film thickness is the liquid thickness normal to the tube surface unless otherwise noted. Both vapour and gas are assumed to be incompressible

and Newtonian fluids.

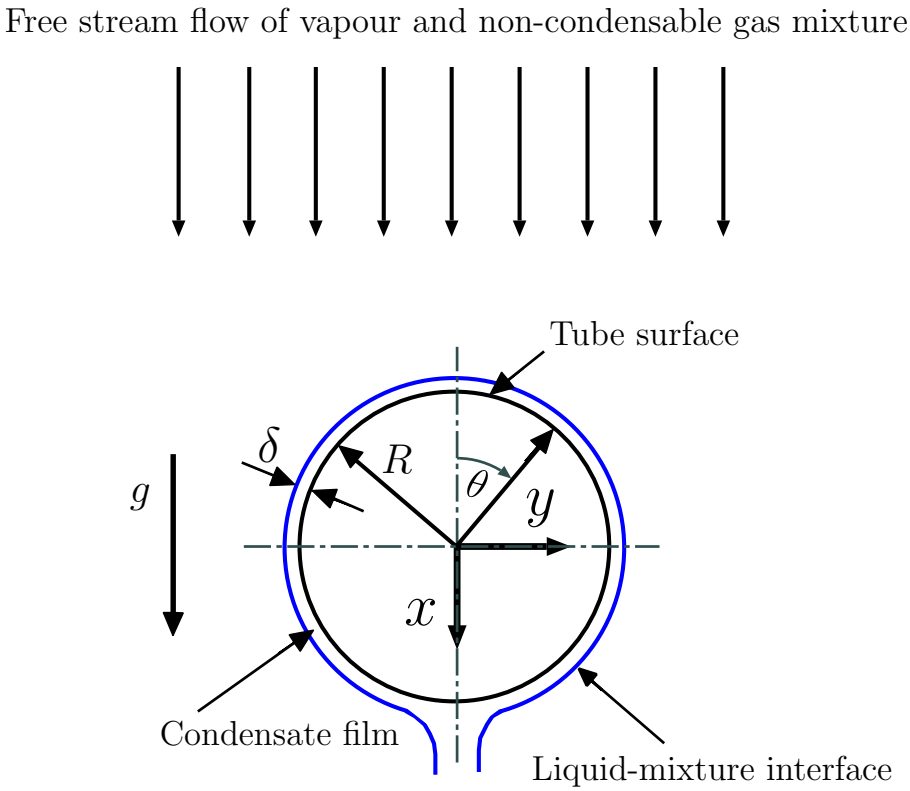

Figure 1.1: Condensation on a horizontal tube.

The condensate film is laminar and smooth for $\mathrm{Re}_L \leq 30$, laminar and wavy for $30 > \mathrm{Re}_L \leq 1000$, and becomes turbulent at $\mathrm{Re}_L \geq 1800$ [1].

To get a better assessment of the problem, the state of the art of analysis of the problem must be understood thoroughly. Therefore, a survey of the previous key theoretical and experimental studies on film condensation over a horizontal tube is now presented.

1.3 Literature Review of Condensation over Horizontal Tubes and Tube Banks

1.3.1 Introduction

Previous studies of condensation over horizontal tubes have examined the effects of changes in the inlet velocity, the temperature difference between the wall and the free stream, the wall temperature uniformity, the pressure variation around the tubes, the presence of a non-condensable gas in the mixture, and the ellipticity of the tube. Various approaches with different degrees of complexity have been followed to model the problem. The review of literature considers two categories of previous work: theoretical and experimental studies.

1.3.2 Review of Previous Theoretical Work

In 1916 Nusselt [2] , a pioneering scientist in modern heat transfer science, solved the problem of laminar filmwise condensation of pure quiescent vapour over an isothermal horizontal tube. In his analysis, only the weight of the condensate film and the diffusion in the normal direction to the tube surface were considered in the momentum equation. Zero shear stress at the outer edge of the film was also assumed. Small condensate film thickness in comparison with the tube radius was considered where the temperature varies linearly across it. Moreover, all fluid properties were held constant. A simple energy balance between the conducted heat flux through the film and the released latent heat of vapourisation at the vapour-liquid interface was used instead of the energy equation. An expression for the average Nusselt number was derived as:

$$\overline{\mathrm{Nu}} = 0.725 \left[\frac{g\ \rho_L \left(\rho_L - \rho_V\right) h_{fg}\ d^3}{\mu_L\ k_L\ \left(T_{sat} - T_w\right)} \right]^{1/4} \tag{1.1}$$

Subsequent studies of the problem suggested replacing the constant 0.725 with 0.728 [3]. This equation has been used through the subsequent years as a milestone for comparison purposes with more sophisticated approaches. A review for the theoretical studies of the previously described problem is now provided for laminar and turbulent flows.

Shekriladze and Gomelauri [4] presented an analytical study for laminar, downward-flowing pure vapour condensation on a horizontal isothermal tube. In their single phase model, both body and inertia forces were neglected. More over, pressure effect was omitted and potential flow was assumed outside the vapour boundary layer. The shear stress at the interface was expressed in terms of the momentum transferred by the condensate mass at the interface assuming sufficiently high suction rate due to condensation. This asymptotic shear expression results from the solution of the vapour boundary layer. They derived analytical equations for the local and average heat transfer coefficients. They attempted to include the effect of a gravitational field but a mathematical difficulty was encountered that prevented any further progress.

Denny and Mills [5] tackled both analytically and numerically the problem of laminar film condensation of a downward flowing vapour on a horizontal isothermal cylinder with gravitational effects. Both the approaches dealt only with the condensate film and utilized the asymptotic expression for the shear stress at the interface [4]. Variation of properties with temperature was considered. In the analytical approach, they included the body force effect to the mathematical model considered by Shekriladze and Gomelauri [4]. A non-linear ODE was obtained for the film thickness which was solved along the cylinder using a fourth order Runge-Kutta integration with 0.5° intervals. In the numerical approach, the boundary layer equations were solved using a finite difference method. They found that the discrepancy in the results for local heat transfer coefficient from the two approaches was less that 2% for $\theta \leq 140°$. This discrepancy increased as θ reached 180°.

Fujii et al. [6] investigated the case of laminar filmwise condensation of a pure vapour on a horizontal tube analytically and experimentally. In the analytical approach, the boundary layer equations were solved for two layers. The first layer represents the condensate film and the second one the vapour. The flow outside the vapour boundary layer was assumed to be potential flow. In addition to boundary layer assumptions, the effects of pressure gradient in the condensate film as well as vapour boundary layer separation were neglected. At each point along the circumference of the tube, the coordinates were aligned along the tube wall and its normal. Also, a quadratic velocity profile was assumed in the vapour boundary layer. Moreover, the authors assumed that heat transfer through the film occurs by conduction only. They concluded that about 80% of the condensation occurs in the upper part of the tube as the inlet vapour velocity increases. Furthermore, an equation for the average Nusselt number was presented that can predict the numerical results with maximum deviation of 5%.

Denny and South [7] presented a two-phase analytical model to investigate laminar film condensation over a horizontal tube from downward flows of steam-air and steam-methanol mixtures. In the gas phase, the boundary layer equations were used. For the liquid film, a simple momentum equation that accounted for body force, pressure gradient, and shear stress in the normal direction to the tube surface was used. Moreover, a simple energy conservation equation in the liquid that contained only the diffusion term in the normal direction to the tube surface was used. At the interface, continuity of shear stress, tangential velocity, and temperature conditions were applied together with a proper mass balance and impermeability condition to connect the two phases. Along the interface, a local energy balance was used to calculate the condensate mass flow rate. The original partial differential equations were transformed to ordinary differential equations by introducing a stream function and a similarity variable. The effects of changing the upstream velocity, the non-condensing gas mass fraction, the upstream-to-wall temperature difference, and the variation of thermophysical properties were considered in the study. For a steam-air mixture, they found that

the average heat flux (normalised by the classical Nusselt solution for pure steam) reached a maximum value as the temperature difference increased.

Gaddis [8] presented a two-phase mathematical model based on the boundary layer equations for laminar condensation of pure saturated vapour on a horizontal isothermal tube. In the model, a vapour boundary layer was assumed that encompass the condensate film. The flow outside the vapour boundary layer was assumed to be potential flow. In the study, physical properties were held constant and surface tension was omitted. Moreover, viscous dissipation was ignored. The pressure gradient around the tube was obtained from potential flow. At the interface, continuity of shear stress, tangential velocity, and temperature conditions were applied together with a proper mass balance to connect the two phases. The original partial differential equations were transformed to ordinary differential equations by introducing a stream function and using the Blasius series. Two expressions in infinite series form were obtained for the local Nusselt number and dimensionless film thickness. Results were presented for water, liquid metal ($Pr \ll 1$), and viscous liquids ($Pr \gg 1$) for both quiescent and moving vapour around a 20mm O.D. tube. For water, results were presented for saturation pressure of 0.1, 1, and 10 atm; and saturation to wall temperature difference of 1, 5, and 20K. Good agreement with Nusselt's solution (Equation (1.1)) was reported for quiescent vapour .

Honda et al. [9] studied heat transfer from pure saturated vapour to coolant flowing in a horizontal tube during condensation of vapour flowing around the tube in horizontal cross flow. They developed a model that considered the vapour to coolant conjugate heat transfer through the tube wall by proposing an equivalent thermal resistance network. The numerical model divided the physical model to two regions: (one before the vapour boundary layer separation point and one after). Both condensate flow and the vapour boundary layer were considered laminar. The main stream velocity distribution was based on experimental observations in [10] to depict pressure distribution around the tube. Vapour shear stress was neglected beyond the stagnation point where an abrupt change of the

condensate film occurs. Two correlation equations were presented for the two regions.

Rose [11] performed an analytical study to show the effect of pressure gradient in forced convection film condensation over a horizontal tube. The single phase model consisted of a single simple momentum balance equation that involved body, pressure, and viscous terms. The asymptotic expression for the shear stress at the condensate surface, ($\tau_{\text{int}} = m_{\text{int}} U_{\infty}$), was used [4]. Moreover, potential flow outside the vapour boundary layer was assumed. The pressure variation with the circumference of the tube was obtained from the potential flow. A marching technique was used where at each station, the coordinates x and y coincided with the tangential and normal direction to the tube surface, respectively. A simple energy balance was applied between the released latent heat of vapourisation and heat conducted across the condensate film. A linear temperature profile was assumed across the liquid film. In order to generalize the results, some dimensionless parameters were introduced. These parameters are: two-phase Reynolds number Re; F; G; and $\tilde{P}$. A single ordinary differential equation (ODE) for the variation of δ with the angle θ was obtained in terms of the preceding mentioned dimensionless parameters. The numerical simulations for the problem were presented for $10^{-3} \leq F \leq 10^{3}$ and $0 \leq \tilde{P} \leq 10$. Rose also presented graphically the variation of the dimensionless thickness of the film with the angle θ for various values of F and $\tilde{P}$. It was concluded that the pressure gradient became important when the dimensionless quantity $(\frac{F}{8\tilde{P}})$ was significantly less than unity. It was believed that including pressure term, increased the prediction of the average Nusselt number along the forward part of the tube. Moreover, it predicted instability of the film when both F and $\tilde{P}$ were less than unity, in which case the predicted value of Nu increased compared to that with omitted pressure gradient. After comparing with various experimental data, three conservative expressions were given for the average Nu. The first expression (Equation (1.2) below), agreed within 0.4% with the numerical results, and is valid for $\tilde{P} = 0$.

$$\overline{\mathrm{Nu}}\ \mathrm{Re}^{-1/2} = \frac{0.9 + 0.728F^{1/2}}{\left(1 + 3.44F^{1/2} + F\right)^{1/4}} \tag{1.2}$$

Equation (1.2) was adjusted to involve a correction regarding usage of the asymptotic shear stress expression so that

$$\overline{\mathrm{Nu}}\ \mathrm{Re}^{-1/2} = \frac{0.9\left(1 + G^{-1}\right)^{1/3} + 0.728F^{1/2}}{\left(1 + 3.44F^{1/2} + F\right)^{1/4}} \tag{1.3}$$

These two equations are based on the work of Shekriladze and Gomelauri [4] and Fujii et al. [6]. For $0 < \tilde{P} < \frac{F}{8}$, it was found that Equations (1.2) and (1.3) can be used with maximum disagreement of 5% from the numerical results. For $\tilde{P} \geq \frac{F}{8}$, $\overline{\mathrm{Nu}}$ can be given by Equation (1.4).

$$\overline{\mathrm{Nu}}\ \mathrm{Re}^{-1/2} = \frac{0.64\left(1 + 1.81\tilde{P}\right)^{0.209}\left(1 + G^{-1}\right)^{1/3} + 0.728F^{1/2}}{\left(1 + 3.51F^{0.53} + F\right)^{1/4}} \tag{1.4}$$

Krupiczka [12] presented an analytical study on the effect of surface tension on a steady laminar film condensation of different quiescent vapours on the outer surface of a cylinder. Only the condensate film was considered in the study. The condensate flow was assumed to be driven only by gravity with zero shear at the liquid-vapour interface. The boundary layer assumptions were applied including neglecting the convective term of the 1D momentum equation. Moreover, conduction within the film was assumed to be the only mechanism for heat transfer. Under these circumstances, the pressure variation results only from surface tension forces. The resultant velocity profile was substituted into the energy equation. A second order non-linear ODE describing variation of film thickness $\delta(\theta)$ along the periphery was obtained. This equation was solved numerically by the second-order Runge-Kutta method. It was found that the effect of surface tension forces is significant for the lower part

of the cylinder where the film thickness is decreased by increasing surface tension forces. This reduction in δ leads to enhancement in the local heat transfer coefficients. On the other hand, results have shown that surface tension has negligible effect on the upper part of the tube.

Jacobi and Goldschmidt [13] presented a theoretical single phase model to study the effect of surface tension variation on condensation characteristics on a horizontal tube. In general, the model is similar to that of Rose [11]. The shear stress at the interface was assumed to be an asymptotic expression accounting for the shear stress and the Marangoni effect. The latter was assumed to balance the surface tension forces. More over, variation of saturation temperature with pressure was considered. A non-linear ODE was obtained for the film thickness which was solved incrementally along the tube using a fourth order Runge-Kutta integration. The solution process had to be terminated as $\delta \rightarrow \infty$ at the bottom of the tube. They concluded that variation in the saturation condition due to high vapour velocity has a significant influence on the local Nusselt number. Consequently, the average Nusselt number decreased by as much as 10% for ($\mathrm{Re} \geq 5{\times}10^5$). Finally, change in the film thickness due to surface tension effects was found to be less than 3% for realistic operating conditions.

Yang [14] presented a theoretical model to study combined forced and natural convection film condensation of pure vapour on a horizontal non-isothermal tube. The effect of superheat, pressure gradient, and interfacial shear stress were also considered in the study. The single phase model was constructed using simplified governing equations for the momentum and energy and the asymptotic expression for the interfacial shear stress. Potential flow was assumed outside the condensate film. Temperature was assumed to vary linearly across the condensate film. It was concluded that heat transfer coefficient can be enhanced by super heating the vapour. Finally, it was reported that an increase in the pressure gradient considerably decreases the heat transfer coefficient for lower values of F (i.e. for high vapour velocity) while no noticeable effect was observed for higher values of F (i.e. for gravity-dominated condensation).

Hsu and Yang [15] analyzed the effects of pressure gradient and variable wall temperature during filmwise condensation from downward flowing pure vapour onto a horizontal tube. A simple model was developed using the boundary layer assumptions, negligible inertia effects, negligible convective heat transfer within the film, linear temperature profile, and potential flow outside the vapour boundary layer. The asymptotic expression for the interfacial shear stress was employed [4]. The curvilinear coordinates are aligned along the circumference of the tube and its normal. An ordinary differential equation of film thickness $\delta(\theta)$ was obtained. The film thickness was found by solving $\delta(\theta)$ equation incrementally from the top of the tube until the critical angle where the film separates from the tube wall. They used a fourth order Runge-Kutta integration. Their results showed that the condensate film would stay sticking to the wall but separated at the bottom ($\theta = \pi$) if ($\frac{Ra}{Ja\ Re^2} \geq 8\frac{\rho_v}{\rho_L}\frac{Pr}{Ja}$). Otherwise, the film separation occurs in the range ($\frac{\pi}{2} < \theta \leq \pi$). Also, they noticed that the pressure gradient for lower vapour velocities did not affect the mean heat transfer coefficient. On the other hand, increasing the pressure gradient led to a considerable decrease in the mean heat transfer coefficient.

Mosaad [16] obtained an analytical solution for the case of forced-convection dominated laminar-film condensation on an inclined circular tube for a pure saturated vapour. Many assumptions were employed to obtain the single phase solution such as: flow is driven only by vapour velocity and not gravity; negligible pressure gradient; negligible convective terms in the momentum equations; and potential flow outside the vapour boundary layer. As a results, only a single viscous term remained in the momentum equations in the axial and x directions. Furthermore, a linear temperature profile was assumed in the condensate film. The possibility of vapour boundary layer separation was eliminated because the shear stress formula had positive value for the whole range of circumference and inclination angles. The partial differential equation that describes the variation of the local film thickness was solved numerically by applying the method of characteristics. Special cases of vertical and horizontal finite and infinite tubes were also considered. It was reported specifically that

the condensation process beyond a short length from the upper end of the inclined tube becomes like that on an infinitely long tube. In addition, it was found that an optimum tube inclination angle that gives the highest mean Nusselt number decreases as the ratio $(\frac{L}{d})$ increases where L is the tube length. However, for tubes with $(\frac{L}{d} \geq 40)$, results showed that horizontal tube gives the highest mean Nu.

Asbik et al. [17] presented a numerical study for laminar condensation of downward flow of pure saturated vapour on a horizontal cylinder and a bank of tubes. The two phase problem was simplified by making the standard boundary layer assumptions in both condensate film and vapour boundary layer that encloses the film. By doing so, the elliptic nature of the axial momentum equation and the energy equation in both regions were changed to parabolic and the transverse velocity momentum equation was not solved. Also, the flow outside the vapour boundary layer was considered to be potential flow. Surface tension effects were neglected in this study. The two sets of the governing equations were made non-dimensional. At the liquid-vapour interface, the two phases were coupled via continuity of velocity, shear stress, temperature conditions and mass balance. For a tube bundle, a continuous free falling sheet with uniform temperature was assumed between successive tubes. An implicit finite difference method was used to discretise the equations, which were solved at each axial station with an angular step of 1 degree by the Gaussian elimination method. The calculation process was stopped when the velocity gradient at either the wall or liquid-vapour interface reached zero because the parabolic nature of the equations is not valid for reverse flows. They presented numerical results for a single tube, for falling liquid film between successive tubes, for interaction between tubes at the same horizontal level, and for flooded tubes . Their finding showed that separation of the vapour boundary layer depends on the Froude number. Also, for $G \geq 5.7$, the boundary layer separation did not occur. For tube banks, they announced that their results for global heat transfer coefficient are in good agreement with available experimental results.

Asbik et al. [18] further extended the work of Asbik et al. [17] to investigate the case

of laminar forced convection film condensation in the gravitational direction on a single horizontal elliptic tubes or a bank of elliptic tubes. They concentrated on the effect of eccentricity (ratio of ellipse semi major axis to ellipse semi minor axis lengths) which cause a pressure gradient due to the surface tension force. They also focused on determining the critical angle, θ_c, at which vapour boundary layer separation take places and its impact on the mean heat transfer coefficient. At any angular location, each equation was solved by the TDMA. For single tubes, they generated numerical results for four tubes with various values of the eccentricity ($e = 0.4,\ 0.6,\ 0.8$ and 1.0) but with equivalent surface area. They noted that vapour boundary layer separation is related to vapour Weber number which represents the ratio of inertia forces to surface tension forces. For all tubes, the higher the Weber number, the earlier occurrence of separation. Also, elliptical cylinders experienced separation at a shorter distance from the top compared with a circular tube. Moreover, they observed that decreasing eccentricity (increasing pressure gradient due to surface tension) leads to decline of the parameter ($\overline{\mathrm{Nu}}\,\mathrm{Re}^{-0.5}$). Finally, the results showed good agreement in comparison with available experimental and empirical results.

Chen and Lin [19] investigated numerically the case of laminar film condensation from a downward-flowing mixture of steam-air on a horizontal circular tube. They studied the effect of air mass fraction, mixture velocity and temperature difference on film thickness and rate of heat transfer. In this work, at any point on the tube wall, a Cartesian coordinate system is aligned on the tangent and normal directions to the wall. Two sets of the governing equations were formulated based on boundary layer assumptions. Both thermal diffusion and viscous dissipation in the flow direction were neglected as well as the surface tension effects. More over, the effect of gravity in the mixture region was ignored. Then, the two sets were coupled at the interface by applying continuity of velocity and shear stress, a mass balance, and an energy balance. Potential flow was assumed outside the mixture boundary layer. An implicit finite volume scheme was used to obtain the non-linear algebraic equations from the conservation equations of mass, momentum, and thermal energy for both phases and for

conservation of species for the gas in the mixture phase. The equations were transformed into non-dimensional form by introducing suitable dimensionless parameters to differentiate the phases clearly. The power law scheme was used to interpolate the variables at the cell faces and a Newton-Raphson linearization was used to handle non-linearity and inter-equation coupling. At each axial location, the governing equations were solved iteratively before proceeding to the next location following the implicit marching procedure. They reported that the film thickness distribution has two maxima: one is approximately at the horizontal axes of the tube which related to vapour shear velocity and the other is at the lower stagnation point due to gravity. Moreover, they noted that increasing Reynolds number of the mixture decreases the thickness of the condensate film in the bottom half of the tube where separation occurs. In addition, the local Nusselt number increases as the mass fraction of air decreases or the mixture Reynolds number increases. Also, it was found that the tube wall temperature affects the condensation process significantly in the presence of non-condensable gases so that both the film thickness and the local Nusselt number increase as the free stream to wall temperature difference increases.

Tang et al. [20] modelled film condensation on a horizontal isothermal tube exposed to an air-steam mixture. Although the potential flow approximation of mixture was not used, the two-phase model did not, in general, differ significantly from that presented by Chen and Lin [19] in terms of the set of governing equations used. The body force term was included in both phases but the effect of pressure variation around the tube was ignored, thus eliminating the need to use the potential flow assumption. By so doing, the phenomenon of vapour boundary layer separation that might occur somewhere at the rear half of the tube (depending on mixture upstream velocity U_∞ and properties) was ignored. The two sets of the governing equations were recast in a dimensionless form by introducing the stream function and appropriate dimensionless variables. Then, the equations were solved by a finite difference technique using the central difference scheme except for the convection terms, where the upwind difference scheme was employed. The numerical solutions were obtained

for air mass fraction in the range $0.005 \leq W_\infty \leq 0.15$ and saturation to wall temperature difference in the range, $5\,\mathrm{K} \leq \Delta T \leq 20$ K. They found that introducing the non-condensing gas led to a dramatic decline in the performance of condensation heat transfer even for very small values of gas mass fraction. Also, a good agreement with experimental results of [21] and [22] for the average heat transfer coefficient was reported.

Recently, Li and Peng [23] presented a mathematical model to study laminar condensation of downward flow of air-steam mixture on a horizontal tube. The two-phase analytical model follows the Prandtl boundary layer theory. In the condensate film, the inertia effect was omitted and the temperature was assumed to vary linearly. In addition to the condensate film, a gas film was assumed where gas concentration varies from the bulk value according to the double boundary layer theory. A simplified gas conservation equation that accounts only for advection and diffusion in the normal direction to the tube surface was used in their model. Furthermore, potential flow was assumed at the edge of the gas film while continuity of shear stress was assumed at the liquid-mixture interface. A similarity approach was followed in which the velocity distribution in each boundary layer was obtained by integrating the corresponding momentum equation. Solutions were obtained for film thickness, local heat transfer coefficient, local condensate mass flux and liquid-mixture interfacial temperature profile for a single tube with 14 mm O.D. The results were presented for three mixtures with gas mass fraction, W, values of 0.01, 0.05 and 0.1, three values of upstream velocity of 0.1, 0.3 and 5.5 m/s (Re_d = 68, 204, and 3740), three values of mixture total pressure of 0.9, 1 and 1.1 atm and three values wall temperature of 348, 353 and 358 K. They reported that separation of gas-liquid film has a significant influence on condensation heat transfer.

Sarma et al. [24] presented a single phase model to simulate the process of turbulent film condensation of pure vapour on a horizontal tube. The vapour flows with high velocity vertically in the gravitational direction and the condensate film that forms on the external surface of the tube was assumed to be driven by the body force and the shear force at the interface. As the advection and diffusion terms were neglected in the analysis, the

longitudinal momentum conservation equation became a simple force balance among both shear stresses at the wall and the liquid vapour interface and the weight force of the liquid element. Moreover, only turbulent conduction across the film was considered in forming the thermal energy conservation equation. The film thickness was obtained by a global energy balance across a condensate element. The interfacial shear stress was estimated using the Colburn heat and mass transfer analogy and assuming that the friction coefficients have the same order of magnitude as those of external flow around a cylinder without condensation. In addition, Kato's expression for turbulence [25] was utilized to obtain the eddy diffusivity. The effect of vapour boundary layer separation was omitted in this study. Based on their comparisons with available experimental data, they concluded that using Colburn's analogy to evaluate the interfacial shear stress was successful. Also, using Kato's expression of eddy diffusivity was found to be capable in investigating turbulent condensate films around tubes.

Homescu and Panday [26] studied numerically the problem of forced convection condensation of pure saturated vapour flowing normally downwards on a horizontal isothermal tube. The investigation covered laminar flow and the influence of turbulence in the vapour and liquid phases. Although, the two phase model retained the pressure gradient, advection and thermal energy terms, the boundary layer assumptions were used which led to eliminating the equation for transverse velocity in both phases. Also, the diffusive terms were discarded in the flow direction which converted the actual elliptical nature of the partial differential equations to parabolic one and made it possible to be solved numerically by following a marching technique around the tube. The two phase sets of equations were coupled at the interface by presuming continuity of axial velocity (U) and shear stress and by using a mass balance. Potential flow outside the vapour boundary layer was assumed. At each axial station, the thickness of the condensate film was calculated by performing a heat balance among the heat transferred by conduction at the wall, the heat liberated at the interface due to condensation process, and the heat advected with leaving liquid. Diverse turbulence models based on Prandtl's mixing length hypothesis were used in both the condensate film

and the vapour phase with the assumption of unity for the turbulent Prandtl number. They applied a Van Driest model, a Pletcher model, a Von Karman similarity hypothesis, and Kato's model for the liquid film. They applied a Pletcher model for the vapour flow. The curvilinear domain was converted into a rectangular one to clearly identify the interface and an implicit finite difference scheme was used. They found that both flow and heat transfer characteristics were significantly influenced when turbulence was considered. Moreover, they noticed that the combination of applying Kato's model in the liquid side and Pletcher's turbulence model in the vapour region gave estimations of average heat transfer coefficients that are in good agreement with available experiments for steam and for refrigerant R-113.

Lin and Yang [27] presented a theoretical study simulating turbulent smooth film condensation of pure saturated vapour on a non-isothermal tube. Only the condensate film was considered in the model. They investigated the effect of non-uniform wall temperature variation, the Froude number, sub-cooling parameter, and system pressure parameter on the condensation and condensing heat transfer characteristics. At any angular location, the proposed Cartesian coordinate system is aligned on the tangent and normal directions to the wall. The partial differential equation that represents conservation of momentum within the film were replaced by a simple force balance on a condensate element which equated the wall shear stress to the sum of interfacial shear stress and the net weight of the element. The interfacial shear stress was obtained from the asymptotic solution of the vapour boundary layer with strong suction due to condensation. Also, both transient and convective terms of the energy equation in the film were omitted because they assumed that turbulent conduction within the film is more significant than the convective terms. Potential flow around a circular tube was assumed to prevail at the liquid-vapour interface. It was also assumed that the film thickness was much smaller than the radius of the tube. A dimensionless set of the governing equations was obtained by introducing suitable parameters. With these assumptions, a simple model consisting of three equations has been evolved to simulate the described problem. The calculation process was started at the top of the tube assuming zero

film thickness. Then, the solution process was proceeded to the next angular station, when the unknown variables ($u,\ \delta,\ \ T$) were solved using marching technique with an angular increment of ($\Delta\theta = \frac{\pi}{500}$) until the whole surface was covered. They noted that their results coincide with same experimental results for higher vapour velocities. Also, despite the magnitude of the vapour velocity, non-uniformity of the wall temperature had an insignificant effect on the mean heat transfer coefficient.

Yang and Lin [28] used their previous model to investigate the effect of the interfacial eddy diffusivity on turbulent film condensation process on a non-isothermal horizontal tube subjected to a forced flow of vapour. form were formulated. However, the advection terms as well as the diffusion term in the flow direction (x) were neglected. The momentum eddy diffusivity appeared in the energy equation after assuming a turbulent Prandtl number of 1. A Hilpert semi-empirical model was used to express the average Nusselt number in terms of Re, Pr, and some constants. Also, Colburn's analogy was utilized to get a formula for the mean friction coefficient. The half tube wall was covered ($0 \leq \theta \leq \pi$) by using 500 steps in a marching technique. The results indicated that the interfacial eddy diffusivity had a considerable effect on both film thickness and heat transfer characteristics. For very high vapour velocity, including the eddy diffusivity led to a decrease in the predicted mean condensing heat transfer coefficient. Also, non-uniformity of the wall temperature had a negligible effect on the predictions of the mean heat transfer coefficient despite the magnitude of vapour velocity.

Chen and Lin [29] extended their previous two phase model to study the problem of 2D steady-state turbulent smooth film condensation in the presence of a non-condensing gas over a horizontal isothermal tube. A finite volume method and a uniform staggered grid were used to obtain the algebraic set of the governing equations. The solution domain extended beyond the momentum, thermal, and mixture concentration boundary layers of the mixture phase. A mixing length turbulence model based on Prandtl theory was followed to simulate turbulence effects in both regions. The effects of free stream velocity, wall temperature, and

water vapour mass fraction in the free stream were considered. It was found that the presence of non-condensable gas leads to a considerable decrease in the local heat flux due to higher heat resistance produced by higher air concentration just above the interface. They also noted that the thickness of condensate film decreased as the free stream velocity increased or vapour concentration decreases in the mean stream. Moreover, they found that at any free stream concentration of non-condensable gas, decreasing surface temperature of the tube leads to an increase in both the local heat flux and the film thickness.

One other study of film flowing on a tube is relevant to this work. Min and Choi [30] studied a free falling film on a horizontal tube for an absorption process. Although this study did not consider the condensation process, it used the fully elliptic set of the governing equations instead of the boundary layer based set and had mass transfer at the phase interface. They modelled the absorption phenomena of water vapour about a free falling liquid film of $LiBr + H_2O$ solution on a horizontal isothermal tube. The mathematical model consisted of the continuity equation, momentum equation, energy equation, and diffusion equation for two dimensional flow. Uniform conditions were assumed for the free stream. Also, the falling film was assumed to approach the top of the tube with a constant thickness. The surface tension effects were included and shear stress at interface was ignored because low Re was assumed. The Marker-and-Cell method (MAC) was used to determine the position of the interface. Their procedure involves using of two fixed grids for the same problem. First, they used an orthogonal grid to determine the interface location using the MAC method. Then, a non-orthogonal grid was constructed using the interface as a fixed boundary. The SIMPLER algorithm was then used to handle the pressure velocity coupling of the Navier-Stokes equations. Results for heat and mass transfer and film thickness were presented for whole range of the tube angle θ. They found that a small and significant recirculation occurs next to the interface in the film region at the lower stagnation point which affect the absorption process especially at low flow rates.

1.3.3 Summary of Previous Theoretical Work

From the review of the previous theoretical works, it can be concluded that the problem of condensation over a horizontal tube was handled using either a single phase (condensate film) models or two-phase models. In the single phase approaches, a single simplified momentum equation was integrated over the film thickness using presumed boundary conditions to obtain an equation for the velocity in the main flow direction. Following the concept of similarity, this velocity profile was assumed to be valid along the circumference of the tube. The only exception is the second model of Denny and Mills [5] where the boundary layer equations were solved numerically using a finite difference method. Energy equation was replaced by a simple energy balance assuming linear profile for the temperature. In studies where pressure changes were considered (such as in [11, 13, 14]) , the pressure gradient around the tube was obtained from potential flow. Shear effects at the interface were included in most studies using the asymptotic expression for the interfacial shear stress.

In the two-phase approaches, the boundary layer equations or a more simplified forms were used for both phases. The boundary layer assumptions change the elliptic spacial behaviour of the governing equations to a parabolic behaviour as the case in the most sophisticated recent studies (such as [17, 19, 29]). Potential flow outside the vapour or mixture boundary layer was assumed and used to account for pressure variation around the tube. Continuity of shear stress condition was applied at the interface. The parabolic set can be solved by using marching technique in the main flow direction (x direction) as the solution is supposed to be affected only by the upstream conditions. The gravity vector is rotated with the moving coordinate along the surface to emulate the correct gravity force. Either a finite difference method or a finite volume method was used in all studies except Fujii et al. [6] and Gaddis [8]. The marching process had to be stopped once reverse flow occurred as the set of the governing equations is no longer valid in representing the problem.

The absorption study [30] managed to solve the fully elliptic set of the governing equa-

tions using MAC method to obtain the the interface location. The interface location was determined by an orthogonal fixed grid then a non-orthogonal fixed grid that coincides with the interface was used treating the interface as a fixed boundary. This method still does not represent shear stress and condensation at the interface with a dynamically moving interface.

1.3.4 Review of Previous Experimental Work

In addition to an analytical study, Fujii et al. [6] also conducted experiments for condensation of steam over a horizontal tube. A 14 mm O.D and 10.4 mm I.D brass tube was inserted into 92 mm circular duct. The peripheral variation of tube wall temperature was measured by eight thermocouples distributed equally on the circumference. Cooling water was pumped in the tube and flow of steam was passed inside the circular duct over the horizontal tube in cross flow mode. The experiments covered steam to wall temperature difference of 0.75 to 1.97 K and oncoming velocity range of 7.2 to 71.3 m/s. The observations showed that the wall temperature varied circumferentially and both inlet velocity of vapour flow and local condensation had an influence on it. Also, they stated specifically that the agreement between theoretical and experimental results is fairly good for average heat transfer coefficient.

Rauscher et al. [31] performed an experimental study to investigate the effects of air on condensation process from pure steam and steam-air mixtures flowing downward over a horizontal tube. Their stainless steel test tube had 0.504" (1.28 cm) I.D. and 0.7505" (1.9 cm) O.D. Five pairs of calibrated thermocouples were mounted on the circumference in equal spaced manner for heat flux measurements. Then, the test tube was put horizontally in a 5" (12.7 cm) I.D. glass chamber where a forced downward flow of well-mixed mixtures were directed towards the tube. For pure saturated vapour, results were presented for saturation temperatures of 108 °F to 152 °F (42.2°C to 66.7°C), bulk to wall temperature difference of 3 °F to 21 °F (1.7°C to 11.7°C) with velocity ranges from 1.25

to 3.16 ft/s (0.38 m/s to 0.96 m/s). The used range of the inlet velocity corresponds to ($357 \leq \mathrm{Re}_d \leq 903$). The average normalised heat flux (compared to the Nusselt solution) for all five peripheral stations was within 0.98 with a deviation of ± 0.10. For the mixtures, the experiments were run for saturation temperatures of 98 °F to 142 °F (36.7°C to 61.1°C), bulk to wall temperature difference of 5.3 °F to 31 °F (2.9°C to 17.2°C), air mass fraction of $0.0006 - 0.07$, and inlet velocities of 0.95 to 5.80 ft/s (0.29 m/s to 1.77 m/s) ($273 \leq \mathrm{Re}_d \leq 1666$). They reported the average values of the normalised heat flux agreed with average and maximum discrepancy of -2.7% and 7.1 %, respectively, compared to a laminar boundary layer model presented by Denny and South [7].

Fujii et al. [32] presented theoretical and experimental study to investigated condensation over horizontal tubes. In the experimental section, they conducted experiments to study the effect of oncoming horizontal velocity of saturated steam on condensation over a horizontal tube. A copper test tube of 37.7 mm O.D and 30.0 mm I.D as well as a brass test tube of 18.6 mm O.D and 12.6 mm I.D were used. The tube wall temperature was measured at eight circumferentially and axially distributed locations. The experiments covered steam saturation temperature range of 296 to 312 K (saturation pressure from 0.03 to 0.125 bar), steam to wall temperature difference of 1.8 to 8 K, and oncoming velocity range of 0.6 to 80 m/s. According to their observations, independently from the steam velocity, the condensate film manifested as either a continuous laminar film, droplets or a broken " wrinkled" liquid film. Based on their experimental data and a collection of experimental data from a number of sources [33–35], two experimental dimensionless correlations were proposed for the average heat transfer coefficient as follows:

$$\overline{\mathrm{Nu}}\,\mathrm{Re}^{-1/2} = 0.96 \left(\frac{\mathrm{Pr}_L}{\mathrm{Fr}\,\mathrm{Ja}}\right)^{1/5} \quad \text{for} \quad 0.03 < \left(\frac{\mathrm{Pr}_L}{\mathrm{Fr}\,\mathrm{Ja}}\right) < 600 \tag{1.5}$$

$$\overline{\mathrm{Nu}} = 0.70 \left(\frac{\mathrm{Ga}\,\mathrm{Pr}_L}{\mathrm{Ja}}\right)^{1/4} \quad \text{for} \quad \left(\frac{\mathrm{Pr}_L}{\mathrm{Fr}\,\mathrm{Ja}}\right) > 600 \tag{1.6}$$

Comparing with experimental data of [33] for horizontal flow and [34] and [35] for downward flow, they concluded that direction of vapour flow has no considerable effect on the average heat transfer coefficient in the investigated range of vapour velocity.

In order to validate their theoretical results, Honda et al. [9] conducted an experimental study on condensation of slightly superheated R-113 vapour flowing downward on a horizontal tube. The test section consisted of a 110 mm x 100 mm rectangular duct. Two copper tubes with 8mm and 37.1 mm O.D. were used. Ten thermocouples were used to measure surface temperature at different longitudinal and circumferential locations of the tubes. The experiments covered vapour to tube wall temperature difference of 9.9 K to 39.1 K and vapour velocity range of 0.1 to 9 m/s. They noticed that a steep increase in the condensate film thickness occurs as a result of vapour boundary layer separation preceded by small ripples. The relation between the normalised heat flux (the experimental condensation heat flux normalised by the heat flux calculated by the thermal resistance network model), and two-phase Reynolds number are presented. For two-phase Reynolds number less than or equal 3×10^4, the experimental value were within 9% for steam from experimental data of [36] and 6% for R-113 from the numerical predictions. For two-phase Reynolds number in the range of 3×10^4 to 10^5, their data for R-113 showed an increase in the heat flux up to 20% with increasing Reynolds number due to heat transfer enhancement caused by the ripples.

An experimental investigation of forced convection film condensation over a horizontal tube was conducted by Lee and Rose [37]. The effect of the presence of non-condensable gas (air and hydrogen) in steam and R-113 vapours were considered in this study. Two different condenser tubes of (7.5 mm I.D and 12.5 mm O.D.) and (22.0 mm I.D and 25.3 mm O.D.) were used. Four thermocouples were embedded in the outer surface of each tube with 90° angular increment. The average tube surface temperature was calculated via the arithmetic mean of the four readings of the thermocouples. Finally, each tube was place individually in a cylindrical test section that had 152.4 mm I.D. where vapours or mixtures flowed vertically

downwards. The experimental data dealt with pressure range of 4 to 124 kPa, vapour velocity of 0.3 to 26 m/s and gas mass fraction of 0.0002 to 0.32. For moderate velocities, they proved that heat transfer measurements of pure vapour for both steam and R-113 were, in general, in good agreement those predictions based on the theoretical approach of Fujii et al. [6]. Moreover, higher predicted average Nusselt number values than the experimental ones were found at the high velocities which was guessed to be a consequence of tube non-uniform wall temperature. Lee and Rose proposed a correlation equation for local interfacial mass flow rate as a function of Reynolds number, Schmidt number, and gas mass fraction at the interface and in the free stream.

Memory and Rose [38] conducted an experimental study on film condensation of ethylene glycol on a horizontal tube with vapour flowing vertically downwards at high velocity. Results were generated for vapour pressure ranging from 1 kPa to 20 kPa, vapour velocity up to 135 m/s and wide range of heat flux. In general, they noted that the obtained experimental results were in good agreement with laminar boundary layer models [4, 6] except at the highest velocities and lowest pressures. They attributed this deviation to properties change (mainly for viscosity) within the condensate film with temperature difference and variations in the tube wall temperature. Moreover, they reported that at high vapour velocity and low pressure, effects of pressure variation around the tube and of interface-mass transfer become significant.

Michael et al. [39] investigated experimentally forced convection condensation of pure steam and mixtures of steam-nitrogen flowing vertically downward on a horizontal tube. Experiments were run for vapour velocity in the range from 5 m/s to 81 m/s ($3468 \leq \mathrm{Re}_d \leq 5.6 \times 10^{+4}$) with degrees of superheat in the range from 2 K to 40 K. These conditions indicate that there will be a laminar and turbulent flow in the film and the vapour. The copper test tube had 14.0 mm O.D., 9.88 mm I.D., and 141.5 mm exposed length. To determine the average surface temperature of the tube, six thermocouples were embedded in the outer surface of the tube wall at equal angular intervals of 60°. Then, the test tube was

inserted in 180 mm x 80 mm rectangular test section where condensation took place at near atmospheric pressure as a result of cooling the tube by demineralized water. They found that steam superheat had negligible effect on the heat transfer coefficient for the range used. Also, it was concluded that the laminar boundary layer condensation approaches by [4, 6] were precise only at low vapour velocity ($F > 1$), while the conjugate vapour to coolant heat transfer model by Honda and Fujii [40] deviated by about $\pm 18\%$ up to $F \approx 0.014$. Finally, they noted that, for $F < 0.014$, the heat transfer coefficient of the steam increased with a rate greater than the square root of the vapour velocity which was attributed to the beginning of turbulence in the condensate film.

Briggs and Sabaratnam [41] conducted an experimental investigation for condensation of steam and steam-air mixtures on a single horizontal tube and a staggered arrangement tube bank. The test section had a rectangular shape with 272 mm length, 52.4 mm width and 250 mm height. Test tubes were made of copper with 19.0 mm O.D., 12.7 mm I.D., and 272 mm length. At an angle of 22.5° from the top and with 90° increments, four thermocouples were implanted in the outer surface of each tube just at the middle. For the tube bank, ten identical tubes were arranged staggeringly with equilateral triangle diagonal of 272 mm. For single tubes, the experiments covered inlet velocities of 1.2 to 5.6 m/s ($1129 \leq \mathrm{Re}_d \leq 5272$) and air mass fractions of 0 to 0.293. For tube banks, the experiments covered inlet velocities of 4.4 to 10.4 m/s and air mass fraction of 0 to 0.152. It was concluded that for pure steam, a good agreement was achieved between the experimental data and predictions for single tube model given by Equation (1.2) when the arithmetic mean velocity was used for both the single tube and tubes bank. For steam-air mixtures, in contrast to the single tube case where a reasonable agreement was found, a poor agreement was noticed for the tubes bank with the single tube models. This disagreement was attributed to the more complex flow pattern in the tube bank.

1.3.5 Summary of Previous Experimental Work

From the review of the previous experimental work, one can conclude that condensation over a horizontal tubes has been the topic of numerous experimental studies. In these studies, pure vapour or/and mixture of vapour and non-condensing gas were considered. In those studies, effects of different flow parameters on the condensation process were considered. More over, effects of both lighter and heavier non-condensing gas compared to the vapour were investigated.

In terms of potential comparison with results from the current work, experimental correlation equations like Equations (1.5) and (1.6) of Fujii et al. [32] could be used for pure vapour case. For steam-air mixture, no correlation equations can be found in the literature. Because the used range of Re_d in Rauscher et al. [31] ($273 \leq \mathrm{Re}_d \leq 1666$) and Briggs and Sabaratnam [41] ($1129 \leq \mathrm{Re}_d \leq 5272$) exceeded the limit of stable flow post a cylinder, comparisons with those studies are not possible with the current model.

1.4 Two Phase Flow Interface Modelling

1.4.1 Problem of the Interface

The interface considered in this work is a surface that separates gas and liquid phases. These phases can be phases for the same substance, like the case of condensation of pure vapour, or different substance as the case of condensation of vapour in mixture of vapour and gas.

At the gas-liquid interface, phenomena such as surface tension and mass transfer may take place while the interface shape is changing. The main challenge of the moving boundary problem is that the exact location of the interface is not known, so it must be part of the solution. Resolving the shape of the interface accurately and having it as a continuous curve enables the precise implementation of models of important interface phenomena. At the

interface, flow fields must be coupled appropriately by forcing certain physical conditions that relate the variables in each side of the interface. These conservation laws and the interfacial conditions have to work in harmony with a suitable method to determine the interface location.

Numerous methods have been developed to determine the location of the interface in two phase flow problems. Depending on how sharp the shape of the interface is resolved, these methods can be roughly classified [42] into two categories: (1) *interface-tracking methods* and (2) *interface-capturing methods*. Alternatively, methods that deal with moving boundary problems can be classified as *Eulerian*, *Lagrangian* and *Mixed Eulerian-Lagrangian* [43]. A brief introduction for each category using the first classification is presented in the next sections.

1.4.2 Interface Tracking Methods

These methods define the interface as a sharp surface that separates the two phases. The grid boundary must coincide with the interface at each time step. The calculations are performed on a fixed overall physical domain. At the end of each time step, the location of the mesh is adjusted to coincide the interface by applying a suitable physical condition. As the shape of the moving boundary is determined sharply, the balances of force, mass, and energy at the interface can be implemented accurately. In practice, moving the grid must be done very carefully in order to avoid artificial mass sources that could cause serious convergence problems. In addition, time step restrictions may occur because of the grid movement algorithm.

1.4.3 Interface Capturing Methods

Two-phase flow problems can also be simulated by using a fixed mesh computational that covers the entire physical domain. In general, the interface between the two phases fluids does not coincide with any of the grid sides. A single set of governing equations is used to model the two-phases. This approach is usually referred to as a one-fluid approach. In order to simulate a two-phase problem, the selected grid has to be smaller than any physical length in the problem and the chosen time step has to be shorter than any time scale of the problem. The position of the interface is captured on a fixed mesh with limited accuracy by either marker points (surface or front tracking) or a marker function (volume tracking). An example of surface tracking is the Marker-and-Cell method, MAC [44]. This section will focus on the volume tracking method.

Methods involving usage of a marker function include the volume-of-fluid (VOF), the level-set method, the phase field method, and the constrained interpolated propagation method [44]. In these methods, a step function f is introduced to distinguish between different fluids and to determine physical properties of fluids due to the discontinuity at the interface. Moreover, this function is used to include effects of interfacial phenomena at the interface like surface tension. These interface concentrated effects are handled by a Dirac delta function.

The value of the step function is assigned to unity where a certain fluid exists and zero elsewhere. Numerically, this function can smoothly change from one to zero over a transition region at the interface. The interface location is inferred by a nonzero gradient of the function f. The marker function f is advected by the flow and the interface location by a pure advection equation. Then, the interface is reconstructed by various algorithms. The main disadvantage of these methods is their inability to depict the interface location and curvature accurately. Also, the resolution is limited by the cell size and may result in smearing of the interface. Therefore, implementing interfacial phenomena requires special

care. On the other hand, these methods can handle complex phenomena such as breaking waves.

1.5 Objectives

Judging from the summary mentioned in Section 1.3.3 for previous theoretical work on condensation over horizontal tubes, no study has yet been done on simulation of the condensation process by solving the actual full elliptic set of Navier-Stokes governing equations even for laminar pure vapour condensation. The present study will investigate the problem with more detailed approach. The main features of the current approach can be summarised as follows:

1. A more fundamental and complete approach that uses a full elliptic set of the governing equations will be developed to study the condensation over the whole range of tube angle ($0^o \leq \theta \leq \pi/2$).
2. Full solution of the film around the tube and in the falling film region below the tube.
3. The film thickness on the top of the tube is found naturally from the solution.
4. Full viscous flow solution for the mixture flow. No assumption of potential flow is needed.
5. The effects of non-condensable gas, pressure variation around the tube, reverse flow, and interfacial shear stress will be considered fundamentally.
6. The shape of the interface boundary will be determined sharply. As a result, the balances of force, mass, and energy at the interface will be implemented accurately. With sharply determined interface, other interfacial phenomena such as surface tension and evaporation can be implemented accurately in the future.

7. The model will be applied for pure vapour condensation as well as condensation of vapour from mixtures of vapour and non-condensing gas.

Chapter 2

Mathematical Model

2.1 Assumptions

A numerical study of fluid flow, heat transfer and other related processes is conducted by applying conservation laws on a volume in space that is called a control volume. In this work, the conservation equations of mass, momentum and energy for the liquid film and the mixture region are formulated by assuming incompressible, laminar, viscous, Newtonian fluid flow in both phases. Variable thermophysical properties are used. A smooth gas-liquid interface is assumed. The phase interface is impermeable to gas; therefore, no gas exists in the liquid. The governing equations are written for each phase. The phase equations are connected through jump conditions enforced at the liquid-mixture interface.

2.2 Governing Equations

For the two-phase flow problem to be modelled as shown in Figure 1.1, the governing partial differential equations (continuity, momentum, energy, and conservation of species for the gas) in Cartesian coordinates for both regions are given below.

2.2.1 Liquid Region

- Liquid continuity equation

$$\frac{\partial}{\partial t}(\rho_L) + \frac{\partial}{\partial x}(\rho_L U_L) + \frac{\partial}{\partial y}(\rho_L V_L) = 0 \tag{2.1}$$

- Liquid x-momentum conservation equation

$$\frac{\partial}{\partial t}\ (\rho_{_L} U_{_L}) + \frac{\partial}{\partial x}(\rho_{_L} U_{_L} U_{_L}) + \frac{\partial}{\partial y}(\rho_{_L} V_{_L} U_{_L}) = -\frac{\partial P_{_L}}{\partial x} + \frac{\partial}{\partial x}\left(\mu_{_L}\frac{\partial U_{_L}}{\partial x}\right) + \frac{\partial}{\partial y}\left(\mu_{_L}\frac{\partial U_{_L}}{\partial y}\right) + \rho_{_L}\ g_x \tag{2.2}$$

- Liquid y-momentum conservation equation

$$\frac{\partial}{\partial t}\ (\rho_{_L} V_{_L}) + \frac{\partial}{\partial x}(\rho_{_L} U_{_L} V_{_L}) + \frac{\partial}{\partial y}(\rho_{_L} V_{_L} V_{_L}) = -\frac{\partial P_{_L}}{\partial y} + \frac{\partial}{\partial x}\left(\mu_{_L}\frac{\partial V_{_L}}{\partial x}\right) + \frac{\partial}{\partial y}\left(\mu_{_L}\frac{\partial V_{_L}}{\partial y}\right) + \rho_{_L}\, g_y \tag{2.3}$$

- Liquid energy conservation equation

$$\frac{\partial}{\partial t}\left(\rho_{_L}\, C_{p_{_L}}\, T_{_L}\right) + \frac{\partial}{\partial x}\left(\rho_{_L}\, U_{_L}\, C_{p_{_L}}\, T_{_L}\right) + \frac{\partial}{\partial y}\left(\rho_{_L}\, V_{_L}\ C_{p_{_L}}\, T_{_L}\right) = \frac{\partial}{\partial x}\left(k_{_L}\frac{\partial T_{_L}}{\partial x}\right) + \frac{\partial}{\partial y}\left(k_{_L}\frac{\partial T_{_L}}{\partial y}\right) \tag{2.4}$$

2.2.2 Mixture Region

- Mixture continuity equation

$$\frac{\partial}{\partial t}(\rho_{_M}) + \frac{\partial}{\partial x}(\rho_{_M}\, U_{_M}) + \frac{\partial}{\partial y}(\rho_{_M}\, V_{_M}) = 0 \tag{2.5}$$

- Mixture x-momentum conservation equation

$$\frac{\partial}{\partial t}\ (\rho_M\, U_M) + \frac{\partial}{\partial x}(\rho_M\, U_M\, U_M) + \frac{\partial}{\partial y}(\rho_M\, V_M\, U_M) = -\frac{\partial P_M}{\partial x} + \frac{\partial}{\partial x}\left(\mu_M\, \frac{\partial U_M}{\partial x}\right) + \frac{\partial}{\partial y}\left(\mu_M\, \frac{\partial U_M}{\partial y}\right) + \rho_M\, g_x \tag{2.6}$$

- Mixture y-momentum conservation equation

$$\frac{\partial}{\partial t}\ (\rho_M\, V_M) + \frac{\partial}{\partial x}(\rho_M\, U_M\, V_M) + \frac{\partial}{\partial y}(\rho_M\, V_M\, V_M) = -\frac{\partial P_M}{\partial y} + \frac{\partial}{\partial x}\left(\mu_M \frac{\partial V_M}{\partial x}\right) + \frac{\partial}{\partial y}\left(\mu_M \frac{\partial V_M}{\partial y}\right) + \rho_M\, g_y \tag{2.7}$$

- Mixture energy conservation equation

$$\frac{\partial}{\partial t}\left(\rho_M\, C_{p_M}\, T_M\right) + \frac{\partial}{\partial x}\left(\rho_M\, U_M\, C_{p_M}\, T_M\right) + \frac{\partial}{\partial y}\left(\rho_M\, V_M\, C_{p_M}\, T_M\right) = \frac{\partial}{\partial x}\left(k_M \frac{\partial T_M}{\partial x}\right) + \frac{\partial}{\partial y}\left(k_M \frac{\partial T_M}{\partial y}\right) + \frac{\partial}{\partial x}\left(\rho_M\, D^{ab}\left(C_{p,G} - C_{p,V}\right) \frac{\partial W}{\partial x} T_M\right) + \frac{\partial}{\partial y}\left(\rho_M\, D^{ab}\left(C_{p,G} - C_{p,V}\right) \frac{\partial W}{\partial y} T_M\right) \tag{2.8}$$

- Gas mass conservation equation

$$\frac{\partial}{\partial t}(\rho_M\, W) + \frac{\partial}{\partial x}(\rho_M\, U_M\, W) + \frac{\partial}{\partial y}(\rho_M\, V_M\ W) = \frac{\partial}{\partial x}\left(\rho_M\, D^{ab} \frac{\partial W}{\partial x}\right) + \frac{\partial}{\partial y}\left(\rho_M\, D^{ab} \frac{\partial W}{\partial y}\right) \tag{2.9}$$

The last two terms in Equation (2.8) arise from energy transport that is associated with mass transfer. Although the scope of this work is to model steady flows, the transient terms in the momentum, energy, and gas mass conservation equations are retained to introduce relaxation towards a steady-state solution in the numerical solution approach.

The other unknown in the model is the location of the phase interface. This is nominally defined as the normal distance of the interface from the tube wall and referred to as the film thickness, δ.

2.3 Model Domain and Boundary Conditions

Because of symmetry, half the physical problem may be solved. The solution domain for the problem is shown in Figure 2.1. A suitable set of boundary conditions must be applied for each variable. These conditions constrain the values or the derivatives of each dependent variable (U, V, P, T, and W) at the boundaries according to the problem being investigated. The boundary conditions are shown in Figure 2.1. These conditions can be summarised for both regions at four boundaries of the computational domain as follows:

- At the first part of the inlet boundary, (free stream boundary 1):

  $U_M = U_\infty$, $\frac{\partial V_M}{\partial n} = 0$, $T_M = T_\infty = T_{\text{sat}}$ and $W = W_\infty$.

- At the second part of the inlet boundary, (free stream boundary 2):

  $\frac{\partial U_M}{\partial y} = 0$, $\frac{\partial V_M}{\partial y} = 0$, $T_M = T_\infty = T_{\text{sat}}$ and $W = W_\infty$.

- On the tube wall, no slip condition for the velocity and constant temperature:

  $U_L = 0$, $V_L = 0$ and $T_L = T_{\text{wall}}$

- At the vertical centre line adjacent to the liquid above and below the tube, symmetry conditions:

  $\frac{\partial U_L}{\partial y} = 0$, $V_L = 0$, and $\frac{\partial T_L}{\partial y} = 0$

  In addition, $\frac{\partial \delta}{\partial y} = 0$ is applied in the liquid at the top of the tube.

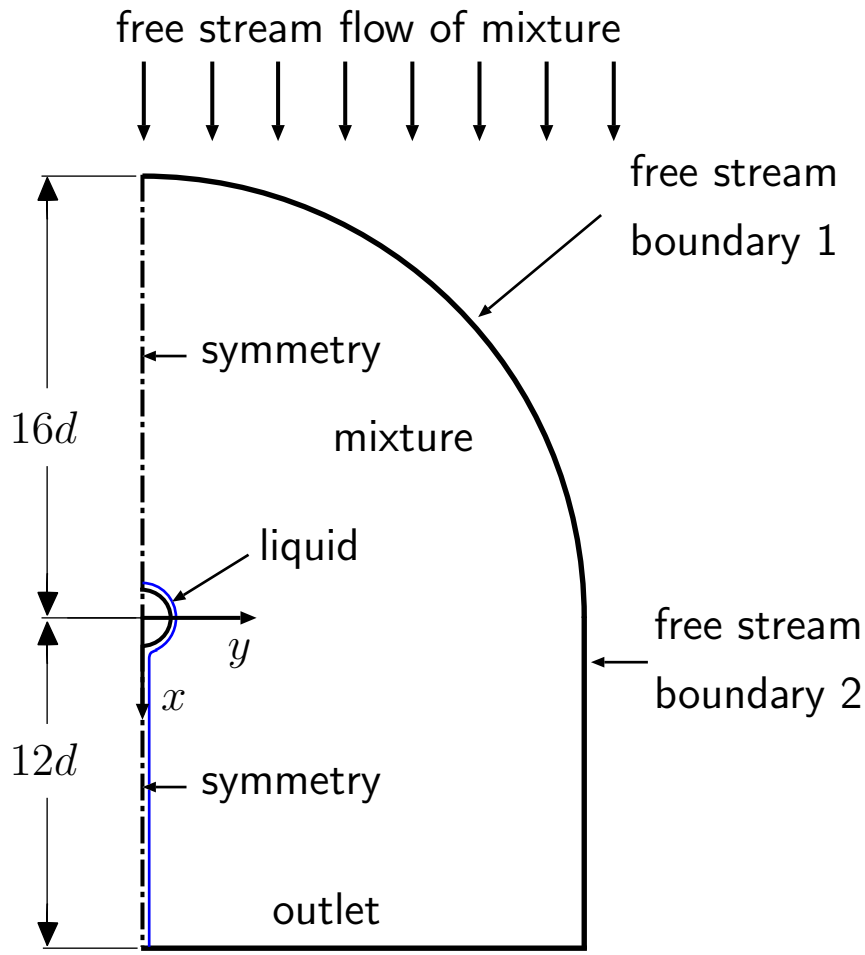

Figure 2.1: Domain definition.

- At the vertical centre line adjacent to the mixture, symmetry conditions:

  $\frac{\partial U_M}{\partial y} = 0$, $V_M = 0$, $\frac{\partial T_M}{\partial y} = 0$, and $\frac{\partial W_M}{\partial y} = 0$

- At the outlet, fully developed flow conditions for both phases:

  $\frac{\partial U_L}{\partial x} = \frac{\partial V_L}{\partial x} = \frac{\partial T_L}{\partial x} = 0$ and $\frac{\partial U_M}{\partial x} = \frac{\partial V_M}{\partial x} = \frac{\partial T_M}{\partial x} = \frac{\partial W_M}{\partial x} = 0$

An alternative boundary condition for V along free stream boundaries 1 and 2 could have been $V = 0$. This condition is strictly applicable only at an infinite distance from the tube. Because a finite solution domain size is used, the zero gradient boundary conditions on V

used in this work that allow entrainment are more appropriate.

The solution pressure is relative to a reference pressure of zero that is specified at a point along the outlet boundary. For the purposes of evaluating the properties only, the difference between the absolute free stream pressure, P_∞, and the solution pressure at $y = 0$ and $x = -16d$ was added to the entire pressure field. The rounded shape of the free stream boundary 1 was selected because of grid generation constraints. More details of those constraints will be discussed in Chapter 3.

2.4 Balance Conditions at the Interface

The equations that relate phase variable at the interface are referred to as the jump conditions (or the *kinematic* and *dynamic* conditions). These conditions ensure balance of force, mass, and energy at the interface.

The conditions are:

1. normal force balance

$$(\hat{n} \cdot \boldsymbol{T})_L \cdot \hat{n} = (\hat{n} \cdot \boldsymbol{T})_M \cdot \hat{n} \tag{2.10}$$

where $\boldsymbol{T}$ is the stress tensor, $\hat{n}$ is the local normal unit vector to the interface. The surface tension effects have been neglected. The stress tensor ($\boldsymbol{T}$) for 2D is defined as follows:

$$\boldsymbol{T} = \begin{pmatrix} \boldsymbol{T}_{xx} & \boldsymbol{T}_{yx} \\ \boldsymbol{T}_{xy} & \boldsymbol{T}_{yy} \end{pmatrix} \tag{2.11}$$

The details of $\boldsymbol{T}_{xx}$, $\boldsymbol{T}_{yx}$, $\boldsymbol{T}_{xy}$, and $\boldsymbol{T}_{yy}$ are given in Equations (4.86) to (4.88).

2. tangential force balance

$$(\hat{n} \cdot \boldsymbol{T})_L \cdot \hat{s} = (\hat{n} \cdot \boldsymbol{T})_M \cdot \hat{s} \tag{2.12}$$

where $\hat{s}$ is the local tangential unit vector at the interface.

3. tangential velocity equality

$$\overrightarrow{V}_{t,L,\text{int}} = \overrightarrow{V}_{t,M,\text{int}} \tag{2.13}$$

4. mass balance at the interface: liquid side

$$\dot{m}_{L,\text{int}} = \dot{m}_{M,\text{int}} \tag{2.14}$$

5. mass balance at the interface: mixture side

$$\dot{m}_{M,\text{int}} = -\dot{m}_{\text{cond}} \tag{2.15}$$

where

$$\dot{m}_{\text{cond}} = \frac{A_n}{h_{fg}} \left(k_L \frac{\partial T_L}{\partial n}\bigg|_{\text{int}} - k_M \frac{\partial T_M}{\partial n}\bigg|_{\text{int}} \right) \tag{2.16}$$

6. mixture side pressure gradient

$$\frac{\partial P}{\partial n}\bigg|_{\text{int},M} = 0 \tag{2.17}$$

This condition is assumed to obtain a second pressure condition at the interface. The second condition for the pressure at the interface is needed because the numerical solution approach uses two rows of nodes at the interface. The interface nodes will be discussed later in Chapters 3 and 4.

7. saturation temperature at the interface

$$T_M = T_{\text{sat}}(P_{V,\text{int}}) \tag{2.18}$$

where vapour pressure at the interface, $P_{V,\text{int}}$, is a function of the pressure and the gas mass fraction at the interface. The vapour and gas pressure are calculated at any point in the mixture region using the following equations:

$$P_{\text{V}} = P_{\text{tot}} - P_{\text{G}} = P_{\text{tot}} \left[\frac{(1 - W)\, M_G}{M_G + W\,(M_V - M_G)} \right] \tag{2.19}$$

8. continuity of temperature

$$T_{L,int} = T_{M,int} \tag{2.20}$$

9. gas impermeability

$$\dot{m}_{M,\text{int}} W_{\text{int}} - \left(\rho_M A D^{ab}\right)_{\text{int}} \left.\frac{\partial W}{\partial n}\right|_{\text{int},M} = 0 \tag{2.21}$$

No condition is needed for W at the interface on the liquid side because W is not defined in the liquid.

2.5 Property Evaluation

Liquid water, steam and air with variable properties are considered in this study to enhance accuracy of the results. In this study, calculation of the properties is based on the work of Siow [45].

The specific heat, thermal conductivity and viscosity for both liquid water and steam are evaluated using linear interpolation in a look-up table based on data from Incropera and DeWitt [46].

For the air, the specific heat, thermal conductivity and viscosity are evaluated for a wide range of temperature using correlation expressions given in Irvine and Liley [47]. The relation between the saturation temperature and pressure for the steam is determined using correlation expressions given in Irvine and Liley [47] for pressure range of 611 Pa to 22.1 MPa

which is corresponding to saturation temperature range of 273.16 K to 674.3 K. Liquid density and latent heat of vaporization are calculated for the same range of P_{sat} and T_{sat} using correlations given in Irvine and Liley [47].

Steam-air mixtures are assumed to behave as an ideal gas. Therefore, both steam and air densities are calculated using ideal gas equation of state and partial pressure of each substance. The assumption of ideal gas behaviour for steam is valid because the steam partial pressure is much lower than the critical point pressure for water. The error introduced in calculating the water vapour density using the ideal gas law for this work is estimated to be 1.5% or less.

Once the properties of the mixture components are determined separately, the overall properties of the mixture can be calculated. The thermal conductivity, viscosity and binary diffusion coefficient of the mixture are calculated as suggested in Reid et al. [48]. According to Dalton model for ideal gas mixtures, the density of the mixture is the sum of both steam and air densities. The specific heat of the mixture is evaluated based on the mass fraction of each component. Detailed equations related to properties determination that were used in this study are given in Appendix A of [45].

2.5.1 Summary of the Governing Equations

The governing equations for the model are nine non-linear coupled partial differential equations for the unknown U_L, V_L, T_L, P_L, U_M, V_M, T_M, P_M, and W. These equations are strongly coupled at the liquid-mixture interface. The location of the phase interface is not known *a prior* and must be found as part of the solution. In addition, thermophysical properties are function of the solution temperature and pressure.

Chapter 3

Grid Generation

3.1 Introduction

In this work a non-orthogonal grid was used for the geometric flexibility needed to match exactly the phase interface shape. A structured grid was chosen because of the simplicity of the sparse matrix and ease of use of available solvers. The grid cells have a quadrilateral shape. The overall solution domain mesh can be constructed using multiple grid segments (panels) in each coordinate direction. The cells in each panel can expand or contract to improve grid quality as needed.

3.2 Grid Generation method

The grid is generated using an algebraic transfinite method. The advantages of transfinite methods include fast generation of the grid and enabling direct control on the positions of grid points [49]. The first advantage is very important in this work because the mesh is re-generated at each time step. Direct control of the grid points on panel boundaries permits refinement of the grid near the phase interface. The disadvantage of transfinite interpolation is poor control of grid smoothness away from boundaries.

In this method, the four vertices that enclose a domain or part of a domain are specified. Then, the four sides that connect the vertices can be specified either as straight lines, an arc with specified radius, or a curve defined by a collection of points. Along each side, distribution of the grid points is controlled by a geometric expansion factor. Then, two-dimensional interpolation is applied to compute location of interior points in respect to the four vertices. Depending on the boundaries, connecting opposite grid points forms a mesh

with square, rectangle or quadrilateral shaped control volumes. All essential grid information including cell-centre coordinates, distances, areas, volumes are computed accordingly. This topic will be discussed in more detail in the next section.

3.2.1 Grid geometry

To illustrate the notation used in grid generation, a sample grid region showing a typical control volume P and its neighbours is presented in Figure 3.1. The control volume P is surrounded by eight neighbouring control volumes. Compass point notation is used to refer to location of neighbouring control volumes relative to the central one. A global indexing system is introduced such that each control volume is identified uniquely by a pair of integer indices (i, j). The control volume surface area consists of four faces. These faces are distinguished by lower case letters according to their relative location to the centre. The control volume centre is assigned to the computational node. As a simple way to illustrate how the

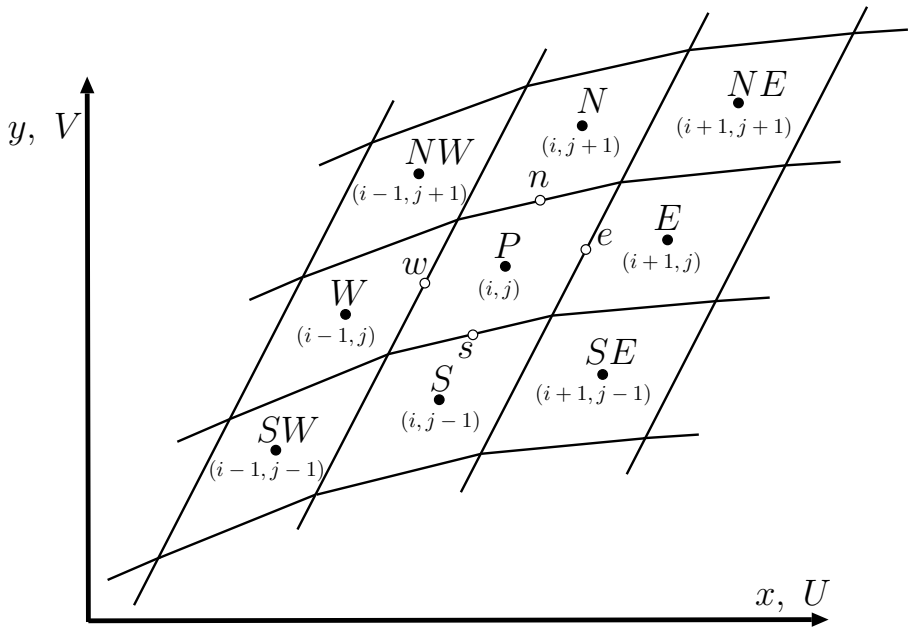

Figure 3.1: Computational molecule: indexing and notation.

interface between the two phases is implemented in the grid generation, a sample complete computational grid for liquid-mixture flow in a horizontal duct is shown in Figure 3.2. Nominally, one grid segment is used in the index i direction and two segments are used in the j direction (one for each phase).

A zero-width interface splits the computational domain into two regions in the j direction: one region for each phase. The region in the computational domain that is below the interface (adjacent to the bottom wall) is designated for the liquid film. The region on the opposite side of the interface is occupied by the mixture.

At the first column of interior control volume, the value of index $i = i_B = 2$. Then, the value of index i advances in the west to east direction to reach $i = i_E = N_x + 1$ where N_x is the number of interior control volumes in the i direction.

At the first row of the interior control volumes, the magnitude of index $j = j_B = 2$. The index j progresses in the south to north direction to reach $j = j_E = N_y + 3$ at the last row where N_y is the number of interior control volumes in the j direction.

In this example grid for illustration purposes, the liquid side has four interior nodes in the j direction ($N_{y,L} = 4$) and eight interior nodes in the i direction ($N_x = 8$) while the mixture region has been divided to five cells in the j direction ($N_{y,M} = 5$). Along the domain outer boundaries, zero width control volumes are used to apply the boundary conditions. These control volumes are usually referred to as fictitious control volumes and denoted by open circles in Figure 3.2.

The interface consists of two rows of zero-width control volumes. The lower row ($j = j_{EL} + 1$) represents the liquid phase side of the interface and the upper row ($j = j_{BM} - 1$) represents the mixture phase side of the interface. The interface nodes are at the same physical location. In Figure 3.2, however, the spacing between those nodes is exaggerated to emphasize that there are two sets of nodes. These two rows are used to couple solution fields in both phases by assigning each interfacial balance condition to a certain flow variable, as

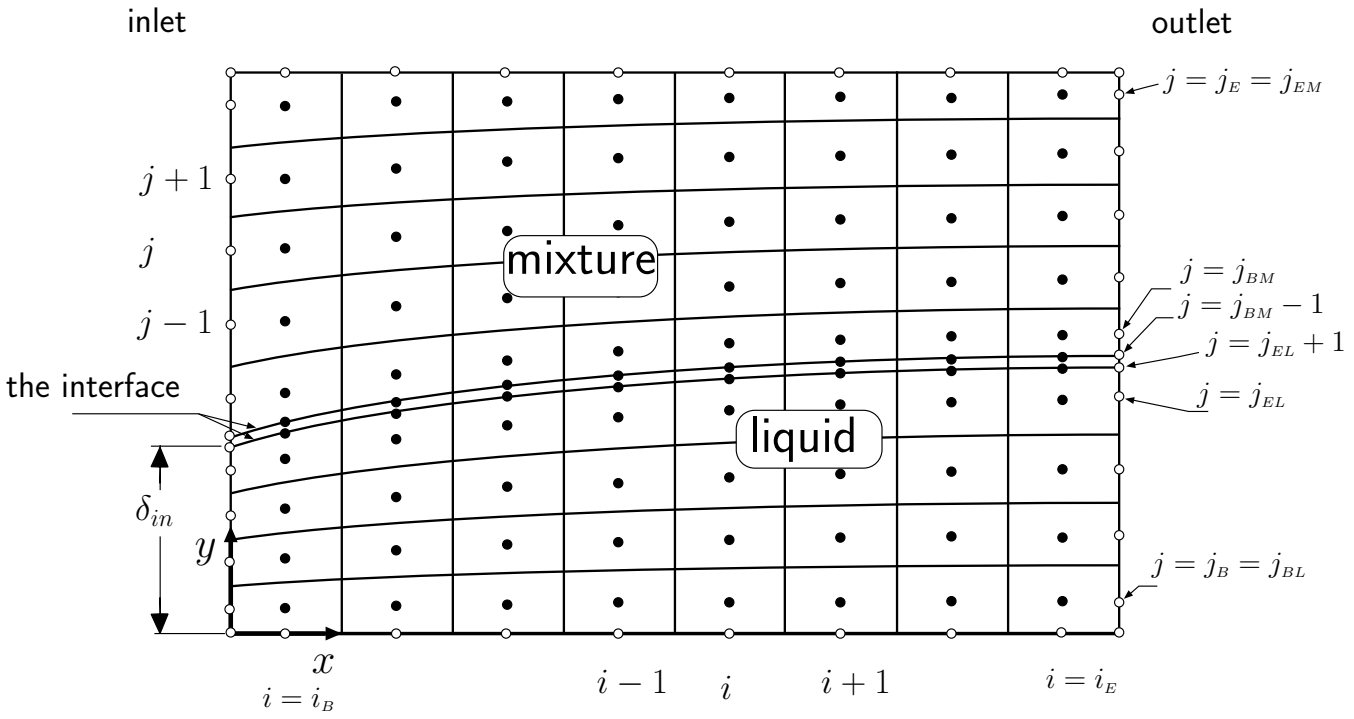

Figure 3.2: Sample grid showing nomenclature used. The spacing between the nodes at the interface is exaggerated for illustration purposes.

discussed later in Chapter 4. The interior nodes including the interfacial nodes are shown as solid circles in Figure 3.2.

It is important to notice that the grid origin and the indices starting point, i.e. $(i_B - 1, j_B - 1)$, do not necessarily coincide on each others. Furthermore, depending on the geometry of the domain, neither index i nor index j will necessarily align with the coordinates directions x and y.

Each control volume consists of four quadrant divisions as shown in Figure 3.3. Each point on a face of the control volume is located at the centre of the face. The control volume nodal point P with the coordinates (x_p, y_p) is located at the geometrical centre of the control volume by interpolating between points e, w, n, and s. To reduce memory usage and avoid redundancy, only the coordinates of points P, e, n and ne (indicated by solid

circles in Figure 3.3) are calculated and stored for all control volumes. Other points are derived as needed from the stored points of neighbouring control volumes. Distances, areas

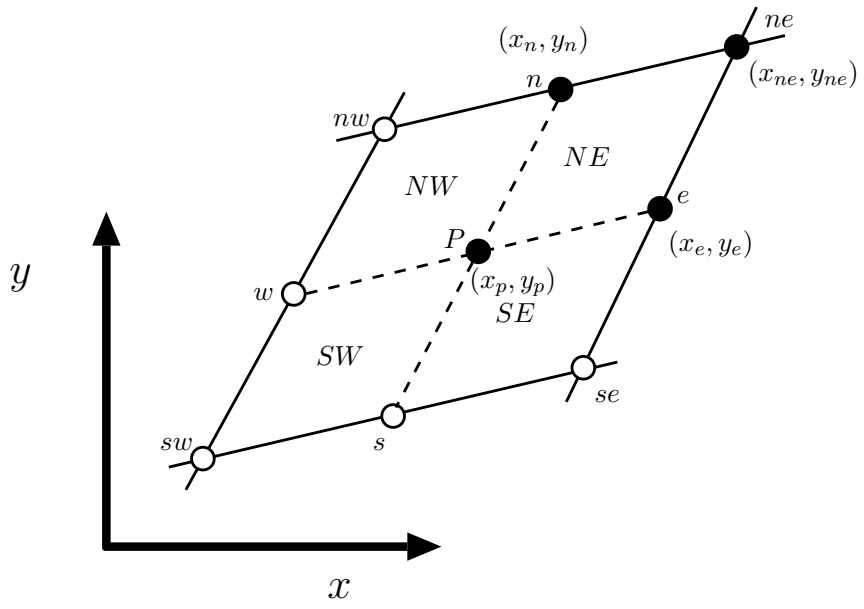

Figure 3.3: Coordinates of control volume points and quadrant notation.

and volumes associated with a typical interior control volume are displayed in Figure 3.4. Knowing the coordinates of both relevant points, each distance indicated in Figure 3.4 is calculated accurately. Areas and volumes are computed using a unit depth.

To ensure precise calculation of the volume of a control volume, each quadrant of a control volume is divided into two triangles. The area of both triangles are calculated, added and multiplied by the depth to determine the volume of each control volume division. Then, the volumes of the four quadrant are added to determine the volume of the control volume.

In order to accurately evaluate different quantities (mass flow, momentum, heat flux) crossing surfaces of any control volume for non-orthogonal grids, some local unit vectors are needed. Figure 3.5 shows directions of unit vectors for the east face, north face and at the node of interior control volume. These unit vectors do not necessarily align with the

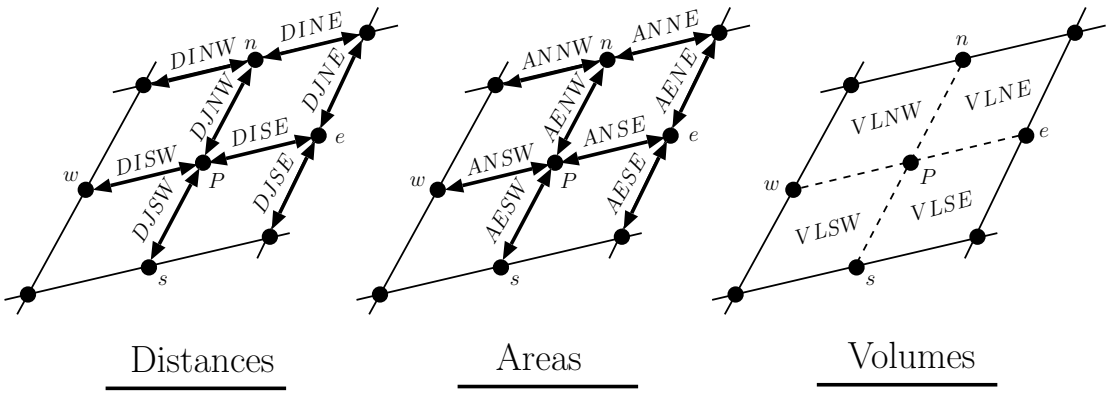

Figure 3.4: Distances, areas and volumes of a control volume.

Cartesian unit vectors $\hat{\imath}$ and $\hat{\jmath}$. In general, the unit vector $\hat{s}$ denotes moving along the i index while the unit vector $\hat{t}$ denotes moving along the j index. The unit vector $\hat{n}$ is the normal to the face (it is outward normal for e and n faces, and inward normal for s and w faces). The subscript e, n, and p are used to refer to east face, north face and the node of the control volume. At the east face, the unit vector $\hat{s}_e$ gives the direction of the line that connects nodal point P to its direct neighbour in i direction; the unit vector $\hat{t}_e$ is tangent to the east face. At the north face, the unit vector $\hat{t}_n$ refers to direction of the line that connects nodal point P to its direct neighbour in j; the unit vector $\hat{s}_n$ is tangent to the north face. At the node P, two unit vectors are introduced. The unit vector $\hat{s}_P$ determines the direction of the imaginary line that connects the centre point of the west face, w, to counterpart point at the east face, e. The unit vector $\hat{t}_P$ gives direction of the imaginary line connecting point s to point n on the south and north face respectively. The unit vectors at the west and south face of control volume P, (i, j), are deduced from those at the adjacent west and south control volumes.

The unit vectors at the east and north faces of a control volume and at the centre that are shown in Figure 3.5 are defined in terms of their components in the x and y direction as:

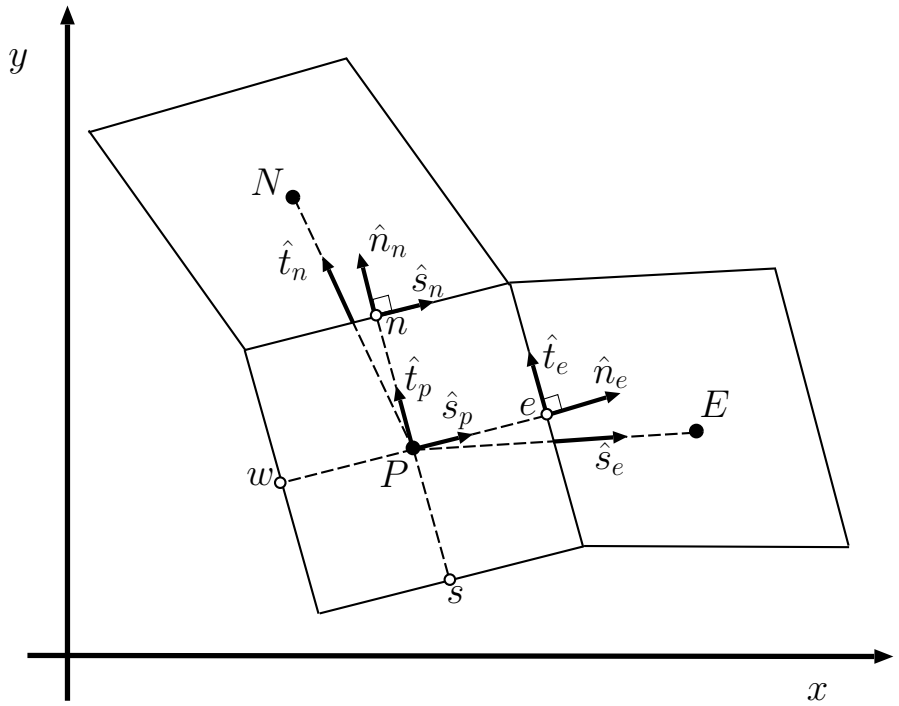

Figure 3.5: Grid directional unit vectors.

$$
\left.
\begin{aligned}
\hat{n}_n &= \left.\frac{\partial x}{\partial n}\right|_n \hat{\imath} + \left.\frac{\partial y}{\partial n}\right|_n \hat{\jmath} = n_{xn}\,\hat{\imath} + n_{yn}\,\hat{\jmath} \\
\hat{n}_e &= \left.\frac{\partial x}{\partial n}\right|_e \hat{\imath} + \left.\frac{\partial y}{\partial n}\right|_e \hat{\jmath} = n_{xe}\,\hat{\imath} + n_{ye}\,\hat{\jmath} \\
\hat{s}_n &= \left.\frac{\partial x}{\partial s}\right|_n \hat{\imath} + \left.\frac{\partial y}{\partial s}\right|_n \hat{\jmath} = s_{xn}\,\hat{\imath} + s_{yn}\,\hat{\jmath} \\
\hat{s}_e &= \left.\frac{\partial x}{\partial s}\right|_e \hat{\imath} + \left.\frac{\partial y}{\partial s}\right|_e \hat{\jmath} = s_{xe}\,\hat{\imath} + s_{ye}\,\hat{\jmath} \\
\hat{s}_p &= \left.\frac{\partial x}{\partial s}\right|_p \hat{\imath} + \left.\frac{\partial y}{\partial s}\right|_p \hat{\jmath} = s_{xp}\,\hat{\imath} + s_{yp}\,\hat{\jmath} \\
\hat{t}_n &= \left.\frac{\partial x}{\partial t}\right|_n \hat{\imath} + \left.\frac{\partial y}{\partial t}\right|_n \hat{\jmath} = t_{xn}\,\hat{\imath} + t_{yn}\,\hat{\jmath} \\
\hat{t}_e &= \left.\frac{\partial x}{\partial t}\right|_e \hat{\imath} + \left.\frac{\partial y}{\partial t}\right|_e \hat{\jmath} = t_{xe}\,\hat{\imath} + t_{ye}\,\hat{\jmath} \\
\hat{t}_p &= \left.\frac{\partial x}{\partial t}\right|_p \hat{\imath} + \left.\frac{\partial y}{\partial t}\right|_p \hat{\jmath} = t_{xp}\,\hat{\imath} + t_{yp}\,\hat{\jmath}
\end{aligned}
\right\} \tag{3.1}
$$

For more details about calculating the components of each unit vector in x and y direction, the reader is referred to [50].

Some distances are repeatedly used in the computations. Therefore, it is worthwhile being calculated and stored once. These distances are shown in Figure 3.6. The distances $(ds)_P$ and $(dt)_P$ for node P are calculated as follows (see also Figure 3.4):

$$(ds)_{P_{(i,j)}} = DISW_{(i,j)} + DISE_{(i,j)} \tag{3.2}$$

$$(dt)_{P_{(i,j)}} = DJSW_{(i,j)} + DJNW_{(i,j)} \tag{3.3}$$

At the east and north faces, the distances $(dt)_e$ and $(ds)_n$ along the grid lines are:

$$(dt)_{e_{(i,j)}} = DJNE_{(i,j)} + DJSE_{(i,j)} \tag{3.4}$$

$$(ds)_{n_{(i,j)}} = DINW_{(i,j)} + DINE_{(i,j)} \tag{3.5}$$

At the west and south faces, the distances $(dt)_w$ and $(ds)_s$ are respectively equal to $(dt)_e$ at $(i-1,j)$ and $(ds)_n$ at $(i,j-1)$.

Two additional distances $(ds)_e$ and $(dt)_n$ are defined for non-orthogonal grids. The distance $(ds)_e$ connects nodal point P to E being calculated as follows:

$$(ds)_{e_{(i,j)}} = \sqrt{\left(XSW_{(i+1,j)}XSW_{(i,j)}\right)^2 + \left(YSW_{(i+1,j)}YSW_{(i,j)}\right)^2} \tag{3.6}$$

Finally, the distance $(dt)_n$ connects nodal point P to N is given by:

$$(dt)_{n_{(i,j)}} = \sqrt{\left(XSW_{(i,j+1)}XSW_{(i,j)}\right)^2 + \left(YSW_{(i,j+1)}YSW_{(i,j)}\right)^2} \tag{3.7}$$

Note that when grid lines orientation changes rapidly between adjacent control volumes, intersection of line $(ds)_e$ with the east face deviates considerably from face centre point e. The amount of the deviation reflects lack of smoothness of the grid. A similar condition exists for line $(dt)_n$ and the north face.

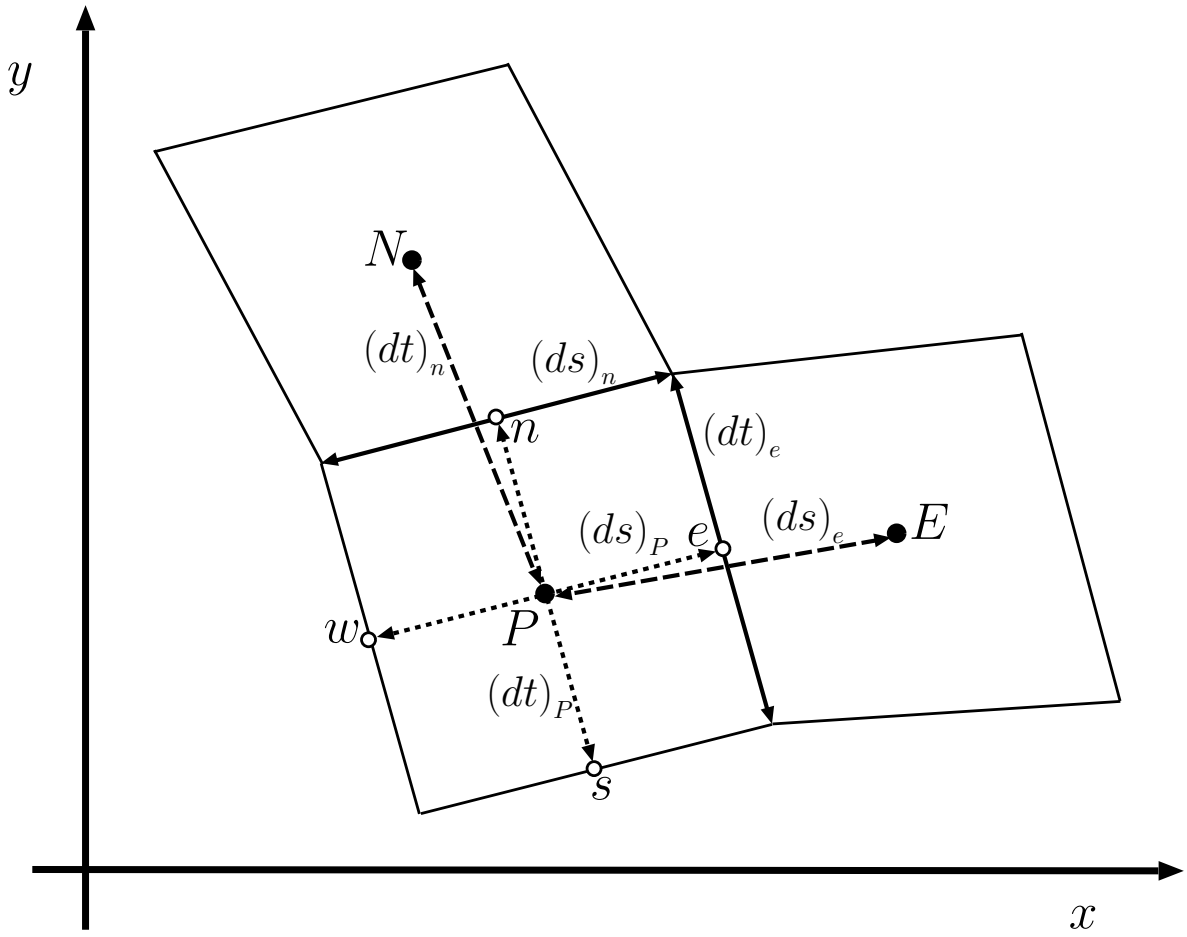

Figure 3.6: Clarification of common distances.

3.2.2 Grid expansion factor

It is often advantageous to refine the grid in regions where relatively rapid changes in flow variables occur, such as near a wall and at an interface between two phases.

A geometric expansion factor is a parameter that can be used independently at each side of a grid segment to specify the length ratio between two adjacent control volumes. For example, along the x direction.

$$r_x = \frac{ds_{n(i+1)}}{ds_{n(i)}} \tag{3.8}$$

According to the value of the expansion factor, grid cells are expanding if $r_x > 1$, contracting if $r_x < 1$, and uniform if $r_x = 1$. If L_x is the length of a grid segment at one side and N_x is the number of nodes along it, the relation between length of the first cell (ds_{n1}), L_x, and N_x is derived by employing the recursive relation in Equation (3.8) as follows:

$$\begin{aligned} L_x &= \sum_{i=1}^{N_x} ds_{ni} = ds_{n1} + ds_{n2} + ds_{n3} + ... + ds_{nN_x} \\ &= ds_{n1} + r_x\ ds_{n1} + {r_x}^2\ ds_{n1} + ... + {r_x}^{N_x-1}\ ds_{n1} \\ &= ds_{n1}\ \sum_{i=1}^{N_x} {r_x}^{i-1} = ds_{n1}\ \frac{\left(1-{r_x}^{N_x}\right)}{(1-r_x)} \end{aligned} \tag{3.9}$$

In the case where the segment is an arc, the expansion factor is applied to the increment of the arc central angle. If the grid is composed of multiple grid segments or panels, it is crucial to ensure smooth transition between grid panels. This can be accomplished when size of the last control volume from the preceding panel and the first control volume of the following panel are comparable in size. Also, large aspect ratio in the grid control volumes should be avoided. Even though a non-orthogonal grid is needed to match exactly the tube wall and phase interface shapes, grid orthogonality should be maintained as much as possible to make use of its favorable numerical performance.

3.3 Grid Assembly (Paneling)

Generating a grid using a paneling technique has many advantages such as exactly matching exterior boundaries and permitting direct control of grid refinement where it is required. The latter can enhance accuracy of the solution and improve the convergence rate. Because a structured grid is used, any two adjacent panels must have the same number of control volumes at the matching side.

Figure 3.7 shows an illustrative example of grid assembly using the paneling technique applied to the solution domain in Figure 2.1. In this example, twelve panels are used to construct the overall computational domain. It is worthwhile to mention that thickness of the liquid film is magnified in Figure 3.7 for clarification. Furthermore, panels boundaries are highlighted by thicker lines to be distinguished easily. The grid indices starting point is located at the top of the tube. Beginning at the top of the tube, panels 1 to 4 represent the liquid film. In the illustrative example in Figure 3.7, the liquid film is divided into four uniformly spaced control volumes in the index j direction. In the sample shown, liquid panels 1, 2, 3 and 4 have five, seven, six and five control volumes in the index i direction, respectively. To resolve the flow near the tube bottom accurately, control volumes of panel 2 are contracting in the i direction. For the same purpose, control volumes of panel 3 are expanding in the i direction.

The mixture region is covered by two rows of panels. The first row consists of panels 5 to 8 with, for this example, five expanding control volumes in the j direction to refine the grid at the interface. The second row contains panels 9 to 12 with, for this example, three control volumes in j direction. A mixture grid panels must have the same number of control volumes in i direction as the liquid panel beneath it. For example, both panels 5 and 9 have 5 control volumes in i direction to be in consistent with panel 1. Finally, it can be noticed that grids in panels 1, 4, 5, 8, 9, 10, 11 and 12 are kept as orthogonal as possible. The arc-shaped boundary of free stream boundary 1 (which is the outer boundary of panel 9) was necessary to avoid strong grid skewing.

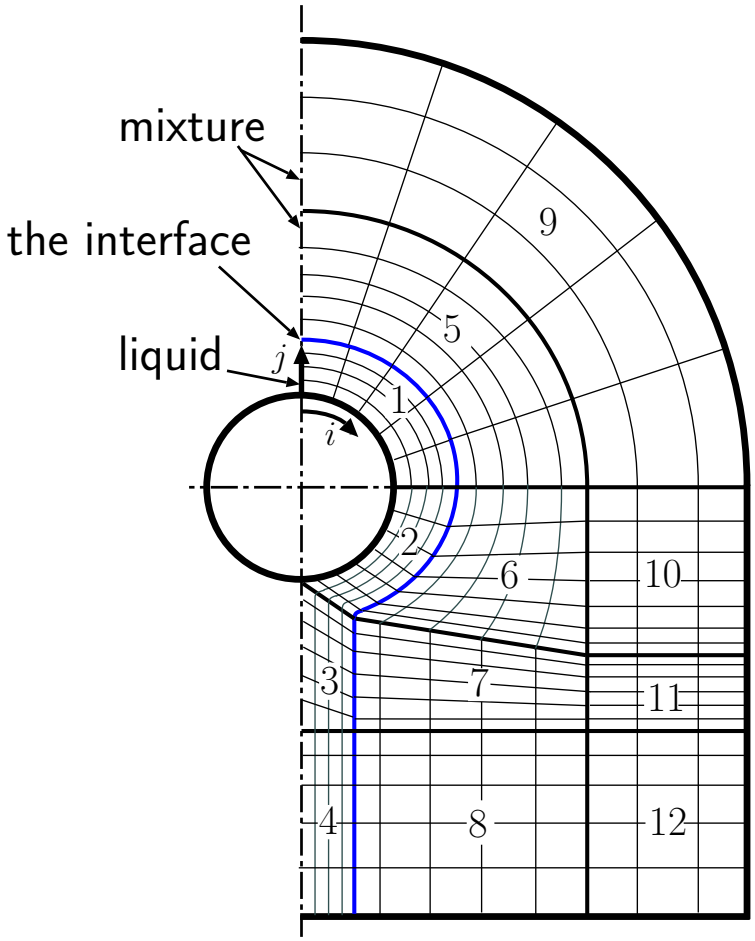

Figure 3.7: Example of grid assembly: condensation over a horizontal tube. The size of the liquid region is exaggerated for clarity.

3.4 Grid Configuration in the Liquid Film

As will be seen later, the location of the interface is re-calculated as the solution progresses, and it converges to a final location for a converged solution. Therefore, a new grid is generated based on the most recent location of the interface in a so-called dynamic grid generation method. The film growth or decrease can be done by moving the interface points along the j direction. Therefore, the local coordinate ξ, as shown in Figure 3.8, was defined. As the interface moves, it is important to ensure that grid lines do not tangle. To accomplish this

task, direction of grid lines in the j direction as well as direction of interface growth are specified so that grid entanglement is unlikely to happen.

For this reason, a scheme for specifying orientation of grid lines along the domain in the liquid film has been developed as will be explained with the aid of Figure 3.8. For $0° \leq \theta \leq 135°$, (i.e. from point A to C), the coordinate ξ is normal to the tube surface. Consequently, an orthogonal grid is obtained at this region of the film. For $135° < \theta \leq 180°$, (i.e. from point C to D), the ξ direction as well as the grid lines are fixed at 135° from the symmetry line to preclude severely skewed control volumes, especially at the bottom of the tube. As a result, angles between grid lines at the bottom of the tube, (at point D), are at at 45° from the horizontal. Then, the ξ orientation changes gradually to coincide later with the y direction at a certain distance downstream of the tube, (at point E).

It is noteworthy that due to the method used to generate the grid that relies only on the four boundary points of a panel, the j index grid lines at a given i index are not guaranteed to be co-linear especially near the bottom of the tube. However, this deviation from all ξ-direction lines falling in a single line is insignificant because the film thickness is very small. In this case, the ξ direction refers to the imaginary line connecting point (x_{ne}, y_{ne}) at $(i, j_B - 1)$ to point (x_{ne}, y_{ne}) at (i, j_{EL}). When the interface location is moved, it always moves along the ξ direction.

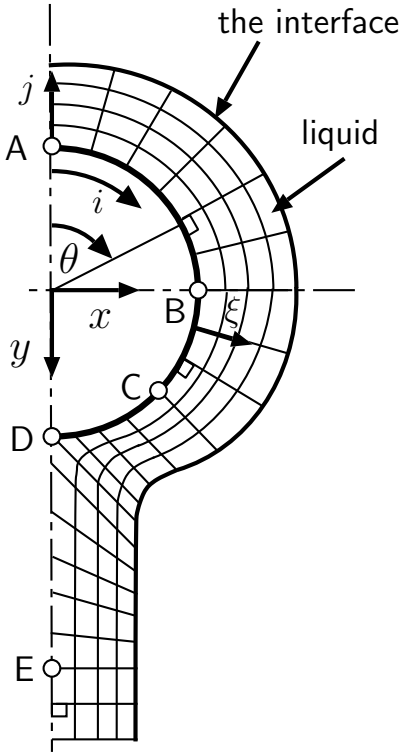

Figure 3.8: Grid configuration in the liquid film.

Chapter 4

Discretisation of the Governing Equations

4.1 Introduction

The numerical solution approach is based on obtaining an algebraic analogue of the governing equations and their boundary conditions. A finite volume method [51] is used to obtain the algebraic equations. The key details of the storage location of variables and the application of the discretisation procedure for the main governing equations are presented in this chapter.

4.2 Finite Volume Method

A co-located variable storage scheme is used in this work, so that all the variables are defined at the centre of a typical control volume as shown in Figure 4.1. The face velocities must satisfy the conservation of mass principle both locally and globally while the nodal velocities satisfy the conservation of momentum principle. The typical computational molecule consists of a central control volume and its eight neighbours as shown in Figure 3.1. The discretisation procedure used in this work integrates each term of each governing equation over the typical control volume and over a time step. The discretisation of the equations in each phase is the same procedure. Therefore, the methodology will be shown only once generically for U and V. These equations will apply to liquid or mixture variables. Because the mixture temperature, T_M, equation contains two more terms than the liquid equation, the discretisation is shown for the mixture equation. Only, the discretisation of those extra terms is given in detail. The W equation discretisation is shown for completeness. In the discretisation, field variables with no superscript represent values at the new time step; variables with a superscript "o" are at the previous time step.

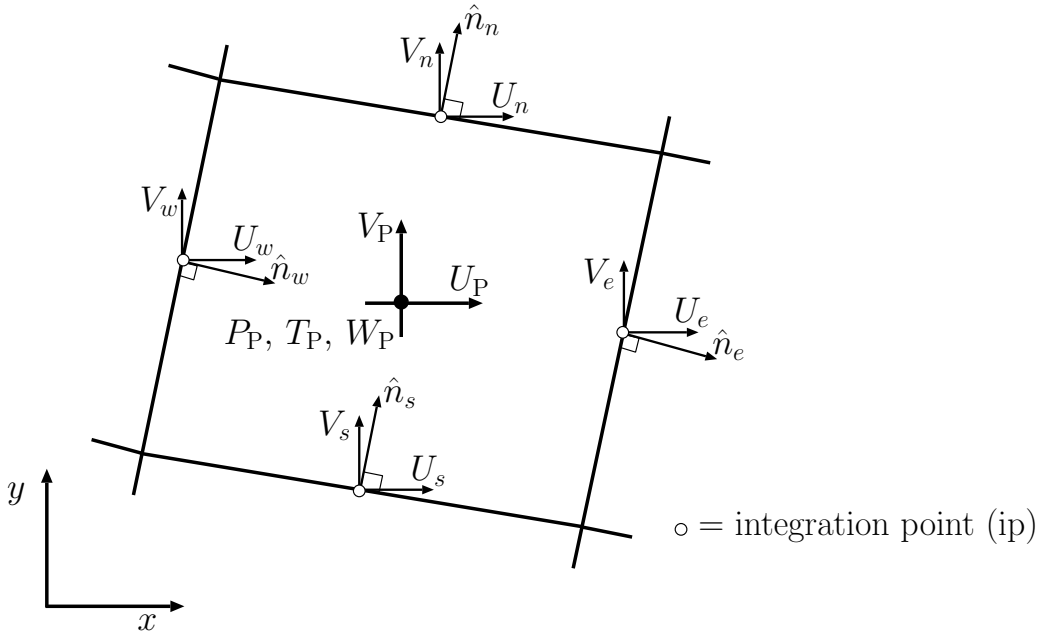

Figure 4.1: Co-located variable storage scheme.

4.3 Algebraic Transport Equations

4.3.1 The Continuity Equation

The discretisation of Equation (2.1) or (2.5) can be shown generally as follows:

$$\underbrace{\int_{\forbar}\int_t \left\{\frac{\partial}{\partial t}(\rho)\right\} d\forbar\, dt}_{I} + \underbrace{\int_{\forbar}\int_t \left\{\frac{\partial}{\partial x}(\rho\, U)\right\} d\forbar\, dt + \int_{\forbar}\int_t \left\{\frac{\partial}{\partial y}(\rho\, V)\right\} d\forbar\, dt}_{II} \quad = \quad 0 \quad (4.1)$$

The first term in Equation (4.1) represents the storage term. Its integration yields

$$I = \int_{\forbar}\int_t \left\{\frac{\partial}{\partial t}(\rho)\right\} d\forbar\, dt = \forbar_P(\rho - \rho^o)_p = M_P - M_P^o \quad (4.2)$$

The second and third terms in Equation (4.1) (term II) represent the net mass flow rate in the x and y directions respectively. The integration in the second term represents an integration over the volume $\forbar$ and it can be carried out together using the Gauss divergence

theorem as follow:

$$II = \int_{\forall}\int_{t}\left\{\frac{\partial}{\partial x}(\rho\, U)\right\} d\forall\, dt + \int_{\forall}\int_{t}\left\{\frac{\partial}{\partial y}(\rho\, V)\right\} d\forall\, dt \approx \Delta t \int_{\forall} \overrightarrow{\nabla} \cdot \left(\rho \overrightarrow{V}\right) d\forall$$
$$= \Delta t \int_{S} \rho \overrightarrow{V} \cdot \hat{n}\; dS = \Delta t \sum_{f} \rho_f A_f \overrightarrow{V}_f \cdot \hat{n}_f$$
$$= \Delta t \left\{(A_e)\rho(U_e n_{xe} + V_e n_{ye}) - (A_w)\rho(U_w n_{xw} + V_w n_{yw})\right\}$$
$$+ \Delta t \left\{(A_n)\rho(U_n n_{xn} + V_n n_{yn}) - (A_s)\rho(U_s n_{xs} + V_s n_{ys})\right\} \quad (4.3)$$

Now substituting all three terms into Equation (4.1) leads to:

$$\left\{\rho(A_e) n_{xe}\, U_e + \rho(A_e) n_{ye}\, V_e\right\} - \left\{\rho(A_w) n_{xw}\, U_w + \rho(A_w) n_{yw}\, V_w\right\}$$
$$+ \left\{\rho(A_n) n_{xn}\, U_n + \rho(A_n) n_{yn}\, V_n\right\} - \left\{\rho(A_s) n_{xs}\, U_s + \rho(A_s) n_{ys}\, V_s\right\}$$
$$+ \frac{M_P - M_P^o}{\Delta t} = 0 \quad (4.4)$$

After collecting and arranging, the mass conservation equation will take the following form:

$$\left(A_{\mathrm{e}}^{c,u}\, U_e + A_{\mathrm{e}}^{c,v}\, V_e\right) + \left(A_{\mathrm{w}}^{c,u}\, U_w + A_{\mathrm{w}}^{c,v}\, V_w\right)$$
$$+ \left(A_{\mathrm{n}}^{c,u}\, U_n + A_{\mathrm{n}}^{c,v}\, V_n\right) + \left(A_{\mathrm{s}}^{c,u}\, U_s + A_{\mathrm{s}}^{c,v}\, V_s\right) + b_{\mathrm{P}}^{c} = 0 \quad (4.5)$$

Where the details of the coefficients are:

$$\left.\begin{array}{ll} A_{\mathrm{e}}^{c,u} = -\rho(A_e) n_{xe} & A_{\mathrm{e}}^{c,v} = -\rho(A_e) n_{ye} \\ A_{\mathrm{w}}^{c,u} = \rho(A_w) n_{xw} & A_{\mathrm{w}}^{c,v} = \rho(A_w) n_{yw} \\ A_{\mathrm{n}}^{c,u} = -\rho(A_n) n_{xn} & A_{\mathrm{n}}^{c,v} = -\rho(A_n) n_{yn} \\ A_{\mathrm{s}}^{c,u} = \rho(A_s) n_{xs} & A_{\mathrm{s}}^{c,v} = \rho(A_s) n_{ys} \\ b_{\mathrm{P}}^{c} = -\frac{\left(M_P - M_P^o\right)}{\Delta t} & \end{array}\right\} \quad (4.6)$$

The mass flow rates across all four faces of any control volume are given by the following expressions:

$$\left.\begin{array}{lllll} \dot{m}_e &=& -A_{\mathrm{e}}^{c,u}\,U_e - A_{\mathrm{e}}^{c,v}\,V_e & \dot{m}_w &=& A_{\mathrm{w}}^{c,u}\,U_w + A_{\mathrm{w}}^{c,v}\,V_w \\ \dot{m}_n &=& -A_{\mathrm{n}}^{c,u}\,U_n - A_{\mathrm{n}}^{c,v}\,V_n & \dot{m}_s &=& A_{\mathrm{s}}^{c,u}\,U_s + A_{\mathrm{s}}^{c,v}\,V_s \end{array}\right\} \tag{4.7}$$

With mass fluxes at the faces, the continuity equation can be rewritten in more compact form as follows:

$$-\dot{m}_e + \dot{m}_w - \dot{m}_n + \dot{m}_s - \frac{(M_P - M_P^o)}{\Delta t} = 0 \tag{4.8}$$

Equation (4.5) will be used later to form a governing equation for the pressure correction, P'.

4.3.2 x-Momentum Conservation Equation

The U equation conserves momentum in the x direction. Each term of the equation is integrated with respect to time and volume as illustrated by the following equation:

$$\underbrace{\int_{\forall}\int_t \left\{\frac{\partial}{\partial t}(\rho U)\right\} d\forall\, dt}_{I} + \underbrace{\int_{\forall}\int_t \left\{\frac{\partial}{\partial x}(\rho UU) + \frac{\partial}{\partial y}(\rho VU)\right\} d\forall\, dt}_{II} = -\underbrace{\int_{\forall}\int_t \left\{\frac{\partial P}{\partial x}\right\} d\forall\, dt}_{III}$$
$$+ \underbrace{\int_{\forall}\int_t \left\{\frac{\partial}{\partial x}\left(\mu\frac{\partial U}{\partial x}\right) + \frac{\partial}{\partial y}\left(\mu\frac{\partial U}{\partial y}\right)\right\} d\forall\, dt}_{IV} + \underbrace{\int_{\forall}\int_t \{\rho\ g\}\, d\forall dt}_{V} \tag{4.9}$$

To derive the discretised algebraic linearized equation for velocity U, a finite volume procedure similar to that used for the continuity equation is used. Details of the derivation are presented below.

The integration of the first term in Equation (4.9) yields

$$I = \int_{\forall}\int_t \left\{\frac{\partial}{\partial t}(\rho\ U)\right\} d\forall\, dt = \forall_P\ (\rho U - \rho^o U^o)_P = M_{\mathrm{P}} U_{\mathrm{P}} - M_{\mathrm{P}}^o U_{\mathrm{P}}^o \tag{4.10}$$

The second term represents the net change in momentum advection across the faces of the control volume (CV).

$$
\begin{aligned}
II = \int_{\forall}\int_{t}\left\{\frac{\partial}{\partial x}\left(\rho UU\right)\right\}dx\,dA\,dt + \int_{\forall}\int_{t}\left\{\frac{\partial}{\partial y}(\rho VU)\right\}dy\,dA\,dt &\approx \Delta t\int_{\forall}\overrightarrow{\nabla}\cdot\left(\rho\overrightarrow{V}\,\overrightarrow{V}\right)d\forall \\
&= \Delta t\int_{S}\rho\overrightarrow{V}\,\overrightarrow{V}\cdot\hat{n}\;dS = \Delta t\sum_{f}\rho\left(\overrightarrow{V}\cdot\hat{n}\right)_{f}\overrightarrow{V}_{f}\;dS \\
= \Delta t\left\{(A_e)\,\rho_e\left(U_{\mathrm{e}}n_{xe}+V_{\mathrm{e}}n_{ye}\right)U_{\mathrm{e}} - (A_w)\,\rho_w\left(U_{\mathrm{w}}n_{xw}+V_{\mathrm{w}}n_{yw}\right)U_{\mathrm{w}}\right\} & \\
+\Delta t\left\{(A_n)\rho_n(U_{\mathrm{n}}n_{xn}+V_{\mathrm{n}}n_{yn})U_{\mathrm{n}} - (A_s)\rho_s(U_{\mathrm{s}}n_{xs}+V_{\mathrm{s}}n_{ys})U_{\mathrm{s}}\right\} & \\
= \Delta t\left(\dot{m}_eU_{\mathrm{e}} - \dot{m}_wU_{\mathrm{w}}\right) + \Delta t\left(\dot{m}_nU_{\mathrm{n}} - \dot{m}_sU_{\mathrm{s}}\right) & \quad (4.11)
\end{aligned}
$$

The third term represents the pressure force.

$$
III = -\int_{\forall}\int_{t}\left\{\frac{\partial P}{\partial x}\right\}d\forall\,dt \approx -\Delta t\;\;\forall_P\left.\frac{\partial P}{\partial x}\right|_P \qquad (4.12)
$$

The fourth term represents viscous stresses at the faces.

$$
\begin{aligned}
IV = \int_{\forall}\int_{t}\left\{\frac{\partial}{\partial x}\left(\mu\frac{\partial U}{\partial x}\right)\right\}d\forall\,dt + \int_{\forall}\int_{t}\left\{\frac{\partial}{\partial y}\left(\mu\frac{\partial U}{\partial y}\right)\right\}d\forall\,dt &\approx \Delta t\int_{\forall}\overrightarrow{\nabla}\cdot\left(\mu\overrightarrow{\nabla}U\right)d\forall \\
= \Delta t\int_{S}\mu\overrightarrow{\nabla}U\cdot\hat{n}\;dS = \Delta t\sum_{f}\mu\left(\overrightarrow{\nabla}U\cdot\hat{n}\right)_{f}\;dS & \\
= \Delta t\int_{A}\left\{\mu\left.\frac{\partial U}{\partial x}\right|_e\cdot\hat{n}_e - \mu\left.\frac{\partial U}{\partial x}\right|_w\cdot\hat{n}_w\right\}dA + \Delta t\int_{A}\left\{\mu\left.\frac{\partial U}{\partial y}\right|_n\cdot\hat{n}_n - \mu\left.\frac{\partial U}{\partial y}\right|_s\cdot\hat{n}_s\right\}dA & \\
= \Delta t\left\{A_e\mu\left.\frac{\partial U}{\partial n}\right|_e - A_w\mu\left.\frac{\partial U}{\partial n}\right|_w\right\} + \Delta t\left\{A_n\mu\left.\frac{\partial U}{\partial n}\right|_n - A_s\mu\left.\frac{\partial U}{\partial n}\right|_s\right\} & \\
= \Delta t\left\{\frac{A_e\mu}{\hat{n}_e\cdot\hat{s}_e}\left(\left.\frac{\partial U}{\partial s}\right|_e - \left.\frac{\partial U}{\partial t}\right|_e\hat{t}_e\cdot\hat{s}_e\right) - \frac{A_w\mu}{\hat{n}_w\cdot\hat{s}_w}\left(\left.\frac{\partial U}{\partial s}\right|_w - \left.\frac{\partial U}{\partial t}\right|_w\hat{t}_w\cdot\hat{s}_w\right)\right\} & \\
+\Delta t\left\{\frac{A_n\mu}{\hat{n}_n\cdot\hat{t}_n}\left(\left.\frac{\partial U}{\partial t}\right|_n - \left.\frac{\partial U}{\partial s}\right|_n\hat{t}_n\cdot\hat{s}_n\right) - \frac{A_s\mu}{\hat{n}_s\cdot\hat{t}_s}\left(\left.\frac{\partial U}{\partial t}\right|_s - \left.\frac{\partial U}{\partial s}\right|_s\hat{t}_s\cdot\hat{s}_s\right)\right\} & \quad (4.13)
\end{aligned}
$$

At each face, the normal derivative of U velocity is divided into two parts. This can be illustrated by the derivative ($\left.\frac{\partial U}{\partial n}\right|_e$) at the east face in Equation (4.13). The first part is the primary derivative term, ($\left.\frac{\partial U}{\partial s}\right|_e$), which evaluates the change in U at the east face along the

primary direction, $\hat{s}$ in this case. The second part is the cross-derivative term, $(\frac{\partial U}{\partial t}\Big|_e)$, which evaluates the change in U along the east face from the southeast corner to the northeast corner of the CV. This term will vanish if an orthogonal grid is used as the dot product of the west to east geometric grid unit vector at the east face, $(\hat{s}_e)$, and the south to north geometric grid unit vector at the same face, $(\hat{t}_e\ )$, goes to zero due to orthogonality of the grids.

The last term is the body force term.

$$\int_{\forall}\int_{t}\{\ \rho\ g\}\, d\forall\ dt = \Delta t\ \forall_P\ \rho\ g \tag{4.14}$$

Now, substitute Equations (4.10) to (4.14) into Equation (4.9) and divide by Δt to get:

$$\begin{aligned}
\frac{1}{\Delta t}\left(M_{\mathrm{P}}U_{\mathrm{P}} - M^o_{\mathrm{P}}U^o_{\mathrm{P}}\right) + \dot{m}_e U_{\mathrm{e}} - \dot{m}_w U_{\mathrm{w}} + \dot{m}_n U_{\mathrm{n}} - \dot{m}_s U_{\mathrm{s}} = \\
- \forall_P \left.\frac{\partial P}{\partial x}\right|_P + \forall_P\ \rho\ g \\
+ \frac{A_e\ \mu}{\hat{n}_e \cdot \hat{s}_e}\frac{(U_{\mathrm{E}} - U_{\mathrm{P}})}{(ds)_e} - \frac{A_e\ \mu}{\hat{n}_e \cdot \hat{s}_e}\frac{(U_{\mathrm{ne}} - U_{\mathrm{se}})}{(dt)_e}\hat{t}_e \cdot \hat{s}_e \\
- \frac{A_w\ \mu}{\hat{n}_w \cdot \hat{s}_w}\frac{(U_{\mathrm{P}} - U_{\mathrm{W}})}{(ds)_w} + \frac{A_w\ \mu}{\hat{n}_w \cdot \hat{s}_w}\frac{(U_{\mathrm{nw}} - U_{\mathrm{sw}})}{(dt)_w}\hat{t}_w \cdot \hat{s}_w \\
+ \frac{A_n\ \mu}{\hat{n}_n \cdot \hat{t}_n}\frac{(U_{\mathrm{N}} - U_{\mathrm{P}})}{(dt)_n} - \frac{A_n\ \mu}{\hat{n}_n \cdot \hat{t}_n}\frac{(U_{\mathrm{ne}} - U_{\mathrm{nw}})}{(ds)_n}\hat{t}_n \cdot \hat{s}_n \\
- \frac{A_s\ \mu}{\hat{n}_s \cdot \hat{t}_s}\frac{(U_{\mathrm{P}} - U_{\mathrm{S}})}{(dt)_s} + \frac{A_s\ \mu}{\hat{n}_s \cdot \hat{t}_s}\frac{(U_{\mathrm{se}} - U_{\mathrm{sw}})}{(ds)_s}\hat{t}_s \cdot \hat{s}_s
\end{aligned} \tag{4.15}$$

The velocity gradients in Equation (4.13) have been evaluated by the Central Differencing Scheme (CDS). A general advection scheme formulation has been used to offer more flexibility in applying various advection schemes in the future. At any face of the CV, take the east face for example, the advective velocity and the velocity gradient can be written in terms of the diffusion weighting coefficient β_e and the convective weighting coefficient α_e as follows:

$$\left.\frac{\partial U}{\partial s}\right|_e = \beta_e\ \frac{U_{\mathrm{E}} - U_{\mathrm{P}}}{(ds)_e} \tag{4.16}$$

$$U_{\mathrm{e}} = (0.5 + \alpha_e)\ U_{\mathrm{P}} + (0.5 - \alpha_e)\, U_{\mathrm{E}} \tag{4.17}$$

Both diffusion and convective weights would be calculated by an appropriate advection scheme. In this work, an algebraic approximation to the Exponential differencing scheme (EDS) proposed by [52] and [53] was used to evaluate the diffusion and convective weights for T and W equations as follows:

$$\alpha_e = \mathrm{sign}\,(\dot{m}_e)\,\frac{0.5\,(Pe_e^2)}{5 + (Pe_e^2)} \qquad \alpha_n = \mathrm{sign}\,(\dot{m}_n)\,\frac{0.5\,(Pe_n^2)}{5 + (Pe_n^2)} \tag{4.18}$$

$$\beta_e = \frac{1 + 0.005\,(Pe_e^2)}{1 + 0.05\,(Pe_e^2)} \qquad \beta_n = \frac{1 + 0.005\,(Pe_n^2)}{1 + 0.05\,(Pe_n^2)} \tag{4.19}$$

For the U and V equations, the Mass-Weighted Upwind Scheme (MAW) was used to achieve better convergence. Details related to the derivation of the advection term using the MAW scheme are provided in Appendix A.

To simplify presenting the resulting U equation, the diffusion coefficients at the faces of the control volume are defined as follows:

$$\left.\begin{array}{llll} D_e = \dfrac{A_e\ \mu_e}{(ds)_e} & D_n = \dfrac{A_n\ \mu_n}{(dt)_n} \\ D_w = \dfrac{A_w\ \mu_w}{(ds)_w} & D_s = \dfrac{A_s\ \mu_s}{(dt)_s} \end{array}\right\} \tag{4.20}$$

Now, using the general advection formulation and the diffusion coefficient definition, the x-

momentum equation can be written as follows:

$$
\begin{aligned}
&\frac{\left(M_{\mathrm{P}}U_{\mathrm{P}} - M^{o}_{\mathrm{P}}U^{o}_{\mathrm{P}}\right)}{\Delta t} \\
&\quad + \dot{m}_e\left\{(0.5+\alpha_e)\,U_{\mathrm{P}} + (0.5-\alpha_e)\,U_{\mathrm{E}}\right\} - \dot{m}_w\left\{(0.5+\alpha_w)\,U_{\mathrm{W}} + (0.5-\alpha_w)\,U_{\mathrm{P}}\right\} \\
&\quad + \dot{m}_n\left\{(0.5+\alpha_n)\,U_{\mathrm{P}} + (0.5-\alpha_n)\,U_{\mathrm{N}}\right\} - \dot{m}_s\left\{(0.5+\alpha_s)\,U_{\mathrm{S}} + (0.5-\alpha_s)\,U_{\mathrm{P}}\right\} = \\
&\qquad\qquad - \forall_P \left.\frac{\partial P}{\partial x}\right|_P + \forall_P\,\rho\,g \\
&\qquad + D_e\beta_e\frac{\left(U_{\mathrm{E}} - U_{\mathrm{P}}\right)}{\hat{n}_e\cdot\hat{s}_e} - D_e\beta_e\frac{(ds)_e}{(dt)_e}\,\frac{\left(U_{\mathrm{ne}} - U_{\mathrm{se}}\right)}{\hat{n}_e\cdot\hat{s}_e}\hat{t}_e\cdot\hat{s}_e \\
&\quad - D_w\beta_w\frac{\left(U_{\mathrm{P}} - U_{\mathrm{W}}\right)}{\hat{n}_w\cdot\hat{s}_w} + D_w\beta_w\frac{(ds)_w}{(dt)_w}\,\frac{\left(U_{\mathrm{nw}} - U_{\mathrm{sw}}\right)}{\hat{n}_w\cdot\hat{s}_w}\hat{t}_w\cdot\hat{s}_w \\
&\qquad + D_n\beta_n\frac{\left(U_{\mathrm{N}} - U_{\mathrm{P}}\right)}{\hat{n}_n\cdot\hat{t}_n} - D_n\beta_n\frac{(dt)_n}{(ds)_n}\,\frac{\left(U_{\mathrm{ne}} - U_{\mathrm{nw}}\right)}{\hat{n}_n\cdot\hat{t}_n}\hat{t}_n\cdot\hat{s}_n \\
&\qquad\qquad - D_s\beta_s\frac{\left(U_{\mathrm{P}} - U_{\mathrm{S}}\right)}{\hat{n}_s\cdot\hat{t}_s} + D_s\beta_s\frac{(dt)_s}{(ds)_s}\,\frac{\left(U_{\mathrm{se}} - U_{\mathrm{sw}}\right)}{\hat{n}_s\cdot\hat{t}_s}\hat{t}_s\cdot\hat{s}_s
\end{aligned}
\tag{4.21}
$$

The velocities at corners of the control volumes, which are used to evaluate the cross-derivative terms, are approximated by the following relations:

$$
\left.
\begin{aligned}
U_{\mathrm{ne}} &= C_{ne1}\,U_{\mathrm{P}} + C_{ne2}\,U_{\mathrm{E}} + C_{ne3}\,U_{\mathrm{NE}} + C_{ne4}\,U_{\mathrm{N}} \\
U_{\mathrm{se}} &= C_{se1}\,U_{\mathrm{S}} + C_{se2}\,U_{\mathrm{SE}} + C_{se3}\,U_{\mathrm{E}} + C_{se4}\,U_{\mathrm{P}} \\
U_{\mathrm{nw}} &= C_{nw1}\,U_{\mathrm{W}} + C_{nw2}\,U_{\mathrm{P}} + C_{nw3}\,U_{\mathrm{N}} + C_{nw4}\,U_{\mathrm{NW}} \\
U_{\mathrm{sw}} &= C_{sw1}\,U_{\mathrm{SW}} + C_{sw2}\,U_{\mathrm{S}} + C_{sw3}\,U_{\mathrm{P}} + C_{sw4}\,U_{\mathrm{W}}
\end{aligned}
\right\}
\tag{4.22}
$$

The coefficients C_{ne}, C_{nw}, C_{se} and C_{sw} are calculated by 2D linear interpolation from the four nodal neighbours.

Substituting the expression of the corner velocities into the discretised U equation and collecting terms produces a discretisation equation of U that involves all eight nodal neighbours. The final form of the algebraic equation for the typical U control volumes takes the

following form:

$$A^u_{\mathrm{P}}\,U_{\mathrm{P}} = A^u_{\mathrm{E}}\,U_{\mathrm{E}} + A^u_{\mathrm{W}}\,U_{\mathrm{W}} + A^u_{\mathrm{N}}\,U_{\mathrm{N}} + A^u_{\mathrm{S}}\,U_{\mathrm{S}} + A^u_{\mathrm{NE}}\,U_{\mathrm{NE}} + A^u_{\mathrm{NW}}\,U_{\mathrm{NW}} + A^u_{\mathrm{SE}}\,U_{\mathrm{SE}} + A^u_{\mathrm{SW}}\,U_{\mathrm{SW}} + b^u_{\mathrm{P}} \quad (4.23)$$

Note that this is a nine point algebraic equation for U_{P}. The coefficients are given by the following equations:

$$A^u_{\mathrm{E}} = \frac{D_e\beta_e}{\hat{n}_e\cdot\hat{s}_e} - 0.5\,\dot{m}_e + \alpha_e\,|\dot{m}_e| - D_n\beta_n\frac{(dt)_n}{(ds)_n}\frac{\hat{t}_n\cdot\hat{s}_n}{\hat{n}_n\cdot\hat{t}_n}\,C_{ne2} + D_s\beta_s\frac{(dt)_s}{(ds)_s}\frac{\hat{t}_s\cdot\hat{s}_s}{\hat{n}_s\cdot\hat{t}_s}\,C_{se3} - D_e\beta_e\frac{(ds)_e}{(dt)_e}\frac{\hat{t}_e\cdot\hat{s}_e}{\hat{n}_e\cdot\hat{s}_e}\,(C_{ne2}-C_{se3}) \quad (4.24)$$

$$A^u_{\mathrm{W}} = \frac{D_w\beta_w}{\hat{n}_w\cdot\hat{s}_w} + 0.5\,\dot{m}_w + \alpha_W\,|\dot{m}_w| + D_n\beta_n\frac{(dt)_n}{(ds)_n}\frac{\hat{t}_n\cdot\hat{s}_n}{\hat{n}_n\cdot\hat{t}_n}\,C_{nw1} - D_s\beta_s\frac{(dt)_s}{(ds)_s}\frac{\hat{t}_s\cdot\hat{s}_s}{\hat{n}_s\cdot\hat{t}_s}\,C_{sw4} + D_w\beta_w\frac{(ds)_w}{(dt)_w}\frac{\hat{t}_w\cdot\hat{s}_w}{\hat{n}_w\cdot\hat{s}_w}\,(C_{nw1}-C_{sw4}) \quad (4.25)$$

$$A^u_{\mathrm{N}} = \frac{D_n\beta_n}{\hat{n}_n\cdot\hat{t}_n} - 0.5\,\dot{m}_n + \alpha_n\,|\dot{m}_n| - D_e\beta_e\frac{(ds)_e}{(dt)_e}\frac{\hat{t}_e\cdot\hat{s}_e}{\hat{n}_e\cdot\hat{s}_e}\,C_{ne4} + D_w\beta_w\frac{(ds)_w}{(dt)_w}\frac{\hat{t}_w\cdot\hat{s}_w}{\hat{n}_w\cdot\hat{s}_w}\,C_{nw3} - D_n\beta_n\frac{(dt)_n}{(ds)_n}\frac{\hat{t}_n\cdot\hat{s}_n}{\hat{n}_n\cdot\hat{t}_n}\,(C_{ne4}-C_{nw3}) \quad (4.26)$$

$$A^u_{\mathrm{S}} = \frac{D_s\beta_s}{\hat{n}_s\cdot\hat{t}_s} + 0.5\,\dot{m}_s + \alpha_s\,|\dot{m}_s| + D_e\beta_e\frac{(ds)_e}{(dt)_e}\frac{\hat{t}_e\cdot\hat{s}_e}{\hat{n}_e\cdot\hat{s}_e}\,C_{se1} - D_w\beta_w\frac{(ds)_w}{(dt)_w}\frac{\hat{t}_w\cdot\hat{s}_w}{\hat{n}_w\cdot\hat{s}_w}\,C_{sw2} + D_s\beta_s\frac{(dt)_s}{(ds)_s}\frac{\hat{t}_s\cdot\hat{s}_s}{\hat{n}_s\cdot\hat{t}_s}\,(C_{se1}-C_{sw2}) \quad (4.27)$$

$$A^u_{\mathrm{NE}} = -D_e\beta_e\frac{(ds)_e}{(dt)_e}\frac{\hat{t}_e\cdot\hat{s}_e}{\hat{n}_e\cdot\hat{s}_e}\,C_{ne3} - D_n\beta_n\frac{(dt)_n}{(ds)_n}\frac{\hat{t}_n\cdot\hat{s}_n}{\hat{n}_n\cdot\hat{t}_n}\,C_{ne3} \quad (4.28)$$

$$A^u_{\mathrm{NW}} = D_w\beta_w\frac{(ds)_w}{(dt)_w}\frac{\hat{t}_w\cdot\hat{s}_w}{\hat{n}_w\cdot\hat{s}_w}\,C_{nw4} + D_n\beta_n\frac{(dt)_n}{(ds)_n}\frac{\hat{t}_n\cdot\hat{s}_n}{\hat{n}_n\cdot\hat{t}_n}\,C_{nw4} \quad (4.29)$$

$$A^u_{\mathrm{SE}} = D_e\beta_e\frac{(ds)_e}{(dt)_e}\frac{\hat{t}_e\cdot\hat{s}_e}{\hat{n}_e\cdot\hat{s}_e}\,C_{se2} + D_s\beta_s\frac{(dt)_s}{(ds)_s}\frac{\hat{t}_s\cdot\hat{s}_s}{\hat{n}_s\cdot\hat{t}_s}\,C_{se2} \quad (4.30)$$

$$A^u_{\mathrm{SW}} = -D_w\beta_w \frac{(ds)_w}{(dt)_w}\frac{\hat{t}_w\cdot\hat{s}_w}{\hat{n}_w\cdot\hat{s}_w}\,C_{sw1} - D_s\beta_s\frac{(dt)_s}{(ds)_s}\frac{\hat{t}_s\cdot\hat{s}_s}{\hat{n}_s\cdot\hat{t}_s}\,C_{sw1} \tag{4.31}$$

$$b^u_{\mathrm{P}} = \left(\frac{M^o_{\mathrm{P}}}{\Delta t}\right)U^o_{\mathrm{P}} - \forall_P\left.\frac{\partial P}{\partial x}\right|_P + Q^u_{\mathrm{P}} \tag{4.32}$$

$$\begin{aligned} A^u_{\mathrm{P}} = {} & \frac{D_e\beta_e}{\hat{n}_e\cdot\hat{s}_e} + 0.5\,\dot{m}_e + |\alpha_e|\,|\dot{m}_e| + \frac{D_w\beta_w}{\hat{n}_w\cdot\hat{s}_w} - 0.5\,\dot{m}_w + |\alpha_W|\,|\dot{m}_w| \\ & + \frac{D_n\beta_n}{\hat{n}_n\cdot\hat{t}_n} + 0.5\,\dot{m}_n + |\alpha_n|\,|\dot{m}_n| + \frac{D_s\beta_s}{\hat{n}_s\cdot\hat{t}_s} - 0.5\,\dot{m}_s + |\alpha_s|\,|\dot{m}_s| \\ & + D_e\beta_e\frac{(ds)_e}{(dt)_e}\frac{\hat{t}_e\cdot\hat{s}_e}{\hat{n}_e\cdot\hat{s}_e}\,(C_{ne1} - C_{se4}) - D_w\beta_w\frac{(ds)_w}{(dt)_w}\frac{\hat{t}_w\cdot\hat{s}_w}{\hat{n}_w\cdot\hat{s}_w}\,(C_{nw2} - C_{sw3}) \\ & + D_n\beta_n\frac{(dt)_n}{(ds)_n}\frac{\hat{t}_n\cdot\hat{s}_n}{\hat{n}_n\cdot\hat{t}_n}\,(C_{ne1} - C_{nw2}) - D_s\beta_s\frac{(dt)_s}{(ds)_s}\frac{\hat{t}_s\cdot\hat{s}_s}{\hat{n}_s\cdot\hat{t}_s}\,(C_{se4} - C_{sw3}) \\ & + \frac{M_P}{\Delta t} \end{aligned} \tag{4.33}$$

The term Q^u_{P} contains only the body force as follows:

$$Q^u_{\mathrm{P}} = g\,\rho\,\forall_P \tag{4.34}$$

Now, let $A^{u^*}_{\mathrm{P}}$ be

$$\begin{aligned} A^{u^*}_{\mathrm{P}} = {} & \frac{D_e\beta_e}{\hat{n}_e\cdot\hat{s}_e} - 0.5\,\dot{m}_e + |\alpha_e|\,|\dot{m}_e| \quad + \frac{D_w\beta_w}{\hat{n}_w\cdot\hat{s}_w} + 0.5\,\dot{m}_w + |\alpha_W|\,|\dot{m}_w| \\ & + \frac{D_n\beta_n}{\hat{n}_n\cdot\hat{t}_n} - 0.5\,\dot{m}_n + |\alpha_n|\,|\dot{m}_n| \quad + \frac{D_s\beta_s}{\hat{n}_s\cdot\hat{t}_s} + 0.5\,\dot{m}_s + |\alpha_s|\,|\dot{m}_s| \end{aligned} \tag{4.35}$$

Next, apply the reduced form of the continuity equation, Equation (4.8), to replace the term $\frac{M_P}{\Delta t}$. This procedure avoids appearance of apparent momentum source if the mass is not precisely satisfied by the computed velocity field. Now, the diagonal coefficient takes the form:

$$A^u_{\mathrm{P}} = A^{u^*}_{\mathrm{P}} + \frac{M^o_{\mathrm{P}}}{\Delta t} \tag{4.36}$$

4.3.3 y-Momentum Conservation Equation

The y momentum equation is integrated with respect to time and volume.

$$\underbrace{\int_{\forall}\int_{t}\left\{\frac{\partial}{\partial t}(\rho V)\right\}d\forall dt}_{I}+\underbrace{\int_{\forall}\int_{t}\left\{\frac{\partial}{\partial x}(\rho UV)+\frac{\partial}{\partial y}(\rho VV)\right\}d\forall dt}_{II}=-\underbrace{\int_{\forall}\int_{t}\left\{\frac{\partial P}{\partial y}\right\}d\forall dt}_{III}$$
$$+\underbrace{\int_{\forall}\int_{t}\left\{\frac{\partial}{\partial x}\left(\mu\frac{\partial V}{\partial x}\right)+\frac{\partial}{\partial y}\left(\mu\frac{\partial V}{\partial y}\right)\right\}d\forall dt}_{IV} \quad (4.37)$$

Following the same procedure that has been used for the coefficients of U equations, the discretised V momentum equation will take the following form:

$$A^v_{\mathrm{P}}V_{\mathrm{P}}=A^v_{\mathrm{E}}V_{\mathrm{E}}+A^v_{\mathrm{W}}V_{\mathrm{W}}+A^v_{\mathrm{N}}V_{\mathrm{N}}+A^v_{\mathrm{S}}V_{\mathrm{S}}+A^v_{\mathrm{NE}}V_{\mathrm{NE}}+A^v_{\mathrm{NW}}V_{\mathrm{NW}}$$
$$+A^v_{\mathrm{SE}}V_{\mathrm{SE}}+A^v_{\mathrm{SW}}V_{\mathrm{SW}}+b^v_{\mathrm{P}} \quad (4.38)$$

The coefficients of Equation (4.38) are expressed as follows:

$$A^v_{\mathrm{E}}=\frac{D_e\beta_e}{\hat{n}_e\cdot\hat{s}_e}-0.5\,\dot{m}_e+|\alpha_e|\,|\dot{m}_e|-D_n\beta_n\frac{(dt)_n}{(ds)_n}\frac{\hat{t}_n\cdot\hat{s}_n}{\hat{n}_n\cdot\hat{t}_n}\,C_{ne2}+D_s\beta_s\frac{(dt)_s}{(ds)_s}\frac{\hat{t}_s\cdot\hat{s}_s}{\hat{n}_s\cdot\hat{t}_s}\,C_{se3}$$
$$+D_e\beta_e\frac{(ds)_e}{(dt)_e}\frac{\hat{t}_e\cdot\hat{s}_e}{\hat{n}_e\cdot\hat{s}_e}\,(C_{ne2}-C_{se3}) \quad (4.39)$$

$$A^v_{\mathrm{W}}=\frac{D_w\beta_w}{\hat{n}_w\cdot\hat{s}_w}+0.5\,\dot{m}_w+|\alpha_W|\,|\dot{m}_w|+D_n\beta_n\frac{(dt)_n}{(ds)_n}\frac{\hat{t}_n\cdot\hat{s}_n}{\hat{n}_n\cdot\hat{t}_n}\,C_{nw1}-D_s\beta_s\frac{(dt)_s}{(ds)_s}\frac{\hat{t}_s\cdot\hat{s}_s}{\hat{n}_s\cdot\hat{t}_s}\,C_{sw4}$$
$$+D_w\beta_w\frac{(ds)_w}{(dt)_w}\frac{\hat{t}_w\cdot\hat{s}_w}{\hat{n}_w\cdot\hat{s}_w}\,(C_{nw1}-C_{sw4}) \quad (4.40)$$

$$A^v_{\mathrm{N}}=\frac{D_n\beta_n}{\hat{n}_n\cdot\hat{t}_n}-0.5\,\dot{m}_n+|\alpha_n|\,|\dot{m}_n|-D_e\beta_e\frac{(ds)_e}{(dt)_e}\frac{\hat{t}_e\cdot\hat{s}_e}{\hat{n}_e\cdot\hat{s}_e}\,C_{ne4}+D_w\beta_w\frac{(ds)_w}{(dt)_w}\frac{\hat{t}_w\cdot\hat{s}_w}{\hat{n}_w\cdot\hat{s}_w}\,C_{nw3}$$
$$+D_n\beta_n\frac{(dt)_n}{(ds)_n}\frac{\hat{t}_n\cdot\hat{s}_n}{\hat{n}_n\cdot\hat{t}_n}\,(C_{ne4}-C_{nw3}) \quad (4.41)$$

$$A^v_{\mathrm{S}} = \frac{D_s\beta_s}{\hat{n}_s\cdot\hat{t}_s} + 0.5\,\dot{m}_s + |\alpha_s|\,|\dot{m}_s| + D_e\beta_e\frac{(ds)_e}{(dt)_e}\frac{\hat{t}_e\cdot\hat{s}_e}{\hat{n}_e\cdot\hat{s}_e}\;C_{se1} - D_w\beta_w\frac{(ds)_w}{(dt)_w}\frac{\hat{t}_w\cdot\hat{s}_w}{\hat{n}_w\cdot\hat{s}_w}\;C_{sw2} + D_s\beta_s\frac{(dt)_s}{(ds)_s}\frac{\hat{t}_s\cdot\hat{s}_s}{\hat{n}_s\cdot\hat{t}_s}\;(C_{se1}-C_{sw2}) \quad (4.42)$$

$$A^v_{\mathrm{NE}} = -D_e\beta_e\frac{(ds)_e}{(dt)_e}\frac{\hat{t}_e\cdot\hat{s}_e}{\hat{n}_e\cdot\hat{s}_e}\;C_{ne3} - D_n\beta_n\frac{(dt)_n}{(ds)_n}\frac{\hat{t}_n\cdot\hat{s}_n}{\hat{n}_n\cdot\hat{t}_n}\;C_{ne3} \quad (4.43)$$

$$A^v_{\mathrm{NW}} = D_w\beta_w\frac{(ds)_w}{(dt)_w}\frac{\hat{t}_w\cdot\hat{s}_w}{\hat{n}_w\cdot\hat{s}_w}\;C_{nw4} + D_n\beta_n\frac{(dt)_n}{(ds)_n}\frac{\hat{t}_n\cdot\hat{s}_n}{\hat{n}_n\cdot\hat{t}_n}\;C_{nw4} \quad (4.44)$$

$$A^v_{\mathrm{SE}} = D_e\beta_e\frac{(ds)_e}{(dt)_e}\frac{\hat{t}_e\cdot\hat{s}_e}{\hat{n}_e\cdot\hat{s}_e}\;C_{se2} + D_s\beta_s\frac{(dt)_s}{(ds)_s}\frac{\hat{t}_s\cdot\hat{s}_s}{\hat{n}_s\cdot\hat{t}_s}\;C_{se2} \quad (4.45)$$

$$A^v_{\mathrm{SW}} = -D_w\beta_w\frac{(ds)_w}{(dt)_w}\frac{\hat{t}_w\cdot\hat{s}_w}{\hat{n}_w\cdot\hat{s}_w}\;C_{sw1} - D_s\beta_s\frac{(dt)_s}{(ds)_s}\frac{\hat{t}_s\cdot\hat{s}_s}{\hat{n}_s\cdot\hat{t}_s}\;C_{sw1} \quad (4.46)$$

$$b^v_{\mathrm{P}} = \left(\frac{M^o_{\mathrm{P}}}{\Delta t}\right)V^o_{\mathrm{P}} - \forbidden_P\,\left.\frac{\partial P}{\partial y}\right|_P + Q^v_{\mathrm{P}} \quad (4.47)$$

$$\begin{aligned} A^v_{\mathrm{P}} = {} & \frac{D_e\beta_e}{\hat{n}_e\cdot\hat{s}_e} + 0.5\,\dot{m}_e + |\alpha_e|\,|\dot{m}_e| + \frac{D_w\beta_w}{\hat{n}_w\cdot\hat{s}_w} - 0.5\,\dot{m}_w + |\alpha_W|\,|\dot{m}_w| \\ & + \frac{D_n\beta_n}{\hat{n}_n\cdot\hat{t}_n} + 0.5\,\dot{m}_n + |\alpha_n|\,|\dot{m}_n| + \frac{D_s\beta_s}{\hat{n}_s\cdot\hat{t}_s} - 0.5\,\dot{m}_s + |\alpha_s|\,|\dot{m}_s| \\ & + D_e\beta_e\frac{(ds)_e}{(dt)_e}\frac{\hat{t}_e\cdot\hat{s}_e}{\hat{n}_e\cdot\hat{s}_e}\;(C_{ne1}-C_{se4}) - D_w\beta_w\frac{(ds)_w}{(dt)_w}\frac{\hat{t}_w\cdot\hat{s}_w}{\hat{n}_w\cdot\hat{s}_w}\;(C_{nw2}-C_{sw3}) \\ & + D_n\beta_n\frac{(dt)_n}{(ds)_n}\frac{\hat{t}_n\cdot\hat{s}_n}{\hat{n}_n\cdot\hat{t}_n}\;(C_{ne1}-C_{nw2}) - D_s\beta_s\frac{(dt)_s}{(ds)_s}\frac{\hat{t}_s\cdot\hat{s}_s}{\hat{n}_s\cdot\hat{t}_s}\;(C_{se4}-C_{sw3}) \\ & + \frac{M_P}{\Delta t} \end{aligned} \quad (4.48)$$

or

$$A^v_{\mathrm{P}} = A^{v^*}_{\mathrm{P}} + \frac{M^o_{\mathrm{P}}}{\Delta t} \quad (4.49)$$

with $A^{v^*}_P$ is defined in similar way to $A^{u^*}_P$. Finally, Q^v_{P} is calculated as follows:

$$Q^v_{\mathrm{P}} = 0 \quad (4.50)$$

4.3.4 Energy Conservation Equation

The energy equation is integrated with respect to time and volume to get the algebraic form for temperature equation in similar procedure to that followed for the x momentum equation Section 4.3.2. To make the derivation more general, the energy equation of the mixture region is considered here. Term V below will be zero for the liquid phase.

$$\underbrace{\int_{\forbar}\int_t \left\{\frac{\partial}{\partial t}(\rho\, C_p\, T)\right\} d\forbar\, dt}_{I} + \underbrace{\int_{\forbar}\int_t \left\{\frac{\partial}{\partial x}(\rho\, C_p\, U\, T) + \frac{\partial}{\partial y}(\,\rho\, C_p\, V\, T)\right\} d\forbar\, dt}_{II} =$$
$$+ \underbrace{\int_{\forbar}\int_t \left\{\frac{\partial}{\partial x}\left(k\,\frac{\partial T}{\partial x}\right) + \frac{\partial}{\partial y}\left(k\,\frac{\partial T}{\partial y}\right)\right\} d\forbar\, dt}_{III} + \underbrace{\int_{\forbar}\int_t \left\{\dot{S}_t'''\right\} d\forbar\, dt}_{IV}$$
$$+ \underbrace{\int_{\forbar}\int_t \left\{\frac{\partial}{\partial x}\left(\rho_M\, D^{ab}(C_{p,G} - C_{p,V})\frac{\partial W}{\partial x} T_M\right) + \frac{\partial}{\partial y}\left(\rho_M\, D^{ab}(C_{p,G} - C_{p,V})\frac{\partial W}{\partial y} T_M\right)\right\} d\forbar\, dt}_{V} \tag{4.51}$$

The term V in Equations (4.51) is only needed in case a mixture of vapour and non-condensable gas is used otherwise this term is dropped. Also, properties without a subscript refer to the mixture. After performing the integrations, the energy equation takes the form:

$$\frac{1}{\Delta t}\left(M_{\mathrm{P}}\, C_p\, T_{\mathrm{P}} - M^o_{\mathrm{P}}\, C_p\, T^o_{\mathrm{P}}\right) + \dot{m}_e\, C_p\, T_{\mathrm{e}} - \dot{m}_w\, C_p\, T_{\mathrm{w}} + \dot{m}_n\, C_p\, T_{\mathrm{n}} - \dot{m}_s\, C_p\, T_{\mathrm{s}} =$$
$$+ \frac{A_e}{\hat{n}_e \cdot \hat{s}_e}\, k\, \frac{(T_{\mathrm{E}} - T_{\mathrm{P}})}{(ds)_e} - \frac{A_e}{\hat{n}_e \cdot \hat{s}_e}\, k\, \frac{(T_{\mathrm{ne}} - T_{\mathrm{se}})}{(dt)_e} \hat{t}_e \cdot \hat{s}_e$$
$$- \frac{A_w}{\hat{n}_w \cdot \hat{s}_w}\, k\, \frac{(T_{\mathrm{P}} - T_{\mathrm{W}})}{(ds)_w} + \frac{A_w}{\hat{n}_w \cdot \hat{s}_w}\, k\, \frac{(T_{\mathrm{nw}} - T_{\mathrm{sw}})}{(dt)_w} \hat{t}_w \cdot \hat{s}_w$$
$$+ \frac{A_n}{\hat{n}_n \cdot \hat{t}_n}\, k\, \frac{(T_{\mathrm{N}} - T_{\mathrm{P}})}{(dt)_n} - \frac{A_n}{\hat{n}_n \cdot \hat{t}_n}\, k\, \frac{(T_{\mathrm{ne}} - T_{\mathrm{nw}})}{(ds)_n} \hat{t}_n \cdot \hat{s}_n$$
$$- \frac{A_s}{\hat{n}_s \cdot \hat{t}_s}\, k\, \frac{(T_{\mathrm{P}} - T_{\mathrm{S}})}{(dt)_s} + \frac{A_s}{\hat{n}_s \cdot \hat{t}_s}\, k\, \frac{(T_{\mathrm{se}} - T_{\mathrm{sw}})}{(ds)_s} \hat{t}_s \cdot \hat{s}_s + \dot{S}^t_P$$
$$+ \widetilde{D}_e\, T_{\mathrm{e}} - \widetilde{D}_w\, T_{\mathrm{w}} + \widetilde{D}_n\, T_{\mathrm{n}} - \widetilde{D}_s\, T_{\mathrm{s}} \tag{4.52}$$

The coefficient $\widetilde{D}$ in Equation (4.52) at all the faces are defined as follows:

$$\left.\begin{aligned} \widetilde{D}_e &= A_e\ \rho_e\ D_e^{ab}\ (C_{p,G} - C_{p,V})\frac{\partial W}{\partial x}\Big|_e \qquad \widetilde{D}_n = A_n\ \rho_n\ D_n^{ab}\ (C_{p,G} - C_{p,V})\frac{\partial W}{\partial y}\Big|_n \\ \widetilde{D}_w &= A_w\ \rho_w\ D_w^{ab}\ (C_{p,G} - C_{p,V})\frac{\partial W}{\partial x}\Big|_w \qquad \widetilde{D}_s = A_s\ \rho_s\ D_s^{ab}\ (C_{p,G} - C_{p,V})\frac{\partial W}{\partial y}\Big|_s \end{aligned}\right\} \tag{4.53}$$

The diffusion coefficients are introduced to Equation (4.52) are defined as follows:

$$\left.\begin{aligned} D_e^t &= \frac{A_e}{(ds)_e}\,k_e \qquad D_n^t = \frac{A_n}{(dt)_n}\,k_n \\ D_w^t &= \frac{A_w}{(ds)_w}\,k_w \qquad D_s^t = \frac{A_s}{(dt)_s}\,k_s \end{aligned}\right\} \tag{4.54}$$

The general advection formulation is also followed here to describe face values in terms of the nodal values.

$$\begin{aligned} &\frac{\left(M_{\mathrm{P}}\,C_p\,T_{\mathrm{P}} - M^o_{\mathrm{P}}\,C_p\,T^o_{\mathrm{P}}\right)}{\Delta t} \\ &+ \dot{m}_e\,C_p\ \left[(0.5+\alpha_e)\,T_{\mathrm{P}} + (0.5-\alpha_e)\,T_{\mathrm{E}}\right] - \dot{m}_w\,C_p\ \left[(0.5+\alpha_w)\,T_{\mathrm{W}} + (0.5-\alpha_w)\,T_{\mathrm{P}}\right] \\ &+ \dot{m}_n\,C_p\ \left[(0.5+\alpha_n)\,T_{\mathrm{P}} + (0.5-\alpha_n)\,T_{\mathrm{N}}\right] - \dot{m}_s\,C_p\ \left[(0.5+\alpha_s)\,T_{\mathrm{S}} + (0.5-\alpha_s)\,T_{\mathrm{P}}\right] = \\ &\qquad + D_e^t\beta_e\frac{(T_{\mathrm{E}} - T_{\mathrm{P}})}{\hat{n}_e\cdot\hat{s}_e} - D_e^t\beta_e\frac{(ds)_e}{(dt)_e}\,\frac{(T_{\mathrm{ne}} - T_{\mathrm{se}})}{\hat{n}_e\cdot\hat{s}_e}\hat{t}_e\cdot\hat{s}_e \\ &\qquad - D_w^t\beta_w\frac{(T_{\mathrm{P}} - T_{\mathrm{W}})}{\hat{n}_w\cdot\hat{s}_w} + D_w^t\beta_w\frac{(ds)_w}{(dt)_w}\,\frac{(T_{\mathrm{nw}} - T_{\mathrm{sw}})}{\hat{n}_w\cdot\hat{s}_w}\hat{t}_w\cdot\hat{s}_w \\ &\qquad + D_n^t\beta_n\frac{(T_{\mathrm{N}} - T_{\mathrm{P}})}{\hat{n}_n\cdot\hat{t}_n} - D_n^t\beta_n\frac{(dt)_n}{(ds)_n}\,\frac{(T_{\mathrm{ne}} - T_{\mathrm{nw}})}{\hat{n}_n\cdot\hat{t}_n}\hat{t}_n\cdot\hat{s}_n \\ &\qquad - D_s^t\beta_s\frac{(T_{\mathrm{P}} - T_{\mathrm{S}})}{\hat{n}_s\cdot\hat{t}_s} + D_s^t\beta_s\frac{(dt)_s}{(ds)_s}\,\frac{(T_{\mathrm{se}} - T_{\mathrm{sw}})}{\hat{n}_s\cdot\hat{t}_s}\hat{t}_s\cdot\hat{s}_s + \dot{S}_P^t \\ &\qquad\qquad + \widetilde{D}_e\ T_{\mathrm{e}} - \widetilde{D}_w\ T_{\mathrm{w}} + \widetilde{D}_n\ T_{\mathrm{n}} - \widetilde{D}_s\ T_{\mathrm{s}} \end{aligned} \tag{4.55}$$

The source term is linearized according to the following expression.

$$\dot{S}_P^t = Q_P^t + R_P^t T_{\mathrm{P}} \tag{4.56}$$

The final nine-point equation will take the following form:

$$A^t_{\mathrm{P}}\, T_{\mathrm{P}} = A^t_{\mathrm{E}}\, T_{\mathrm{E}} + A^t_{\mathrm{W}}\, T_{\mathrm{W}} + A^t_{\mathrm{N}}\, T_{\mathrm{N}} + A^t_{\mathrm{S}}\, T_{\mathrm{S}} + A^t_{\mathrm{NE}}\, T_{\mathrm{NE}} + A^t_{\mathrm{NW}}\, T_{\mathrm{NW}} + A^t_{\mathrm{SE}}\, T_{\mathrm{SE}} + A^t_{\mathrm{SW}}\, T_{\mathrm{SW}} + b^t_{\mathrm{P}} \quad (4.57)$$

The details of the coefficients in Equation (4.57) are presented below:

$$A^t_{\mathrm{E}} = \frac{D^t_e \beta_e}{\hat{n}_e \cdot \hat{s}_e} - 0.5\, \dot{m}_e C_p + |\alpha_e|\, |\dot{m}_e|\, C_p - D^t_n \beta_n \frac{(dt)_n}{(ds)_n} \frac{\hat{t}_n \cdot \hat{s}_n}{\hat{n}_n \cdot \hat{t}_n}\, C_{ne2} + D^t_s \beta_s \frac{(dt)_s}{(ds)_s} \frac{\hat{t}_s \cdot \hat{s}_s}{\hat{n}_s \cdot \hat{t}_s}\, C_{se3} + D^t_e \beta_e \frac{(ds)_e}{(dt)_e} \frac{\hat{t}_e \cdot \hat{s}_e}{\hat{n}_e \cdot \hat{s}_e}\, (C_{ne2} - C_{se3}) \quad (4.58)$$

$$A^t_{\mathrm{W}} = \frac{D^t_w \beta_w}{\hat{n}_w \cdot \hat{s}_w} + 0.5\, \dot{m}_w C_p + |\alpha_W|\, |\dot{m}_w|\, C_p + D^t_n \beta_n \frac{(dt)_n}{(ds)_n} \frac{\hat{t}_n \cdot \hat{s}_n}{\hat{n}_n \cdot \hat{t}_n}\, C_{nw1} - D^t_s \beta_s \frac{(dt)_s}{(ds)_s} \frac{\hat{t}_s \cdot \hat{s}_s}{\hat{n}_s \cdot \hat{t}_s}\, C_{sw4} + D^t_w \beta_w \frac{(ds)_w}{(dt)_w} \frac{\hat{t}_w \cdot \hat{s}_w}{\hat{n}_w \cdot \hat{s}_w}\, (C_{nw1} - C_{sw4}) \quad (4.59)$$

$$A^t_{\mathrm{N}} = \frac{D^t_n \beta_n}{\hat{n}_n \cdot \hat{t}_n} - 0.5\, \dot{m}_n C_p + |\alpha_n|\, |\dot{m}_n|\, C_p - D^t_e \beta_e \frac{(ds)_e}{(dt)_e} \frac{\hat{t}_e \cdot \hat{s}_e}{\hat{n}_e \cdot \hat{s}_e}\, C_{ne4} + D^t_w \beta_w \frac{(ds)_w}{(dt)_w} \frac{\hat{t}_w \cdot \hat{s}_w}{\hat{n}_w \cdot \hat{s}_w}\, C_{nw3} + D^t_n \beta_n \frac{(dt)_n}{(ds)_n} \frac{\hat{t}_n \cdot \hat{s}_n}{\hat{n}_n \cdot \hat{t}_n}\, (C_{ne4} - C_{nw3}) \quad (4.60)$$

$$A^t_{\mathrm{S}} = \frac{D^t_s \beta_s}{\hat{n}_s \cdot \hat{t}_s} + 0.5\, \dot{m}_s C_p + |\alpha_s|\, |\dot{m}_s|\, C_p + D^t_e \beta_e \frac{(ds)_e}{(dt)_e} \frac{\hat{t}_e \cdot \hat{s}_e}{\hat{n}_e \cdot \hat{s}_e}\, C_{se1} - D^t_w \beta_w \frac{(ds)_w}{(dt)_w} \frac{\hat{t}_w \cdot \hat{s}_w}{\hat{n}_w \cdot \hat{s}_w}\, C_{sw2} + D^t_s \beta_s \frac{(dt)_s}{(ds)_s} \frac{\hat{t}_s \cdot \hat{s}_s}{\hat{n}_s \cdot \hat{t}_s}\, (C_{se1} - C_{sw2}) \quad (4.61)$$

$$A^t_{\mathrm{NE}} = -D^t_e \beta_e \frac{(ds)_e}{(dt)_e} \frac{\hat{t}_e \cdot \hat{s}_e}{\hat{n}_e \cdot \hat{s}_e}\, C_{ne3} - D^t_n \beta_n \frac{(dt)_n}{(ds)_n} \frac{\hat{t}_n \cdot \hat{s}_n}{\hat{n}_n \cdot \hat{t}_n}\, C_{ne3} \quad (4.62)$$

$$A^t_{\mathrm{NW}} = D^t_w \beta_w \frac{(ds)_w}{(dt)_w} \frac{\hat{t}_w \cdot \hat{s}_w}{\hat{n}_w \cdot \hat{s}_w}\, C_{nw4} + D^t_n \beta_n \frac{(dt)_n}{(ds)_n} \frac{\hat{t}_n \cdot \hat{s}_n}{\hat{n}_n \cdot \hat{t}_n}\, C_{nw4} \quad (4.63)$$

$$A^t_{\mathrm{SE}} = D^t_e \beta_e \frac{(ds)_e}{(dt)_e} \frac{\hat{t}_e \cdot \hat{s}_e}{\hat{n}_e \cdot \hat{s}_e}\, C_{se2} + D^t_s \beta_s \frac{(dt)_s}{(ds)_s} \frac{\hat{t}_s \cdot \hat{s}_s}{\hat{n}_s \cdot \hat{t}_s}\, C_{se2} \quad (4.64)$$

$$A^t_{\mathrm{SW}} = -D^t_w \beta_w \frac{(ds)_w}{(dt)_w} \frac{\hat{t}_w \cdot \hat{s}_w}{\hat{n}_w \cdot \hat{s}_w}\, C_{sw1} - D^t_s \beta_s \frac{(dt)_s}{(ds)_s} \frac{\hat{t}_s \cdot \hat{s}_s}{\hat{n}_s \cdot \hat{t}_s}\, C_{sw1} \quad (4.65)$$

$$b_{\mathrm{P}}^{t} = \left(\frac{M_{\mathrm{P}}^{o}}{\Delta t}\right) T_{\mathrm{P}}^{o} + Q_{\mathrm{P}}^{t} + \widetilde{D}_{e}\, T_{e}^{o} - \widetilde{D}_{w}\, T_{w}^{o} + \widetilde{D}_{n}\, T_{n}^{o} - \widetilde{D}_{s}\, T_{s}^{o} \tag{4.66}$$

$$\begin{aligned} A_{\mathrm{P}}^{t} = {} & \frac{D_{e}^{t}\beta_{e}}{\hat{n}_{e}\cdot\hat{s}_{e}} + 0.5\,\dot{m}_{e}C_{p} + |\alpha_{e}|\,|\dot{m}_{e}|\,C_{p} + \frac{D_{w}^{t}\beta_{w}}{\hat{n}_{w}\cdot\hat{s}_{w}} - 0.5\,\dot{m}_{w}C_{p} + |\alpha_{W}|\,|\dot{m}_{w}|\,C_{p} \\ & + \frac{D_{n}^{t}\beta_{n}}{\hat{n}_{n}\cdot\hat{t}_{n}} + 0.5\,\dot{m}_{n}C_{p} + |\alpha_{n}|\,|\dot{m}_{n}|\,C_{p} + \frac{D_{s}^{t}\beta_{s}}{\hat{n}_{s}\cdot\hat{t}_{s}} - 0.5\,\dot{m}_{s}C_{p} + |\alpha_{s}|\,|\dot{m}_{s}|\,C_{p} \\ & + D_{e}^{t}\beta_{e}\frac{(ds)_{e}}{(dt)_{e}}\frac{\hat{t}_{e}\cdot\hat{s}_{e}}{\hat{n}_{e}\cdot\hat{s}_{e}}\,(C_{ne1} - C_{se4}) - D_{w}^{t}\beta_{w}\frac{(ds)_{w}}{(dt)_{w}}\frac{\hat{t}_{w}\cdot\hat{s}_{w}}{\hat{n}_{w}\cdot\hat{s}_{w}}\,(C_{nw2} - C_{sw3}) \\ & + D_{n}^{t}\beta_{n}\frac{(dt)_{n}}{(ds)_{n}}\frac{\hat{t}_{n}\cdot\hat{s}_{n}}{\hat{n}_{n}\cdot\hat{t}_{n}}\,(C_{ne1} - C_{nw2}) - D_{s}^{t}\beta_{s}\frac{(dt)_{s}}{(ds)_{s}}\frac{\hat{t}_{s}\cdot\hat{s}_{s}}{\hat{n}_{s}\cdot\hat{t}_{s}}\,(C_{se4} - C_{sw3}) \\ & + \frac{M_{P}}{\Delta t} - R_{\mathrm{P}}^{t} \end{aligned} \tag{4.67}$$

The terms that account for the energy transport by mass transfer in b_p^t are evaluated explicitly from the old time step. The diagonal coefficient $A_P^{t^*}$ is defined in similar way to $A_P^{u^*}$ to obtain:

$$A_{\mathrm{P}}^{t} = A_{\mathrm{P}}^{t^*} - R_{P}^{t} + \frac{M_{P}^{o}}{\Delta t} \tag{4.68}$$

In this work, Q_{P}^{t} and R_{P}^{t} are zero for both the liquid and the mixture.

4.3.5 Gas mass conservation equation

Gas mass conservation in the mixture is accomplished by including an additional transport equation to the model for the scalar property W, the gas mass fraction. The gas mass conservation equation is integrated with respect to time and volume in a procedure analogous to that used in the T equation.

$$\begin{aligned} & \underbrace{\int_{\forall}\int_{t}\left[\frac{\partial}{\partial t}(\rho\, W)\right] d\forall\, dt}_{I} + \underbrace{\int_{\forall}\int_{t}\left[\frac{\partial}{\partial x}(\rho\, U\, W) + \frac{\partial}{\partial y}(\,\rho\, V\, W)\right] d\forall\, dt}_{II} = \\ & \qquad + \underbrace{\int_{\forall}\int_{t}\left[\frac{\partial}{\partial x}\left(\rho\, D^{ab}\,\frac{\partial W}{\partial x}\right) + \frac{\partial}{\partial y}\left(\rho\, D^{ab}\,\frac{\partial W}{\partial y}\right)\right] d\forall\, dt}_{III} \end{aligned} \tag{4.69}$$

The discretisation procedure of the gas mass conservation equation is an analogous to that used for the T equations. The diffusion coefficients are defined as follows:

$$\left.\begin{array}{llll} D_e^w = \dfrac{A_e}{(ds)_e}\,\rho_e\,D_e^{ab} & D_n^w = \dfrac{A_n}{(dt)_n}\,\rho_n\,D_n^{ab} \\ D_w^w = \dfrac{A_w}{(ds)_w}\,\rho_w\,D_w^{ab} & D_s^w = \dfrac{A_s}{(dt)_s}\,\rho_s\,D_s^{ab} \end{array}\right\} \tag{4.70}$$

Then, the nine-point algebraic equation for W is given by the following:

$$A_{\mathrm{P}}^w\,W_{\mathrm{P}} = A_{\mathrm{E}}^w\,W_{\mathrm{E}} + A_{\mathrm{W}}^w\,W_{\mathrm{W}} + A_{\mathrm{N}}^w\,W_{\mathrm{N}} + A_{\mathrm{S}}^w\,W_{\mathrm{S}} + A_{\mathrm{NE}}^w\,W_{\mathrm{NE}} + A_{\mathrm{NW}}^w\,W_{\mathrm{NW}} + A_{\mathrm{SE}}^w\,W_{\mathrm{SE}} + A_{\mathrm{SW}}^w\,W_{\mathrm{SW}} + b_{\mathrm{P}}^w \tag{4.71}$$

The coefficients of Equation (4.71) are given by:

$$A_{\mathrm{E}}^w = \frac{D_e^w\beta_e}{\hat{n}_e\cdot\hat{s}_e} - 0.5\,\dot{m}_e + |\alpha_e|\,|\dot{m}_e| - D_n^w\beta_n\frac{(dt)_n}{(ds)_n}\frac{\hat{t}_n\cdot\hat{s}_n}{\hat{n}_n\cdot\hat{t}_n}\,C_{ne2} + D_s^w\beta_s\frac{(dt)_s}{(ds)_s}\frac{\hat{t}_s\cdot\hat{s}_s}{\hat{n}_s\cdot\hat{t}_s}\,C_{se3} + D_e^w\beta_e\frac{(ds)_e}{(dt)_e}\frac{\hat{t}_e\cdot\hat{s}_e}{\hat{n}_e\cdot\hat{s}_e}\,(C_{ne2} - C_{se3}) \tag{4.72}$$

$$A_{\mathrm{W}}^w = \frac{D_w^w\beta_w}{\hat{n}_w\cdot\hat{s}_w} + 0.5\,\dot{m}_w + |\alpha_W|\,|\dot{m}_w| + D_n^w\beta_n\frac{(dt)_n}{(ds)_n}\frac{\hat{t}_n\cdot\hat{s}_n}{\hat{n}_n\cdot\hat{t}_n}\,C_{nw1} - D_s^w\beta_s\frac{(dt)_s}{(ds)_s}\frac{\hat{t}_s\cdot\hat{s}_s}{\hat{n}_s\cdot\hat{t}_s}\,C_{sw4} + D_w^w\beta_w\frac{(ds)_w}{(dt)_w}\frac{\hat{t}_w\cdot\hat{s}_w}{\hat{n}_w\cdot\hat{s}_w}\,(C_{nw1} - C_{sw4}) \tag{4.73}$$

$$A_{\mathrm{N}}^w = \frac{D_n^w\beta_n}{\hat{n}_n\cdot\hat{t}_n} - 0.5\,\dot{m}_n + |\alpha_n|\,|\dot{m}_n| - D_e^w\beta_e\frac{(ds)_e}{(dt)_e}\frac{\hat{t}_e\cdot\hat{s}_e}{\hat{n}_e\cdot\hat{s}_e}\,C_{ne4} + D_w^w\beta_w\frac{(ds)_w}{(dt)_w}\frac{\hat{t}_w\cdot\hat{s}_w}{\hat{n}_w\cdot\hat{s}_w}\,C_{nw3} + D_n^w\beta_n\frac{(dt)_n}{(ds)_n}\frac{\hat{t}_n\cdot\hat{s}_n}{\hat{n}_n\cdot\hat{t}_n}\,(C_{ne4} - C_{nw3}) \tag{4.74}$$

$$A_{\mathrm{S}}^w = \frac{D_s^w\beta_s}{\hat{n}_s\cdot\hat{t}_s} + 0.5\,\dot{m}_s + |\alpha_s|\,|\dot{m}_s| + D_e^w\beta_e\frac{(ds)_e}{(dt)_e}\frac{\hat{t}_e\cdot\hat{s}_e}{\hat{n}_e\cdot\hat{s}_e}\,C_{se1} - D_w^w\beta_w\frac{(ds)_w}{(dt)_w}\frac{\hat{t}_w\cdot\hat{s}_w}{\hat{n}_w\cdot\hat{s}_w}\,C_{sw2} + D_s^w\beta_s\frac{(dt)_s}{(ds)_s}\frac{\hat{t}_s\cdot\hat{s}_s}{\hat{n}_s\cdot\hat{t}_s}\,(C_{se1} - C_{sw2}) \tag{4.75}$$

$$A^w_{\mathrm{NE}} = -D^w_e \beta_e \frac{(ds)_e}{(dt)_e} \frac{\hat{t}_e \cdot \hat{s}_e}{\hat{n}_e \cdot \hat{s}_e} \; C_{ne3} - D^w_n \beta_n \frac{(dt)_n}{(ds)_n} \frac{\hat{t}_n \cdot \hat{s}_n}{\hat{n}_n \cdot \hat{t}_n} \; C_{ne3} \tag{4.76}$$

$$A^w_{\mathrm{NW}} = D^w_w \beta_w \frac{(ds)_w}{(dt)_w} \frac{\hat{t}_w \cdot \hat{s}_w}{\hat{n}_w \cdot \hat{s}_w} \; C_{nw4} + D^w_n \beta_n \frac{(dt)_n}{(ds)_n} \frac{\hat{t}_n \cdot \hat{s}_n}{\hat{n}_n \cdot \hat{t}_n} \; C_{nw4} \tag{4.77}$$

$$A^w_{\mathrm{SE}} = D^w_e \beta_e \frac{(ds)_e}{(dt)_e} \frac{\hat{t}_e \cdot \hat{s}_e}{\hat{n}_e \cdot \hat{s}_e} \; C_{se2} + D^w_s \beta_s \frac{(dt)_s}{(ds)_s} \frac{\hat{t}_s \cdot \hat{s}_s}{\hat{n}_s \cdot \hat{t}_s} \; C_{se2} \tag{4.78}$$

$$A^w_{\mathrm{SW}} = -D^w_w \beta_w \frac{(ds)_w}{(dt)_w} \frac{\hat{t}_w \cdot \hat{s}_w}{\hat{n}_w \cdot \hat{s}_w} \; C_{sw1} - D^w_s \beta_s \frac{(dt)_s}{(ds)_s} \frac{\hat{t}_s \cdot \hat{s}_s}{\hat{n}_s \cdot \hat{t}_s} \; C_{sw1} \tag{4.79}$$

$$b^w_{\mathrm{P}} = \left(\frac{M^o_{\mathrm{P}}}{\Delta t} \right) W^o_{\mathrm{P}} \tag{4.80}$$

$$\begin{aligned} A^w_{\mathrm{P}} = {} & \frac{D^w_e \beta_e}{\hat{n}_e \cdot \hat{s}_e} + 0.5\, \dot{m}_e + |\alpha_e|\, |\dot{m}_e| + \frac{D^w_w \beta_w}{\hat{n}_w \cdot \hat{s}_w} - 0.5\, \dot{m}_w + |\alpha_W|\, |\dot{m}_w| \\ & + \frac{D^w_n \beta_n}{\hat{n}_n \cdot \hat{t}_n} + 0.5\, \dot{m}_n + |\alpha_n|\, |\dot{m}_n| + \frac{D^w_s \beta_s}{\hat{n}_s \cdot \hat{t}_s} - 0.5\, \dot{m}_s + |\alpha_s|\, |\dot{m}_s| \\ & + D^w_e \beta_e \frac{(ds)_e}{(dt)_e} \frac{\hat{t}_e \cdot \hat{s}_e}{\hat{n}_e \cdot \hat{s}_e} \; (C_{ne1} - C_{se4}) - D^w_w \beta_w \frac{(ds)_w}{(dt)_w} \frac{\hat{t}_w \cdot \hat{s}_w}{\hat{n}_w \cdot \hat{s}_w} \; (C_{nw2} - C_{sw3}) \\ & + D^w_n \beta_n \frac{(dt)_n}{(ds)_n} \frac{\hat{t}_n \cdot \hat{s}_n}{\hat{n}_n \cdot \hat{t}_n} \; (C_{ne1} - C_{nw2}) - D^w_s \beta_s \frac{(dt)_s}{(ds)_s} \frac{\hat{t}_s \cdot \hat{s}_s}{\hat{n}_s \cdot \hat{t}_s} \; (C_{se4} - C_{sw3}) \\ & + \frac{M_{\mathrm{P}}}{\Delta t} \end{aligned} \tag{4.81}$$

With $A^{w^*}_P$ is defined in similar way to $A^{u^*}_P$, the diagonal coefficient is given by

$$A^w_{\mathrm{P}} = A^{w^*}_{\mathrm{P}} + \frac{M^o_P}{\Delta t} \tag{4.82}$$

4.4 Algebraic Interface Equations

4.4.1 Derivation of the Equations

At the interface, each interface equation is employed to form an algebraic equation for a certain flow variable at either the liquid or the mixture side of the interface. For a given i

index, there are nine unknowns at the two interface nodes. These unknowns are: liquid and mixture values for the two velocity components, the pressure correction in each phase, the temperature in each phase, and the gas mass fraction at only the mixture interfacial node. In this section, steps of deriving these equations and the final forms of the coefficients will be presented. The notation of the j index was explained in Figure 3.2.

1. Normal force balance

   The normal force balance equation is given in Equation (2.10). The algebraic normal force balance condition is used as an equation for $P'_{L,int}$ (at $j = j_{EL} + 1$). At the interface, all components of unit vectors at the interface are the same either from the liquid or the mixture side.

   The stress tensor ($\boldsymbol{T}$) for 2D is defined in terms of the normal and shear stress as follows

   $$\boldsymbol{T} = \begin{pmatrix} \boldsymbol{T}_{xx} & \boldsymbol{T}_{yx} \\ \boldsymbol{T}_{xy} & \boldsymbol{T}_{yy} \end{pmatrix} \tag{4.83}$$

   For incompressible fluids, the stress tensor can be written in the compact form

   $$\boldsymbol{T}_{ij} = -P\ \delta_{ij} + \mu_{L}\ \left(\frac{\partial U_i}{\partial x_j} + \frac{\partial U_j}{\partial x_i} \right) \tag{4.84}$$

   Where i and j refer to the coordinates x and y and δ_{ij} in the index notation is the Kronecker delta.

   The left hand side of Equation (2.10) can be written in terms of the normal and shear stresses at the interface

   $$I = \left(\hat{n} \cdot \boldsymbol{T}\right)_{L} \cdot \hat{n} = \boldsymbol{T}_{xx}\ n_{xn}^2 + 2\ \boldsymbol{T}_{xy}\ n_{xn}\ n_{yn} + \boldsymbol{T}_{yy}\ n_{yn}^2 \tag{4.85}$$

   where

   $$\boldsymbol{T}_{xx} = -P + 2\mu_{L} \left(\frac{\partial U}{\partial x} \right) \tag{4.86}$$

$$\boldsymbol{T}_{yx} = \boldsymbol{T}_{xy} = \mu_{L} \left(\frac{\partial U}{\partial y} + \frac{\partial V}{\partial x} \right) \tag{4.87}$$

$$\boldsymbol{T}_{yy} = -P + 2\mu_{L} \left(\frac{\partial V}{\partial y} \right) \tag{4.88}$$

Substitute all stresses into Equation (4.85), we get

$$I = (\hat{n} \cdot \boldsymbol{T})_{L} \cdot \hat{n} = - P_{L} + 2\ \mu_{L} \left(\frac{\partial U}{\partial x} \right)_{L} n_{xn}^{2} + 2\ \mu_{L} \left(\frac{\partial U}{\partial y} + \frac{\partial V}{\partial x} \right)_{L} n_{xn}\ n_{yn} + 2\ \mu_{L} \left(\frac{\partial V}{\partial y} \right)_{L} n_{yn}^{2} \tag{4.89}$$

Following the same procedure, the right hand side term of Equation (2.10) is given by Equation(4.90)

$$II = (\hat{n} \cdot \boldsymbol{T})_{M} \cdot \hat{n} = - P_{M} + 2\ \mu_{M} \left(\frac{\partial U}{\partial x} \right)_{M} n_{xn}^{2} + 2\ \mu_{M} \left(\frac{\partial U}{\partial y} + \frac{\partial V}{\partial x} \right)_{M} n_{xn}\ n_{yn} + 2\ \mu_{M} \left(\frac{\partial V}{\partial y} \right)_{M} n_{yn}^{2} \tag{4.90}$$

Central differencing is used to evaluate the velocity derivatives and a 1D interpolation is employed to determine the corner values (U_{ne} and U_{nw})) for the liquid side of the interface and (U_{se} and U_{sw})) for the mixture side of the interface from its interfacial two neighbours. For example, U_{ne} at the liquid side of the interface is determine by ($U_{\text{ne}} = f_{ne}\ U_{\text{N}} + (1 - f_{ne})\ U_{\text{NE}}$) where f_{ne} is a linear interpolation factor based on the grid spacing. The derivatives at the interface for any velocity component (U and V) can be given in general forms by the following expressions:

$$\left. \frac{\partial \phi}{\partial x} \right|_{\text{n,L,int}} = A_{\text{x1}}\ \phi_{\text{P}} + A_{\text{x2}}\ \phi_{\text{N}} + A_{\text{x3}}\ \phi_{\text{NE}} + A_{\text{x4}}\ \phi_{\text{NW}} \tag{4.91}$$

$$\left. \frac{\partial \phi}{\partial y} \right|_{\text{n,L,int}} = A_{\text{y1}}\ \phi_{\text{P}} + A_{\text{y2}}\ \phi_{\text{N}} + A_{\text{y3}}\ \phi_{\text{NE}} + A_{\text{y4}}\ \phi_{\text{NW}} \tag{4.92}$$

where ϕ can stand for any variable and the coefficients are

$$\left.\begin{aligned} A_{x1} &= \frac{s_{yn}}{(dt)_n\ \Psi} & A_{x2} &= \frac{1}{\Psi}\left[\frac{t_{yn}}{(ds)_n}\left(f_{ne}-(1-f_{nw})\right)-\frac{s_{yn}}{(dt)_n}\right] \\ A_{x3} &= \frac{t_{yn}}{(ds)_n\ \Psi}\ (1-f_{ne}) & A_{x4} &= -\frac{t_{yn}}{(ds)_n\ \Psi}\ f_{nw} \end{aligned}\right\} \tag{4.93}$$

and

$$\left.\begin{aligned} A_{y1} &= -\frac{s_{xn}}{(dt)_n\ \Psi} & A_{y2} &= \frac{1}{\Psi}\left[\frac{s_{xn}}{(dt)_n}-\frac{t_{xn}}{(ds)_n}\left(f_{ne}-(1-f_{nw})\right)\right] \\ A_{y3} &= -\frac{t_{xn}}{(ds)_n\ \Psi}\ (1-f_{ne}) & A_{y4} &= -\frac{t_{xn}}{(ds)_n\ \Psi}\ f_{nw} \end{aligned}\right\} \tag{4.94}$$

The geometrical term , Ψ, is given by

$$\Psi = (s_{xn}\ t_{yn} - t_{xn}\ s_{yn}) \tag{4.95}$$

The notation here is for the last control volume in the liquid side ($j = j_{EL}$). Now, making use of Equations (4.91) and (4.92) to evaluate various velocity gradients in Equation (4.89) yields

$$\begin{aligned} I = (\hat{n}\cdot\boldsymbol{T})_L\cdot\hat{n} = -P_L &+ 2\ \mu_L\ n_{xn}^2\left(A_{\mathrm{x1}}\ U_{\mathrm{P}} + A_{\mathrm{x2}}\ U_{\mathrm{N}} + A_{\mathrm{x3}}\ U_{\mathrm{NE}} + A_{\mathrm{x4}}\ U_{\mathrm{NW}}\right)_L \\ &+2\ \mu_L\ n_{xn}n_{yn}\left(A_{\mathrm{y1}}\ U_{\mathrm{P}} + A_{\mathrm{y2}}\ U_{\mathrm{N}} + A_{\mathrm{y3}}\ U_{\mathrm{NE}} + A_{\mathrm{y4}}\ U_{\mathrm{NW}}\right)_L \\ &+2\ \mu_L\ n_{xn}n_{yn}\left(A_{\mathrm{x1}}\ V_{\mathrm{P}} + A_{\mathrm{x2}}\ V_{\mathrm{N}} + A_{\mathrm{x3}}\ V_{\mathrm{NE}} + A_{\mathrm{x4}}\ V_{\mathrm{NW}}\right)_L \\ &+2\ \mu_L\ n_{yn}^2\left(A_{\mathrm{y1}}\ V_{\mathrm{P}} + A_{\mathrm{y2}}\ V_{\mathrm{N}} + A_{\mathrm{y3}}\ V_{\mathrm{NE}} + A_{\mathrm{y4}}\ V_{\mathrm{NW}}\right)_L \end{aligned} \tag{4.96}$$

Following a similar procedure, Equation (4.90) can be written in terms of mixture

nodal velocities and interfacial pressure as follows:

$$\begin{aligned} II = (\hat{n}\cdot\boldsymbol{T})_M\cdot\hat{n} = -P_M &+ 2\ \mu_M\ n_{xs}^2\,(B_{\mathrm{x1}}\ U_{\mathrm{P}} + B_{\mathrm{x2}}\ U_{\mathrm{S}} + B_{\mathrm{x3}}\ U_{\mathrm{SE}} + B_{\mathrm{x4}}\ U_{\mathrm{SW}})_M \\ &+2\ \mu_M\ n_{xs}n_{ys}\,(B_{\mathrm{y1}}\ U_{\mathrm{P}} + B_{\mathrm{y2}}\ U_{\mathrm{S}} + B_{\mathrm{y3}}\ U_{\mathrm{SE}} + B_{\mathrm{y4}}\ U_{\mathrm{SW}})_M \\ &+2\ \mu_M\ n_{xs}n_{ys}\,(B_{\mathrm{x1}}\ V_{\mathrm{P}} + B_{\mathrm{x2}}\ V_{\mathrm{S}} + B_{\mathrm{x3}}\ V_{\mathrm{NE}} + B_{\mathrm{x4}}\ V_{\mathrm{NW}})_M \\ &+2\ \mu_M\ n_{ys}^2\,(B_{\mathrm{y1}}\ V_{\mathrm{P}} + B_{\mathrm{y2}}\ V_{\mathrm{S}} + B_{\mathrm{y3}}\ V_{\mathrm{SE}} + B_{\mathrm{y4}}\ V_{\mathrm{SW}})_M \end{aligned} \tag{4.97}$$

Here it is noteworthy that the notation that is used here is for the first control volume on the mixture side (i. e $j = j_{BM}$). Also, the coefficients are given by

$$\left.\begin{aligned} B_{x1} &= -\frac{s_{ys}}{(dt)_s\ \Psi} & B_{x2} &= \frac{1}{\Psi}\left[\frac{t_{ys}}{(ds)_s}\,(f_{se}-(1-f_{sw})) + \frac{s_{ys}}{(dt)_s}\right] \\ B_{x3} &= \frac{t_{ys}}{(ds)_s\ \Psi}\ (1-f_{ne}) & B_{x4} &= -\frac{t_{ys}}{(ds)_s\ \Psi}\ f_{sw} \end{aligned}\right\} \tag{4.98}$$

and

$$\left.\begin{aligned} B_{y1} &= \frac{s_{xs}}{(dt)_s\ \Psi} & B_{y2} &= \frac{1}{\Psi}\left[\frac{-s_{xs}}{(dt)_s} - \frac{t_{xs}}{(ds)_s}\,(f_{se}-(1-f_{sw}))\right] \\ B_{y3} &= -\frac{t_{xs}}{(ds)_s\ \Psi}\ (1-f_{se}) & B_{y4} &= \frac{t_{xs}}{(ds)_s\ \Psi}\ f_{nw} \end{aligned}\right\} \tag{4.99}$$

Now, substitute Equations (4.96) and (4.97) into Equation (2.10) and collect terms to

get

$$
\begin{aligned}
P_{\mathrm{L,int}} = P_{\mathrm{M,int}} \\
&+ 2\ \mu_L \left(n_{xn}^2 A_{x1} + n_{xn} n_{yn} A_{y1}\right) U_{L,P} + 2\ \mu_L \left(n_{xn} n_{yn} A_{x1} + n_{yn}^2 A_{y1}\right) V_{L,P} \\
&+ 2\ \mu_L \left(n_{xn}^2 A_{x2} + n_{xn} n_{yn} A_{y2}\right) U_{L,int} + 2\ \mu_L \left(n_{xn} n_{yn} A_{x2} + n_{yn}^2 A_{y2}\right) V_{L,int} \\
&+ 2\ \mu_L \left(n_{xn}^2 A_{x3} + n_{xn} n_{yn} A_{y3}\right) U_{L,NE} + 2\ \mu_L \left(n_{xn} n_{yn} A_{x3} + n_{yn}^2 A_{y3}\right) V_{L,NE} \\
&+ 2\ \mu_L \left(n_{xn}^2 A_{x4} + n_{xn} n_{yn} A_{y4}\right) U_{L,NW} + 2\ \mu_L \left(n_{xn} n_{yn} A_{x4} + n_{yn}^2 A_{y4}\right) V_{L,NW} \\
&- 2\ \mu_M \left(n_{xs}^2 B_{x1} + n_{xs} n_{ys} B_{y1}\right) U_{M,P} - 2\ \mu_M \left(n_{xs} n_{ys} B_{x1} + n_{ys}^2 B_{y1}\right) V_{M,P} \\
&- 2\ \mu_M \left(n_{xs}^2 B_{x2} + n_{xs} n_{ys} B_{y2}\right) U_{M,int} - 2\ \mu_M \left(n_{xs} n_{ys} B_{x2} + n_{ys}^2 B_{y2}\right) V_{M,int} \\
&- 2\ \mu_M \left(n_{xs}^2 B_{x3} + n_{xs} n_{ys} B_{y3}\right) U_{M,SE} - 2\ \mu_M \left(n_{xs} n_{ys} B_{x3} + n_{ys}^2 B_{y3}\right) V_{M,SE} \\
&- 2\ \mu_M \left(n_{xs}^2 B_{x4} + n_{xs} n_{ys} B_{y4}\right) U_{M,SW} - 2\ \mu_M \left(n_{xs} n_{ys} B_{x4} + n_{ys}^2 B_{y4}\right) V_{M,SW}
\end{aligned}
\tag{4.100}
$$

Equation (4.100) will be used for pressure correction as explained later.

2. Tangential force balance

The algebraic tangential force balance condition is used for either $U_{L,int}$ or $V_{L,int}$. In this section, the tangential force balance will be used to derive an equation for $U_{L,int}$ (at $j = j_{EL} + 1$). A scheme for assigning interfacial conditions to specific velocity components U and V at the interface will be introduced later. The tangential force balance is divided into two parts.

$$
\underbrace{\left(\hat{n} \cdot \boldsymbol{T}\right)_L \cdot \hat{s}}_{I} = \underbrace{\left(\hat{n} \cdot \boldsymbol{T}\right)_M \cdot \hat{s}}_{II} \tag{4.101}
$$

The left hand side of Equation (4.101) can be written in terms of the normal and shear stresses at the interface as follows

$$
I = \left(\hat{n} \cdot \boldsymbol{T}\right)_L \cdot \hat{s} = \boldsymbol{T}_{xx}\ \ n_{xn}\ s_{xn} + \boldsymbol{T}_{xy}\left(n_{yn}\ s_{xn} + n_{xn} s_{yn}\right) + \boldsymbol{T}_{yy}\ n_{yn}\ s_{yn} \tag{4.102}
$$

which can be further expressed in terms of velocity gradients by applying relations in Equations (4.86) to (4.88).

$$I = (\hat{n} \cdot \boldsymbol{T})_{L} \cdot \hat{s} = 2\,\mu_L \left(\frac{\partial U}{\partial x}\right)_L n_{xn}\, s_{xn} + \mu_L \left(\frac{\partial U}{\partial y} + \frac{\partial V}{\partial x}\right)_L (n_{yn}\, s_{xn} + n_{xn}\, s_{yn}) + 2\,\mu_L \left(\frac{\partial V}{\partial y}\right)_L n_{yn}\, s_{yn} \tag{4.103}$$

The right hand side term of Equation (4.101) is given by Equation(4.104)

$$II = (\hat{n} \cdot \boldsymbol{T})_{M} \cdot \hat{s} = 2\,\mu_M \left(\frac{\partial U}{\partial x}\right)_M n_{xn}\, s_{xn} + \mu_M \left(\frac{\partial U}{\partial y} + \frac{\partial V}{\partial x}\right)_M (n_{yn}\, s_{xn} + n_{xn}\, s_{yn}) + 2\,\mu_M \left(\frac{\partial V}{\partial y}\right)_M n_{yn}\, s_{yn} \tag{4.104}$$

Using Equations (4.91) and (4.92) and their analogues at the mixture side of the interface, Equations (4.103) and (4.104) become

$$\begin{aligned} I = (\hat{n} \cdot \boldsymbol{T})_{L} \cdot \hat{s} = {} & 2\,\mu_L\, n_{xn}\, s_{xn} \left(A_{\mathrm{x1}}\, U_{\mathrm{P}} + A_{\mathrm{x2}}\, U_{\mathrm{N}} + A_{\mathrm{x3}}\, U_{\mathrm{NE}} + A_{\mathrm{x4}}\, U_{\mathrm{NW}}\right)_L \\ & + \mu_L\, (n_{yn}\, s_{xn} + n_{xn}\, s_{yn}) \left(A_{\mathrm{y1}}\, U_{\mathrm{P}} + A_{\mathrm{y2}}\, U_{\mathrm{N}} + A_{\mathrm{y3}}\, U_{\mathrm{NE}} + A_{\mathrm{y4}}\, U_{\mathrm{NW}}\right)_L \\ & + \mu_L\, (n_{yn}\, s_{xn} + n_{xn}\, s_{yn}) \left(A_{\mathrm{x1}}\, V_{\mathrm{P}} + A_{\mathrm{x2}}\, V_{\mathrm{N}} + A_{\mathrm{x3}}\, V_{\mathrm{NE}} + A_{\mathrm{x4}}\, V_{\mathrm{NW}}\right)_L \\ & + 2\,\mu_L\, n_{yn}\, s_{yn} \left(A_{\mathrm{y1}}\, V_{\mathrm{P}} + A_{\mathrm{y2}}\, V_{\mathrm{N}} + A_{\mathrm{y3}}\, V_{\mathrm{NE}} + A_{\mathrm{y4}}\, V_{\mathrm{NW}}\right)_L \end{aligned} \tag{4.105}$$

$$\begin{aligned} II = (\hat{n} \cdot \boldsymbol{T})_{M} \cdot \hat{s} = {} & 2\,\mu_M\, n_{xs}\, s_{xs} \left(B_{\mathrm{x1}}\, U_{\mathrm{P}} + B_{\mathrm{x2}}\, U_{\mathrm{S}} + B_{\mathrm{x3}}\, U_{\mathrm{SE}} + B_{\mathrm{x4}}\, U_{\mathrm{SW}}\right)_M \\ & + \mu_M\, (n_{ys}\, s_{xs} + n_{xs}\, s_{ys}) \left(B_{\mathrm{y1}}\, U_{\mathrm{P}} + B_{\mathrm{y2}}\, U_{\mathrm{S}} + B_{\mathrm{y3}}\, U_{\mathrm{SE}} + B_{\mathrm{y4}}\, U_{\mathrm{SW}}\right)_M \\ & + \mu_M\, (n_{ys}\, s_{xs} + n_{xs}\, s_{ys}) \left(B_{\mathrm{x1}}\, V_{\mathrm{P}} + B_{\mathrm{x2}}\, V_{\mathrm{S}} + B_{\mathrm{x3}}\, V_{\mathrm{SE}} + B_{\mathrm{x4}}\, V_{\mathrm{SW}}\right)_M \\ & + 2\,\mu_M\, n_{ys}\, s_{ys} \left(B_{\mathrm{y1}}\, V_{\mathrm{P}} + B_{\mathrm{y2}}\, V_{\mathrm{S}} + B_{\mathrm{y3}}\, V_{\mathrm{SE}} + B_{\mathrm{y4}}\, V_{\mathrm{SW}}\right)_M \end{aligned} \tag{4.106}$$

Equations (4.105) and (4.106) are substituted into Equation (4.101). After collecting terms, the resulting algebraic equation would be used as an equation for U or V at the interface for either the liquid or the mixture side. During testing of the code, it was found that this choice can strongly affect the stability and convergence of the

solution. The scheme to over come these problems using a correct assignment of interface algebraic equations will be discussed later. For now, this condition is assigned to U in the liquid side of the interface. Therefore, the algebraic equation for U at ($j = j_{EL} + 1$) is

$$A^u_{\rm P}\, U_{\rm P} = A^u_{\rm E}\, U_{\rm E} + A^u_{\rm W}\, U_{\rm W} + A^u_{\rm N}\, U_{\rm N} + A^u_{\rm S}\, U_{\rm S} + A^u_{\rm SE}\, U_{\rm SE} + A^u_{\rm SW}\, U_{\rm SW} + b^u_{\rm P} \tag{4.107}$$

where

$$\left.\begin{aligned}
&A^u_{\rm P} = -\left(L_1\ A_{x2} + L_2\ A_{y2}\right) && A^u_{\rm N} = -\left(M_1\ B_{x2} + M_2\ B_{y2}\right)\\
&A^u_{\rm E} = \left(L_1\ A_{x3} + L_2\ A_{y3}\right) && A^u_{\rm W} = \left(L_1\ A_{x4} + L_2\ A_{y4}\right)\\
&A^u_{\rm NE} = -\left(M_1\ B_{x3} + M_2\ A_{y3}\right) && A^u_{\rm NW} = -\left(M_1\ B_{x4} + M_2\ B_{y4}\right)\\
&A^u_{\rm SE} = 0 && A^u_{\rm SW} = 0\\
&A^u_{\rm S} = \left(L_1\ A_{x1} + L_2\ A_{y1}\right)\\
&b^u_{\rm P} = +\left(L_2\ A_{x2} + L_3\ A_{y2}\right)\ V_{\rm P} + \left(L_2\ A_{x3} + L_3\ A_{y3}\right)\ V_{\rm E}\\
&+\left(L_2\ A_{x4} + L_3\ A_{y4}\right)\ V_{\rm W} + \left(L_2\ A_{x1} + L_3\ A_{y1}\right)\ V_{\rm S}\\
&-\left(M_1\ B_{x1} + M_2\ B_{y1}\right)\ U_{\rm NN} - \left(M_2\ B_{x1} + M_3\ B_{y1}\right)\ V_{\rm NN}\\
&-\left(M_2\ B_{x2} + M_3\ B_{y2}\right)\ V_{\rm N} - \left(M_2\ B_{x3} + M_3\ B_{y3}\right)\ V_{\rm NE}\\
&-\left(M_2\ B_{x4} + M_3\ B_{y4}\right)\ V_{\rm NW}
\end{aligned}\right\} \tag{4.108}$$

and

$$\left.\begin{aligned}
&L_1 = 2\ \mu_L\ n_{xn}\ s_{xn} \quad L_2 = \mu_L\ \left(n_{yn}\ s_{xn} + n_{xn}\ s_{yn}\right) \quad L_3 = 2\ \mu_L\ n_{yn}\ s_{yn}\\
&M_1 = 2\ \mu_M\ n_{xs}\ s_{xs} \quad M_2 = \mu_M\left(n_{ys}\ s_{xs} + n_{xs}\ s_{ys}\right) \quad M_3 = 2\ \mu_M\ n_{ys}\ s_{ys}
\end{aligned}\right\} \tag{4.109}$$

3. Tangential velocity equality

The condition of continuous tangential velocity is given by Equation (2.13). The tan-

gential component of the velocity vector is given by

$$\overrightarrow{V}_{\mathrm{M,int}} \cdot \hat{s}_{n_M} = \overrightarrow{V}_{\mathrm{L,int}} \cdot \hat{s}_{n_L} \tag{4.110}$$

which can be written as

$$(U\ \hat{\imath} + V\ \hat{\jmath})_{\mathrm{M,int}} \cdot (s_{xn}\ \hat{\imath} + s_{yn}\ \hat{\jmath})_{\mathrm{M,int}} = (U\ \hat{\imath} + V\ \hat{\jmath})_{\mathrm{L,int}} \cdot (s_{xn}\ \hat{\imath} + s_{yn}\ \hat{\jmath})_{\mathrm{L,int}} \tag{4.111}$$

Now, solve for $U_{\mathrm{M,int}}$ knowing that $((\hat{s}_n)_{\mathrm{L,int}} = (\hat{s}_n)_{\mathrm{M,int}})$ to get the algebraic equation for tangential velocity equality condition at $j = j_{BM} - 1$.

$$A^u_{\mathrm{P}}\, U_{\mathrm{P}} = A^u_{\mathrm{S}}\, U_{\mathrm{S}} + b^u_{\mathrm{P}} \tag{4.112}$$

where:

$$\left.\begin{aligned} A^u_{\mathrm{P}} &= 1 & A^u_{\mathrm{S}} &= 1 \\ b^u_{\mathrm{P}} &= -\frac{s_{yn_{\mathrm{int}}} \left(V_{\mathrm{M,int}} - V_{\mathrm{L,int}}\right)}{s_{xn_{\mathrm{int}}}} \end{aligned}\right\} \tag{4.113}$$

4. Mass balance across the interface: liquid side

Equation (2.14) can be written in terms of the velocity vector and normal unit vector at the interface as follows:

$$\rho_L\, A_n\ \overrightarrow{V}_{\mathrm{L,int}} \cdot \hat{n}_n = \rho_M\, A_n\ \overrightarrow{V}_{\mathrm{M,int}} \cdot \hat{n}_n \tag{4.114}$$

After performing the dot product, the algebraic mass balance condition, Equation (2.14), is written in this section to govern $V_{\mathrm{L,int}}$ (at $j = j_{EL} + 1$) with the final form

$$A^v_{\mathrm{P}}\, V_{\mathrm{P}} = A^v_{\mathrm{N}}\, V_{\mathrm{N}} + b^v_{\mathrm{P}} \tag{4.115}$$

where

$$\left.\begin{aligned} A^v_{\mathrm{P}} &= 1 & A^v_{\mathrm{N}} &= \frac{\rho_M}{\rho_L} \\ b^v_{\mathrm{P}} &= \frac{n_{xn}}{n_{yn}} \left[\frac{\rho_M}{\rho_L}\ U_{\mathrm{N}} - U_{\mathrm{P}}\right] \end{aligned}\right\} \tag{4.116}$$

5. Mass balance across the interface: mixture side

   Equation (2.15) is used in this section to form a governing equation for V at the mixture side of interface.

$$\dot{m}_{\mathrm{M,int}} = \rho_M \, A_n \, \overrightarrow{V}_{\mathrm{M,int}} \cdot \hat{n}_n = \dot{m}_{\mathrm{cond}} \tag{4.117}$$

   which can be rearranged for $(j = j_{BM} - 1)$. The resulting algebraic equation is given below.

$$A^v_{\mathrm{P}} \, V_{\mathrm{P}} = b^v_{\mathrm{P}} \tag{4.118}$$

   where:

$$\left.\begin{aligned} A^v_{\mathrm{P}} &= 1 \\ b^v_{\mathrm{P}} &= \frac{-n_{xn}}{n_{yn}} \, U_{\mathrm{P}} + \frac{\dot{m}_{\mathrm{cond}}}{\rho_M \, A_n \, n_{yn}} \end{aligned}\right\} \tag{4.119}$$

6. Zero pressure gradient near the mixture side

   This condition is employed near the mixture side of the interface. Using 1D interpolation at the east and west sides of the boundary control volume at $(j = j_{BM} - 1)$ and collecting geometrical terms , Equation (2.17) can be written as

$$\begin{aligned} \left.\frac{\partial P}{\partial n}\right|_{int,m} &= \left(D_{x1} \, P_{\mathrm{P}} + D_{x2} \, P_{\mathrm{E}} + D_{x3} \, P_{\mathrm{W}} + D_{x4} \, P_{\mathrm{N}}\right) \, n_{xn} \\ &+ \left(D_{y1} \, P_{\mathrm{P}} + D_{y2} \, P_{\mathrm{E}} + D_{y3} \, P_{\mathrm{W}} + D_{y4} \, P_{\mathrm{N}}\right) \, n_{yn} = \, 0 \end{aligned} \tag{4.120}$$

where

$$\left.\begin{aligned}
D_{x1} &= \frac{1}{\Psi}\left[\frac{t_{yn}}{(ds)_n}\left(f_e + f_w - 1\right) - \frac{s_{yn}}{(dt)_n}\right] \\
D_{x2} &= \frac{1}{\Psi}\left[\frac{t_{yn}}{(ds)_n}\left(1 - f_e\right)\right] \\
D_{x3} &= \frac{-1}{\Psi}\left[\frac{t_{yn}}{(ds)_n}\ f_w\right] \\
D_{x4} &= \frac{-1}{\Psi}\left[\frac{s_{yn}}{(dt)_n}\right] \\
D_{y1} &= \frac{-1}{\Psi}\left[\frac{t_{xn}}{(ds)_n}\left(f_e + f_w - 1\right) + \frac{s_{xn}}{(dt)_n}\right] \\
D_{y2} &= \frac{-1}{\Psi}\left[\frac{t_{xn}}{(ds)_n}\left(1 - f_e\right)\right] \\
D_{y3} &= \frac{1}{\Psi}\left[\frac{t_{xn}}{(ds)_n}\ f_w\right] \\
D_{y4} &= \frac{1}{\Psi}\left[\frac{s_{xn}}{(dt)_n}\right]
\end{aligned}\right\} \tag{4.121}$$

Equation (4.120) will be used to form a governing equation for the pressure correction as explained later.

7. Saturation temperature at the interface

This condition is used for the mixture side of the interface ($j = j_{BM} - 1$). The local temperature of the mixture that is adjacent to the interface is held equal to the saturation temperature corresponding to the partial pressure of the vapour. The algebraic equation for the temperature becomes

$$A^t_{\mathrm{P}}\, T_{\mathrm{P}} = b^t_{\mathrm{P}} \tag{4.122}$$

where:

$$\left.\begin{aligned}
A^t_{\mathrm{P}} &= 1 \\
b^t_{\mathrm{P}} &= T_{\mathrm{sat}}(P_{\mathrm{V,int}})
\end{aligned}\right\} \tag{4.123}$$

where $T_{\mathrm{sat}}(P_{\mathrm{V,int}})$ function is explained in Section 2.5.

8. Continuity of temperature

   This condition is used for the liquid side of the interface ($j = j_{EL} + 1$). The algebraic equation for the temperature becomes

$$A^t_{\mathrm{P}}\, A^T_{\mathrm{P}} = A^t_{\mathrm{N}}\, T_{\mathrm{N}} \tag{4.124}$$

   where:

$$\left.\begin{aligned} A^t_{\mathrm{P}} &= 1 \\ A^t_{\mathrm{N}} &= 1 \end{aligned}\right\} \tag{4.125}$$

9. Gas impermeability

   This condition is employed at the mixture side of the interface for W. It ensures that the non-condensable gas diffuses back from the interface at the same rate as advection toward the interface to keep the net mass flow of gas at the interface equal to zero. Using an equation analogous to Equation (4.120) to evaluate the gradient of W at the interface and solving for W at ($j = j_{BM} - 1$) yields

$$A^w_{\mathrm{P}}\, W_{\mathrm{P}} = A^w_{\mathrm{E}}\, W_{\mathrm{E}} + A^w_{\mathrm{W}}\, W_{\mathrm{W}} + A^w_{\mathrm{N}}\, W_{\mathrm{N}} + b^w_{\mathrm{P}} \tag{4.126}$$

   where

$$\left.\begin{aligned} &A^w_{\mathrm{P}} = \dot{m}_{M,int} - \left(\rho_M\, D^{ab}\right)_{int} \left[D_{x1}\; n_{xn} + D_{y1}\; n_{yn}\right] \quad A^w_{\mathrm{E}} = \left(\rho_M\, D^{ab}\right)_{int} \left[D_{x2}\; n_{xn} + D_{y2}\; n_{yn}\right] \\ &A^w_{\mathrm{W}} = \left(\rho_M\, D^{ab}\right)_{int} \left[D_{x3}\; n_{xn} + D_{y3}\; n_{yn}\right] \qquad\qquad A^w_{\mathrm{N}} = \left(\rho_M\, D^{ab}\right)_{int} \left[D_{x4}\; n_{xn} + D_{y4}\; n_{yn}\right] \\ &b^w_{\mathrm{P}} = 0 \end{aligned}\right\} \tag{4.127}$$

4.4.2 Modified Assignment of the Interface Algebraic Equations

As described in Section 4.4.1, the four algebraic interface conditions for the velocity components are derived from the tangential force balance (Equation (4.101)), the equality of

tangential velocity condition (Equation (4.110)), and the mass balances (Equations (4.114) and (4.117)). It is very important how these equations are assigned to the interface velocity algebraic equations, as explained below.

The orientation of the liquid film changes significantly around the tube surface. At the top of the tube, the interface is nearly parallel to the y direction so that the V velocity is essentially parallel to the interface. Consequently, the interface mass balance equations must be used for algebraic equations for the interface U velocities. Using the mass balance equations for the V velocity equations leads to ill-conditioned equations.

Farther along the tube surface at $\theta = 90°$, the interface is nearly parallel to the x direction so that the U velocity is essentially parallel to the interface. At this location, the interface mass balance equations must be assigned to the algebraic equations for the interface V velocities to avoid ill-conditioned equations.

Therefore, a scheme for changing the equations used for the algebraic equations for interface velocities was devised. Along the tube for ($0° \leq \theta < 45°$) and ($135° < \theta < 180°$), mass balances (Equations ((4.114) and (4.117)) are used to form algebraic equations for U velocities on both sides of the interface. The tangential force balance Equation (4.101) is assigned for the V velocity component on the liquid side. The equality of tangential velocity condition (Equation (4.110)) is used as the equation for the V velocity on the mixture side. For ($45° \leq \theta \leq 135°$) and in the free falling film region, Equation (4.101) is assigned for the U velocity component on the liquid side. The equality of tangential velocity condition (Equation (4.110)) is used as the equation for the U velocity on the mixture side. Both mass balances are then used to write algebraic equations for V velocity in both phases at the interface.

4.5 Boundary Condition Equation Implementation

The boundary conditions are employed at the domain edges to impose the necessary information on the domain and hence the solution. Appropriate predetermination of the boundary conditions helps in conserving the reality of the problem. Two types of the boundary conditions are used in this work: Dirichlet and Neumann. In the next sections, a description of formulating and implementing these boundary conditions is presented for a general variable, ϕ, on one boundary side of the domain. The same approach is applied to nodal velocity components U and V, temperature, T, and gas mass fraction, W.

On all edges of the domain, zero width control volumes for the boundary nodes are used. To explain the method of formulating the boundary condition equations, the south boundary is selected. Figure 4.2(a) shows schematically a typical boundary node on the south boundary of the domain and its neighbours. At the south boundary, $(j = j_B - 1)$, the boundary condition must connect the fictitious node P to its adjacent interior node N.

$$A^{\phi}_{P(i,j_B-1)}\phi_{P(i,j_B-1)} = A^{\phi}_{N(i,j_B-1)}\phi_{N(i,j_B-1)} + b^{\phi}_{(i,j_B-1)} \tag{4.128}$$

The coefficients of Equation (4.128) should be set to the prescribed the desired boundary condition at the south boundary. The next sections describe how those coefficients are set to prescribe Dirichlet and Neumann boundary conditions.

4.5.1 Dirichlet

A Dirichlet boundary condition is used when the value of the variable ϕ at the boundary is specified. This boundary condition is obtained by setting the coefficients of Equation (4.128) to:

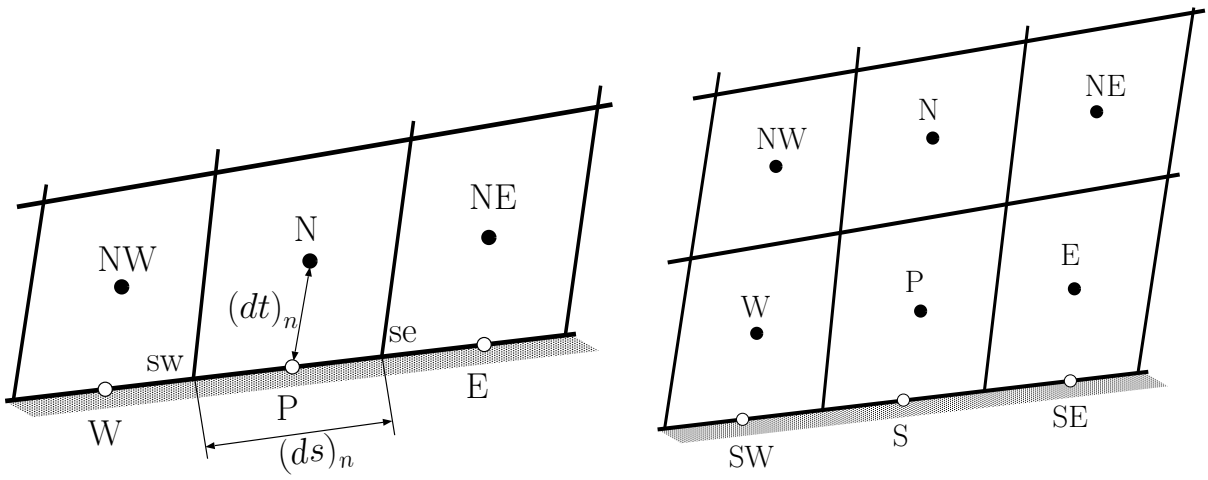

(a) $(j = j_B - 1)$ (b) $(j = j_B)$

Figure 4.2: South Boundary Computational Molecule.

$$\left.\begin{aligned} A^{\phi}_{P(i,j_B-1)} &= 1 \\ A^{\phi}_{N(i,j_B-1)} &= 0 \\ b^{\phi}_{(i,j_B-1)} &= \phi_{bnd} \end{aligned}\right\} \tag{4.129}$$

where ϕ_{bnd} is the specified boundary value.

4.5.2 Neumann

A Neumann boundary condition is used when the variable gradient along a direction is prescribed (for example $\frac{\partial \phi}{\partial x} = J^{\phi}_{bnd}$). In the case where the heat flux on a boundary is known, the Neumann condition is used by setting, for example, $k\frac{\partial T}{\partial n} = J^{t}_{bnd} = q^{''}$ where $q^{''}$ is the heat flux at the boundary. For Cartesian orthogonal grids, a Neumann boundary condition is employed through gradients in the x and y coordinate directions , i.e. $\frac{\partial \phi}{\partial x}$ and $\frac{\partial \phi}{\partial y}$, for the west and east boundaries and the south and north boundaries respectively. For non-orthogonal grids, a gradient in the direction normal to the boundary surface, $\frac{\partial \phi}{\partial n}$, should be derived carefully when implementing a Neumann condition. Numerical difficulties can

occur if the grid is highly non-orthogonal near the boundary or when Cartesian coordinate direction gradient is small at the boundary. An example of this issue is when the derivative $\frac{\partial \phi}{\partial n}$ at the west boundary has very small component in the x direction. For a non-orthogonal grid, gradients with respect to x and y at a control volume face are expressed in terms of gradients along directions of unit vectors $\hat{s}$ and $\hat{t}$.

In this section, expressions that evaluate gradients of ϕ in both x and y directions in terms of local unit vectors $\hat{s}$ and $\hat{t}$ are derived for both east and north faces of a control volume. Then, the derived expression for $\left.\frac{\partial \phi}{\partial y}\right|_n$ can be used to set a Neumann condition on the south boundary. The other expressions are presented here for later use.

Using the chain rule, gradients of ϕ along the unit vectors $\hat{s}$ and $\hat{t}$ are expressed in terms of gradient along x and y as follows:

$$\frac{\partial \phi}{\partial s} = \frac{\partial \phi}{\partial x}\frac{\partial x}{\partial s} + \frac{\partial \phi}{\partial y}\frac{\partial y}{\partial s} \tag{4.130}$$

$$\frac{\partial \phi}{\partial t} = \frac{\partial \phi}{\partial x}\frac{\partial x}{\partial t} + \frac{\partial \phi}{\partial y}\frac{\partial y}{\partial t} \tag{4.131}$$

Now, Cramer's rule is used to evaluate gradient of ϕ in x direction as follows:

$$\frac{\partial \phi}{\partial x} = \frac{\begin{vmatrix} \frac{\partial \phi}{\partial s} & \frac{\partial y}{\partial s} \\ \frac{\partial \phi}{\partial t} & \frac{\partial y}{\partial t} \end{vmatrix}}{\begin{vmatrix} \frac{\partial x}{\partial s} & \frac{\partial y}{\partial s} \\ \frac{\partial x}{\partial t} & \frac{\partial y}{\partial t} \end{vmatrix}} = \frac{\frac{\partial \phi}{\partial s}\frac{\partial y}{\partial t} - \frac{\partial \phi}{\partial t}\frac{\partial y}{\partial s}}{\frac{\partial x}{\partial s}\frac{\partial y}{\partial t} - \frac{\partial y}{\partial s}\frac{\partial x}{\partial t}} \tag{4.132}$$

Using Equation (4.132), the gradient at the east face becomes:

$$\left.\frac{\partial\phi}{\partial x}\right|_e = \frac{\left.\frac{\partial\phi}{\partial s}\right|_e \left.\frac{\partial y}{\partial t}\right|_e - \left.\frac{\partial\phi}{\partial t}\right|_e \left.\frac{\partial y}{\partial s}\right|_e}{\left.\frac{\partial x}{\partial s}\right|_e \left.\frac{\partial y}{\partial t}\right|_e - \left.\frac{\partial y}{\partial s}\right|_e \left.\frac{\partial x}{\partial t}\right|_e} = \frac{\left.\frac{\partial\phi}{\partial s}\right|_e t_{ye} - \left.\frac{\partial\phi}{\partial t}\right|_e s_{ye}}{s_{xe}t_{ye} - t_{xe}s_{ye}} \tag{4.133}$$

Similarly, Equation (4.132) can rewritten for the north face as follows:

$$\left.\frac{\partial\phi}{\partial x}\right|_n = \frac{\left.\frac{\partial\phi}{\partial s}\right|_n \left.\frac{\partial y}{\partial t}\right|_n - \left.\frac{\partial\phi}{\partial t}\right|_n \left.\frac{\partial y}{\partial s}\right|_n}{\left.\frac{\partial x}{\partial s}\right|_n \left.\frac{\partial y}{\partial t}\right|_n - \left.\frac{\partial y}{\partial s}\right|_n \left.\frac{\partial x}{\partial t}\right|_n} = \frac{\left.\frac{\partial\phi}{\partial s}\right|_n t_{yn} - \left.\frac{\partial\phi}{\partial t}\right|_n s_{yn}}{s_{xn}t_{yn} - t_{xn}s_{yn}} \tag{4.134}$$

To evaluate gradients of ϕ in y direction, Cramer's rule is employed as follows:

$$\frac{\partial\phi}{\partial y} = \frac{\begin{vmatrix} \frac{\partial x}{\partial s} & \frac{\partial\phi}{\partial s} \\ \frac{\partial x}{\partial t} & \frac{\partial\phi}{\partial t} \end{vmatrix}}{\begin{vmatrix} \frac{\partial x}{\partial s} & \frac{\partial y}{\partial s} \\ \frac{\partial x}{\partial t} & \frac{\partial y}{\partial t} \end{vmatrix}} = \frac{\frac{\partial\phi}{\partial t}\frac{\partial x}{\partial s} - \frac{\partial\phi}{\partial s}\frac{\partial x}{\partial t}}{\frac{\partial x}{\partial s}\frac{\partial y}{\partial t} - \frac{\partial y}{\partial s}\frac{\partial x}{\partial t}} \tag{4.135}$$

Using Equation (4.135), the gradient at the north face becomes:

$$\left.\frac{\partial\phi}{\partial y}\right|_n = \frac{\left.\frac{\partial\phi}{\partial t}\right|_n \left.\frac{\partial x}{\partial s}\right|_n - \left.\frac{\partial\phi}{\partial s}\right|_n \left.\frac{\partial x}{\partial t}\right|_n}{\left.\frac{\partial x}{\partial s}\right|_n \left.\frac{\partial y}{\partial t}\right|_n - \left.\frac{\partial y}{\partial s}\right|_n \left.\frac{\partial x}{\partial t}\right|_n} = \frac{\left.\frac{\partial\phi}{\partial t}\right|_n s_{xn} - \left.\frac{\partial\phi}{\partial s}\right|_n t_{xn}}{s_{xn}t_{yn} - t_{xn}s_{yn}} \tag{4.136}$$

Equation (4.135) can be rewritten for the east to obtain:

$$\left.\frac{\partial\phi}{\partial y}\right|_e = \frac{\left.\frac{\partial\phi}{\partial t}\right|_e \left.\frac{\partial x}{\partial s}\right|_e - \left.\frac{\partial\phi}{\partial s}\right|_e \left.\frac{\partial x}{\partial t}\right|_e}{\left.\frac{\partial x}{\partial s}\right|_e \left.\frac{\partial y}{\partial t}\right|_e - \left.\frac{\partial y}{\partial s}\right|_e \left.\frac{\partial x}{\partial t}\right|_e} = \frac{\left.\frac{\partial\phi}{\partial t}\right|_e s_{xe} - \left.\frac{\partial\phi}{\partial s}\right|_e t_{xe}}{s_{xe}t_{ye} - t_{xe}s_{ye}} \tag{4.137}$$

Now, using Equation (4.136), a Neumann condition can be applied on the south boundary. Derivatives along the unit vectors $\hat{s}$ and $\hat{t}$ in Equation (4.136) are evaluated using nodal and corner values of ϕ. The result is:

$$\left.\frac{\partial\phi}{\partial y}\right|_{n_{(i,j_B-1)}} = J^{\phi}_{bnd} = \frac{\dfrac{\phi_N - \phi_P}{(dt)_n}s_{xn} - \dfrac{\phi_{ne} - \phi_{nw}}{(ds)_n}t_{xn}}{s_{xn}t_{yn} - t_{xn}s_{yn}} \tag{4.138}$$

Rearranging Equation (4.138) to write an equation for the boundary node leads to:

$$\phi_{\mathrm{P}} = \phi_{\mathrm{N}} - (\phi_{ne} - \phi_{nw})\frac{(dt)_n}{(ds)_n}\frac{t_{xn}}{s_{xn}} - J^{\phi}_{bnd}(dt)_n\frac{s_{xn}t_{yn} - t_{xn}s_{yn}}{s_{xn}} \tag{4.139}$$

Finally, the coefficients of the south boundary algebraic equation are set to:

$$\left.\begin{aligned} A^{\phi}_{P_{(i,j_B-1)}} &= 1 \qquad A^{\phi}_{N_{(i,j_B-1)}} = 1 \\ b^{\phi}_{(i,j_B-1)} &= -(\phi_{ne} - \phi_{nw})\frac{(dt)_n}{(ds)_n}\frac{t_{xn}}{s_{xn}} - J^{\phi}_{bnd}(dt)_n\frac{s_{xn}t_{yn} - t_{xn}s_{yn}}{s_{xn}} \end{aligned}\right\} \tag{4.140}$$

Corner values in Equation (4.140) are interpolated from the closest nodal boundary values. At domain corners, special attention is required. For example, at the southwest corner (i_B, j_B), if a Neumann condition is specified for both west and south boundaries, then $\phi_{se} = \phi_{(i_B,j_B)}$. If a Dirichlet condition is specified for one boundary, then ϕ_{se} is set to ϕ_{bnd} [50].

In regular domain geometries such as the domain shown in Figure 3.2 , domain boundaries are usually parallel or semi-parallel to the x axis at the west and east boundaries and to the y axis at the south and north boundaries. Therefore, the derivative $\frac{\partial\phi}{\partial x}$ is used to implement a Neumann condition on the west and east boundaries while the derivative $\frac{\partial\phi}{\partial y}$ is used on the south and north boundaries. Taking into consideration the problem being investigated in the present work and as the grid turns around the tube, the derivative $\frac{\partial\phi}{\partial x}$, for example, can not be used to represent a Neumann boundary conditions at the symmetry line above the tube, i.e. the west boundary. To explain the reason, let us consider the analogous equation to Equation (4.139) at the west boundary.

$$\phi_{\mathrm{P}} = \phi_{\mathrm{E}} - (\phi_{ne} - \phi_{se})\frac{(ds)_e}{(dt)_e}\frac{s_{ye}}{t_{ye}} - J^{\phi}_{bnd}(ds)_e\frac{s_{xe}t_{ye} - t_{xe}s_{ye}}{t_{ye}} \tag{4.141}$$

The component of the unit vector $\hat{t}_e$ in the y direction, t_{ye}, is practically zero because the i direction grid lines are almost parallel to the y direction. Numerically, the values of this component are very small. Unless $(\phi_{ne} - \phi_{se})$ and J^{ϕ}_{bnd} are both exactly zero, division by t_{ye} results in unrealistically large values. For more clarification, let us assume $(J^{\phi}_{bnd} = 0)$. In this case, the correct equation should be $(\phi_{\mathrm{P}} = \phi_{\mathrm{E}})$. Clearly, the second term in the RHS of Equation (4.141) is not expected to be exactly zero. Therefore, Equation (4.141) is no longer valid to represent a Neumann condition in this case. This fact will lead to the risk of obtaining ill-conditioned equations for the boundary conditions at this boundary and the possibility of division by zero if t_{ye} happens to be exactly zero at any moment of the simulation. To avoid this problem, the gradient in the normal direction to the boundary, $\frac{\partial \phi}{\partial n}$, is utilized. At the west boundary, the Neumann boundary condition equation would take the following general form:

$$\left.\frac{\partial \phi}{\partial n}\right|_{e_{(i_B-1,j)}} = J^{\phi}_{bnd} = \frac{1}{\hat{n}_e \cdot \hat{s}_e}\left(\left.\frac{\partial \phi}{\partial s}\right|_e - \left.\frac{\partial \phi}{\partial t}\right|_e \hat{t}_e \cdot \hat{s}_e\right) \tag{4.142}$$

Now, evaluate the primary and cross-derivative terms in term of nodal and corner values to get:

$$\left.\frac{\partial \phi}{\partial n}\right|_{e_{(i_B-1,j)}} = J^{\phi}_{bnd} = \frac{1}{\hat{n}_e \cdot \hat{s}_e}\frac{\left(\phi_{\mathrm{E}} - \phi_{\mathrm{P}}\right)}{(ds)_e} - \frac{1}{\hat{n}_e \cdot \hat{s}_e}\frac{\left(\phi_{\mathrm{ne}} - \phi_{\mathrm{se}}\right)}{(dt)_e}\hat{t}_e \cdot \hat{s}_e \tag{4.143}$$

By reshaping Equation (4.143) to write an equation for the boundary node at $i = i_B - 1$, we obtain

$$\phi_{\mathrm{P}} = \phi_{\mathrm{E}} - \left(\phi_{\mathrm{ne}} - \phi_{\mathrm{se}}\right)\frac{(ds)_e}{(dt)_e}\left(\hat{t}_e \cdot \hat{s}_e\right) - J^{\phi}_{bnd}\,(ds)_e\;\left(\hat{n}_e \cdot \hat{s}_e\right) \tag{4.144}$$

Equation (4.144) can be transformed to the symbolic algebraic equation format for the west boundary. The resulted coefficients are:

$$\left.\begin{aligned} A^{\phi}_{P_{(i_B-1,j)}} &= 1 \qquad A^{\phi}_{E_{(i_B-1,j)}} = 1 \\ b^{\phi}_{(i_B-1,j)} &= -\left(\phi_{\mathrm{ne}} - \phi_{\mathrm{se}}\right)\frac{(ds)_e}{(dt)_e}\left(\hat{t}_e \cdot \hat{s}_e\right) - J^{\phi}_{bnd}\,(ds)_e\;\left(\hat{n}_e \cdot \hat{s}_e\right) \end{aligned}\right\} \tag{4.145}$$

The first term of $b^{\phi}_{(i_B-1,j)}$ becomes zero when the corner values ϕ_{ne} and ϕ_{se} are equal or when the unit vectors $\hat{t}_e$ and $\hat{s}_e$ are normal to each other, i.e. grid lines are orthogonal at the boundary.

4.5.3 Absorption of the Boundary Conditions

The boundary conditions can be expressed implicitly in the algebraic equations of the interior nodes adjacent to the boundaries. As a result, the boundary nodes are eliminated from the solution fields. This process is referred to as absorption of the boundary conditions. To explain the process, consider a computational molecule for a control volume P adjacent to the south boundary as shown in Figure 4.2(b). The nine-point equation for the variable ϕ is:

$$\begin{aligned} A^{\phi}_{P_{(i,j_B)}}\phi_{P_{(i,j_B)}} &= A^{\phi}_{E_{(i,j_B)}}\phi_{E_{(i,j_B)}} + A^{\phi}_{W_{(i,j_B)}}\phi_{W_{(i,j_B)}} + A^{\phi}_{N_{(i,j_B)}}\phi_{N_{(i,j_B)}} + A^{\phi}_{S_{(i,j_B)}}\phi_{S_{(i,j_B)}} \\ &+ A^{\phi}_{NE_{(i,j_B)}}\phi_{NE_{(i,j_B)}} + A^{\phi}_{SW_{(i,j_B)}}\phi_{SW_{(i,j_B)}} + A^{\phi}_{NW_{(i,j_B)}}\phi_{NW_{(i,j_B)}} + A^{\phi}_{SE_{(i,j_B)}}\phi_{SE_{(i,j_B)}} + b^{\phi}_{(i,j_B)} \end{aligned} \tag{4.146}$$

From Figure 4.2(b), the nodes SW, S and SE belong to the south boundary. Therefore, their values are controlled by the boundary condition equations. Using Equation (4.128), the boundary condition equations on the south boundary for nodes SW, S and SE can be written respectively as follows:

$$A^{\phi}_{P_{(i-1,j_B-1)}}\phi_{SW_{(i-1,j_B-1)}} = A^{\phi}_{N_{(i-1,j_B-1)}}\phi_{W_{(i-1,j_B-1)}} + b^{\phi}_{(i-1,j_B-1)} \tag{4.147}$$

$$A^{\phi}_{P_{(i,j_B-1)}}\phi_{S_{(i,j_B-1)}} = A^{\phi}_{N_{(i,j_B-1)}}\phi_{P_{(i,j_B-1)}} + b^{\phi}_{(i,j_B-1)} \tag{4.148}$$

$$A^{\phi}_{P_{(i+1,j_B-1)}}\phi_{SE_{(i+1,j_B-1)}} = A^{\phi}_{N_{(i+1,j_B-1)}}\phi_{E_{(i+1,j_B-1)}} + b^{\phi}_{(i+1,j_B-1)} \tag{4.149}$$

Substituting Equations (4.147) to (4.149) into Equation (4.146), and collecting the coefficients produces

$$\left(A^{\phi}_{P(i,j_B)}\right)^{\oplus}\phi_{P_{(i,j_B)}} = \left(A^{\phi}_{E(i,j_B)}\right)^{\oplus}\phi_{E_{(i,j_B)}} + \left(A^{\phi}_{W(i,j_B)}\right)^{\oplus}\phi_{W_{(i,j_B)}} + A^{\phi}_{N_{(i,j_B)}}\phi_{N_{(i,j_B)}} + A^{\phi}_{NE_{(i,j_B)}}\phi_{NE_{(i,j_B)}} + A^{\phi}_{SE_{(i,j_B)}}\phi_{SE_{(i,j_B)}} + \left(b^{\phi}_{(i,j_B)}\right)^{\oplus} \quad (4.150)$$

where the modified coefficients $\left(A^{\phi}\right)^{\oplus}$ are:

$$\left.\begin{aligned}
\left(A^{\phi}_{P(i,j_B)}\right)^{\oplus} &= \left(A^{\phi}_{P_{(i,j_B)}} - A^{\phi}_{S_{(i,j_B)}}\frac{A^{\phi}_{N_{(i,j_B-1)}}}{A^{\phi}_{P_{(i,j_B-1)}}}\right)\\
\left(A^{\phi}_{E(i,j_B)}\right)^{\oplus} &= \left(A^{\phi}_{E_{(i,j_B)}} + A^{\phi}_{SE_{(i,j_B)}}\frac{A^{\phi}_{N_{(i+1,j_B-1)}}}{A^{\phi}_{P_{(i+1,j_B-1)}}}\right)\\
\left(A^{\phi}_{W(i,j_B)}\right)^{\oplus} &= \left(A^{\phi}_{W_{(i,j_B)}} + A^{\phi}_{SW_{(i,j_B)}}\frac{A^{\phi}_{N_{(i-1,j_B-1)}}}{A^{\phi}_{P_{(i-1,j_B-1)}}}\right)\\
\left(b^{\phi}_{(i,j_B)}\right)^{\oplus} &= \left(b^{\phi}_{(i,j_B)} + A^{\phi}_{S_{(i,j_B)}}\frac{b^{\phi}_{(i,j_B-1)}}{A^{\phi}_{P_{(i,j_B-1)}}}\right.\\
&\quad \left. + A^{\phi}_{SW_{(i,j_B)}}\frac{b^{\phi}_{(i-1,j_B-1)}}{A^{\phi}_{P_{(i-1,j_B-1)}}} + A^{\phi}_{SE_{(i,j_B)}}\frac{b^{\phi}_{(i+1,j_B-1)}}{A^{\phi}_{P_{(i+1,j_B-1)}}}\right)
\end{aligned}\right\} \quad (4.151)$$

After absorbing the boundary condition equations, A^{ϕ}_{SW}, A^{ϕ}_{S} and A^{ϕ}_{SE} are set to zero. For the corners, two additional coefficients are set to zero. For example, at the south west corner node (i_B, j_B), the west and north west coefficients are also set to zero. Once the solution of the interior field is available, values of ϕ on the south boundary are updated using the boundary node equations.

4.5.4 Face Velocity Boundary Conditions

Face velocity boundary conditions are derived from the nodal velocity boundary conditions. In this section, derivation of the face velocity boundary conditions on the south boundary, ($j = j_B - 1$), are presented as an example. Then, the resulting equations are implemented in the continuity equation of the adjacent interior control volume.

Consider control volume P in Figure 4.2(b) for which the continuity equation can be also applied on the south boundary as follows:

$$\left(A^{c,u}_{\mathrm{e(i},j_B\text{-}1)}U_e + A^{c,v}_{\mathrm{e(i},j_B\text{-}1)}V_e\right) + \left(A^{c,u}_{\mathrm{w(i},j_B\text{-}1)}U_w + A^{c,v}_{\mathrm{w(i},j_B\text{-}1)}V_w\right) + \left(A^{c,u}_{\mathrm{n(i},j_B\text{-}1)}U_n + A^{c,v}_{\mathrm{n(i},j_B\text{-}1)}V_n\right) + \left(A^{c,u}_{\mathrm{s(i},j_B\text{-}1)}U_s + A^{c,v}_{\mathrm{s(i},j_B\text{-}1)}V_s\right) + b^c_P = 0 \quad (4.152)$$

To progress in the derivation, its beneficial to highlight the requirements of the desired formulation. Firstly, only flow rates through the south and north face of the control volume P are needed to set the boundary condition on the south boundary. Secondly, the U and V face velocity boundary conditions are set separately. Consequently, two equations are derived from Equation (4.152) for U_s and V_s,respectively, as follows:

$$-A^{c,u}_{\mathrm{s(i},j_B\text{-}1)}U_s = A^{c,u}_{\mathrm{n(i},j_B\text{-}1)}U_n + A^{c,u}_{\mathrm{s(i},j_B\text{-}1)} \quad (4.153)$$

$$-A^{c,v}_{\mathrm{s(i},j_B\text{-}1)}V_s = A^{c,v}_{\mathrm{n(i},j_B\text{-}1)}V_n + A^{c,v}_{\mathrm{s(i},j_B\text{-}1)} \quad (4.154)$$

To simplify Equations (4.153 and 4.154), let $-A^{c,u}_{\mathrm{s(i},j_B\text{-}1)} = -A^{c,v}_{\mathrm{s(i},j_B\text{-}1)} = 1$. The results are:

$$U_s = A^{c,u}_{\mathrm{n(i},j_B\text{-}1)}U_n + A^{c,u}_{\mathrm{s(i},j_B\text{-}1)} \quad (4.155)$$

$$V_s = A^{c,v}_{\mathrm{n(i},j_B\text{-}1)}V_n + A^{c,v}_{\mathrm{s(i},j_B\text{-}1)} \quad (4.156)$$

To obtain the Dirichlet condition on the south boundary for U and V face velocities, the coefficients in Equations (4.155 and 4.156) are set respectively to:

$$\left.\begin{aligned} A^{c,u}_{\mathrm{n(i,}j_B\mathrm{-1)}} &= 0 \\ A^{c,u}_{\mathrm{s(i,}j_B\mathrm{-1)}} &= U_{bnd} \end{aligned}\right\} \tag{4.157}$$

$$\left.\begin{aligned} A^{c,v}_{\mathrm{n(i,}j_B\mathrm{-1)}} &= 0 \\ A^{c,v}_{\mathrm{s(i,}j_B\mathrm{-1)}} &= V_{bnd} \end{aligned}\right\} \tag{4.158}$$

To obtain the Neumann condition on the south boundary for U and V face velocities, the derivative $(\frac{\partial \phi}{\partial y})$ in Equation (4.136) is first approximated in terms of face velocities as follows:

$$\left.\frac{\partial \phi}{\partial y}\right|_{(i,j_B)} = J^{\phi}_{bnd} = \frac{\dfrac{\phi_n - \phi_s}{(dt)_p} s_{xs} - \dfrac{\phi_{se} - \phi_{sw}}{(ds)_s} t_{xp}}{s_{xs} t_{yp} - t_{xp} s_{ys}} \tag{4.159}$$

Here, the derivative $(\frac{\partial \phi}{\partial y})$ is evaluated across the first interior control volume adjacent to the south boundary. Rearranging Equation (4.159) to get an expression for ϕ_s equivalent to Equations (4.155 and 4.156) leads to:

$$\phi_s = \phi_n - (\phi_{se} - \phi_{sw}) \frac{(dt)_p}{(ds)_s} \frac{t_{xp}}{s_{xs}} - J^{\phi}_{bnd} (dt)_p \frac{s_{xs} t_{yp} - t_{xp} s_{ys}}{s_{xn}} \tag{4.160}$$

To define the Neumann condition on the south boundary, the continuity coefficients in Equations (4.155 and 4.156) are set to:

$$\left.\begin{aligned} A^{c,u}_{\mathrm{n(i,}j_B\mathrm{-1)}} &= 1 \\ A^{c,u}_{\mathrm{s(i,}j_B\mathrm{-1)}} &= -(U_{se} - U_{sw}) \frac{(dt)_p}{(ds)_s} \frac{t_{xp}}{s_{xs}} - J^{u}_{bnd} (dt)_p \frac{s_{xs} t_{yp} - t_{xp} s_{ys}}{s_{xn}} \end{aligned}\right\} \tag{4.161}$$

$$\left.\begin{aligned} A^{c,v}_{\mathrm{n(i,}j_B\mathrm{-1)}} &= 1 \\ A^{c,v}_{\mathrm{s(i,}j_B\mathrm{-1)}} &= -(V_{se} - V_{sw}) \frac{(dt)_p}{(ds)_s} \frac{t_{xp}}{s_{xs}} - J^{v}_{bnd} (dt)_p \frac{s_{xs} t_{yp} - t_{xp} s_{ys}}{s_{xn}} \end{aligned}\right\} \tag{4.162}$$

The rest of the continuity coefficients in Equation (4.152) are set to zero.

The following step is absorbing the prescribed face velocity boundary condition to the interior control volumes. The continuity equation is written for the regular control volume

P in Figure 4.2(b). Then, substituting Equations (4.155 and 4.156) to the resulting equation leads to:

$$\begin{aligned}\left(A^{c,u}_{\mathrm{e(i,}j_B\mathrm{)}}U_e + A^{c,v}_{\mathrm{e(i,}j_B\mathrm{)}}V_e\right) + \left(A^{c,u}_{\mathrm{w(i,}j_B\mathrm{)}}U_w + A^{c,v}_{\mathrm{w(i,}j_B\mathrm{)}}V_w\right) + \left(A^{c,u}_{\mathrm{n(i,}j_B\mathrm{)}}U_n + A^{c,v}_{\mathrm{n(i,}j_B\mathrm{)}}V_n\right) \\ + A^{c,u}_{\mathrm{s(i,}j_B\mathrm{)}}\left(A^{c,u}_{\mathrm{n(i,}j_B\mathrm{-1)}}U_n + A^{c,u}_{\mathrm{s(i,}j_B\mathrm{-1)}}\right) + A^{c,v}_{\mathrm{s(i,}j_B\mathrm{)}}\left(A^{c,v}_{\mathrm{n(i,}j_B\mathrm{-1)}}V_n + A^{c,v}_{\mathrm{s(i,}j_B\mathrm{-1)}}\right) + b^c_P = 0\end{aligned} \tag{4.163}$$

Now collect terms to obtain:

$$\begin{aligned}\left(A^{c,u}_{\mathrm{e(i,}j_B\mathrm{)}}U_e + A^{c,v}_{\mathrm{e(i,}j_B\mathrm{)}}V_e\right) + \left(A^{c,u}_{\mathrm{w(i,}j_B\mathrm{)}}U_w + A^{c,v}_{\mathrm{w(i,}j_B\mathrm{)}}V_w\right) \\ + \left(\left(A^{c,u}_{\mathrm{n(i,}j_B\mathrm{)}}\right)^{\oplus}U_n + \left(A^{c,v}_{\mathrm{n(i,}j_B\mathrm{)}}\right)^{\oplus}V_n\right) + \left(b^c_{P(i,j_B)}\right)^{\oplus} = 0\end{aligned} \tag{4.164}$$

where the modified coefficients in Equations (4.164) are specified as follows:

$$\left.\begin{aligned}\left(A^{c,u}_{\mathrm{e(i,}j_B\mathrm{)}}\right)^{\oplus} &= A^{c,u}_{\mathrm{n(i,}j_B\mathrm{)}} + A^{c,u}_{\mathrm{s(i,}j_B\mathrm{)}}A^{c,u}_{\mathrm{n(i,}j_B\mathrm{-1)}} \\ \left(A^{c,v}_{\mathrm{n(i,}j_B\mathrm{)}}\right)^{\oplus} &= A^{c,v}_{\mathrm{n(i,}j_B\mathrm{)}} + A^{c,v}_{\mathrm{s(i,}j_B\mathrm{)}}A^{c,v}_{\mathrm{n(i,}j_B\mathrm{-1)}} \\ \left(b^c_{P(i,j_B)}\right)^{\oplus} &= b^c_{P(i,j_B)} + A^{c,u}_{\mathrm{s(i,}j_B\mathrm{)}}A^{c,u}_{\mathrm{s(i,}j_B\mathrm{-1)}} + A^{c,v}_{\mathrm{s(i,}j_B\mathrm{)}}A^{c,v}_{\mathrm{s(i,}j_B\mathrm{-1)}}\end{aligned}\right\} \tag{4.165}$$

4.5.5 Face Value of a Property

Once the properties at all nodes are determined, values of the properties at faces of the control volumes should be calculated. The harmonic mean is used to get face value of the properties. For example, the value of the viscosity at the east face is calculated as follows:

$$\mu_{\mathrm{e}} = \frac{\mu_{\mathrm{P}}\,\mu_{\mathrm{E}}}{f_e\,\mu_{\mathrm{P}} + (1 - f_e)\,\mu_{\mathrm{E}}} \tag{4.166}$$

where f_e is a grid weight that gives a linear interpolation between nodes P and E for the value at face e.

4.6 E-factor Formulation

To improve the convergence rate, the governing equations are made fully implicit. Also, the transient terms are kept even though they are not needed theoretically because only the steady-state solution is required in this study. Retaining the transient term for the non-linear governing equations improves the dominance of the diagonal coefficients in the coefficient matrix and offers relaxation to the iterative solution towards the steady-state solution.

Van Doormaal and Raithby [54] recommended formulating the true transient term using a distorted transient scheme. For this purpose, the transient term is rewritten as (using the U equation, for example):

$$\frac{M_P^o}{\Delta t} = \frac{A_{\mathrm{P}}^{u^*}}{E^u} \tag{4.167}$$

where E^u is called the E-factor. Now, applying the E-factor formulation in Equation (4.167) to Equations (4.36 and 4.32) for the central node coefficient and the RHS term respectively to obtain

$$A_{\mathrm{P}}^u = A_{\mathrm{P}}^{u^*} + \frac{A_{\mathrm{P}}^{u^*}}{E^u} = \left(1 + \frac{1}{E^u}\right) A_{\mathrm{P}}^{u^*} \tag{4.168}$$

and

$$b_{\mathrm{P}}^u = \left(\frac{A_{\mathrm{P}}^{u^*}}{E^u}\right) U_P^o - \forall_P \left.\frac{\partial P}{\partial x}\right|_P + Q_{\mathrm{P}}^u \tag{4.169}$$

The E-factor formulation allows the solution of each variable at each node to proceed at different rates according to control volume size. Furthermore, different value of the E-factor can be assigned for each variable to make the solution fields progress at different rates which could enhance the convergence rate [53, 55]. Both true transient and E-factor formulation of the transient term are implemented in the computer code. Choosing either formulation is administrated through the selection of E^u and Δt values.

Chapter 5

The Numerical Solution Method

5.1 Pressure Velocity Coupling

In this work, the pressure-velocity coupling of the momentum equations was treated using the SIMPLE-Consistent (SIMPLEC) method by Van Doormaal and Raithby [54]. This method is an improved version of the SIMPLE method, (Semi-Implicit Method for Pressure Linked Equations), by Patankar and Spalding [56] in terms of robustness and computational cost. In both SIMPLE and SIMPLEC methods, the momentum equations are solved using the most updated pressure field. Then, the continuity equation is used indirectly to furnish a correctional constraint for the pressure through so-called pressure correction (P'). The pressure correction field is used to correct the pressure and the velocity fields. This procedure is repeated until the *correct* pressure field is achieved, i.e. the pressure field that is when substituted in the momentum equations, produces mass conserving velocity fields.

In this work, a co-located variable arrangement was used. The pressure-velocity coupling was treated using a technique referred to as the *Pressure Weight Interpolation Method* (PWIM) [57].

In a typical control volume with co-located variable arrangement, there are advected velocities and advecting velocities defined on the centre of each face. The advecting velocities are responsible for conserving mass through the continuity equation. The advected velocities are computed using interpolations in the prescribed advection scheme (MAW) in Appendix A. The nodal (cell-centre) are the solution to the algebraic momentum equations.

5.1.1 Pressure Weight Interpolation Method

Rhie and Chow [58] presented a method to evaluate advecting velocities in co-located variable arrangement. The method is referred to as the Pressure Weighted Interpolation Method (PWIM). In the PWIM, the advecting velocity is interpolated from the discretized momentum equations of its nodal neighbours from both sides. This crucial step couples both pressure and velocity fields and eliminates non-physical pressure and velocity fields. However, subsequent studies on Rhie and Chow version of the PWIM revealed some serious weaknesses. These weaknesses include dependency of fully converged solutions on the values of relaxation factor, time step and difficulties when simulating flow problems with discontinuities [59].

Miller and Schmidt [57] proposed a proper implementation procedure of the PWIM that takes into account the relaxation factor in the momentum equation. While this procedure eliminates dependency of the solutions on the values of the relaxation factor, Miller and Schmidt reported non-physical predictions for the advective velocity in regions where rapid change in the pressure occurs. Similar observations were noticed by Majumdar [60]. In this work, a modified time step independent version of the PWIM based on the work of Miller and Schmidt [57] was used.

The steps for deriving expressions for advecting (face) velocities based on the concept of momentum interpolation are given here. For the central control volume, the $x-$momentum equation, U_P equation, is:

$$A^u_{\mathrm{P}} U_{\mathrm{P}} = \sum_P A^u_{\mathrm{NB}} U_{\mathrm{NB}} + \left(\frac{M^o_P}{\Delta t}\right) U^o_P - \forall_P \left.\frac{\partial P}{\partial x}\right|_P + Q^u_P + b^u_P \tag{5.1}$$

A similar equation can be written for the east control volume.

$$A^u_{\mathrm{PE}} U_{\mathrm{E}} = \sum_E A^u_{\mathrm{NB}} U_{\mathrm{NB}} + \left(\frac{M^o_E}{\Delta t}\right) U^o_E - \forall_E \left.\frac{\partial P}{\partial x}\right|_E + Q^u_E + b^u_E \tag{5.2}$$

For a control volume centered at the centre of the east face between P and E, an analogous

expression for U_e can be written as follows:

$$A^u_{\mathrm{Pe}} U_{\mathrm{e}} = \sum_e A^u_{\mathrm{nb}} U_{\mathrm{nb}} + \left(\frac{M^o_e}{\Delta t}\right) U^o_e - \forall_e \left.\frac{\partial P}{\partial x}\right|_e + Q^u_e + b^u_e \tag{5.3}$$

Now, divide each equation (Equations (5.1 to 5.3)) with the coefficient of its central variable to obtain:

$$U_{\mathrm{P}} = \underbrace{\frac{\sum_P A^u_{\mathrm{NB}} U_{\mathrm{NB}} + Q^u_P}{A^u_{\mathrm{P}}}}_{\widetilde{U}_{\mathrm{P}}} + \left(\frac{M^o_P}{\Delta t}\right) \frac{U^o_P}{A^u_{\mathrm{P}}} - \frac{\forall_P}{A^u_{\mathrm{P}}} \left.\frac{\partial P}{\partial x}\right|_P + \frac{b^u_P}{A^u_{\mathrm{P}}} \tag{5.4}$$

$$U_{\mathrm{E}} = \underbrace{\frac{\sum_E A^u_{\mathrm{NB}} U_{\mathrm{NB}} + Q^u_E}{A^u_{\mathrm{P}}\big|_{\mathrm{E}}}}_{\widetilde{U}_{\mathrm{E}}} + \left(\frac{M^o_E}{\Delta t}\right) \frac{U^o_E}{A^u_{\mathrm{P}}\big|_{\mathrm{E}}} - \frac{\forall_E}{A^u_{\mathrm{P}}\big|_{\mathrm{E}}} \left.\frac{\partial P}{\partial x}\right|_E + \frac{b^u_E}{A^u_{\mathrm{P}}\big|_{\mathrm{E}}} \tag{5.5}$$

$$U_{\mathrm{e}} = \underbrace{\frac{\sum_e A^u_{\mathrm{nb}} U_{\mathrm{nb}} + Q^u_e}{A^u_{\mathrm{P}}\big|_{\mathrm{e}}}}_{\widetilde{U}_{\mathrm{e}}} + \left(\frac{M^o_e}{\Delta t}\right) \frac{U^o_e}{A^u_{\mathrm{P}}\big|_{\mathrm{e}}} - \frac{\forall_e}{A^u_{\mathrm{P}}\big|_{\mathrm{e}}} \left.\frac{\partial P}{\partial x}\right|_e + \frac{b^u_e}{A^u_{\mathrm{P}}\big|_{\mathrm{e}}} \tag{5.6}$$

The underlined term in Equation (5.6), $\widetilde{U}_{\mathrm{e}}$, is obtained by linear interpolation from its corresponding terms in Equations (5.4) and (5.5) as follows:

$$\widetilde{U}_{\mathrm{e}} = f_e \, \widetilde{U_{\mathrm{P}}} + (1 - f_e) \, \widetilde{U_{\mathrm{E}}} \tag{5.7}$$

where $\widetilde{U_{\mathrm{P}}}$ and $\widetilde{U_{\mathrm{E}}}$ are defined in Equations (5.8 and 5.9) respectively.

$$\widetilde{U_{\mathrm{P}}} = U_{\mathrm{P}} - \left(\frac{M^o_P}{\Delta t}\right) \frac{U^o_P}{A^u_{\mathrm{P}}\big|_{\mathrm{P}}} + \frac{\overline{\forall_P}}{A^u_{\mathrm{P}}\big|_{\mathrm{P}}} \left.\frac{\partial P}{\partial x}\right|_P - \frac{b^u_P}{A^u_{\mathrm{P}}\big|_{\mathrm{P}}} \tag{5.8}$$

$$\widetilde{U_{\mathrm{E}}} = U_{\mathrm{E}} - \left(\frac{M^o_E}{\Delta t}\right) \frac{U^o_E}{A^u_{\mathrm{P}}\big|_{\mathrm{E}}} + \frac{\overline{\forall_E}}{A^u_{\mathrm{P}}\big|_{\mathrm{E}}} \left.\frac{\partial P}{\partial x}\right|_E - \frac{b^u_E}{A^u_{\mathrm{P}}\big|_{\mathrm{E}}} \tag{5.9}$$

To obtain numerical solutions that do not depend on the value of the time step size, the following assumptions are made

$$\left.\begin{aligned} \left(\frac{M_P^o}{\Delta t}\right)\frac{1}{A^u_{\mathrm{P}}\big|_{\mathrm{P}}} &\approx \left(\frac{M_e^o}{\Delta t}\right)\frac{1}{A^u_{\mathrm{P}}\big|_{\mathrm{e}}} \\ \left(\frac{M_E^o}{\Delta t}\right)\frac{1}{A^u_{\mathrm{P}}\big|_{\mathrm{E}}} &\approx \left(\frac{M_e^o}{\Delta t}\right)\frac{1}{A^u_{\mathrm{P}}\big|_{\mathrm{e}}} \end{aligned}\right\} \tag{5.10}$$

$$\left.\begin{aligned} \frac{\forall_P}{A^u_{\mathrm{P}}\big|_{\mathrm{P}}} &\approx \frac{\forall_e}{A^u_{\mathrm{P}}\big|_{\mathrm{e}}} \\ \frac{\forall_E}{A^u_{\mathrm{P}}\big|_{\mathrm{E}}} &\approx \frac{\forall_e}{A^u_{\mathrm{P}}\big|_{\mathrm{e}}} \end{aligned}\right\} \tag{5.11}$$

The east face coefficients in Equations (5.10) and (5.11) are interpolated from nodal central and east ones as follows:

$$\left(\frac{M_e^o}{\Delta t}\right)\frac{1}{A^u_{\mathrm{P}}\big|_{\mathrm{e}}} = f_e\left(\frac{M_P^o}{\Delta t}\right)\frac{1}{A^u_{\mathrm{P}}\big|_{\mathrm{P}}} + (1-f_e)\left(\frac{M_E^o}{\Delta t}\right)\frac{1}{A^u_{\mathrm{P}}\big|_{\mathrm{E}}} \tag{5.12}$$

$$\frac{\forall_e}{A^u_{\mathrm{P}}\big|_{\mathrm{e}}} = f_e\frac{\forall_P}{A^u_{\mathrm{P}}\big|_{\mathrm{P}}} + (1-f_e)\frac{\forall_E}{A^u_{\mathrm{P}}\big|_{\mathrm{E}}} \tag{5.13}$$

Substituting Equations (5.8) and (5.9) into Equation (5.7) yields:

$$\begin{aligned} \widetilde{U}_{\mathrm{e}} = f_e\,U_{\mathrm{P}} + (1-f_e)\,U_{\mathrm{E}} - f_e\left(\frac{M_P^o}{\Delta t}\right)\frac{U_P^o}{A^u_{\mathrm{P}}\big|_{\mathrm{P}}} - (1-f_e)\left(\frac{M_E^o}{\Delta t}\right)\frac{U_E^o}{A^u_{\mathrm{P}}\big|_{\mathrm{E}}} \\ + f_e\,\frac{\forall_P}{A^u_{\mathrm{P}}\big|_{\mathrm{P}}}\left.\frac{\partial P}{\partial x}\right|_P + (1-f_e)\,\frac{\forall_P}{A^u_{\mathrm{P}}\big|_{\mathrm{P}}}\left.\frac{\partial P}{\partial x}\right|_E - f_e\,\frac{b^u_{\mathrm{P}}}{A^u_{\mathrm{P}}\big|_{\mathrm{P}}} - (1-f_e)\,\frac{b^u_{\mathrm{E}}}{A^u_{\mathrm{P}}\big|_{\mathrm{E}}} \end{aligned} \tag{5.14}$$

Then, applying the assumptions presented in Equations (5.10) and (5.11)

$$\widetilde{U}_{\mathrm{e}} = f_e\, U_{\mathrm{P}} + (1-f_e)\, U_{\mathrm{E}} + \left(\frac{M_e^o}{\Delta t}\right) \frac{1}{A_{\mathrm{P}}^u\big|_{\mathrm{e}}} \Big[- f_e\, U_P^o - (1-f_e)\, U_E^o \Big] + f_e\, \frac{\forall_{Pe}}{A_{\mathrm{P}}^u\big|_{\mathrm{e}}} \left.\frac{\partial P}{\partial x}\right|_P + (1-f_e)\, \frac{\forall_E}{A_{\mathrm{P}}^u\big|_{\mathrm{e}}} \left.\frac{\partial P}{\partial x}\right|_E - f_e\, \frac{b_{\mathrm{P}}^u}{A_{\mathrm{P}}^u\big|_{\mathrm{P}}} - (1-f_e)\, \frac{b_{\mathrm{E}}^u}{A_{\mathrm{P}}^u\big|_{\mathrm{E}}} \tag{5.15}$$

Finally, substituting Equation (5.15) into Equation (5.6) yields:

$$U_{\mathrm{e}} = f_e\, U_{\mathrm{P}} + (1-f_e)\, U_{\mathrm{E}} + \left(\frac{M_e^o}{\Delta t}\right) \frac{1}{A_{\mathrm{P}}^u\big|_{\mathrm{e}}} \Big[U_e^o - f_e\, U_P^o - (1-f_e)\, U_E^o \Big] - \frac{\forall_e}{A_{\mathrm{P}}^u\big|_{\mathrm{e}}} \left.\frac{\partial P}{\partial x}\right|_e + f_e\, \frac{\forall_e}{A_{\mathrm{P}}^u\big|_{\mathrm{e}}} \left.\frac{\partial P}{\partial x}\right|_P + (1-f_e)\, \frac{\forall_e}{A_{\mathrm{P}}^u\big|_{\mathrm{e}}} \left.\frac{\partial P}{\partial x}\right|_E + \frac{b_e^u}{A_{\mathrm{P}}^u\big|_{\mathrm{e}}} - f_e\, \frac{b_{\mathrm{P}}^u}{A_{\mathrm{P}}^u\big|_{\mathrm{P}}} - (1-f_e)\, \frac{b_{\mathrm{E}}^u}{A_{\mathrm{P}}^u\big|_{\mathrm{E}}} \tag{5.16}$$

Following the same steps, the V velocity at the east face can be shown to be given by:

$$V_{\mathrm{e}} = f_e\, V_{\mathrm{P}} + (1-f_e)\, V_{\mathrm{E}} + \left(\frac{M_e^o}{\Delta t}\right) \frac{1}{A_{\mathrm{P}}^v\big|_{\mathrm{e}}} \Big[V_e^o - f_e\, V_P^o - (1-f_e)\, V_E^o \Big] - \frac{\forall_e}{A_{\mathrm{P}}^v\big|_{\mathrm{e}}} \left.\frac{\partial P}{\partial y}\right|_e + f_e\, \frac{\forall_P}{A_{\mathrm{P}}^v\big|_{\mathrm{e}}} \left.\frac{\partial P}{\partial y}\right|_P + (1-f_e)\, \frac{\forall_E}{A_{\mathrm{P}}^v\big|_{\mathrm{e}}} \left.\frac{\partial P}{\partial y}\right|_E + \frac{b_{\mathrm{e}}^v}{A_{\mathrm{P}}^v\big|_{\mathrm{e}}} - f_e\, \frac{b_{\mathrm{P}}^v}{A_{\mathrm{P}}^v\big|_{\mathrm{P}}} - (1-f_e)\, \frac{b_{\mathrm{E}}^v}{A_{\mathrm{P}}^v\big|_{\mathrm{E}}} \tag{5.17}$$

For the north face of the control volume, the components of the convective velocity in x and

y directions are presented by:

$$U_{\mathrm{n}} = f_n\, U_{\mathrm{P}} + (1-f_n)\, U_{\mathrm{N}} + \left(\frac{M_n^o}{\Delta t}\right) \frac{1}{A^u_{\mathrm{P}}\Big|_{\mathrm{n}}} \left[U_n^o - f_n\, U_P^o - (1-f_n)\, U_N^o\right] - \frac{\forall_n}{A^u_{\mathrm{P}}\Big|_{\mathrm{n}}} \left.\frac{\partial P}{\partial x}\right|_n + f_n \frac{\forall_P}{A^u_{\mathrm{P}}\Big|_{\mathrm{n}}} \left.\frac{\partial P}{\partial x}\right|_P + (1-f_n) \frac{\forall_N}{A^u_{\mathrm{P}}\Big|_{\mathrm{n}}} \left.\frac{\partial P}{\partial x}\right|_N + \frac{b^u_n}{A^u_{\mathrm{P}}\Big|_{\mathrm{n}}} - f_n \frac{b^u_{\mathrm{P}}}{A^u_{\mathrm{P}}\Big|_{\mathrm{P}}} - (1-f_n) \frac{b^u_{\mathrm{N}}}{A^u_{\mathrm{P}}\Big|_{\mathrm{N}}} \quad (5.18)$$

$$V_{\mathrm{n}} = f_n\, V_{\mathrm{P}} + (1-f_n)\, V_{\mathrm{N}} + \left(\frac{M_n^o}{\Delta t}\right) \frac{1}{A^v_{\mathrm{P}}\Big|_{\mathrm{n}}} \left[V_n^o - f_n\, V_P^o - (1-f_n)\, V_N^o\right] - \frac{\forall_n}{A^v_{\mathrm{P}}\Big|_{\mathrm{n}}} \left.\frac{\partial P}{\partial y}\right|_n + f_n \frac{\forall_P}{A^v_{\mathrm{P}}\Big|_{\mathrm{n}}} \left.\frac{\partial P}{\partial y}\right|_P + (1-f_n) \frac{\forall_N}{A^v_{\mathrm{P}}\Big|_{\mathrm{n}}} \left.\frac{\partial P}{\partial y}\right|_N + \frac{b^v_{\mathrm{n}}}{A^v_{\mathrm{P}}\Big|_{\mathrm{n}}} - f_n \frac{b^v_{\mathrm{P}}}{A^v_{\mathrm{P}}\Big|_{\mathrm{P}}} - (1-f_n) \frac{b^u_{\mathrm{N}}}{A^v_{\mathrm{P}}\Big|_{\mathrm{N}}} \quad (5.19)$$

5.1.2 Velocity Corrections

Steady fluid flow problems can be solved efficiently with an implicit method in a segregated manner. The steady state solution is obtained by repeated iterative solution of the linearised equations at each time step. A momentum equation is solved for each velocity component for the nodal velocities. A correction strategy can be used in the segregated solution procedure. The velocities are written as the addition of a correction to a current iteration value. The velocities are therefore written as

$$\left.\begin{aligned} U &= U^* + U' \\ V &= V^* + V' \end{aligned}\right\} \quad (5.20)$$

Where U^* and V^* are the most updated solution of the momentum equations and U' and V' are the required correction to the velocity to enforce mass conservation at each time step.

From Equation (5.20), the correction value are simply calculated from:

$$\left.\begin{aligned} U' &= U - U^* \\ V' &= V - V^* \end{aligned}\right\} \tag{5.21}$$

The velocity correction will be obtained from the pressure correction as described in Section 5.1.3. For convenience, U^* and V^* values will be referred to as "guessed" values from now on.

To illustrate steps of deriving the expressions for the velocity corrections, focus will be made on the U momentum equation. For a guessed pressure field, P^*, the resulting guessed velocity field U^* at control volume P is:

$$U_{\mathrm{P}}{}^* = \frac{\sum_P A^u_{\mathrm{NB}} U_{\mathrm{NB}}{}^* + Q^u_P}{A^u_{\mathrm{P}}} + \left(\frac{M^o_P}{\Delta t}\right)\frac{U^o_P}{A^u_{\mathrm{P}}} - \frac{\forall_P}{A^u_{\mathrm{P}}}\left.\frac{\partial P^*}{\partial x}\right|_P + \frac{b^{u*}}{A^u_{\mathrm{P}}} \tag{5.22}$$

When the corrected pressure field P is used, the mass conserving U field can be given in a similar manner:

$$U_{\mathrm{P}} = \frac{\sum_P A^u_{\mathrm{NB}} U_{\mathrm{NB}} + Q^u_P}{A^u_{\mathrm{P}}} + \left(\frac{M^o_P}{\Delta t}\right)\frac{U^o_P}{A^u_{\mathrm{P}}} - \frac{\forall_P}{A^u_{\mathrm{P}}}\left.\frac{\partial P}{\partial x}\right|_P + \frac{b^u}{A^u_{\mathrm{P}}} \tag{5.23}$$

Now, subtracting Equation (5.22) from Equation (5.23) and making use of Equation (5.21) produces the nodal velocity correction formula as follows:

$$U_{\mathrm{P}}{}' = \frac{\sum_P A^u_{\mathrm{NB}} U_{\mathrm{NB}}{}'}{A^u_{\mathrm{P}}} - \frac{\forall_P}{A^u_{\mathrm{P}}}\left.\frac{\partial P'}{\partial x}\right|_P \tag{5.24}$$

Following a similar procedure, the correction formula for the east face velocity, U_e, can be obtained from Equation (5.16) as follows:

$$U_{\mathrm{e}}{}' = f_e\, U_{\mathrm{P}}{}' + (1-f_e)\, U_{\mathrm{E}}{}' - \frac{\forall_e}{A^u_{\mathrm{P}}\big|_{\mathrm{e}}}\left.\frac{\partial P'}{\partial x}\right|_e + f_e\,\frac{\forall_P}{A^u_{\mathrm{P}}\big|_{\mathrm{P}}}\left.\frac{\partial P'}{\partial x}\right|_P + (1-f_e)\,\frac{\forall_E}{A^u_{\mathrm{P}}\big|_{\mathrm{E}}}\left.\frac{\partial P'}{\partial x}\right|_E \tag{5.25}$$

Now, replacing nodal velocity correction, $U_{\mathrm{P}}{}'$ and $U_{\mathrm{E}}{}'$, with Equation (5.24) and its analogous for the east control volume produces:

$$U_{\mathrm{e}}{}' = f_e \left[\frac{\sum_P A^u_{\mathrm{NB}} U'_{\mathrm{NB}}}{A^u_{\mathrm{P}}\big|_{\mathrm{P}}} - \frac{\forall_P}{A^u_{\mathrm{P}}\big|_{\mathrm{P}}} \left.\frac{\partial P'}{\partial x}\right|_P \right] + (1 - f_e) \left[\frac{\sum_E A^u_{\mathrm{NB}} U'_{\mathrm{NB}}}{A^u_{\mathrm{P}}\big|_{\mathrm{E}}} - \frac{\forall_E}{A^u_{\mathrm{P}}\big|_{\mathrm{E}}} \left.\frac{\partial P'}{\partial x}\right|_E \right] - \frac{\forall_e}{A^u_{\mathrm{P}}\big|_{\mathrm{e}}} \left.\frac{\partial P'}{\partial x}\right|_e + f_e \frac{\forall_P}{A^u_{\mathrm{P}}\big|_{\mathrm{P}}} \left.\frac{\partial P'}{\partial x}\right|_P + (1 - f_e) \frac{\forall_E}{A^u_{\mathrm{P}}\big|_{\mathrm{E}}} \left.\frac{\partial P'}{\partial x}\right|_E \tag{5.26}$$

Finally, using the following assumption:

$$\frac{\sum_e A^u_{\mathrm{nb}} U'_{\mathrm{nb}}}{A^u_{\mathrm{P}}\big|_{\mathrm{e}}} = f_e \left[\frac{\sum_P A^u_{\mathrm{NB}} U'_{\mathrm{NB}}}{A^u_{\mathrm{P}}\big|_{\mathrm{P}}} \right] + (1 - f_e) \left[\frac{\sum_E A^u_{\mathrm{NB}} U'_{\mathrm{NB}}}{A^u_{\mathrm{P}}\big|_{\mathrm{E}}} \right] \tag{5.27}$$

the face velocity correction equation is:

$$U_{\mathrm{e}}{}' = \frac{\sum_e A^u_{\mathrm{nb}} U'_{\mathrm{nb}}}{A^u_{\mathrm{P}}\big|_{\mathrm{e}}} - \frac{\forall_e}{A^u_{\mathrm{P}}\big|_{\mathrm{e}}} \left.\frac{\partial P'}{\partial x}\right|_e \tag{5.28}$$

Analogous equation can be derived for V velocity at nodal point P and east face e. The results are:

$$V'_{\mathrm{P}} = \frac{\sum_P A^v_{\mathrm{NB}} V'_{\mathrm{NB}}}{A^v_{\mathrm{P}}\big|_{\mathrm{P}}} - \frac{\forall_P}{A^v_{\mathrm{P}}\big|_{\mathrm{P}}} \left.\frac{\partial P'}{\partial y}\right|_P \tag{5.29}$$

$$V'_{\mathrm{e}} = \frac{\sum_e A^v_{\mathrm{nb}} V'_{\mathrm{nb}}}{A^v_{\mathrm{P}}\big|_{\mathrm{e}}} - \frac{\forall_e}{A^v_{\mathrm{P}}\big|_{\mathrm{e}}} \left.\frac{\partial P'}{\partial y}\right|_e \tag{5.30}$$

Correction equations for the U and V velocity at the north face can be derived similarly to Equations (5.28) and (5.30)).

5.1.3 The SIMPLEC Algorithm

Van Doormaal and Raithby [54] modified the well known SIMPLE algorithm to improve its robustness and eliminate necessity to use under relaxation for the pressure correction, P', equation.

To start the derivation, the nodal U velocity correction formula, Equation (5.24), can be rewritten to get:

$$A^u_{\mathrm{P}} U'_{\mathrm{P}} = \sum_P A^u_{\mathrm{NB}} U'_{\mathrm{NB}} - \forall_P \left.\frac{\partial P'}{\partial x}\right|_P \tag{5.31}$$

Now, subtracting the term $\sum_P A^u_{\mathrm{NB}} U_{\mathrm{P}}{}'$ from both sides of Equation (5.31) yields:

$$\left(A^u_{\mathrm{P}} - \sum_P A^u_{\mathrm{NB}}\right) U'_{\mathrm{P}} = \sum_P A^U_{\mathrm{NB}} \left(U'_{\mathrm{NB}} - U'_{\mathrm{P}}\right) - \forall_P \left.\frac{\partial P'}{\partial x}\right|_P \tag{5.32}$$

In the SIMPLEC method, the term $\sum_P A^u_{\mathrm{NB}} \left(U'_{\mathrm{NB}} - U'_{\mathrm{P}}\right)$ is dropped to introduce a more consistent approximation than the SIMPLE algorithm. By so doing, the following expression is produced for the nodal U velocity correction:

$$U'_{\mathrm{P}} = - \frac{\forall_P}{\left(A^u_{\mathrm{P}} - \sum_P A^u_{\mathrm{NB}}\right)} \left.\frac{\partial P'}{\partial x}\right|_P \tag{5.33}$$

Similarly, the nodal V velocity correction can be expressed in terms of the P' gradient in the y direction as follows:

$$V'_{\mathrm{P}} = - \frac{\forall_P}{\left(A^v_{\mathrm{P}} - \sum_P A^v_{\mathrm{NB}}\right)} \left.\frac{\partial P'}{\partial y}\right|_P \tag{5.34}$$

The east face U and V velocity correction equations are obtained from Equation (5.28) and Equation (5.30) respectively in a similar manner. The results are:

$$U'_{\mathrm{e}} = - \frac{\forall_e}{\left(A^u_{\mathrm{P}}\Big|_{\mathrm{e}} - \sum_e A^u_{\mathrm{nb}}\right)} \left.\frac{\partial P'}{\partial x}\right|_e \tag{5.35}$$

$$V'_{\mathrm{e}} = - \frac{\forall_e}{\left(A^v_{\mathrm{P}}\Big|_{\mathrm{e}} - \sum_e A^v_{\mathrm{nb}}\right)} \left.\frac{\partial P'}{\partial y}\right|_e \tag{5.36}$$

The north face U and V velocity correction equations are obtained following an analogous approach. Face velocity correction expressions are incorporated in the continuity equation to form a constraint for the pressure correction. Once the pressure correction field is obtained, face and nodal velocities are corrected accordingly to ensure mass conservation.

5.1.4 Formulation of the Pressure Correction Equation

Due to the pressure velocity coupling of the momentum equation, only when the *correct* pressure field is used in the momentum equations will produce velocity fields that conserve mass and momentum locally and globally. Because there is no clear governing equation that can be used directly for the pressure, the SIMPLE-like methods form a correction pressure equation based on the continuity equation.

The pressure is defined as a summation of a guessed, P^*, and a correction, P'.

$$P = P^* + P' \tag{5.37}$$

The continuity equation (Equation (4.5)) is used indirectly to derive a constraint on the pressure, P, via the pressure correction P'. To derive the P' equation for a typical control volume, each component of the face velocity at all four faces of the control volume is substituted as a combination of a guessed value and a correction value.

$$\begin{aligned}&\left[A_{\mathrm{e}}^{c,u}(U_{\mathrm{e}}^{*}+U_{\mathrm{e}}{}')+A_{\mathrm{e}}^{c,v}(V_{\mathrm{e}}^{*}+V_{\mathrm{e}}')\right]+\left[A_{\mathrm{w}}^{c,u}(U_{\mathrm{w}}{}^{*}+U_{\mathrm{w}}{}')+A_{\mathrm{w}}^{c,v}(V_{\mathrm{w}}{}^{*}+V_{\mathrm{w}}{}')\right]\\&+\left[A_{\mathrm{n}}^{c,u}(U_{\mathrm{n}}{}^{*}+U_{\mathrm{n}}{}')+A_{\mathrm{n}}^{c,v}(V_{\mathrm{n}}^{*}+V_{\mathrm{n}}')\right]+\left[A_{\mathrm{s}}^{c,u}(U_{\mathrm{s}}^{*}+U_{\mathrm{s}}')+A_{\mathrm{s}}^{c,v}(V_{\mathrm{s}}^{*}+V_{\mathrm{s}}')\right]+b_{\mathrm{P}}^{c}=0\end{aligned} \tag{5.38}$$

Rearranging Equation (5.38) yields

$$\begin{aligned}-\left[(A_{\mathrm{e}}^{c,u}U'_{\mathrm{e}}+A_{\mathrm{e}}^{c,v}V'_{\mathrm{e}})+(A_{\mathrm{w}}^{c,u}U'_{\mathrm{w}}+A_{\mathrm{w}}^{c,v}V'_{\mathrm{w}})+(A_{\mathrm{n}}^{c,u}U'_{\mathrm{n}}+A_{\mathrm{n}}^{c,v}V'_{\mathrm{n}})+(A_{\mathrm{s}}^{c,u}U'_{\mathrm{s}}+A_{\mathrm{s}}^{c,v}V'_{\mathrm{s}})\right]\\=(A_{\mathrm{e}}^{c,u}U_{\mathrm{e}}^{*}+A_{\mathrm{e}}^{c,v}V_{\mathrm{e}}^{*})+(A_{\mathrm{w}}^{c,u}U_{\mathrm{w}}{}^{*}+A_{\mathrm{w}}^{c,v}V_{\mathrm{w}}{}^{*})\\+(A_{\mathrm{n}}^{c,u}U_{\mathrm{n}}{}^{*}+A_{\mathrm{n}}^{c,v}V_{\mathrm{n}}{}^{*})+(A_{\mathrm{s}}^{c,u}U_{\mathrm{s}}^{*}+A_{\mathrm{s}}^{c,v}V_{\mathrm{s}}^{*})+b_{\mathrm{P}}^{c}=\Delta m\end{aligned} \tag{5.39}$$

Substituting face velocity corrections in terms of the pressure correction as indicated by Equations (5.35) and (5.36) for the east face and their analogous expressions for the other

faces to yields

$$\Delta m = -\left[A_{\mathrm{e}}^{c,u} \left\{ \frac{-\not{V}_e}{\left(A_{\mathrm{P}}^{u}\Big|_{\mathrm{e}} - \sum_{e} A_{\mathrm{nb}}^{u} \right)} \left.\frac{\partial P'}{\partial x}\right|_{e} \right\} + A_{\mathrm{e}}^{c,v} \left\{ \frac{-\not{V}_e}{\left(A_{\mathrm{P}}^{v}\Big|_{\mathrm{e}} - \sum_{e} A_{\mathrm{nb}}^{v} \right)} \left.\frac{\partial P'}{\partial y}\right|_{e} \right\} \right.$$
$$+ A_{\mathrm{w}}^{c,u} \left\{ \frac{-\not{V}_w}{\left(A_{\mathrm{P}}^{u}\Big|_{\mathrm{w}} - \sum_{w} A_{\mathrm{nb}}^{u} \right)} \left.\frac{\partial P'}{\partial x}\right|_{w} \right\} + A_{\mathrm{w}}^{c,v} \left\{ \frac{-\not{V}_w}{\left(A_{\mathrm{P}}^{v}\Big|_{\mathrm{w}} - \sum_{w} A_{\mathrm{nb}}^{v} \right)} \left.\frac{\partial P'}{\partial y}\right|_{w} \right\}$$
$$+ A_{\mathrm{n}}^{c,u} \left\{ \frac{-\not{V}_n}{\left(A_{\mathrm{P}}^{u}\Big|_{\mathrm{n}} - \sum_{n} A_{\mathrm{nb}}^{u} \right)} \left.\frac{\partial P'}{\partial x}\right|_{n} \right\} + A_{\mathrm{n}}^{c,v} \left\{ \frac{-\not{V}_n}{\left(A_{\mathrm{P}}^{v}\Big|_{\mathrm{n}} - \sum_{n} A_{\mathrm{nb}}^{v} \right)} \left.\frac{\partial P'}{\partial y}\right|_{n} \right\}$$
$$\left. + A_{\mathrm{s}}^{c,u} \left\{ \frac{-\not{V}_s}{\left(A_{\mathrm{P}}^{u}\Big|_{\mathrm{s}} - \sum_{s} A_{\mathrm{nb}}^{u} \right)} \left.\frac{\partial P'}{\partial x}\right|_{s} \right\} + A_{\mathrm{s}}^{c,v} \left\{ \frac{-\not{V}_s}{\left(A_{\mathrm{P}}^{v}\Big|_{\mathrm{s}} - \sum_{s} A_{\mathrm{nb}}^{v} \right)} \left.\frac{\partial P'}{\partial y}\right|_{s} \right\} \right] \tag{5.40}$$

Then, the pressure correction gradients at the east and north faces are approximated according to Equations (4.133), (4.134), (4.136) and (4.137). For the west and south faces,

analogous expressions are used to produce:

$$\begin{aligned}
\Delta m = -\Bigg[& A_{\mathrm{e}}^{c,u} \left\{ \frac{-\forall_e}{\left(A_{\mathrm{P}}^{u}\Big|_{\mathrm{e}} - \sum_e A_{\mathrm{nb}}^{u} \right)} \frac{\left.\frac{\partial P'}{\partial s}\right|_e t_{ye} - \left.\frac{\partial P'}{\partial t}\right|_e s_{ye}}{s_{xe}t_{ye} - t_{xe}s_{ye}} \right\} \\
& + A_{\mathrm{e}}^{c,v} \left\{ \frac{-\forall_e}{\left(A_{\mathrm{P}}^{v}\Big|_{\mathrm{e}} - \sum_e A_{\mathrm{nb}}^{v} \right)} \frac{\left.\frac{\partial P'}{\partial t}\right|_e s_{xe} - \left.\frac{\partial P'}{\partial s}\right|_e t_{xe}}{s_{xe}t_{ye} - t_{xe}s_{ye}} \right\} \\
& + A_{\mathrm{w}}^{c,u} \left\{ \frac{-\forall_w}{\left(A_{\mathrm{P}}^{u}\Big|_{\mathrm{w}} - \sum_w A_{\mathrm{nb}}^{u} \right)} \frac{\left.\frac{\partial P'}{\partial s}\right|_w t_{yw} - \left.\frac{\partial P'}{\partial t}\right|_w s_{yw}}{s_{xw}t_{yw} - t_{xw}s_{yw}} \right\} \\
& + A_{\mathrm{w}}^{c,v} \left\{ \frac{-\forall_w}{\left(A_{\mathrm{P}}^{v}\Big|_{\mathrm{w}} - \sum_w A_{\mathrm{nb}}^{v} \right)} \frac{\left.\frac{\partial P'}{\partial t}\right|_w s_{xw} - \left.\frac{\partial P'}{\partial s}\right|_w t_{xw}}{s_{xw}t_{yw} - t_{xw}s_{yw}} \right\} \\
& + A_{\mathrm{n}}^{c,u} \left\{ \frac{-\forall_n}{\left(A_{\mathrm{P}}^{u}\Big|_{\mathrm{n}} - \sum_n A_{\mathrm{nb}}^{u} \right)} \frac{\left.\frac{\partial P'}{\partial s}\right|_n t_{yn} - \left.\frac{\partial P'}{\partial t}\right|_n s_{yn}}{s_{xn}t_{yn} - t_{xn}s_{yn}} \right\} \\
& + A_{\mathrm{n}}^{c,v} \left\{ \frac{-\forall_n}{\left(A_{\mathrm{P}}^{v}\Big|_{\mathrm{n}} - \sum_n A_{\mathrm{nb}}^{v} \right)} \frac{\left.\frac{\partial P'}{\partial t}\right|_n s_{xn} - \left.\frac{\partial P'}{\partial s}\right|_n t_{xn}}{s_{xn}t_{yn} - t_{xn}s_{yn}} \right\} \\
& + A_{\mathrm{s}}^{c,u} \left\{ \frac{-\forall_s}{\left(A_{\mathrm{P}}^{u}\Big|_{\mathrm{s}} - \sum_s A_{\mathrm{nb}}^{u} \right)} \frac{\left.\frac{\partial P'}{\partial s}\right|_s t_{ys} - \left.\frac{\partial P'}{\partial t}\right|_s s_{ys}}{s_{xs}t_{ys} - t_{xs}s_{ys}} \right\} \\
& + A_{\mathrm{s}}^{c,v} \left\{ \frac{-\forall_s}{\left(A_{\mathrm{P}}^{v}\Big|_{\mathrm{s}} - \sum_s A_{\mathrm{nb}}^{v} \right)} \frac{\left.\frac{\partial P'}{\partial t}\right|_s s_{xs} - \left.\frac{\partial P'}{\partial s}\right|_s t_{xs}}{s_{xs}t_{ys} - t_{xs}s_{ys}} \right\} \Bigg]
\end{aligned} \tag{5.41}$$

Now, the nodal and corner values of P' are used to evaluate the gradients as follows:

$$\Delta m = -\Bigg[A_{\mathrm{e}}^{c,u} \left\{ \frac{-\forall_e}{\left(A_{\mathrm{P}}^{u}\Big|_{\mathrm{e}} - \sum_e A_{\mathrm{nb}}^{u} \right)} \frac{\frac{P'_{\mathrm{E}} - P'_{\mathrm{P}}}{(ds)_e} t_{ye} - \frac{P'_{\mathrm{ne}} - P'_{\mathrm{se}}}{(dt)_e} s_{ye}}{s_{xe}t_{ye} - t_{xe}s_{ye}} \right\}$$
$$+ A_{\mathrm{e}}^{c,v} \left\{ \frac{-\forall_e}{\left(A_{\mathrm{P}}^{v}\Big|_{\mathrm{e}} - \sum_e A_{\mathrm{nb}}^{v} \right)} \frac{\frac{P'_{\mathrm{ne}} - P'_{\mathrm{se}}}{(dt)_e} s_{xe} - \frac{P'_{\mathrm{E}} - P'_{\mathrm{P}}}{(ds)_e} t_{xe}}{s_{xe}t_{ye} - t_{xe}s_{ye}} \right\}$$
$$+ A_{\mathrm{w}}^{c,u} \left\{ \frac{-\forall_w}{\left(A_{\mathrm{P}}^{u}\Big|_{\mathrm{w}} - \sum_w A_{\mathrm{nb}}^{u} \right)} \frac{\frac{P'_{\mathrm{P}} - P'_{\mathrm{W}}}{(ds)_w} t_{yw} - \frac{P'_{\mathrm{nw}} - P'_{\mathrm{sw}}}{(dt)_w} s_{yw}}{s_{xw}t_{yw} - t_{xw}s_{yw}} \right\}$$
$$+ A_{\mathrm{w}}^{c,v} \left\{ \frac{-\forall_w}{\left(A_{\mathrm{P}}^{v}\Big|_{\mathrm{w}} - \sum_w A_{\mathrm{nb}}^{v} \right)} \frac{\frac{P'_{\mathrm{nw}} - P'_{\mathrm{sw}}}{(dt)_w} s_{xw} - \frac{P'_{\mathrm{P}} - P'_{\mathrm{W}}}{(ds)_w} t_{xw}}{s_{xw}t_{yw} - t_{xw}s_{yw}} \right\}$$
$$+ A_{\mathrm{n}}^{c,u} \left\{ \frac{-\forall_n}{\left(A_{\mathrm{P}}^{u}\Big|_{\mathrm{n}} - \sum_n A_{\mathrm{nb}}^{u} \right)} \frac{\frac{P'_{\mathrm{ne}} - P'_{\mathrm{nw}}}{(ds)_n} t_{yn} - \frac{P'_{\mathrm{N}} - P'_{\mathrm{P}}}{(dt)_n} s_{yn}}{s_{xn}t_{yn} - t_{xn}s_{yn}} \right\}$$
$$+ A_{\mathrm{n}}^{c,v} \left\{ \frac{-\forall_n}{\left(A_{\mathrm{P}}^{v}\Big|_{\mathrm{n}} - \sum_n A_{\mathrm{nb}}^{v} \right)} \frac{\frac{P'_{\mathrm{N}} - P'_{\mathrm{P}}}{(dt)_n} s_{xn} - \frac{P'_{\mathrm{ne}} - P'_{\mathrm{nw}}}{(ds)_n} t_{xn}}{s_{xn}t_{yn} - t_{xn}s_{yn}} \right\}$$
$$+ A_{\mathrm{s}}^{c,u} \left\{ \frac{-\forall_s}{\left(A_{\mathrm{P}}^{u}\Big|_{\mathrm{s}} - \sum_s A_{\mathrm{nb}}^{u} \right)} \frac{\frac{P'_{\mathrm{se}} - P'_{\mathrm{sw}}}{(ds)_s} t_{ys} - \frac{P'_{\mathrm{P}} - P'_{\mathrm{S}}}{(dt)_s} s_{ys}}{s_{xs}t_{ys} - t_{xs}s_{ys}} \right\}$$
$$+ A_{\mathrm{s}}^{c,v} \left\{ \frac{-\forall_s}{\left(A_{\mathrm{P}}^{v}\Big|_{\mathrm{s}} - \sum_s A_{\mathrm{nb}}^{v} \right)} \frac{\frac{P'_{\mathrm{P}} - P'_{\mathrm{S}}}{(dt)_s} s_{xs} - \frac{P'_{\mathrm{se}} - P'_{\mathrm{sw}}}{(ds)_s} t_{xs}}{s_{xs}t_{ys} - t_{xs}s_{ys}} \right\} \Bigg] \quad (5.42)$$

To simplify the resulting $P^{'}$ equation, some terms are suggested to be gathered in the following coefficients:

$$\left.\begin{array}{llll} C^u_{\mathrm{e}} = \dfrac{\forall_e}{(ds)_e} & C^v_{\mathrm{e}} = \dfrac{\forall_e}{(dt)_e} \\ C^u_{\mathrm{n}} = \dfrac{\forall_n}{(ds)_n} & C^v_{\mathrm{n}} = \dfrac{\forall_n}{(dt)_n} \\ C^u_{\mathrm{P}} = \dfrac{\forall_p}{(ds)_p} & C^v_{\mathrm{P}} = \dfrac{\forall_p}{(dt)_p} \end{array}\right\} \tag{5.43}$$

Also, the repetitive geometrical terms are gathered in the following compact coefficients:

$$\left.\begin{array}{llll} h_{t_y} = \dfrac{t_y}{s_x t_y - t_x s_y} & h_{s_y} = \dfrac{s_y}{s_x t_y - t_x s_y} \\ h_{s_x} = \dfrac{s_x}{s_x t_y - t_x s_y} & h_{t_x} = \dfrac{t_x}{s_x t_y - t_x s_y} \end{array}\right\} \tag{5.44}$$

Using the definitions in Equations (5.43) and (5.44), additional coefficients are defined that are needed to simplify the presentation of Equation (5.42). Those coefficients are as fol-

lows [50]:

$$\left.\begin{aligned}
\widehat{C}_{\mathrm{e}}^{u,u} &= \frac{-\not{V}_e\, t_{ye}}{\left(A_{\mathrm{P}}^{u}\big|_{\mathrm{e}} - \sum_e A_{\mathrm{nb}}^{u}\right)(ds)_e\,(s_{xe}t_{ye} - t_{xe}s_{ye})} = \frac{-C_{\mathrm{e}}^{u}\, h_{t_{ye}}}{A_{\mathrm{P}}^{u}\big|_{\mathrm{e}} - \sum_e A_{\mathrm{nb}}^{u}} \\
\widehat{C}_{\mathrm{e}}^{u,v} &= \frac{-\not{V}_e\, s_{ye}}{\left(A_{\mathrm{P}}^{u}\big|_{\mathrm{e}} - \sum_e A_{\mathrm{nb}}^{u}\right)(dt)_e\,(s_{xe}t_{ye} - t_{xe}s_{ye})} = \frac{-C_{\mathrm{e}}^{v}\, h_{s_{ye}}}{A_{\mathrm{P}}^{u}\big|_{\mathrm{e}} - \sum_e A_{\mathrm{nb}}^{u}} \\
\widehat{C}_{\mathrm{e}}^{v,v} &= \frac{-\not{V}_e\, s_{xe}}{\left(A_{\mathrm{P}}^{v}\big|_{\mathrm{e}} - \sum_e A_{\mathrm{nb}}^{v}\right)(dt)_e\,(s_{xe}t_{ye} - t_{xe}s_{ye})} = \frac{-C_{\mathrm{e}}^{v}\, h_{s_{xe}}}{A_{\mathrm{P}}^{v}\big|_{\mathrm{e}} - \sum_e A_{\mathrm{nb}}^{v}} \\
\widehat{C}_{\mathrm{e}}^{v,u} &= \frac{-\not{V}_e\, t_{xe}}{\left(A_{\mathrm{P}}^{v}\big|_{\mathrm{e}} - \sum_e A_{\mathrm{nb}}^{v}\right)(ds)_e\,(s_{xe}t_{ye} - t_{xe}s_{ye})} = \frac{-C_{\mathrm{e}}^{u}\, h_{t_{xe}}}{A_{\mathrm{P}}^{v}\big|_{\mathrm{e}} - \sum_e A_{\mathrm{nb}}^{v}} \\
\widehat{C}_{\mathrm{n}}^{u,u} &= \frac{-\not{V}_n\, t_{yn}}{\left(A_{\mathrm{P}}^{u}\big|_{\mathrm{n}} - \sum_n A_{\mathrm{nb}}^{u}\right)(ds)_n\,(s_{xn}t_{yn} - t_{xn}s_{yn})} = \frac{-C_{\mathrm{n}}^{u}\, h_{t_{yn}}}{A_{\mathrm{P}}^{u}\big|_{\mathrm{n}} - \sum_n A_{\mathrm{nb}}^{u}} \\
\widehat{C}_{\mathrm{n}}^{u,v} &= \frac{-\not{V}_n\, s_{yn}}{\left(A_{\mathrm{P}}^{u}\big|_{\mathrm{n}} - \sum_n A_{\mathrm{nb}}^{u}\right)(dt)_n\,(s_{xn}t_{yn} - t_{xn}s_{yn})} = \frac{-C_{\mathrm{n}}^{v}\, h_{s_{yn}}}{A_{\mathrm{P}}^{u}\big|_{\mathrm{n}} - \sum_n A_{\mathrm{nb}}^{u}} \\
\widehat{C}_{\mathrm{n}}^{v,v} &= \frac{-\not{V}_n\, s_{xn}}{\left(A_{\mathrm{P}}^{v}\big|_{\mathrm{n}} - \sum_n A_{\mathrm{nb}}^{v}\right)(dt)_n\,(s_{xn}t_{yn} - t_{xn}s_{yn})} = \frac{-C_{\mathrm{n}}^{v}\, h_{s_{xn}}}{A_{\mathrm{P}}^{v}\big|_{\mathrm{n}} - \sum_n A_{\mathrm{nb}}^{v}} \\
\widehat{C}_{\mathrm{n}}^{v,u} &= \frac{-\not{V}_n\, t_{xn}}{\left(A_{\mathrm{P}}^{v}\big|_{\mathrm{n}} - \sum_n A_{\mathrm{nb}}^{v}\right)(ds)_n\,(s_{xn}t_{yn} - t_{xn}s_{yn})} = \frac{-C_{\mathrm{n}}^{u}\, h_{t_{xn}}}{A_{\mathrm{P}}^{v}\big|_{\mathrm{n}} - \sum_n A_{\mathrm{nb}}^{v}}
\end{aligned}\right\} \tag{5.45}$$

Using the definitions in Equations (5.43) to (5.45), Equation (5.42) can be rewritten as

$$\begin{aligned}\Delta m = -\Bigg[& A_{\mathrm{e}}^{c,u}\left\{\widehat{C}_{\mathrm{e}}^{u,u}\left(P_{\mathrm{E}}^{'}-P_{\mathrm{P}}^{'}\right)-\widehat{C}_{\mathrm{e}}^{u,v}\left(P_{\mathrm{ne}}^{'}-P_{\mathrm{se}}^{'}\right)\right\} \\ & +A_{\mathrm{e}}^{c,v}\left\{\widehat{C}_{\mathrm{e}}^{v,v}\left(P_{\mathrm{ne}}^{'}-P_{\mathrm{se}}^{'}\right)-\widehat{C}_{\mathrm{e}}^{v,u}\left(P_{\mathrm{E}}^{'}-P_{\mathrm{P}}^{'}\right)\right\} \\ & +A_{\mathrm{w}}^{c,u}\left\{\widehat{C}_{\mathrm{w}}^{u,u}\left(P_{\mathrm{P}}^{'}-P_{\mathrm{W}}^{'}\right)-\widehat{C}_{\mathrm{w}}^{u,v}\left(P_{\mathrm{nw}}^{'}-P_{\mathrm{sw}}^{'}\right)\right\} \\ & +A_{\mathrm{w}}^{c,v}\left\{\widehat{C}_{\mathrm{w}}^{v,v}\left(P_{\mathrm{nw}}^{'}-P_{\mathrm{sw}}^{'}\right)-\widehat{C}_{\mathrm{w}}^{v,u}\left(P_{\mathrm{P}}^{'}-P_{\mathrm{W}}^{'}\right)\right\} \\ & +A_{\mathrm{n}}^{c,u}\left\{\widehat{C}_{\mathrm{n}}^{u,u}\left(P_{\mathrm{ne}}^{'}-P_{\mathrm{nw}}^{'}\right)-\widehat{C}_{\mathrm{n}}^{u,v}\left(P_{\mathrm{N}}^{'}-P_{\mathrm{P}}^{'}\right)\right\} \\ & +A_{\mathrm{n}}^{c,v}\left\{\widehat{C}_{\mathrm{n}}^{v,v}\left(P_{\mathrm{N}}^{'}-P_{\mathrm{P}}^{'}\right)-\widehat{C}_{\mathrm{n}}^{v,u}\left(P_{\mathrm{ne}}^{'}-P_{\mathrm{nw}}^{'}\right)\right\} \\ & +A_{\mathrm{s}}^{c,u}\left\{\widehat{C}_{\mathrm{s}}^{u,u}\left(P_{\mathrm{se}}^{'}-P_{\mathrm{sw}}^{'}\right)-\widehat{C}_{\mathrm{s}}^{u,v}\left(P_{\mathrm{P}}^{'}-P_{\mathrm{S}}^{'}\right)\right\} \\ & +A_{\mathrm{s}}^{c,v}\left\{\widehat{C}_{\mathrm{s}}^{v,v}\left(P_{\mathrm{P}}^{'}-P_{\mathrm{S}}^{'}\right)-\widehat{C}_{\mathrm{s}}^{v,u}\left(P_{\mathrm{se}}^{'}-P_{\mathrm{sw}}^{'}\right)\right\}\Bigg] \end{aligned} \tag{5.46}$$

The pressure correction values at control volume corners can be evaluated in terms of the nodal neighbouring values in a general manner as suggested by the following relations:

$$\left.\begin{aligned} P_{\mathrm{ne}}^{'} &= C_{ne1}\,P_{\mathrm{P}}^{'}+C_{ne2}\,P_{\mathrm{E}}^{'}+C_{ne3}\,P_{\mathrm{NE}}^{'}+C_{ne4}\,P_{\mathrm{N}}^{'} \\ P_{\mathrm{se}}^{'} &= C_{se1}\,P_{\mathrm{S}}^{'}+C_{se2}\,P_{\mathrm{SE}}^{'}+C_{se3}\,P_{\mathrm{E}}^{'}+C_{se4}\,P_{\mathrm{P}}^{'} \\ P_{\mathrm{nw}}^{'} &= C_{nw1}\,P_{\mathrm{W}}^{'}+C_{nw2}\,P_{\mathrm{P}}^{'}+C_{nw3}\,P_{\mathrm{N}}^{'}+C_{nw4}\,P_{\mathrm{NW}}^{'} \\ P_{\mathrm{sw}}^{'} &= C_{sw1}\,P_{\mathrm{SW}}^{'}+C_{sw2}\,P_{\mathrm{S}}^{'}+C_{sw3}\,P_{\mathrm{P}}^{'}+C_{sw4}\,P_{\mathrm{W}}^{'} \end{aligned}\right\} \tag{5.47}$$

For uniform grids, each nodal neighbouring value contributes by a quarter of its value. For non-uniform grids, the contribution weight of each nodal neighbour is estimated by 2D linear

interpolation. Using the corner interpolation equations, Equation (5.46) becomes

$$
\begin{aligned}
\Delta m = -\Bigg[& A_{\mathrm{e}}^{c,u}\Bigg\{\widehat{C}_{\mathrm{e}}^{u,u}\left(P_{\mathrm{E}}^{'}-P_{\mathrm{P}}^{'}\right) \\
& -\widehat{C}_{\mathrm{e}}^{u,v}\Big(\left(C_{ne1}P_{\mathrm{P}}^{'}+C_{ne2}P_{\mathrm{E}}^{'}+C_{ne3}P_{\mathrm{NE}}^{'}+C_{ne4}P_{\mathrm{N}}^{'}\right)-\left(C_{se1}P_{\mathrm{S}}^{'}+C_{se2}P_{\mathrm{SE}}^{'}+C_{se3}P_{\mathrm{E}}^{'}+C_{se4}P_{\mathrm{P}}^{'}\right)\Big)\Bigg\} \\
& +A_{\mathrm{e}}^{c,v}\Bigg\{\widehat{C}_{\mathrm{e}}^{v,v}\Big(\left(C_{ne1}P_{\mathrm{P}}^{'}+C_{ne2}P_{\mathrm{E}}^{'}+C_{ne3}P_{\mathrm{NE}}^{'}+C_{ne4}P_{\mathrm{N}}^{'}\right)-\left(C_{se1}P_{\mathrm{S}}^{'}+C_{se2}P_{\mathrm{SE}}^{'}+C_{se3}P_{\mathrm{E}}^{'}+C_{se4}P_{\mathrm{P}}^{'}\right)\Big) \\
& \qquad -\widehat{C}_{\mathrm{e}}^{v,u}\left(P_{\mathrm{E}}^{'}-P_{\mathrm{P}}^{'}\right)\Bigg\} \\
& \qquad +A_{\mathrm{w}}^{c,u}\Bigg\{\widehat{C}_{\mathrm{w}}^{u,u}\left(P_{\mathrm{P}}^{'}-P_{\mathrm{W}}^{'}\right) \\
& -\widehat{C}_{\mathrm{w}}^{u,v}\Big(\left(C_{nw1}P_{\mathrm{W}}^{'}+C_{nw2}P_{\mathrm{P}}^{'}+C_{nw3}P_{\mathrm{N}}^{'}+C_{nw4}P_{\mathrm{NW}}^{'}\right)-\left(C_{sw1}P_{\mathrm{SW}}^{'}+C_{sw2}P_{\mathrm{S}}^{'}+C_{sw3}P_{\mathrm{P}}^{'}+C_{sw4}P_{\mathrm{W}}^{'}\right)\Big)\Bigg\} \\
& +A_{\mathrm{w}}^{c,v}\Bigg\{\widehat{C}_{\mathrm{w}}^{v,v}\Big(\left(C_{nw1}P_{\mathrm{W}}^{'}+C_{nw2}P_{\mathrm{P}}^{'}+C_{nw3}P_{\mathrm{N}}^{'}+C_{nw4}P_{\mathrm{NW}}^{'}\right)-\left(C_{sw1}P_{\mathrm{SW}}^{'}+C_{sw2}P_{\mathrm{S}}^{'}+C_{sw3}P_{\mathrm{P}}^{'}+C_{sw4}P_{\mathrm{W}}^{'}\right)\Big) \\
& \qquad -\widehat{C}_{\mathrm{w}}^{v,u}\left(P_{\mathrm{P}}^{'}-P_{\mathrm{W}}^{'}\right)\Bigg\} \\
& +A_{\mathrm{n}}^{c,u}\Bigg\{\widehat{C}_{\mathrm{n}}^{u,u}\Big(\left(C_{ne1}P_{\mathrm{P}}^{'}+C_{ne2}P_{\mathrm{E}}^{'}+C_{ne3}P_{\mathrm{NE}}^{'}+C_{ne4}P_{\mathrm{N}}^{'}\right)-\left(C_{nw1}P_{\mathrm{W}}^{'}+C_{nw2}P_{\mathrm{P}}^{'}+C_{nw3}P_{\mathrm{N}}^{'}+C_{nw4}P_{\mathrm{NW}}^{'}\right)\Big) \\
& \qquad -\widehat{C}_{\mathrm{n}}^{u,v}\left(P_{\mathrm{N}}^{'}-P_{\mathrm{P}}^{'}\right)\Bigg\} \\
& \qquad +A_{\mathrm{n}}^{c,v}\Bigg\{\widehat{C}_{\mathrm{n}}^{v,v}\left(P_{\mathrm{N}}^{'}-P_{\mathrm{P}}^{'}\right) \\
& -\widehat{C}_{\mathrm{n}}^{v,u}\Big(\left(C_{ne1}P_{\mathrm{P}}^{'}+C_{ne2}P_{\mathrm{E}}^{'}+C_{ne3}P_{\mathrm{NE}}^{'}+C_{ne4}P_{\mathrm{N}}^{'}\right)-\left(C_{nw1}P_{\mathrm{W}}^{'}+C_{nw2}P_{\mathrm{P}}^{'}+C_{nw3}P_{\mathrm{N}}^{'}+C_{nw4}P_{\mathrm{NW}}^{'}\right)\Big)\Bigg\} \\
& +A_{\mathrm{s}}^{c,u}\Bigg\{\widehat{C}_{\mathrm{s}}^{u,u}\Big(\left(C_{se1}P_{\mathrm{S}}^{'}+C_{se2}P_{\mathrm{SE}}^{'}+C_{se3}P_{\mathrm{E}}^{'}+C_{se4}P_{\mathrm{P}}^{'}\right)-\left(C_{sw1}P_{\mathrm{SW}}^{'}+C_{sw2}P_{\mathrm{S}}^{'}+C_{sw3}P_{\mathrm{P}}^{'}+C_{sw4}P_{\mathrm{W}}^{'}\right)\Big) \\
& \qquad -\widehat{C}_{\mathrm{s}}^{u,v}\left(P_{\mathrm{P}}^{'}-P_{\mathrm{S}}^{'}\right)\Bigg\} \\
& \qquad +A_{\mathrm{s}}^{c,v}\Bigg\{\widehat{C}_{\mathrm{s}}^{v,v}\left(P_{\mathrm{P}}^{'}-P_{\mathrm{S}}^{'}\right) \\
& -\widehat{C}_{\mathrm{s}}^{v,u}\Big(\left(C_{se1}P_{\mathrm{S}}^{'}+C_{se2}P_{\mathrm{SE}}^{'}+C_{se3}P_{\mathrm{E}}^{'}+C_{se4}P_{\mathrm{P}}^{'}\right)-\left(C_{sw1}P_{\mathrm{SW}}^{'}+C_{sw2}P_{\mathrm{S}}^{'}+C_{sw3}P_{\mathrm{P}}^{'}+C_{sw4}P_{\mathrm{W}}^{'}\right)\Big)\Bigg\}\Bigg]
\end{aligned}
\tag{5.48}
$$

Finally, collecting terms to get a nine-point algebraic equation for $P^{'}$ yields:

$$A_{\mathrm{P}}^{p'} P_{\mathrm{P}}^{'} = A_{\mathrm{E}}^{p'} P_{\mathrm{E}}^{'} + A_{\mathrm{W}}^{p'} P_{\mathrm{W}}^{'} + A_{\mathrm{N}}^{p'} P_{\mathrm{N}}^{'} + A_{\mathrm{S}}^{p'} P_{\mathrm{S}}^{'} + A_{\mathrm{NE}}^{p'} P_{\mathrm{NE}}^{'} + A_{\mathrm{NW}}^{p'} P_{\mathrm{NW}}^{'} + A_{\mathrm{SE}}^{p'} P_{\mathrm{SE}}^{'} + A_{\mathrm{SW}}^{p'} P_{\mathrm{SW}}^{'} + b_{\mathrm{P}}^{p'} \quad (5.49)$$

where:

$$A_{\mathrm{E}}^{P'} = A_{\mathrm{e}}^{c,u} \left(\widehat{C}_{\mathrm{e}}^{u,u} - \widehat{C}_{\mathrm{e}}^{u,v} \left(C_{ne2} - C_{se3} \right) \right) - A_{\mathrm{e}}^{c,v} \left(\widehat{C}_{\mathrm{e}}^{v,u} - \widehat{C}_{\mathrm{e}}^{v,v} \left(C_{ne2} - C_{se3} \right) \right) + A_{\mathrm{n}}^{c,u} \widehat{C}_{\mathrm{n}}^{u,u} C_{ne2} - A_{\mathrm{n}}^{c,v} \widehat{C}_{\mathrm{n}}^{v,u} C_{ne2} + A_{\mathrm{s}}^{c,u} \widehat{C}_{\mathrm{s}}^{u,u} C_{se3} - A_{\mathrm{s}}^{c,v} \widehat{C}_{\mathrm{s}}^{v,u} C_{se3} \quad (5.50)$$

$$A_{\mathrm{W}}^{P'} = -A_{\mathrm{w}}^{c,u} \left(\widehat{C}_{\mathrm{w}}^{u,u} + \widehat{C}_{\mathrm{w}}^{u,v} \left(C_{nw1} - C_{sw4} \right) \right) + A_{\mathrm{w}}^{c,v} \left(\widehat{C}_{\mathrm{w}}^{v,u} + \widehat{C}_{\mathrm{w}}^{v,v} \left(C_{nw1} - C_{sw4} \right) \right) - A_{\mathrm{n}}^{c,u} \widehat{C}_{\mathrm{n}}^{u,u} C_{nw1} + A_{\mathrm{n}}^{c,v} \widehat{C}_{\mathrm{n}}^{v,u} C_{nw1} - A_{\mathrm{s}}^{c,u} \widehat{C}_{\mathrm{s}}^{u,u} C_{sw4} + A_{\mathrm{s}}^{c,v} \widehat{C}_{\mathrm{s}}^{v,u} C_{sw4} \quad (5.51)$$

$$A_{\mathrm{N}}^{P'} = A_{\mathrm{n}}^{c,u} \left(\widehat{C}_{\mathrm{n}}^{u,u} \left(C_{ne4} - C_{se3} \right) - \widehat{C}_{\mathrm{n}}^{u,v} \right) - A_{\mathrm{n}}^{c,v} \left(\widehat{C}_{\mathrm{n}}^{v,u} \left(C_{ne4} - C_{se3} \right) - \widehat{C}_{\mathrm{n}}^{v,v} \right) - A_{\mathrm{e}}^{c,u} \widehat{C}_{\mathrm{e}}^{u,v} C_{ne4} + A_{\mathrm{e}}^{c,v} \widehat{C}_{\mathrm{e}}^{v,v} C_{ne4} - A_{\mathrm{w}}^{c,u} \widehat{C}_{\mathrm{w}}^{u,v} C_{nw3} + A_{\mathrm{w}}^{c,v} \widehat{C}_{\mathrm{w}}^{v,v} C_{nw3} \quad (5.52)$$

$$A_{\mathrm{S}}^{P'} = A_{\mathrm{s}}^{c,u} \left(\widehat{C}_{\mathrm{s}}^{u,u} \left(C_{se1} - C_{sw2} \right) + \widehat{C}_{\mathrm{s}}^{u,v} \right) - A_{\mathrm{s}}^{c,v} \left(\widehat{C}_{\mathrm{s}}^{v,u} \left(C_{se1} - C_{sw2} \right) + \widehat{C}_{\mathrm{s}}^{v,v} \right) + A_{\mathrm{e}}^{c,u} \widehat{C}_{\mathrm{e}}^{u,v} C_{se1} - A_{\mathrm{e}}^{c,v} \widehat{C}_{\mathrm{e}}^{v,v} C_{se1} + A_{\mathrm{w}}^{c,u} \widehat{C}_{\mathrm{w}}^{u,v} C_{sw2} - A_{\mathrm{w}}^{c,v} \widehat{C}_{\mathrm{w}}^{v,v} C_{sw2} \quad (5.53)$$

$$A_{\mathrm{NE}}^{P'} = -A_{\mathrm{e}}^{c,u} \widehat{C}_{\mathrm{e}}^{u,v} C_{ne3} + A_{\mathrm{e}}^{c,v} \widehat{C}_{\mathrm{e}}^{v,v} C_{ne3} + A_{\mathrm{n}}^{c,u} \widehat{C}_{\mathrm{n}}^{u,u} C_{ne3} - A_{\mathrm{n}}^{c,v} \widehat{C}_{\mathrm{n}}^{v,u} C_{ne3} \quad (5.54)$$

$$A_{\mathrm{NW}}^{P'} = -A_{\mathrm{w}}^{c,u} \widehat{C}_{\mathrm{w}}^{u,v} C_{nw4} + A_{\mathrm{w}}^{c,v} \widehat{C}_{\mathrm{w}}^{v,v} C_{nw4} - A_{\mathrm{n}}^{c,u} \widehat{C}_{\mathrm{n}}^{u,u} C_{nw4} + A_{\mathrm{n}}^{c,v} \widehat{C}_{\mathrm{n}}^{v,u} C_{nw4} \quad (5.55)$$

$$A_{\mathrm{SE}}^{P'} = A_{\mathrm{e}}^{c,u} \widehat{C}_{\mathrm{e}}^{u,v} C_{se2} - A_{\mathrm{e}}^{c,v} \widehat{C}_{\mathrm{e}}^{v,v} C_{se2} + A_{\mathrm{s}}^{c,u} \widehat{C}_{\mathrm{s}}^{u,u} C_{se2} - A_{\mathrm{s}}^{c,v} \widehat{C}_{\mathrm{s}}^{v,u} C_{se2} \quad (5.56)$$

$$A_{\mathrm{SW}}^{P'} = A_{\mathrm{w}}^{c,u} \widehat{C}_{\mathrm{w}}^{u,v} C_{sw1} - A_{\mathrm{w}}^{c,v} \widehat{C}_{\mathrm{w}}^{v,v} C_{sw1} - A_{\mathrm{s}}^{c,u} \widehat{C}_{\mathrm{s}}^{u,u} C_{sw1} + A_{\mathrm{s}}^{c,v} \widehat{C}_{\mathrm{s}}^{v,u} C_{sw1} \quad (5.57)$$

$$
\begin{aligned}
A_{\mathrm{P}}^{P'} = & A_{\mathrm{e}}^{c,u}\left(\widehat{C}_{\mathrm{e}}^{u,u}+\widehat{C}_{\mathrm{e}}^{u,v}\ \left(C_{ne1}-C_{se4}\right)\right)-A_{\mathrm{e}}^{c,v}\left(\widehat{C}_{\mathrm{e}}^{v,u}+\widehat{C}_{\mathrm{e}}^{v,v}\ \left(C_{ne1}-C_{se4}\right)\right)\\
& -A_{\mathrm{w}}^{c,u}\left(\widehat{C}_{\mathrm{w}}^{u,u}-\widehat{C}_{\mathrm{w}}^{u,v}\ \left(C_{nw2}-C_{sw3}\right)\right)+A_{\mathrm{w}}^{c,v}\left(\widehat{C}_{\mathrm{w}}^{v,u}-\widehat{C}_{\mathrm{w}}^{v,v}\ \left(C_{nw2}-C_{sw3}\right)\right)\\
& -A_{\mathrm{n}}^{c,u}\left(\widehat{C}_{\mathrm{n}}^{u,u}\ \left(C_{ne1}-C_{nw2}\right)+\widehat{C}_{\mathrm{n}}^{u,v}\right)+A_{\mathrm{n}}^{c,v}\left(\widehat{C}_{\mathrm{n}}^{v,u}\ \left(C_{ne1}-C_{nw2}\right)+\widehat{C}_{\mathrm{n}}^{v,v}\right)\\
& -A_{\mathrm{s}}^{c,u}\left(\widehat{C}_{\mathrm{s}}^{u,u}\ \left(C_{se4}-C_{sw3}\right)-\widehat{C}_{\mathrm{s}}^{u,v}\right)+A_{\mathrm{s}}^{c,v}\left(\widehat{C}_{\mathrm{s}}^{v,u}\ \left(C_{se4}-C_{sw3}\right)-\widehat{C}_{\mathrm{s}}^{v,v}\right) \qquad (5.58)
\end{aligned}
$$

$$
\begin{aligned}
b_{\mathrm{P}}^{P'} = & \left(A_{\mathrm{e}}^{c,u}U_e^*+A_{\mathrm{e}}^{c,v}V_e^*\right)+\left(A_{\mathrm{w}}^{c,u}U_w^*+A_{\mathrm{w}}^{c,v}V_w^*\right)+\left(A_{\mathrm{n}}^{c,u}U_n^*+A_{\mathrm{n}}^{c,v}V_n^*\right)\\
& +\left(A_{\mathrm{s}}^{c,u}U_s^*+A_{\mathrm{s}}^{c,v}V_s^*\right)+b_P^c=-\dot{m}_e+\dot{m}_w-\dot{m}_n+\dot{m}_s+b_{\mathrm{P}}^c \qquad (5.59)
\end{aligned}
$$

5.1.5 Boundary Conditions for the Pressure Correction Equation

Because the role of the continuity equation, hence the P' equation, is to conserve mass across the domain, the face velocity boundary conditions are used to implement P' equation boundary conditions.

In this section, the P' boundary conditions are presented in detail only for the south boundary ($j = j_B$). The equations for the other domain boundaries are derived in a similar manner.

At the south boundary, after applying the face velocity boundary condition, (Equation (4.164)), and applying the velocity correction principle, the continuity equation may be written as

$$
\begin{aligned}
& -\left[\left(A_{\mathrm{e}}^{c,u}U_{\mathrm{e}}{}'+A_{\mathrm{e}}^{c,v}V_{\mathrm{e}}{}'\right)+\left(A_{\mathrm{w}}^{c,u}U_{\mathrm{w}}{}'+A_{\mathrm{w}}^{c,v}V_{\mathrm{w}}{}'\right)+\left(A_{\mathrm{n}}^{c,u}\right)^{\oplus}U_{\mathrm{n}}{}'+\left(A_{\mathrm{n}}^{c,v}\right)^{\oplus}V_{\mathrm{n}}{}'\right]\\
& \qquad =A_{\mathrm{e}}^{c,u}U_{\mathrm{e}}{}^*+A_{\mathrm{e}}^{c,v}V_{\mathrm{e}}{}^*+A_{\mathrm{w}}^{c,u}U_{\mathrm{w}}{}^*+A_{\mathrm{w}}^{c,v}V_{\mathrm{w}}{}^*\\
& \qquad\quad +\left(\left(A_{\mathrm{n}}^{c,u}\right)^{\oplus}U_{\mathrm{n}}{}^*+\left(A_{\mathrm{n}}^{c,v}\right)^{\oplus}V_{\mathrm{n}}{}^*\right)+\left(b_{\mathrm{P}}^c\right)^{\oplus}=\Delta m \qquad (5.60)
\end{aligned}
$$

Starting with Equation (5.60) and following the same procedure of deriving P' equation for a typical control volume produces:

$$\begin{aligned}\Delta m = -\Bigg[& A_{\mathrm{e}}^{c,u}\left\{\widehat{C}_{\mathrm{e}}^{u,u}\left(P'_{\mathrm{E}}-P'_{\mathrm{P}}\right)-\widehat{C}_{\mathrm{e}}^{u,v}\left(P'_{\mathrm{ne}}-P'_{\mathrm{se}}\right)\right\} \\ & + A_{\mathrm{e}}^{c,v}\left\{\widehat{C}_{\mathrm{e}}^{v,v}\left(P'_{\mathrm{ne}}-P'_{\mathrm{se}}\right)-\widehat{C}_{\mathrm{e}}^{v,u}\left(P'_{\mathrm{E}}-P'_{\mathrm{P}}\right)\right\} \\ & + A_{\mathrm{w}}^{c,u}\left\{\widehat{C}_{\mathrm{w}}^{u,u}\left(P'_{\mathrm{P}}-P'_{\mathrm{W}}\right)-\widehat{C}_{\mathrm{w}}^{u,v}\left(P'_{\mathrm{nw}}-P'_{\mathrm{sw}}\right)\right\} \\ & + A_{\mathrm{w}}^{c,v}\left\{\widehat{C}_{\mathrm{w}}^{v,v}\left(P'_{\mathrm{nw}}-P'_{\mathrm{sw}}\right)-\widehat{C}_{\mathrm{w}}^{v,u}\left(P'_{\mathrm{P}}-P'_{\mathrm{W}}\right)\right\} \\ & + \left(A_{\mathrm{n}}^{c,u}\right)^{\oplus}\left\{\widehat{C}_{\mathrm{n}}^{u,u}\left(P'_{\mathrm{ne}}-P'_{\mathrm{nw}}\right)-\widehat{C}_{\mathrm{n}}^{u,v}\left(P'_{\mathrm{N}}-P'_{\mathrm{P}}\right)\right\} \\ & + \left(A_{\mathrm{n}}^{c,v}\right)^{\oplus}\left\{\widehat{C}_{\mathrm{n}}^{v,v}\left(P'_{\mathrm{N}}-P'_{\mathrm{P}}\right)-\widehat{C}_{\mathrm{n}}^{v,u}\left(P'_{\mathrm{ne}}-P'_{\mathrm{nw}}\right)\right\}\Bigg] \end{aligned} \tag{5.61}$$

The northeast and northwest corner values are substituted using the corner interpolation scheme in Equation (5.47). For the control volume corners that are located on the boundary, (i.e. southeast and southwest corners), P' values are interpolated from the nearest fictitious values as follows:

$$\left.\begin{aligned} P'_{\mathrm{se}} &= f_e\ P'_{\mathrm{S}} + (1-f_e)\ P'_{\mathrm{SE}} \\ P'_{\mathrm{sw}} &= f_w\ P'_{\mathrm{SW}} + (1-f_w)\ P'_{\mathrm{S}} \end{aligned}\right\} \tag{5.62}$$

where

$$\left.\begin{aligned} f_e &= \frac{DINW_{(i+1,j_B-1)}}{DINW_{(i+1,j_B-1)}+DINE_{(i,j_B-1)}} \\ f_w &= \frac{DINW_{(i,j_B-1)}}{DINW_{(i,j_B-1)}+DINE_{(i-1,j_B-1)}} \end{aligned}\right\} \tag{5.63}$$

Applying approximation Equation (5.62) and Equation (5.47) for the northeast and north

west corners into Equation (5.61) yields:

$$\begin{aligned}
\Delta m = -\Bigg[& A_{\mathrm{e}}^{c,u}\Big\{\widehat{C}_{\mathrm{e}}^{u,u}\left(P_{\mathrm{E}}^{'}-P_{\mathrm{P}}^{'}\right)-\widehat{C}_{\mathrm{e}}^{u,v}\Big(\left(C_{ne1}P_{\mathrm{P}}^{'}+C_{ne2}P_{\mathrm{E}}^{'}+C_{ne3}P_{\mathrm{NE}}^{'}+C_{ne4}P_{\mathrm{N}}^{'}\right) \\
& -\left(f_e P_{\mathrm{S}}^{'}+(1-f_e)\,P_{\mathrm{SE}}^{'}\right)\Big)\Big\} \\
& + A_{\mathrm{e}}^{c,v}\Big\{\widehat{C}_{\mathrm{e}}^{v,v}\Big(\left(C_{ne1}P_{\mathrm{P}}^{'}+C_{ne2}P_{\mathrm{E}}^{'}+C_{ne3}P_{\mathrm{NE}}^{'}+C_{ne4}P_{\mathrm{N}}^{'}\right)-\left(f_e P_{\mathrm{S}}^{'}+(1-f_e)\,P_{\mathrm{SE}}^{'}\right)\Big) \\
& -\widehat{C}_{\mathrm{e}}^{v,u}\left(P_{\mathrm{E}}^{'}-P_{\mathrm{P}}^{'}\right)\Big\} \\
& + A_{\mathrm{w}}^{c,u}\Big\{\widehat{C}_{\mathrm{w}}^{u,u}\left(P_{\mathrm{P}}^{'}-P_{\mathrm{W}}^{'}\right)-\widehat{C}_{\mathrm{w}}^{u,v}\Big(\left(C_{nw1}P_{\mathrm{W}}^{'}+C_{nw2}P_{\mathrm{P}}^{'}+C_{nw3}P_{\mathrm{N}}^{'}+C_{nw4}P_{\mathrm{NW}}^{'}\right) \\
& -\left(f_w P_{\mathrm{SW}}^{'}+(1-f_w)\,P_{\mathrm{S}}^{'}\right)\Big)\Big\} \\
& + A_{\mathrm{w}}^{c,v}\Big\{\widehat{C}_{\mathrm{w}}^{v,v}\Big(\left(C_{nw1}P_{\mathrm{W}}^{'}+C_{nw2}P_{\mathrm{P}}^{'}+C_{nw3}P_{\mathrm{N}}^{'}+C_{nw4}P_{\mathrm{NW}}^{'}\right)-\left(f_w P_{\mathrm{SW}}^{'}+(1-f_w)\,P_{\mathrm{S}}^{'}\right)\Big) \\
& -\widehat{C}_{\mathrm{w}}^{v,u}\left(P_{\mathrm{P}}^{'}-P_{\mathrm{W}}^{'}\right)\Big\} \\
& + \left(A_{\mathrm{n}}^{c,u}\right)^{\oplus}\Big\{\widehat{C}_{\mathrm{n}}^{u,u}\Big(\left(C_{ne1}P_{\mathrm{P}}^{'}+C_{ne2}P_{\mathrm{E}}^{'}+\ C_{ne3}\ P_{\mathrm{NE}}^{'}\ +\ C_{ne4}\ P_{\mathrm{N}}^{'}\ \right) \\
& -\left(C_{nw1}P_{\mathrm{W}}^{'}+C_{nw2}P_{\mathrm{P}}^{'}+C_{nw3}P_{\mathrm{N}}^{'}+C_{nw4}P_{\mathrm{NW}}^{'}\right)\Big)-\widehat{C}_{\mathrm{n}}^{u,v}\left(P_{\mathrm{N}}^{'}-P_{\mathrm{P}}^{'}\right)\Big\} \\
& + \left(A_{\mathrm{n}}^{c,v}\right)^{\oplus}\Big\{\widehat{C}_{\mathrm{n}}^{v,v}\left(P_{\mathrm{N}}^{'}-P_{\mathrm{P}}^{'}\right)-\widehat{C}_{\mathrm{n}}^{v,u}\Big(\left(C_{ne1}P_{\mathrm{P}}^{'}+C_{ne2}P_{\mathrm{E}}^{'}+C_{ne3}P_{\mathrm{NE}}^{'}+C_{ne4}P_{\mathrm{N}}^{'}\right) \\
& -\left(C_{nw1}P_{\mathrm{W}}^{'}+C_{nw2}P_{\mathrm{P}}^{'}+C_{nw3}P_{\mathrm{N}}^{'}+C_{nw4}P_{\mathrm{NW}}^{'}\right)\Big)\Big\}\Bigg] \qquad (5.64)
\end{aligned}$$

To eliminate the boundary pressure correction, a relationship with nodal neighbouring values must be specified first. Two proper boundary conditions that can be applied for the pressure correction and inherently for the pressure are: linear extrapolation or zero change in the direction normal to the boundary. These conditions are introduced at the southwest,

south and southeast fictitious nodes as follows:

$$\left.\begin{aligned} P'_{\mathrm{SW}} =& A^{P'}_{\mathrm{P}\ (i-1,JB-1)}\, P'_{\mathrm{W}} + A^{P'}_{\mathrm{N}\ (i-1,JB-1)}\, P'_{\mathrm{NW}} \\ P'_{\mathrm{S}} =& A^{P'}_{\mathrm{P}\ (i,JB-1)}\, P'_{\mathrm{P}} + A^{P'}_{\mathrm{N}\ (i,JB-1)}\, P'_{\mathrm{N}} \\ P'_{\mathrm{SE}} =& A^{P'}_{\mathrm{P}\ (i+1,JB-1)}\, P'_{\mathrm{E}} + A^{P'}_{\mathrm{N}\ (i+1,JB-1)}\, P'_{\mathrm{NE}} \end{aligned}\right\} \tag{5.65}$$

Substituting Equation (5.65) into Equation (5.64) and collecting terms yields the modified nine-points P' equation at the south boundary. The coefficients of that equation are:

$$\begin{aligned} A^{p'}_{\mathrm{E}} = A^{c,u}_{\mathrm{e}} \Big(\widehat{C}^{u,u}_{\mathrm{e}} - \widehat{C}^{u,v}_{\mathrm{e}} \ \Big(C_{ne2} - (1-f_e)\ A^{P'}_{\mathrm{P}\ (i+1,JB-1)} \Big) \Big) \\ - A^{c,v}_{\mathrm{e}} \Big(\widehat{C}^{v,u}_{\mathrm{e}} - \widehat{C}^{v,v}_{\mathrm{e}} \ \Big(C_{ne2} - (1-f_e)\ A^{P'}_{\mathrm{P}\ (i+1,JB-1)} \Big) \Big) \\ + \Big(A^{c,u}_{\mathrm{n}} \Big)^{\oplus} \widehat{C}^{u,u}_{\mathrm{n}} C_{ne2} - \Big(A^{c,v}_{\mathrm{n}} \Big)^{\oplus} \widehat{C}^{v,u}_{\mathrm{n}} C_{ne2} \end{aligned} \tag{5.66}$$

$$\begin{aligned} A^{p'}_{\mathrm{W}} = -A^{c,u}_{\mathrm{w}} \Big(\widehat{C}^{u,u}_{\mathrm{w}} + \widehat{C}^{u,v}_{\mathrm{w}} \ \Big(C_{nw1} - f_w\, A^{P'}_{\mathrm{P}\ (i-1,JB-1)} \Big) \Big) \\ + A^{c,v}_{\mathrm{w}} \Big(\widehat{C}^{v,u}_{\mathrm{w}} + \widehat{C}^{v,v}_{\mathrm{w}} \ \Big(C_{nw1} - f_w\, A^{P'}_{\mathrm{P}\ (i-1,JB-1)} \Big) \Big) \\ - \Big(A^{c,u}_{\mathrm{n}} \Big)^{\oplus} \widehat{C}^{u,u}_{\mathrm{n}} C_{nw1} + \Big(A^{c,v}_{\mathrm{n}} \Big)^{\oplus} \widehat{C}^{v,u}_{\mathrm{n}} C_{nw1} \end{aligned} \tag{5.67}$$

$$\begin{aligned} A^{p'}_{\mathrm{N}} = \Big(A^{c,u}_{\mathrm{n}} \Big)^{\oplus} \Big(\widehat{C}^{u,u}_{\mathrm{n}} \ (C_{ne4} - C_{se3}) - \widehat{C}^{u,v}_{\mathrm{n}} \Big) - \Big(A^{c,v}_{\mathrm{n}} \Big)^{\oplus} \Big(\widehat{C}^{v,u}_{\mathrm{n}} \ (C_{ne4} - C_{se3}) - \widehat{C}^{v,v}_{\mathrm{n}} \Big) \\ - A^{c,u}_{\mathrm{e}} \widehat{C}^{u,v}_{\mathrm{e}} \Big(C_{ne4} - f_e\, A^{P'}_{\mathrm{N}\ (i,JB-1)} \Big) + A^{c,v}_{\mathrm{e}} \widehat{C}^{v,v}_{\mathrm{e}} \Big(C_{ne4} - f_e\, A^{P'}_{\mathrm{N}\ (i,JB-1)} \Big) \\ + A^{c,u}_{\mathrm{w}} \widehat{C}^{u,v}_{\mathrm{w}} \left((1-f_w)\, A2 - C_{nw3} \right) - A^{c,v}_{\mathrm{w}} \widehat{C}^{v,v}_{\mathrm{w}} \left((1-f_w)\, A2 - C_{nw3} \right) \end{aligned} \tag{5.68}$$

$$\begin{aligned} A^{p'}_{\mathrm{NE}} = -A^{c,u}_{\mathrm{e}} \widehat{C}^{u,v}_{\mathrm{e}} \Big(C_{ne3} - (1-f_e)\ A^{P'}_{\mathrm{N}\ (i+1,JB-1)} \Big) \\ + A^{c,v}_{\mathrm{e}} \widehat{C}^{v,v}_{\mathrm{e}} \Big(C_{ne3} - (1-f_e)\ A^{P'}_{\mathrm{N}\ (i+1,JB-1)} \Big) \\ + \Big(A^{c,u}_{\mathrm{n}} \Big)^{\oplus} \widehat{C}^{u,u}_{\mathrm{n}} C_{ne3} - \Big(A^{c,v}_{\mathrm{n}} \Big)^{\oplus} \widehat{C}^{v,u}_{\mathrm{n}} C_{ne3} \end{aligned} \tag{5.69}$$

$$A_{\mathrm{NW}}^{p'} = -A_{\mathrm{w}}^{c,u}\widehat{C}_{\mathrm{w}}^{u,v}\left(C_{nw4} - f_w\, A_{\mathrm{N}\ (i-1,JB-1)}^{P'}\right) + A_{\mathrm{w}}^{c,v}\widehat{C}_{\mathrm{w}}^{v,v}\left(C_{nw4} - f_w\, A_{\mathrm{N}\ (i-1,JB-1)}^{P'}\right) - \left(A_{\mathrm{n}}^{c,u}\right)^{\oplus}\widehat{C}_{\mathrm{n}}^{u,u}C_{nw4} + \left(A_{\mathrm{n}}^{c,v}\right)^{\oplus}\widehat{C}_{\mathrm{n}}^{v,u}C_{nw4} \quad (5.70)$$

$$\begin{aligned} A_{\mathrm{P}}^{p'} = {} & A_{\mathrm{e}}^{c,u}\left(\widehat{C}_{\mathrm{e}}^{u,u} + \widehat{C}_{\mathrm{e}}^{u,v}\ \left(C_{ne1} - f_e\, A_{\mathrm{P}\ (i,JB-1)}^{P'}\right)\right) \\ & - A_{\mathrm{e}}^{c,v}\left(\widehat{C}_{\mathrm{e}}^{v,u} + \widehat{C}_{\mathrm{e}}^{v,v}\ \left(C_{ne1} - f_e\, A_{\mathrm{P}\ (i,JB-1)}^{P'}\right)\right) \\ & - A_{\mathrm{w}}^{c,u}\left(\widehat{C}_{\mathrm{w}}^{u,u} - \widehat{C}_{\mathrm{w}}^{u,v}\ \left(C_{nw2} - (1-f_w)\ A_{\mathrm{P}\ (i,JB-1)}^{P'}\right)\right) \\ & + A_{\mathrm{w}}^{c,v}\left(\widehat{C}_{\mathrm{w}}^{v,u} - \widehat{C}_{\mathrm{w}}^{v,v}\ \left(C_{nw2} - (1-f_w)\ A_{\mathrm{P}\ (i,JB-1)}^{P'}\right)\right) \\ & - \left(A_{\mathrm{n}}^{c,u}\right)^{\oplus}\left(\widehat{C}_{\mathrm{n}}^{u,u}\ \left(C_{ne1} - C_{nw2}\right) + \widehat{C}_{\mathrm{n}}^{u,v}\right) \\ & + \left(A_{\mathrm{n}}^{c,v}\right)^{\oplus}\left(\widehat{C}_{\mathrm{n}}^{v,u}\ \left(C_{ne1} - C_{nw2}\right) + \widehat{C}_{\mathrm{n}}^{v,v}\right) \end{aligned} \quad (5.71)$$

$$b_{\mathrm{P}}^{p'} = (A_{\mathrm{e}}^{c,u}U_{\mathrm{e}}^{*} + A_{\mathrm{e}}^{c,v}V_{\mathrm{e}}^{*}) + (A_{\mathrm{w}}^{c,u}U_{\mathrm{w}}^{*} + A_{\mathrm{w}}^{c,v}V_{\mathrm{w}}^{*}) + (A_{\mathrm{n}}^{c,u}U_{\mathrm{n}}^{*} + A_{\mathrm{n}}^{c,v}V_{\mathrm{n}}^{*}) + (A_{\mathrm{s}}^{c,u}U_{\mathrm{s}}^{*} + A_{\mathrm{s}}^{c,v}V_{\mathrm{s}}^{*}) + b_{\mathrm{P}}^{c} = -\dot{m}_e + \dot{m}_w - \dot{m}_n + \dot{m}_s + b_{\mathrm{P}}^{c} \quad (5.72)$$

Because the southwest, south, and southeast P' are already expressed implicitly, the coefficients $A_{\mathrm{SW}}^{P'}$, $A_{\mathrm{S}}^{P'}$ and $A_{\mathrm{SE}}^{P'}$ are set to zero. For domain corners, two additional coefficients are set to zero after implementing the boundary condition. For instance, at the southwest corner, $A_{\mathrm{W}}^{P'}$ and $A_{\mathrm{NW}}^{P'}$ are also set to zero.

Equation (4.100) is used to write a governing equation for the pressure correction in the liquid side of the interface. The equation takes the following compact algebraic form

$$A_{\mathrm{P}}^{P'}\ P_{\mathrm{P}}' = A_{\mathrm{N}}^{P'}\ P_{\mathrm{N}}' + b_{\mathrm{P}}^{P'} \quad (5.73)$$

where

$$
\begin{aligned}
A_{\mathrm{P}}^{P'} &= 1 \qquad A_{\mathrm{N}}^{P'} = 1 \\
b_{\mathrm{P}}^{P'} &= +2\ \mu_L \left(n_{xn}^2 A_{x1} + n_{xn} n_{yn} A_{y1}\right) U_S + 2\ \mu_L \left(n_{xn} n_{yn} A_{x1} + n_{yn}^2 A_{y1}\right) V_S \\
&\quad + 2\ \mu_L \left(n_{xn}^2 A_{x2} + n_{xn} n_{yn} A_{y2}\right) U_P + 2\ \mu_L \left(n_{xn} n_{yn} A_{x2} + n_{yn}^2 A_{y2}\right) V_P \\
&\quad + 2\ \mu_L \left(n_{xn}^2 A_{x3} + n_{xn} n_{yn} A_{y3}\right) U_E + 2\ \mu_L \left(n_{xn} n_{yn} A_{x3} + n_{yn}^2 A_{y3}\right) V_E \\
&\quad + 2\ \mu_L \left(n_{xn}^2 A_{x4} + n_{xn} n_{yn} A_{y4}\right) U_W + 2\ \mu_L \left(n_{xn} n_{yn} A_{x4} + n_{yn}^2 A_{y4}\right) V_W \\
&\quad - 2\ \mu_M \left(n_{xs}^2 B_{x1} + n_{xs} n_{ys} B_{y1}\right) U_{NN} - 2\ \mu_M \left(n_{xs} n_{ys} B_{x1} + n_{ys}^2 B_{y1}\right) V_{NN} \\
&\quad - 2\ \mu_M \left(n_{xs}^2 B_{x2} + n_{xs} n_{ys} B_{y2}\right) U_N - 2\ \mu_M \left(n_{xs} n_{ys} B_{x2} + n_{ys}^2 B_{y2}\right) V_N \\
&\quad - 2\ \mu_M \left(n_{xs}^2 B_{x3} + n_{xs} n_{ys} B_{y3}\right) U_{NE} - 2\ \mu_M \left(n_{xs} n_{ys} B_{x3} + n_{ys}^2 B_{y3}\right) V_{NE} \\
&\quad - 2\ \mu_M \left(n_{xs}^2 B_{x4} + n_{xs} n_{ys} B_{y4}\right) U_{NW} - 2\ \mu_M \left(n_{xs} n_{ys} B_{x4} + n_{ys}^2 B_{y4}\right) V_{NW} \\
&\quad + \left(P_{\mathrm{N}} - P_{\mathrm{P}}\right)
\end{aligned}
\tag{5.74}
$$

The algebraic analogous of Equation (4.120) (zero normal direction pressure gradient), is used for the pressure correction at $j = j_{BM} - 1$. It becomes

$$
A_{\mathrm{P}}^{P'}\ P_{\mathrm{P}}' = A_{\mathrm{E}}^{P'}\ P_{\mathrm{E}}' + A_{\mathrm{W}}^{P'}\ P_{\mathrm{W}}' + A_{\mathrm{N}}^{P'}\ A_{\mathrm{N}}^{P'} + b_{\mathrm{P}}^{P'} \tag{5.75}
$$

where

$$
\left.
\begin{aligned}
A_{\mathrm{P}}^{P'} &= \left[D_{x1}\ n_{xn} + D_{y1}\ n_{yn}\right] & A_{\mathrm{E}}^{P'} &= -\left[D_{x2}\ n_{xn} + D_{y2}\ n_{yn}\right] \\
A_{\mathrm{W}}^{P'} &= -\left[D_{x3}\ n_{xn} + D_{y3}\ n_{yn}\right] & A_{\mathrm{N}}^{P'} &= -\left[D_{x4}\ n_{xn} + D_{y4}\ n_{yn}\right] \\
A_{\mathrm{NE}}^{P'} &= 0 & A_{\mathrm{NW}}^{P'} &= 0 \\
A_{\mathrm{SE}}^{P'} &= 0 & A_{\mathrm{SW}}^{P'} &= 0 \\
A_{\mathrm{S}}^{P'} &= 0 & & \\
b_{\mathrm{P}}^{P'} &= \left.\frac{\partial P}{\partial n}\right|_{int,M} = A_{\mathrm{E}}^{P'}\ P_{\mathrm{E}} + A_{\mathrm{W}}^{P'}\ P_{\mathrm{W}} + A_{\mathrm{N}}^{P'}\ P_{\mathrm{N}} - A_{\mathrm{P}}^{P'}\ P_{\mathrm{P}} = 0 & &
\end{aligned}
\right\}
\tag{5.76}
$$

5.2 Interface Moving Strategies

A significant contribution of this work is the development of a precise phase interface tracking scheme. The non-orthogonal mesh lines are moved at each time step to coincide precisely with the liquid-mixture interface. The approach used in this work is an adaptive-grid Eulerian method. The governing equations are first solved on a fixed mesh, then the new interface location is determined, followed by a re-generation of the mesh. This section describes the ILMB method used to determine the new phase interface location.

5.2.1 Integral liquid mass balance (ILMB)

At each column of the liquid region, the film thickness is calculated by performing a mass balance at the end of each time step on the column of liquid at index i shown shaded in Figure 5.1. This principle can be illustrated by Equation (5.77) which states that the total mass flow rate that crosses the control volumes through all the west faces and the condensate mass flow rate crossing the interface must equal the total mass flow rate that leaves the column from all the east faces. The interface height $h_{L,i}$ is defined at the east faces of the liquid column at i. The balance on a liquid column at index i can be written as:

$$\underbrace{\Delta z \int_0^{h_{L,i-1}} \rho_L \left(\overrightarrow{V}\cdot\hat{n}\right)_w d\xi}_{\dot{m}_w} + \underbrace{\dot{m}_{\text{cond}}}_{\text{mass crossing the interface}} \underbrace{-\Delta z \int_0^{h_{L,i}} \rho_L \left(\overrightarrow{V}\cdot\hat{n}\right)_e d\xi}_{\dot{m}_e} = 0 \tag{5.77}$$

This integral relation can be converted to numerical integral by using a single integration point at each face of the control volume.

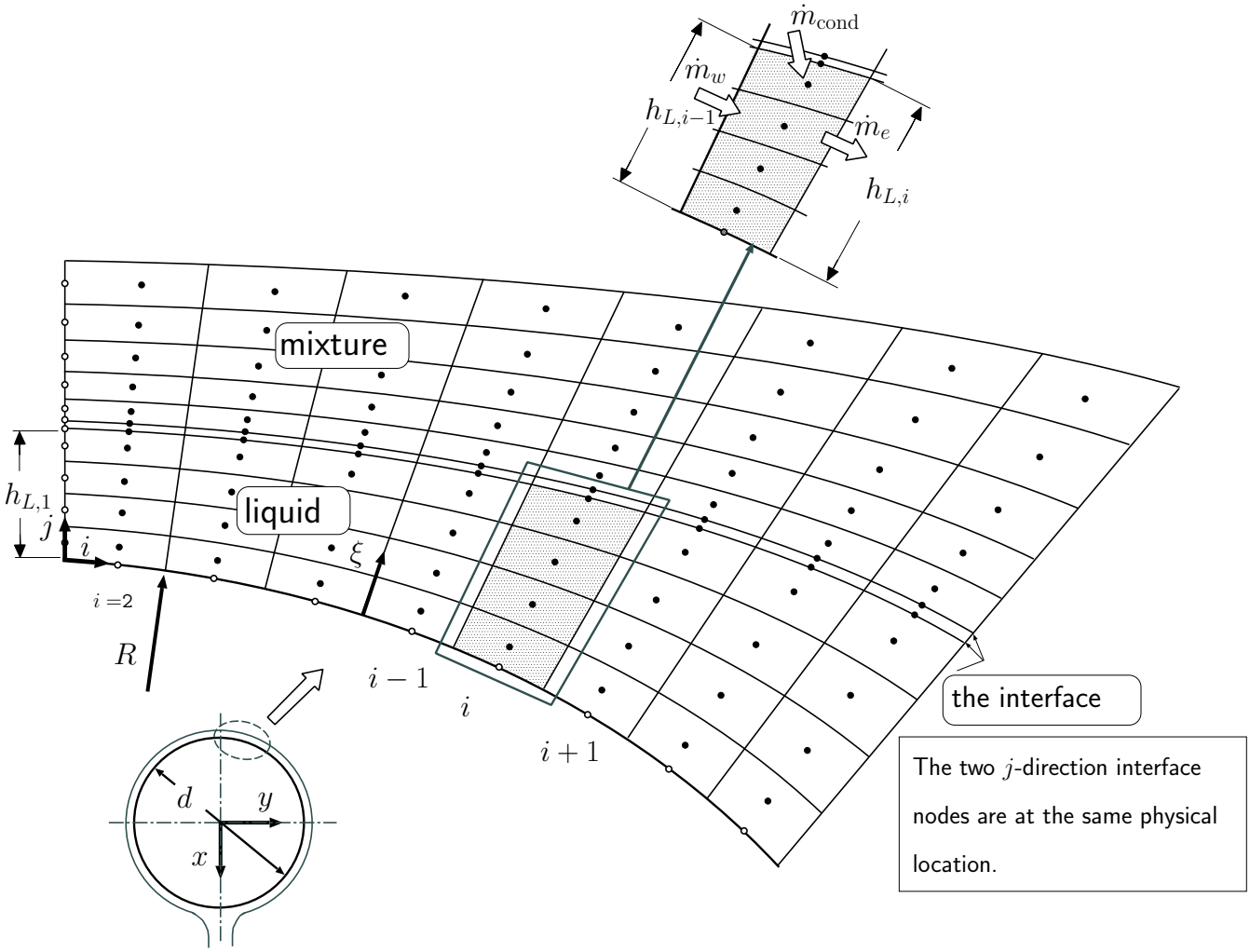

Figure 5.1: Nomenclature used in the ILMB method. The interface node spacing is exaggerated for illustration purposes.

$$\Delta z \sum_{j=j_{BL}}^{j_{EL}} \rho_w \left(U_{\text{w}}\, n_{xw} + V_{\text{w}}\, n_{yw}\right) \Delta\xi_w + \dot{m}_{\text{cond}} - \Delta z \sum_{j=j_{BL}}^{j_{EL}} \rho_e \left(U_{\text{e}}\, n_{xe} + V_{\text{e}}\, n_{ye}\right) \Delta\xi_e = 0 \quad (5.78)$$

For uniform grid spacing in the ξ direction ($h_{L,i} = N_{y,L}\,\Delta\xi_e$) in the liquid region and after rearrangement, the following equation is written for $h_{L,i}$ for unit depth (i.e. $\Delta z = 1$).

$$\frac{1}{N_{y,L}}\left[\sum_{j=j_{BL}}^{j_{EL}}\rho_e\ \left(U_{\mathrm{e}}\ n_{xe}+V_{\mathrm{e}}\ n_{ye}\right)\right]\ h_{L,i}=\frac{1}{N_{y,L}}\left[\sum_{j=j_{BL}}^{j_{EL}}\rho_w\ \left(U_{\mathrm{w}}\ n_{xw}+V_{\mathrm{w}}\ n_{yw}\right)\right]\ h_{L,i-1}+\dot{m}_{\mathrm{cond}} \tag{5.79}$$

The resulting equation connects the interface heights at i and $i-1$. The location of the interface at the second station, $(h_{L,2})$, is calculated by conducting a simple mass balance along the first liquid column. In conformity with the symmetry condition above the tube, the location of the interface at the first station is set equal to $h_{L,2}$. Then, the location of the interface at the successive stations can be found by a forward marching along the index i direction, starting at $i=2$. The interface height normal to the tube wall, δ, can be calculated at each point along the interface. The interface movement can be relaxed by introducing an under-relaxation factor γ_δ according to the following equation:

$$h_L{}^{new}=\gamma_\delta\, h_{L,i}{}^{new}+(1-\gamma_\delta)\ h_{L,i}{}^{old} \tag{5.80}$$

Tests indicated that under-relaxation is necessary for flows around tubes and rarely needed for flows along flat surfaces. The typical values for γ_δ ranges from 0.1 to 0.3.

5.3 Velocity Fields Initial Guess

To start the numerical simulation, an initial guess for the solution fields and the interface location should be specified. In general, the proper selection of the initial guess enables smooth start of the numerical simulation and faster achievement of the final solution. The initial guess becomes even more important in two-phase flow problems with a moving interface in a complex geometry. Improper initial guess could lead to irreversible sharp changes in the interface profile and the velocity fields in the liquid film at the tube bottom. These sharp changes may lead to divergence.

Taking into account the importance of the initial guess on the performance of the numerical solution procedure, a sophisticated initial guess for the velocity fields in the liquid film was developed in this work. The scheme presented for the velocity field initial guess is based on observations on the preliminary solutions of thin liquid film flows around a horizontal tube.

First, the interfacial tangential velocity at the middle of the tube is guessed. The typical value for the guessed interfacial tangential velocity at the middle of the tube revolves around $5 \times 10^{-2}\,\mathrm{m/s}$. This value is based on accumulative experience through out this work with falling liquid film and condensation over a vertical wall. Then, the value of the interfacial tangential velocity decreases gradually toward the top of the tube to reach zero at the top vertical symmetry line. For the lower part of the tube, the value of the interfacial tangential velocity increases linearly up to a factor of twice the guessed value by the bottom of the tube. The interface velocity is set constant for the rest of the domain. Next, a linear velocity profile is constructed in the liquid at each station assuming $U = V = 0$ at the tube wall.

A linear profile is used as an initial guess for the temperature in the liquid film. At the interface, value of the temperature is T_{sat} while at the south boundary the temperature is set to the wall value T_{w} for both the liquid film around the tube and in the falling film region.

Experience has shown that there is no need to use a customized initial guess in the mixture zone. Therefore, the inlet conditions are specified as an initial guess for all fields in the mixture.

5.4 Velocity Coupling at the Interface

In each time step, the solution of the U and V velocity components is performed separately for the whole domain. Solving U and V equations separately causes a disconnect in the interface conditions. Therefore, the interfacial conditions in Equation (2.12) to Equation (2.15) are

enforced again simultaneously by solving for U and V velocity components coupled at the interface. It was found that coupling U and V equations at the interface is crucial to avoid any possibility for discontinuity in enforcing the interfacial conditions that might be inherited due to the segregated nature of the SIMPLEC method. The coupled equation for conditions in Equation (2.12) to Equation (2.15) can be written as follows:

$$\begin{pmatrix} A_{\mathrm{PL}}^{UL,UL} & A_{\mathrm{PL}}^{UL,VL} & A_{\mathrm{PM}}^{UL,UM} & A_{\mathrm{PM}}^{UL,VM} \\ A_{\mathrm{PL}}^{VL,UL} & A_{\mathrm{PL}}^{VL,VL} & A_{\mathrm{PM}}^{VL,UM} & A_{\mathrm{PM}}^{VL,VM} \\ A_{\mathrm{PL}}^{UM,UL} & A_{\mathrm{PL}}^{UM,VL} & A_{\mathrm{PM}}^{UM,UM} & A_{\mathrm{PM}}^{UM,VM} \\ A_{\mathrm{PL}}^{VM,UL} & A_{\mathrm{PL}}^{VM,VL} & A_{\mathrm{PM}}^{VM,UM} & A_{\mathrm{PM}}^{VM,VM} \end{pmatrix} \begin{pmatrix} U_{\mathrm{L,P}} \\ V_{\mathrm{L,P}} \\ U_{\mathrm{M,P}} \\ V_{\mathrm{M,P}} \end{pmatrix} = \begin{pmatrix} A_{\mathrm{EL}}^{UL,UL} & A_{\mathrm{EL}}^{UL,VL} & A_{\mathrm{EM}}^{UL,UM} & A_{\mathrm{EM}}^{UL,VM} \\ A_{\mathrm{EL}}^{VL,UL} & A_{\mathrm{EL}}^{VL,VL} & A_{\mathrm{EM}}^{VL,UM} & A_{\mathrm{EM}}^{VL,VM} \\ A_{\mathrm{EL}}^{UM,UL} & A_{\mathrm{EL}}^{UM,VL} & A_{\mathrm{EM}}^{UM,UM} & A_{\mathrm{EM}}^{UM,VM} \\ A_{\mathrm{EL}}^{VM,UL} & A_{\mathrm{EL}}^{VM,VL} & A_{\mathrm{EM}}^{VM,UM} & A_{\mathrm{EM}}^{VM,VM} \end{pmatrix} \begin{pmatrix} U_{\mathrm{L,E}} \\ V_{\mathrm{L,E}} \\ U_{\mathrm{M,E}} \\ V_{\mathrm{M,E}} \end{pmatrix}$$

$$+ \begin{pmatrix} A_{\mathrm{WL}}^{UL,UL} & A_{\mathrm{WL}}^{UL,VL} & A_{\mathrm{WM}}^{UL,UM} & A_{\mathrm{WM}}^{UL,VM} \\ A_{\mathrm{WL}}^{VL,UL} & A_{\mathrm{WL}}^{VL,VL} & A_{\mathrm{WM}}^{VL,UM} & A_{\mathrm{WM}}^{VL,VM} \\ A_{\mathrm{WL}}^{UM,UL} & A_{\mathrm{WL}}^{UM,VL} & A_{\mathrm{WM}}^{UM,UM} & A_{\mathrm{WM}}^{UM,VM} \\ A_{\mathrm{WL}}^{VM,UL} & A_{\mathrm{WL}}^{VM,VL} & A_{\mathrm{WM}}^{VM,UM} & A_{\mathrm{WM}}^{VM,VM} \end{pmatrix} \begin{pmatrix} U_{\mathrm{L,W}} \\ V_{\mathrm{L,W}} \\ U_{\mathrm{M,W}} \\ V_{\mathrm{M,W}} \end{pmatrix} + \begin{pmatrix} b_{\mathrm{L,W}}^{U} \\ b_{\mathrm{L,W}}^{V} \\ b_{\mathrm{M,W}}^{U} \\ b_{\mathrm{M,W}}^{V} \end{pmatrix} \tag{5.81}$$

As indicated in Equation (5.81), each coefficient element consists of 4x4 matrix. The variables are vectors with four unknowns, $U_{\mathrm{L}}, V_{\mathrm{L}}, U_{\mathrm{M}}$ and V_{M}, at either P, E or W. Terms that involve variables outside the computational molecule for the coupled approach are lagged in the right hand side term. A specific nomenclature is followed in this section. For the 4x4 matrices, the first two letters in the superscripts of each entry refer to the variable for which the equation is assigned. The last two letters in the superscripts indicate the variable to which the coefficient is multiplied. The subscripts consists of two letters referring to the position of the variable in the computational molecule and the phase. The scheme for assigning interfacial conditions

to U and V velocity components that is explained in Section 4.4 was used. The resulting coupled set of equations forms a linear system with a block tridiagonal coefficient matrix. Each element in the coefficients matrix is 4x4 matrix. A direct solver based on the Block Tridiagonal Matrix Algorithm TDMA was developed to solve this set of equations.

5.5 Solution Algorithm

The main steps of the numerical solution procedure can be summarised in sequence as follows:

1. Start with an initial guess of the interface location (to generate the grid) and a guess for the velocity, temperature, gas mass fraction, and pressure fields.
2. Calculate all coefficients based on the most recent fields.
3. Solve the two momentum equations implicitly and separately for the whole domain (each for both phases at once).
4. Solve for U and V coupled along the interface.
5. Solve for $P^{'}$ implicitly for the whole domain.
6. Correct solution fields (U, V and P) as well as the face velocities.
7. Solve for T implicitly for the whole domain.
8. Solve for W implicitly for the mixture region.
9. Move the interface using the ILMB strategy.
10. Generate a new grid based on the most recent location of the interface.
11. Repeat Steps 2 to 10 until steady-state convergence is obtained.

5.6 Solving the Linearized Elliptic Equations

For each flow variable, the corresponding algebraic conservation equation, that is derived from an elliptic PDE, is applied at all nodes of the computational domain. The arising set of algebraic equations forms a linear system of the form:

$$[A]\{\phi\} = \{b\} \tag{5.82}$$

Where $[A]$ is the coefficient matrix, $\{\phi\}$ is the solution vector and $\{b\}$ is the right hand side vector. For non-orthogonal 2D grids, the coefficient matrix consists of nine diagonals of non-zero elements while the rest of the matrix is zeroes. This type of sparse matrix is referred to as a nine-banded matrix. Solving such a system of equations with a direct solution procedure, such as Gaussian Elimination or LU Decomposition schemes is very costly and often impractical for large numbers of nodes. Moreover, because the governing equations are non-linear and coupled, iteration is required and therefore solving the linearized form of the equations very accurately at each time step is usually not justified economically.

Many iterative solution procedures are available that take advantageous of the known structure of the coefficient matrix. In addition to the significant reduction in the computational cost, iterative schemes suit better the iterative nature of the solution procedure.

In this work, significant testing of iterative solvers was performed to find a robust and economical solution to the sets of algebraic equations. Three iterative solvers were implemented.

1. Peric's Nine Points Solver (LR and RL) [61]
2. GMRES (Krylov subspace solver) [62]
3. Modified Strongly Implicit Procedure (MSI) [63]

Preliminary tests showed that the MSI solver is more robust than the Peric's solver. For the computation cost, both the MSI and Peric's have comparable computational cost. The

computational cost of using the GMRES solver is much higher than that for the MSI solver. Therefore, the MSI solver was used for all the results presented in Chapters 6 and 7.

5.7 Convergence Criteria

5.7.1 Linearized Equations Convergence

Iterative solution of the algebraic equation set for variable ϕ, for example, involves repeated application of the solver algorithm until a stopping condition is met. The stopping condition can be a maximum iteration count or a residual reduction target.

The residual vector, $\{R\}$, at the n^{th} iteration and the absolute sum of its elements [61] are defined in Equations (5.83) and (5.84) respectively.

$$\{R^{\mathrm{n}}\} = \{b\} - [A]\,.\,\{\phi^{\mathrm{n}}\} \tag{5.83}$$

$$R^{\mathrm{n}} = \sum_{k}^{N_x * N_y} |R_k^{\mathrm{n}}| \tag{5.84}$$

The iteration may be stopped when

$$\frac{R^{\phi,\mathrm{n}}}{R^{\phi,0}} \leq R^{\phi}_{spec} \tag{5.85}$$

where $R^{\phi,0}$ is the absolute sum of the residual vector elements before starting the solution process and R^{ϕ}_{spec} is a specified residual reduction factor. For most of the cases considered in this work, the specified residual reduction factors for each variable were: $R^{U}_{spec} = 1\times10^{-3}$, $R^{V}_{spec} = 1\times10^{-3}$, $R^{P}_{spec} = 1\times10^{-5}$, $R^{T}_{spec} = 1\times10^{-5}$ and $R^{W}_{spec} = 1\times10^{-5}$.

5.7.2 Global Steady State Convergence

For each flow variable field, the range-normalised maximum change convergence test was used to check for convergence at all nodal points. In this test, numerical solution for a flow

variable ϕ, ($\phi = U$, V, P, T and W), is considered to be a fully converged when values of ϕ at all control volumes satisfy the following inequality:

$$\left| \frac{\phi^{\text{new}} - \phi^{\text{old}}}{\phi^{\text{new}}_{\text{max}} - \phi^{\text{new}}_{\text{min}}} \right| \leq \epsilon^{\phi}_{\text{ss}} \tag{5.86}$$

In addition, convergence of the interface height at all locations was investigated using the relative difference convergence test as follows:

$$\left| \frac{\delta^{\text{new}} - \delta^{\text{old}}}{\delta^{\text{old}}} \right| \leq \epsilon^{\delta}_{\text{ss}} \tag{5.87}$$

In this work, fully converged solution was considered when both all flow fields and interface height satisfy convergence criteria give in Equations (5.86) and (5.87) respectively. The chosen criteria values were: $\epsilon^{u}_{\text{ss}} = 5\times10^{-6}$, $\epsilon^{v}_{\text{ss}} = 5\times10^{-6}$, $\epsilon^{p}_{\text{ss}} = 1\times10^{-5}$, $\epsilon^{t}_{\text{ss}} = 1\times10^{-6}$ and $\epsilon^{w}_{\text{ss}} = 1\times10^{-6}$. For the interface height, $\epsilon^{\delta}_{\text{ss}}$ was set to 1×10^{-5}. At convergence, however, the maximum relative change of the interface height was $\leq 5\times10^{-6}$.

Chapter 6

Comparison with Previous Work

6.1 Introduction

The numerical model was implemented in an in-house computer code using FORTRAN 95 with double precision. The code was developed in successive steps in order to eventually model condensation over a horizontal tube. After each step, the validity of the current model was examined by solving suitable steady-state two-phase problems such as stratified flows in horizontal channels, falling liquid film along vertical walls, and condensation of steam in steam-air mixtures in a vertical channel. The accuracy of the generated results from the current numerical model were validated against the available relevant analytical, numerical, and experimental results in the literature.

In this chapter, very brief summaries of the key tests made during the process of code development are given for isothermal two-phase flows followed by a detailed comparison for steam condensation in steam-air mixtures in a vertical channel. Because the goal was to verify the functionality of the code, the results of these tests are not necessarily grid independent. Then, selection of the domain and grid sizes and validity examination of the current results for condensation of steam from pure steam and steam-air mixture on a horizontal tube are discussed in detail.

6.2 Development of the Code

In the early stages of the code development, the current model was applied to two two-phase problems that include a flat wall. The first test was 2D stratified flow in a horizontal parallel plate channel in which both liquid water and air enter with uniform velocity profiles at one

end of the channel. At the channel outlet, fully-developed flow conditions are assumed. The channel length and height are 2.0 m and 0.01 m respectively. The liquid water enters with a uniform velocity of $U_{in,L} = 0.2$ m/s and height of 5×10^{-3}m. The air enters with uniform velocity profile of $U_{in,G} = 0.60284$ m/s. Both fluids' properties were evaluated at 20°C. The grid was constructed of two panels, one panel for each fluid, with each panel made up of $N_x = 80$ along the flow direction. There were 20 equally spaced control volumes in the transverse direction (y) in each panel. For fully-developed stratified flow, there exists an analytical solution that predicts the equilibrium liquid height and the velocity profile for both fluids [64]. The results from the current model were compared against the analytical solution at the channel outlet. The percentage of deviation from the analytical solution at the channel outlet was about (0.66%) for the interface height and 0.9% for the velocity profile at the peak in the gas region.

Second isothermal two-phase test problem was that of a falling thin liquid film over a vertical wall. The results from the current model were validated against those of the theoretical model of Rahman et al. [65], an analytical solution for the fully-developed film thickness, the laminar film flow experiments of Cook and Clark [66], and the numerical model of Ruschak and Weinstein [67]. In general, good agreements were observed. Details of this study can be found in [68].

The current model was also compared against the parabolic numerical model of Siow [45] for film condensation from a steam-air mixture in a vertical parallel plate channel with isothermal walls. Siow's model is based on the boundary layer assumptions. The problem domain and specification are defined in Figure 6.1. A steam-air mixture enters with uniform velocity at the top of the domain. Numerous tests were conducted and sample of three of the cases is presented here. For these three cases $\Delta T = 1$, 5, and 20 K. The other problem parameters are $P_{\text{in}} = 100\,k\text{Pa}$, $W_{\text{in}} = 0.1$ and $\text{Re}_H = 500$. The Re_H for the problem was defined as $\text{Re}_H = \frac{4\rho_M U_{\text{in}} H}{\mu_M}$. Because the domain is symmetric about the centre line, only one half of the domain was modeled. A no-slip condition was prescribed at the wall and

fully developed conditions were prescribed at the exit. Zero normal gradients for U, T, and W and $V = 0$ were prescribed at $y = H$.

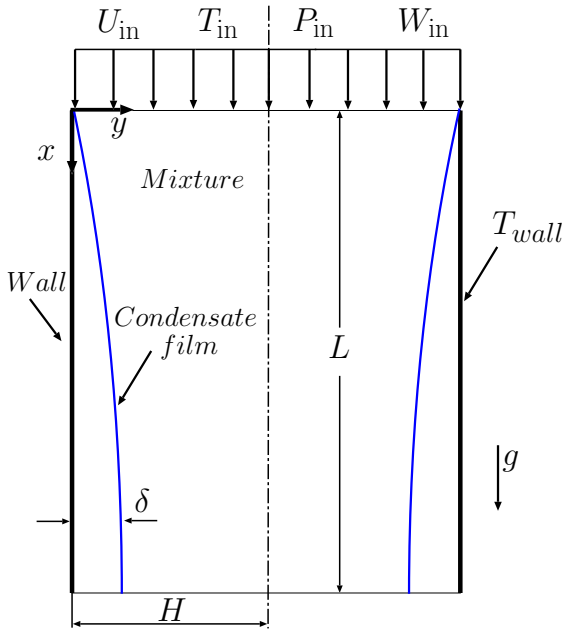

Figure 6.1: Laminar Film condensation in a vertical channel: Domain definition.

The solution domain dimensions are $L = 0.25$ m and $H = 2.5 \times 10^{-3}$ m. A grid size of 100×80 ($N_x \times N_y$) was used with 20 control volumes in the liquid region. The grid expands away from the channel entrance with a geometric expansion factor of $r_x = 1.03$ to accurately capture the interface height at the inlet. At the interface, the grid in the mixture region expands in the y direction with a factor of $r_y = 1.1$ to capture the high gradients at the interface.

Figure 6.2 compares the liquid film thickness predictions of the current model and the Siow model for the three cases. The vertical axis represents the film thickness normalised by half width of the channel and the horizontal axis represents the dimensionless axial distance, x/H. The results of the two models are indistinguishable for $\Delta T = 1$ K and 5 K. For $\Delta T = 20$ K, there is a slight difference for $x/H < 30$. The maximum deviation in the film

thickness is 1.75% in this region.

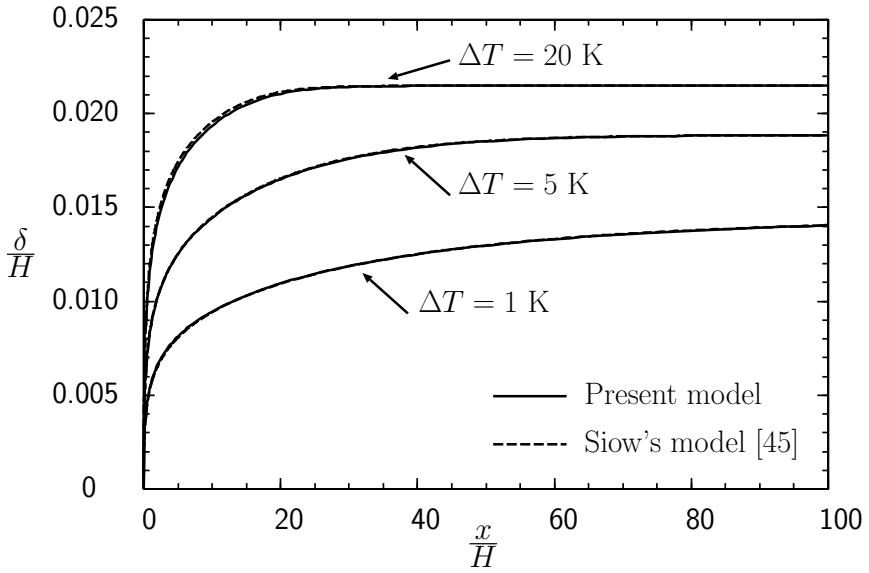

Figure 6.2: Comparison with Siow's model: effect of ΔT on film thickness (δ).

Figure 6.3 shows the gas mass fraction profiles along the the interface for the three cases. Except for very insignificant differences for $\Delta T = 20$ K near the channel inlet, the predictions of the current model are in very good agreement with the parabolic model.

Figures 6.4 and 6.5 compare the U velocity profiles for respectively the liquid film and the mixture at certain axial locations along the channel . To differentiate between the two phases and clearly present the results, a transformed coordinate η in the y direction, defined in Equation (6.1), was used. According to Equation (6.1), $\eta = 0$ at the wall, $\eta = 1$ at the interface, and $\eta = 2$ at the centre of the channel.

$$\begin{aligned} \eta &= \frac{y}{\delta} & 0 \leq\ y\ &\leq\ \delta \\ \eta &= \frac{y-\delta}{H-\delta} + 1 & \delta \leq\ y\ &\leq\ H \end{aligned} \tag{6.1}$$

The profiles from both models are plotted at approximately the same axial locations. Comparing the profiles at exactly the same axial locations is not available because Siow's code

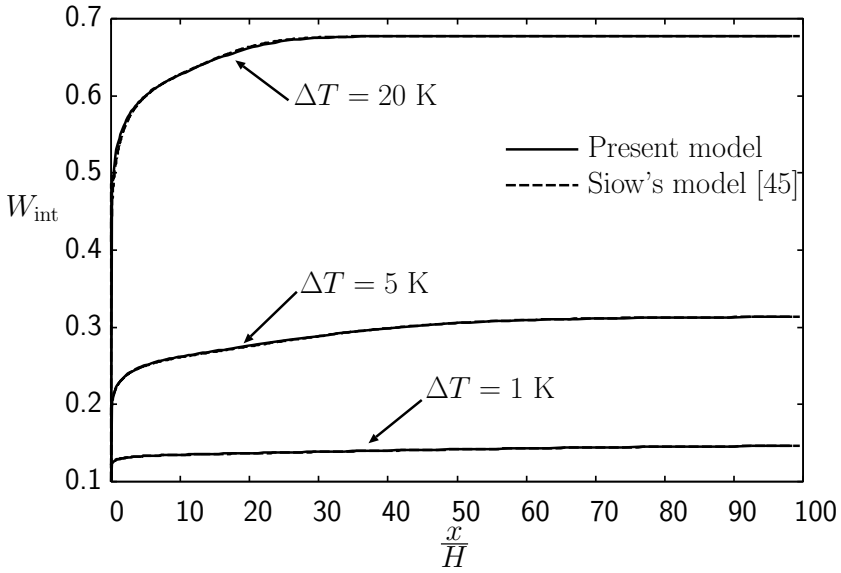

Figure 6.3: Comparison with Siow's model: gas mass fraction along the interface (W_{int}).

prints out the results at only locations where nodal values are available. Matching the nodal locations with the current code was not possible. In Figures 6.4, noticeable differences between the results of the two models can be seen near the duct inlet. These differences are believed to be due to mainly the slightly mismatched axial locations. For the mixture, the differences increase towards the centre line of the channel. This can be attribute to the fundamental differences between the current elliptic model and the parabolic model of Siow [45] that is based on the boundary layer assumptions. However, the differences in the U profiles for both regions diminish in the x direction and the two results coincide at the end of the channel where fully-developed conditions are encountered. Similar trends can be seen for the temperature and the gas mass fraction profiles in Figures 6.6 and 6.7, respectively. The uniform profiles of T and W at the end of the channel indicate the end of the condensation region.

Figure 6.8 shows the pressure profiles versus η at different axial locations. The profiles are uniform and in good agreement except at the channel inlet where slight differences can be seen. The non-uniform profile of the present model is due to the axial development of

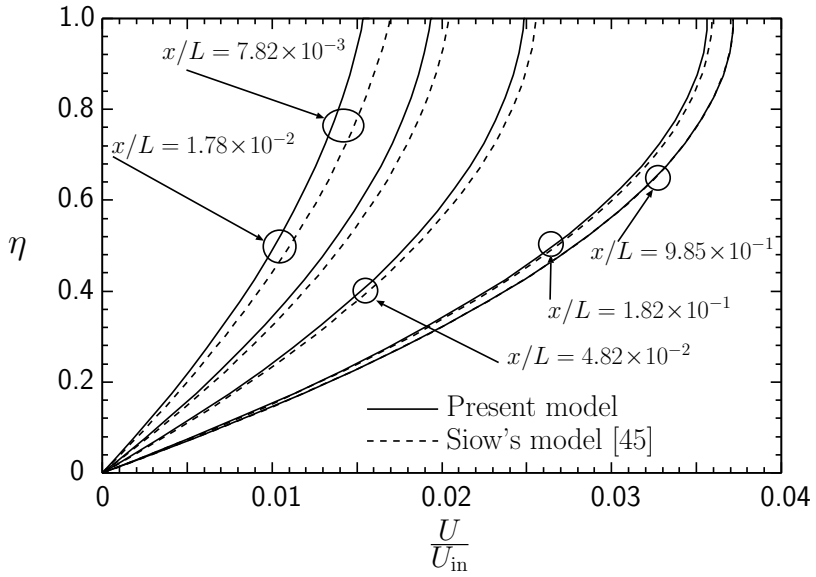

Figure 6.4: Comparison with Siow's model: the U velocity profiles in the liquid film at different axial locations for $\Delta T = 20$ K.

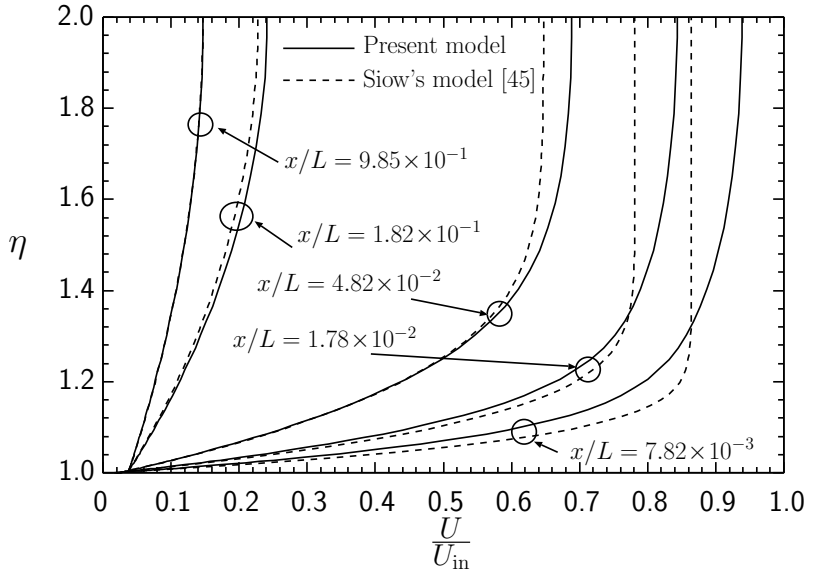

Figure 6.5: Comparison with Siow's model: the U velocity profiles in the mixture at different axial locations for $\Delta T = 20$ K.

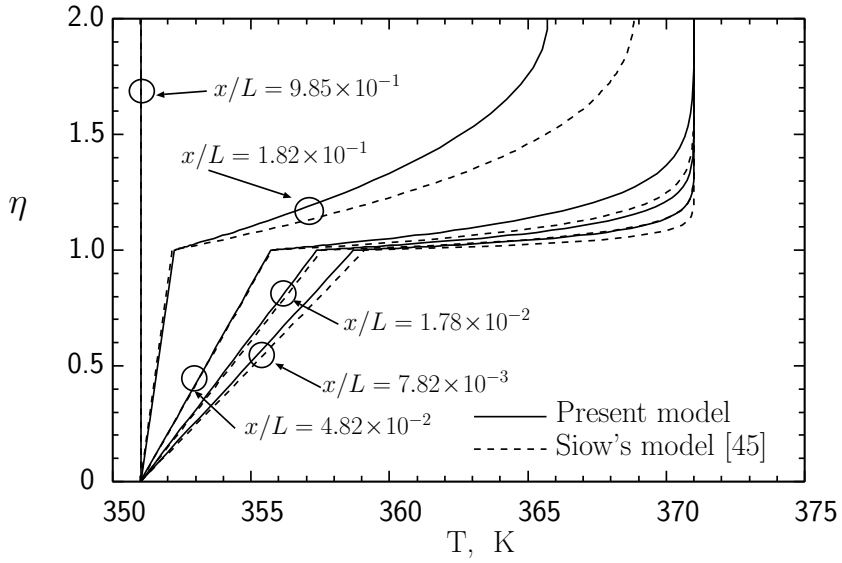

Figure 6.6: Comparison with Siow's model: temperature profiles at different axial locations for $\Delta T = 20$ K.

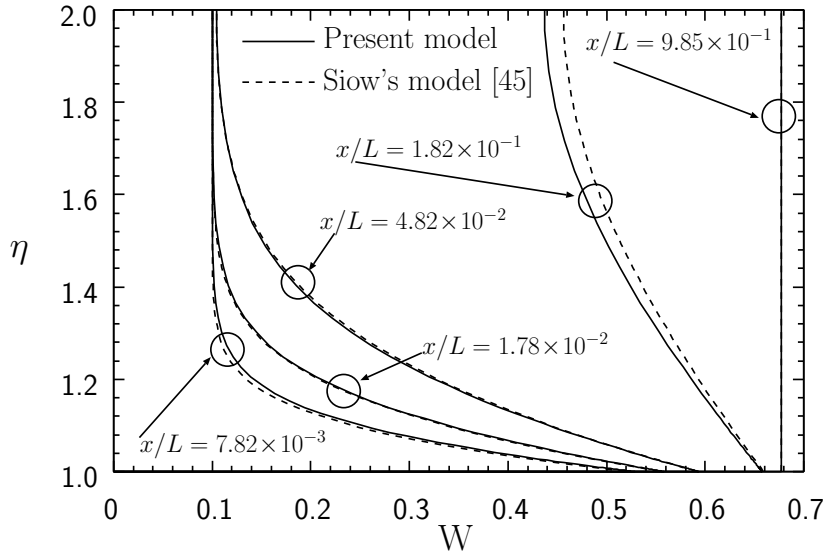

Figure 6.7: Comparison with Siow's model: gas mass fraction profiles at different axial locations for $\Delta T = 20$ K.

the mixture flow from the uniform inlet profile. The small differences in the pressure in the transverse direction have negligible effect on the condensation process.

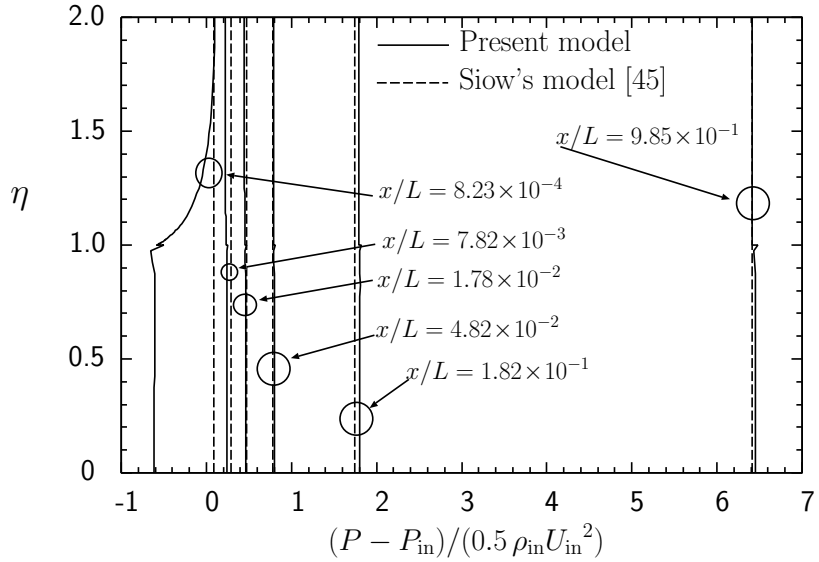

Figure 6.8: Comparison with Siow's model: pressure profiles at different axial locations for $\Delta T = 20$ K.

6.3 Domain size Selection

For condensation over a horizontal tube, the extent of the solution domain was determined through a series of tests that examined the effect of the boundary placement on the flow solution. The tests were conducted for the case of water vapour with an inlet pressure of 1 atm, $\mathrm{Re}_d = 100$, and $\Delta T = 20$ K. A single tube with 14mm O.D. was used in all the tests during this work. Six different domain sizes ranging from $6d$ to $20d$ in width and $10d$ to $16d$ in length from the centre of the tube to the domain outlet (see Figure 3.7) were tested. In those tests, the grid sizes ranged from 380×160 ($N_x \times N_y$) for the smallest domain to 420×320 ($N_x \times N_y$) for the largest domain. All the grids have 20 control volumes in the j direction in the liquid film and 40 control volumes in the j direction in the vapour panels that are adjacent to the liquid film. There were 180 control volumes around the tube in the i direction to maintain the same grid quality in the vicinity of the tube.

Domain dimensions of $16d$ in width and $12d$ in length below the centre of the tube were found to be sufficient. For that domain size, change in the U before the outlet boundary was within -0.025% of the exit value. The maximum change in the U velocity at the free stream boundaries were found to be within -0.08% of the U value at the boundary. This maximum value occurs at the location where the circular shape of free-steam boundary 1 connects to free-stream boundary 2 (see Figure 2.1). Further increase in the domain dimensions had negligible effect on the solution.

6.4 Grid Selection

The grid dependence of the solution was examined by varying the number of nodes in the i direction, N_x, from 380 to 600 and the number of nodes in the j direction, N_y, from 250 to 370 using eight grids. Those grids are A, B, B2, C, C2, D, D2, and E. The case of steam condensation at 1 atm, $\mathrm{Re}_d = 100$, and $\Delta T = 20$ K over a 14mm O.D. tube was considered

for all grid dependence tests. Each grid consists of four panels in the i direction and four panels in the j direction. The number and distribution of nodes along panel boundaries is varied to obtain appropriate refinement in the liquid region, at the phase interface, and in the region just below the tube. In the j direction, there is one panel in the liquid region and three panels in the vapour region. The first of the panels in the vapour region is a relatively thin panel that permits a concentration of nodes near the phase interface. In those tests the number of control volumes in the j direction in the liquid film was 20 except for tests B2, C2, and D2 where 30 control volumes were assigned for the liquid film.

A sample coarse grid for the entire domain is shown in Figure 6.9 for illustration purposes. The first two panels in the j direction (one in the liquid and one in the vapour) are in the continuously darkened region next to the tube and then next to the symmetry line below the tube.

Results for Re_L, $\overline{\mathrm{Nu}}$, and $\dot{m}_{\mathrm{cond}}$ for the eight grids are given in Table 6.1. Also given are the percentage differences $\Delta\overline{\mathrm{Nu}}$, Δm_{cond}, and $\Delta\delta|_{\max}$ from the finest grid (grid E).

For the whole range of θ, $\Delta\delta|_{\max}$ is the percentage of the maximum difference in the interface height between the particular grid and the finest grid. It can be noticed that results from all tests are very close to each other in terms of the overall quantities. The maximum difference is -0.055% in $\overline{\mathrm{Nu}}$ and -0.09% in $\dot{m}_{\mathrm{cond}}$ for grid B2. However, for the film height, relatively larger differences can be noticed. For example, the maximum difference in δ profile is 7.01% and 3.58% for grids C and C2 respectively. These differences occur over a very limited region at the bottom of the tube as will be shown later in this section. Also included in Table 6.1 is the computational time to perform $50,000$ time steps, which is roughly the number of time steps needed to obtain a converged solution.

Figure 6.10 shows the normalised liquid film height versus the tube central angle θ for $0^\circ \leq \theta \leq 177^\circ$ for all eight grids. No distinguishable difference among them can be noticed. In Figure 6.11, a region at the bottom of the tube was enlarged to show the shape of the

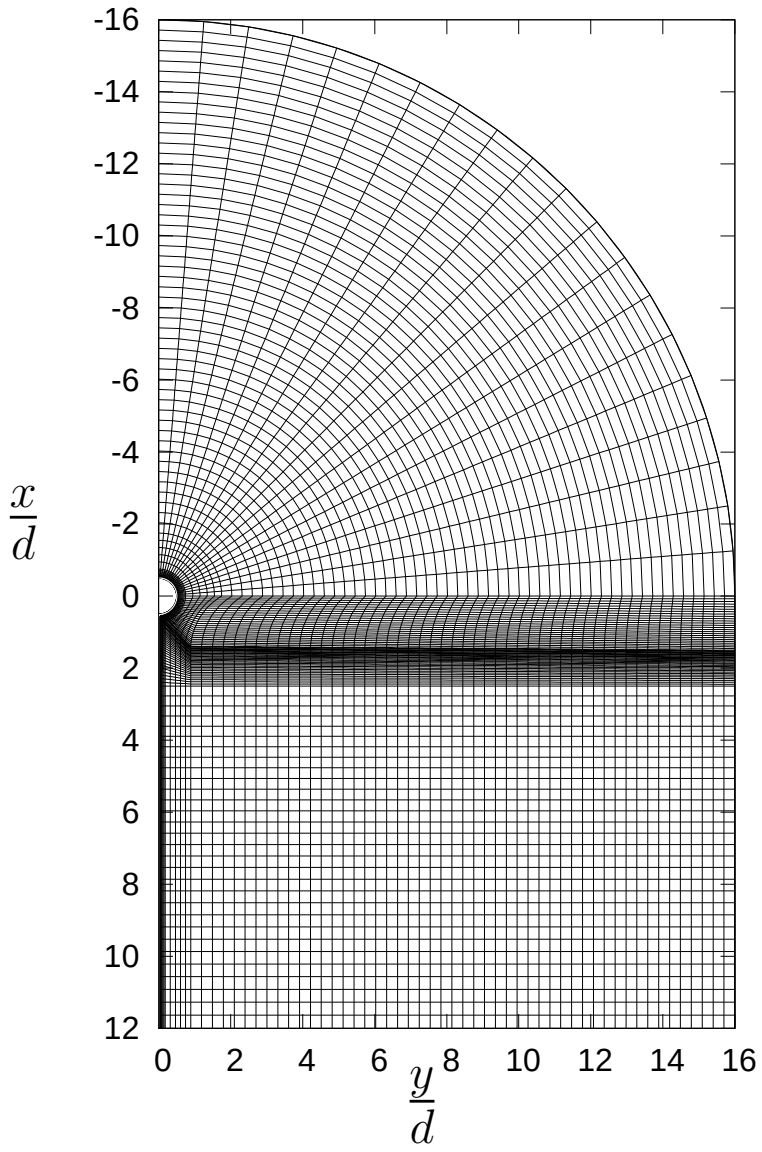

Figure 6.9: Sample coarse grid

Table 6.1: Effect of grid size on heat transfer characteristics and computational time.

Grid	size $N_x \times N_y$	Re_L	$\overline{\mathrm{Nu}}$	$\Delta\overline{\mathrm{Nu}}$ [%]	$\dot{m}_{\mathrm{cond}}$ [kg/s]	Δm_{cond} [%]	$\Delta\delta\|_{\max}$ [%]	Compute time/50k [day]
A	380 × 250	34.078	254.31	-0.022	2.375×10^{-3}	-0.026	1.248	7.3
B	420 × 280	34.071	254.28	-0.033	2.374×10^{-3}	-0.045	1.324	9.2
B2	420 × 290	34.056	254.23	-0.055	2.373×10^{-3}	-0.090	- 1.270	9.4
C	480 × 300	34.072	254.26	-0.040	2.374×10^{-3}	-0.042	7.010	10.9
C2	480 × 310	34.058	254.23	-0.052	2.373×10^{-3}	-0.084	3.583	11.3
D	520 × 340	34.080	254.32	-0.018	2.375×10^{-3}	-0.020	0.976	13.4
D2	520 × 350	34.064	254.28	-0.034	2.374×10^{-3}	-0.065	- 0.916	13.8
E	600 × 370	34.086	254.37	0.000	2.375×10^{-3}	0.000	0.000	16.3

interface for all tests where differences in δ profiles occur ($177° < \theta < 180°$). Although tests C and C2 have slightly thicker films compared to the other tests, no significant impact on the heat and mass transfer characteristics can be observed in Table 6.1.

To help in comparing profiles of variables in the liquid at different locations, a local dimensionless y variable ($y_L^\star$) is defined as follows:

$$y_L^\star = \frac{y}{d} + \frac{y_{ref}}{d} \tag{6.2}$$

where y_{ref} is the minimum y at the same location.

The U profiles in the liquid film near $\theta = 90°$, (the set of nodes adjacent to $\theta = 90°$), are plotted in Figure 6.12 against $y_L^\star$ for all grids and show no differences from each other. At this point, it was observed that the three grids with greater refinement in the j direction in the liquid region (30 control volumes compared to 20 control volumes for all the other grids) did not provide greater accuracy. In fact, the larger number of control volumes corresponded to

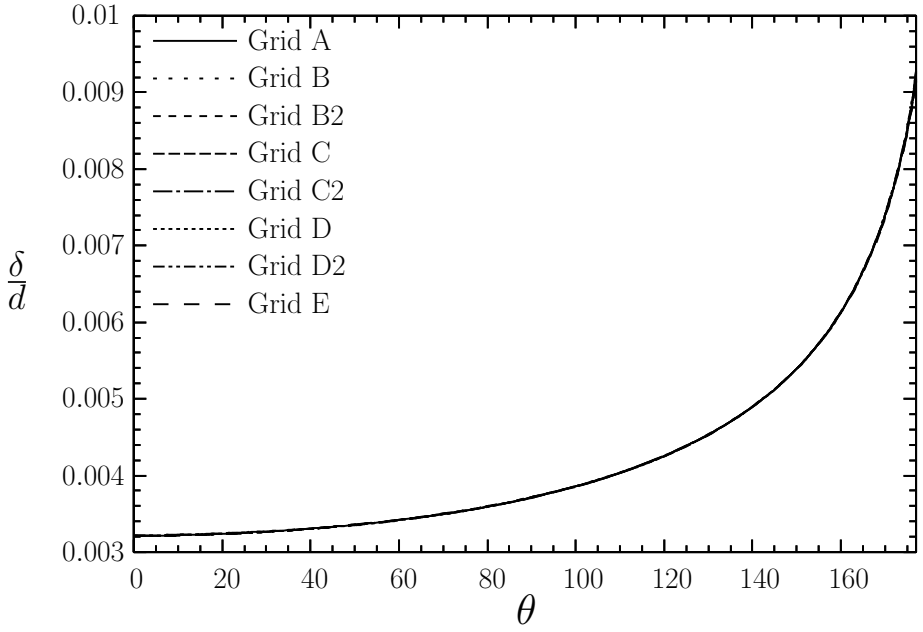

Figure 6.10: Condensate film thickness along the tube.

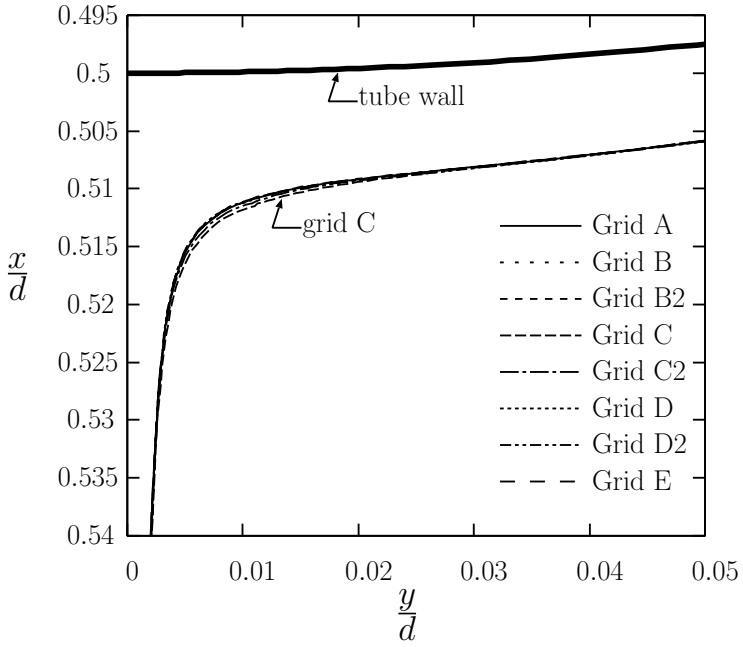

Figure 6.11: Condensate film at the tube bottom.

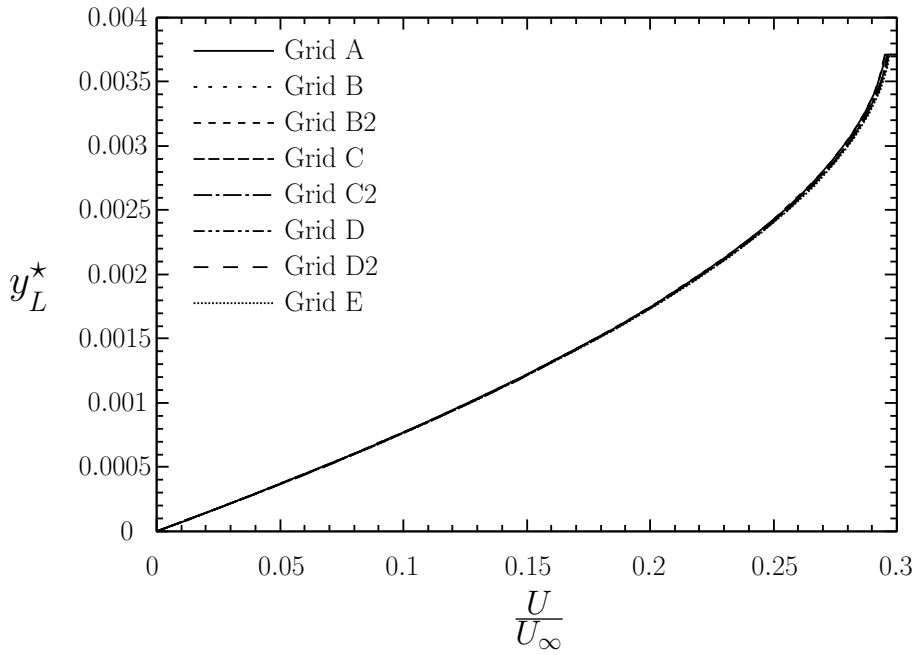

Figure 6.12: Condensate U velocity profiles near $\theta = 90°$.

a much slower interface movement for those grids. This behaviour was attributed to smaller control volumes in the liquid next to the interface. These smaller control volumes had smaller mass deficits (which drive the interface movement) so convergence was much slower. Because they provided no benefit and were much slower to converge, grids B2, C2, and D2 were eliminated from further consideration at this stage. As shown in Figure 6.11, grid C had the largest discrepancy in the interface height at the bottom of the tube compared to the other grids. This discrepancy can be attributed to inadequate distribution of the nodes at the bottom of the tube. Therefore, grid C was also eliminated from further consideration at the stage.

The U profiles in the vapour versus $\frac{y}{d}$ near $\theta = 90°$, (the set of nodes adjacent to $\theta = 90°$), are shown in Figure 6.13 for grids A, B, D, and E. Increasing the number of control volumes from 230 in grid A to 260 in grid B has improved the U profile specially in the vicinity of the tube. Further refinement of the grid has little effect in the U profile as seen in Figure 6.14.

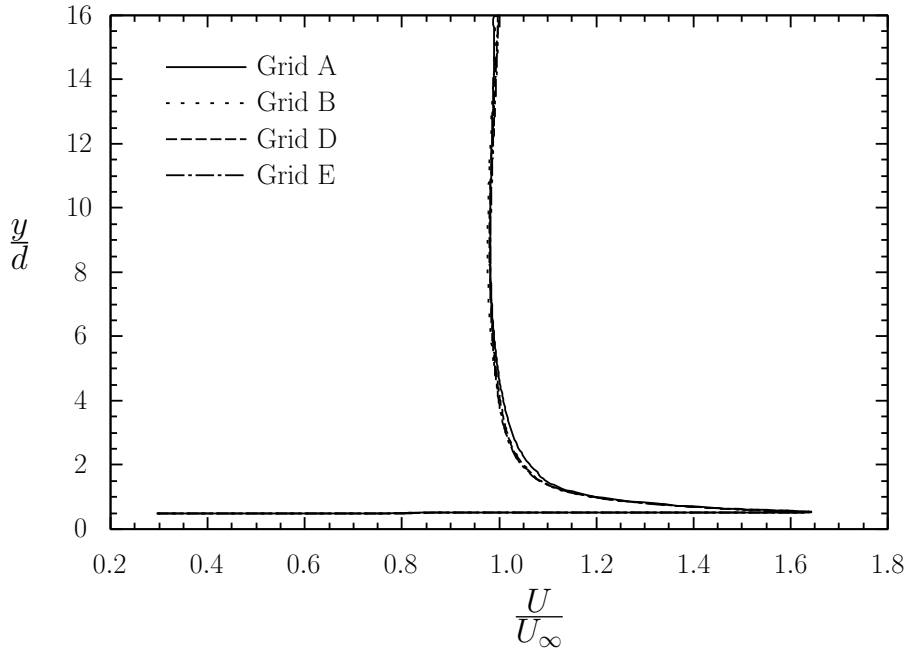

Figure 6.13: The U velocity profiles in the vapour region near $\theta = 90°$.

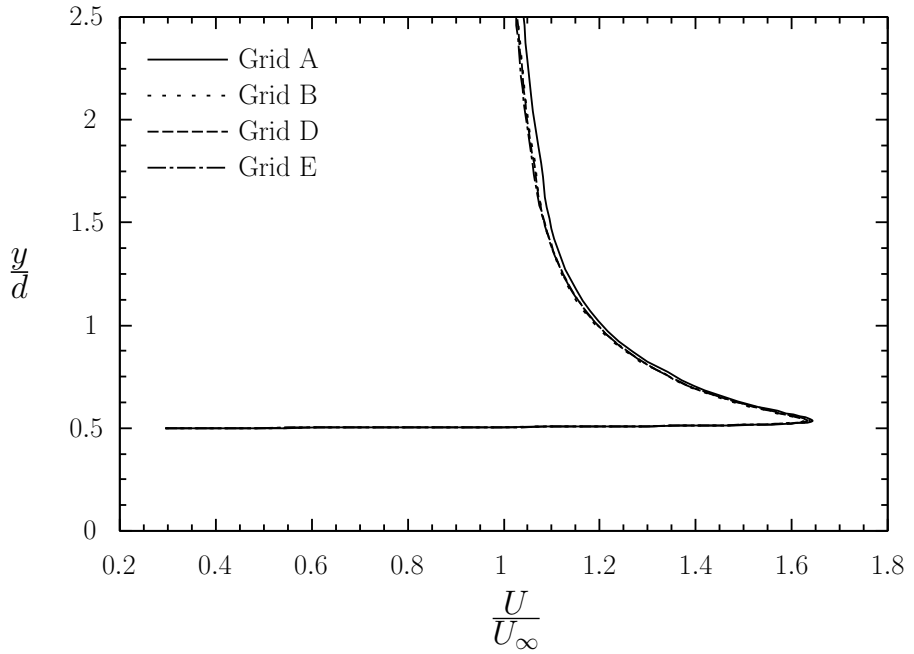

Figure 6.14: Details of the U velocity profiles in the vapour near the interface near $\theta = 90°$.

The V profiles near $\theta = 90°$ versus $y_L^\star$ are shown in Figure 6.15 for the liquid region. No significant difference can be noticed in the liquid film. Figure 6.16 shows the V profiles in the vapour versus $\frac{y}{d}$ at the same location. Noticeable differences can be observed in the vapour for $\frac{y}{d} > 5$. This region is enlarged in Figure 6.17. The V profile from grid D matches that of grid E for the most of the vapour region. Also, it has smoother profile at the free-stream boundary compared to grids A and B. The results from grid B, on the other hand, are closer those of grids D and E up to $\frac{y}{d} > 12.5$. It is noteworthy that the V profiles are shown at the location where the two free-stream boundaries meet. At this location there is small disturbance because of the change in the boundary condition. More over, those local differences have no distinguishable effect on the overall results. For example, the maximum difference in the film thickness for grid B compared to the finest grid was 1.324%; this discrepancy was mainly over a very limited region at the bottom of the tube. More over, for grid B, the percentage difference in $\overline{\mathrm{Nu}}$ was -0.033% compared to the finest grid. Taking into account the significantly larger computational efforts associated with grids D and E and the small differences in the results for grid B compared to finer grids, grid B was selected to perform the rest of the tests in this work.

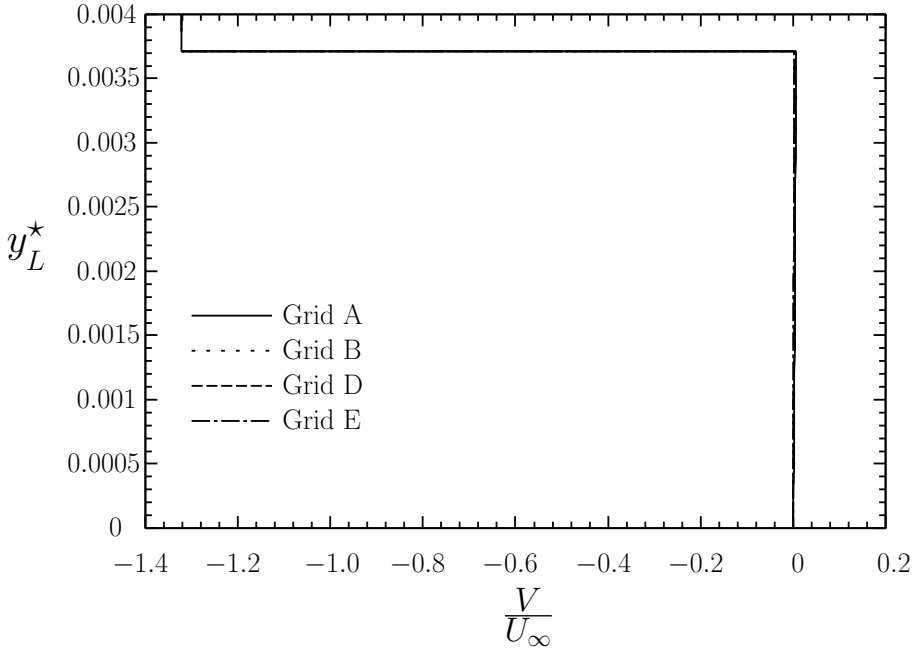

Figure 6.15: The V velocity profiles near $\theta = 90°$ in the liquid region.

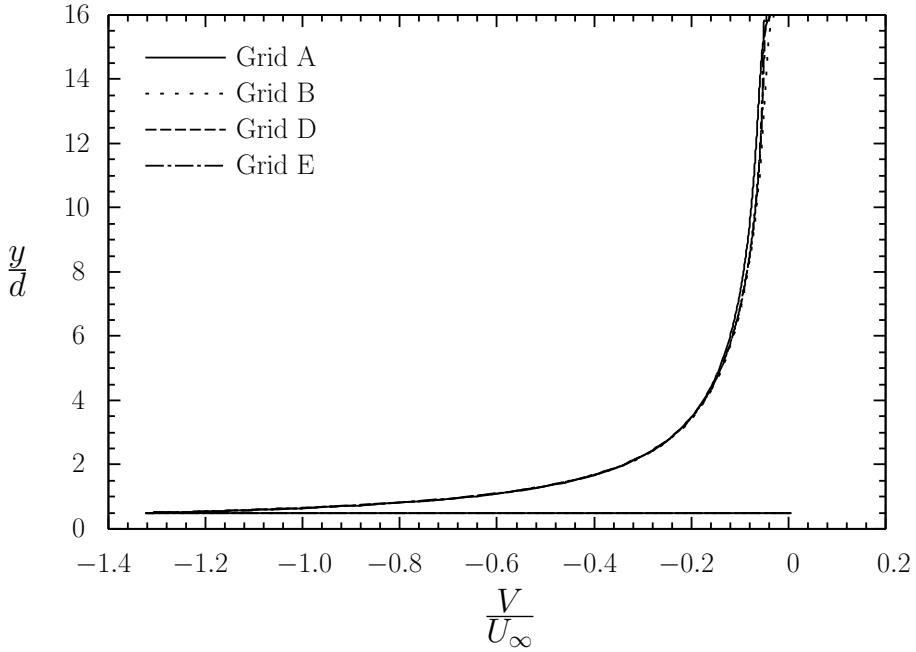

Figure 6.16: The V velocity profiles near $\theta = 90°$ in the vapour region.

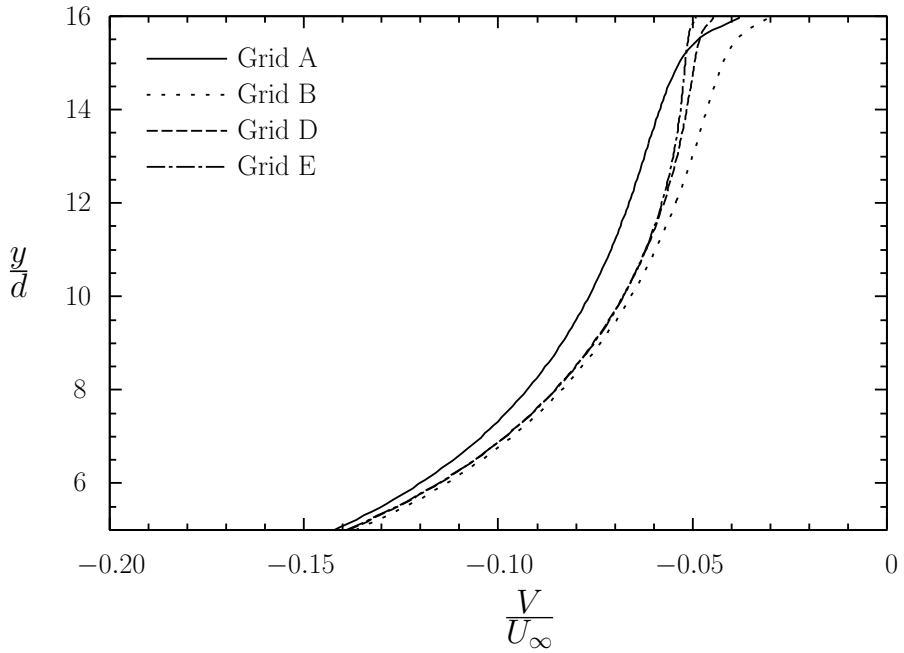

Figure 6.17: Details of the V velocity profiles in the vapour near $\theta = 90°$.

6.5 Model Validation

6.5.1 Validation Tests for Pure Vapour Condensation

The validity of the present model is demonstrated by two comparisons with earlier works for condensation on a horizontal tube: one for predictions of local film thickness and the other for predictions of average Nusselt number. The first comparison is with the theoretical single-phase model of Yang [14] and the two-phase model of Chen and Lin [19] for the case of pure vapour. The second comparison is with the experimental correlations of Fujii et al. [32], the theoretical equation of Rose [11], and the original Nusselt solution. In both comparisons, the fluid was water, the properties were held constant to maintain consistency with relevant references, and a tube diameter of 14 mm was used.

Comparison of Film Thickness

The first comparison is based on the local film thickness, δ, which is the height of the liquid measured normal to the tube surface. For the present work, h_L computed along the grid lines as described in Section 5.2.1 corresponds to the film thickness for $0° \leq \theta \leq 135°$ where grid lines are normal to the tube surface. For $\theta > 135°$, δ is computed from the local value of h_L. As θ approaches 180°, the film transitions to a falling film below the tube and the value of δ increases rapidly. For values of θ that correspond to the falling film region at the bottom of the tube, $\delta \to \infty$.

The dimensionless film thickness prediction of the present model is compared with the results of Yang [14] and Chen and Lin [19] for $P_\infty = 1$ atm, $\mathrm{Re}_d = 74.8$, and $\mathrm{Pr}_L/(\mathrm{Fr}\,\mathrm{Ja}) = 100$, as shown in Figure 6.18. Note that two-phase Reynolds number, Re, is used in the presentation of the the dimensionless film thickness results. Figure 6.19 shows, for a converged solution, detailed views of portions of a sample grid in the vicinity of the tube. For illustration purposes, the phase interface is shown as a thickened white line in Figure 6.19(a).

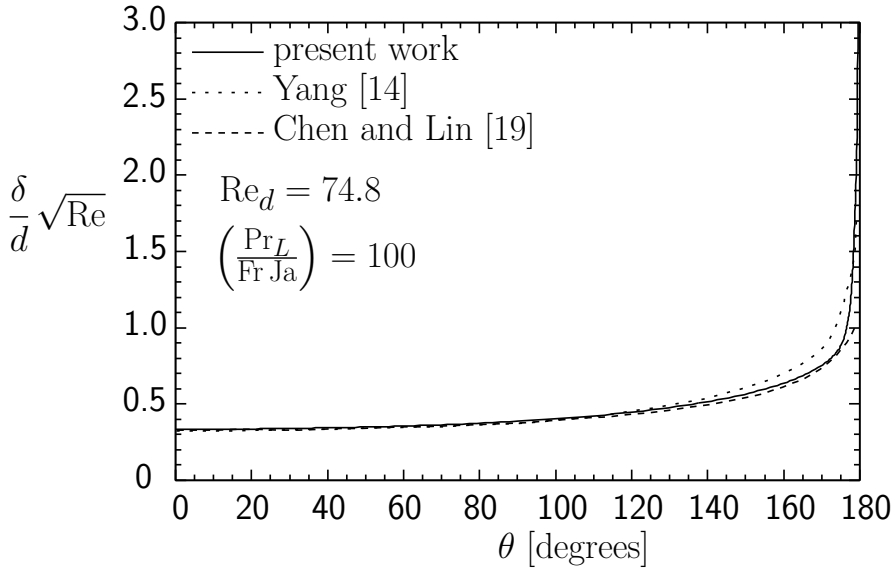

Figure 6.18: Condensate film thickness along the tube: comparison with [14] and [19].

Figure 6.19(b) shows the details of the liquid region panel and the refinement of the grid towards the interface in the first panel in the vapour region. Figure 6.19(c) shows the details of the shape of the grid as it matches the interface shape below the tube. The current results are very similar to those of both models up to $\theta \approx 110°$ with maximum difference of 3.3% and 2.9% compared to results of Yang [14] and Chen and Lin [19], respectively. For $110° < \theta < 170°$, the present work predictions of δ are in between the two models' results; in this range the present results are closer to those of Chen and Lin [19] with maximum deviation of -13.6% and 4.3% compared to the results of Yang [14] and Chen and Lin [19], respectively. For $\theta > 170°$, the current result varies substantially from both models. This discrepancy may be attributed to major differences in model equations between the current approach and those of [14] and [19].

Comparison of Average Nusselt Number

In this section, the average Nusselt number is compared with two correlations from the literature over a wide range of values of the parameter $\mathrm{Pr}_L/(\mathrm{Fr\,Ja})$. The range of $\mathrm{Pr}_L/(\mathrm{Fr\,Ja})$

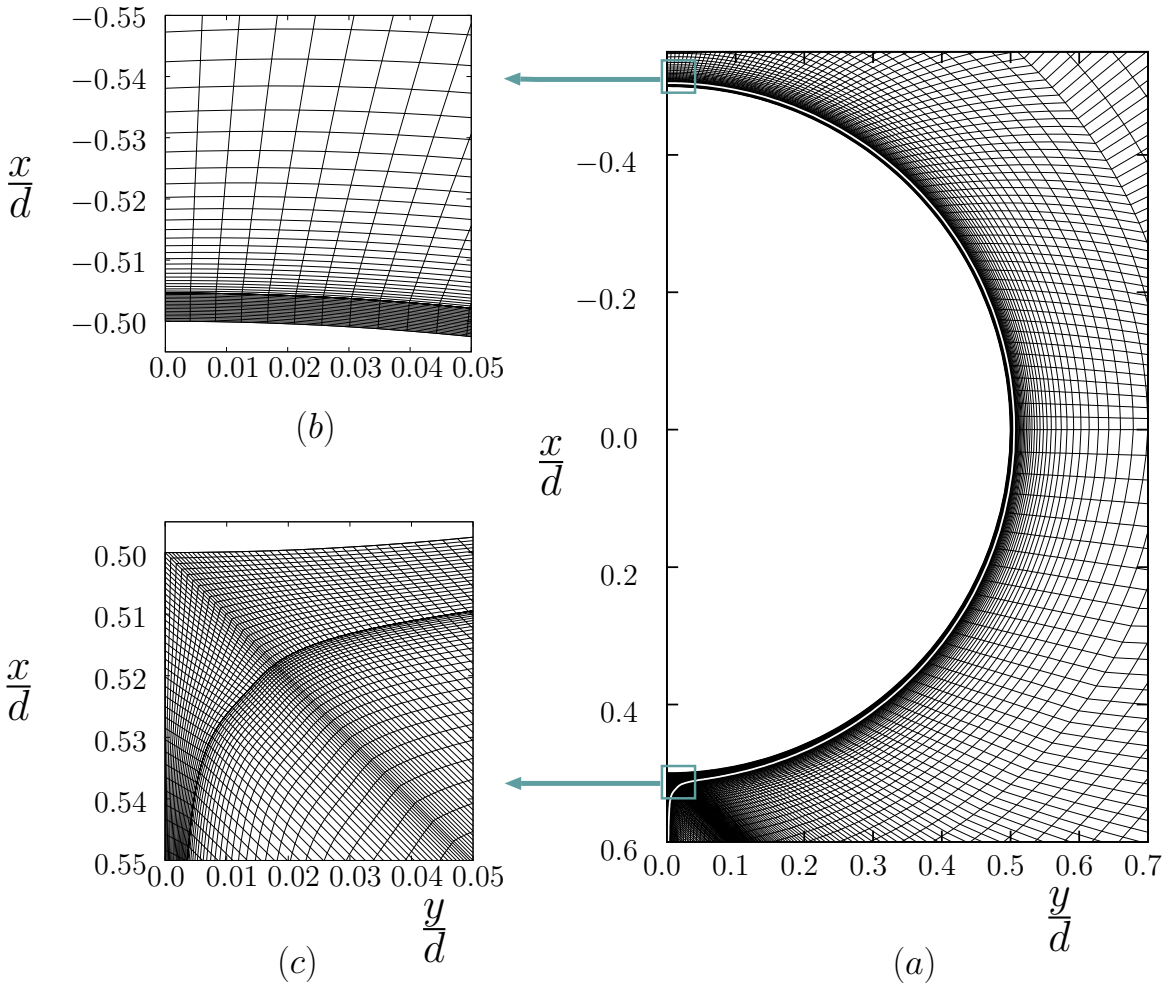

Figure 6.19: Sample grid showing details: (a) around the tube, (b) at the top of the tube, and (c) at the bottom of the tube.

corresponds to a change from a flow with strong effects of free stream velocity (low values) to a flow with strong buoyancy effects (high values). The comparison is presented in Figure 6.20 for the variation of $\overline{\mathrm{Nu}}/\sqrt{\mathrm{Re}}$ with $\mathrm{Pr}_L/(\mathrm{Fr}\,\mathrm{Ja})$. The current results agree well with Equa-

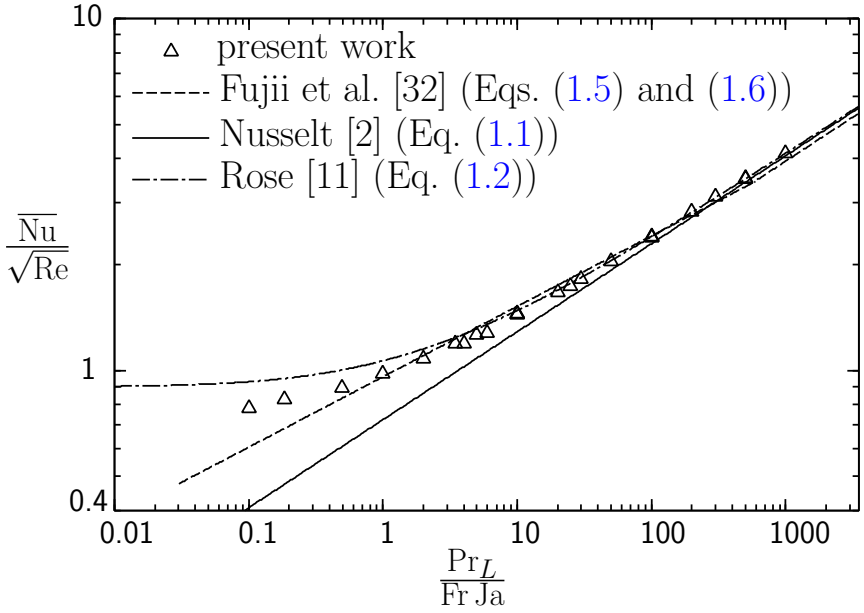

Figure 6.20: Comparison with theoretical and experimental correlation equations.

tions (1.5), (1.6) and (1.2) for large values of $\mathrm{Pr}_L/(\mathrm{Fr}\,\mathrm{Ja})$. For lower values of $\mathrm{Pr}_L/(\mathrm{Fr}\,\mathrm{Ja})$, however, both the current model and Equation (1.2) overpredict value of $\overline{\mathrm{Nu}}$ compared to the experimental correlation. Rose [69] indicated that this deviation may be related to a relatively stronger variation in the tube wall temperature with stronger vapour free stream velocity, U_∞, that is seen in experiments. In the range of low values of $\mathrm{Pr}_L/(\mathrm{Fr}\,\mathrm{Ja})$, the predictions of the present model are closer to the experimental correlation than Rose's model.

6.5.2 Validation Tests for Condensation with a Vapour-Gas Mixture

To demonstrate the validity of the present model in the presence of non-condensing gas, comparisons with two earlier works that dealt with condensation of steam from steam-air mixtures on a horizontal tube are presented. The first comparison is with the mathematical model of Li and Peng [23]. The second comparison is with the numerical model results of Chen and Lin [19]. In both the works of Li and of Peng [23] and Chen and Lin [19] constant physical properties were assumed whereas the present model has complete variable properties, including those of the mixture. Also, all the comparisons presented in this section are made for $P_\infty = 1$ atm.

Comparison with Li and Peng [23]

The current numerical results were compared with the results in Li and Peng [23] for two test cases at $\mathrm{Re}_d = 68.5$. These comparisons are based on the film thickness, local heat transfer coefficient, condensate mass flux, and local interfacial temperature. The operating parameters for the first case are W_∞ =0.01 and $T_{\mathrm{wall}} = 353$ K ($\Delta T = 20.06$ K). The second case conditions are W_∞ =0.05 and $T_{\mathrm{wall}} = 358$ K ($\Delta T = 14.34$ K).

The normalised film thickness versus θ is plotted in Figure 6.21 for both models. The results of [23] covered the range for $\theta = 0°$ to values of θ between 167° to 172°. In general, the present work predictions of δ are lower than those of Li and Peng [23]. At $\theta = 0°$, the deviations in predicting the film thickness between the two models are 1.25% and 8.7% for the first and second case, respectively. This deviation in δ prediction increases along the tube circumference to reach 7.7% and 12.2% for the first and second cases, respectively, at $\theta = 160°$. Because the end value of θ was varying between 167° to 172°, a value of $\theta = 160°$ was chosen for comparison.

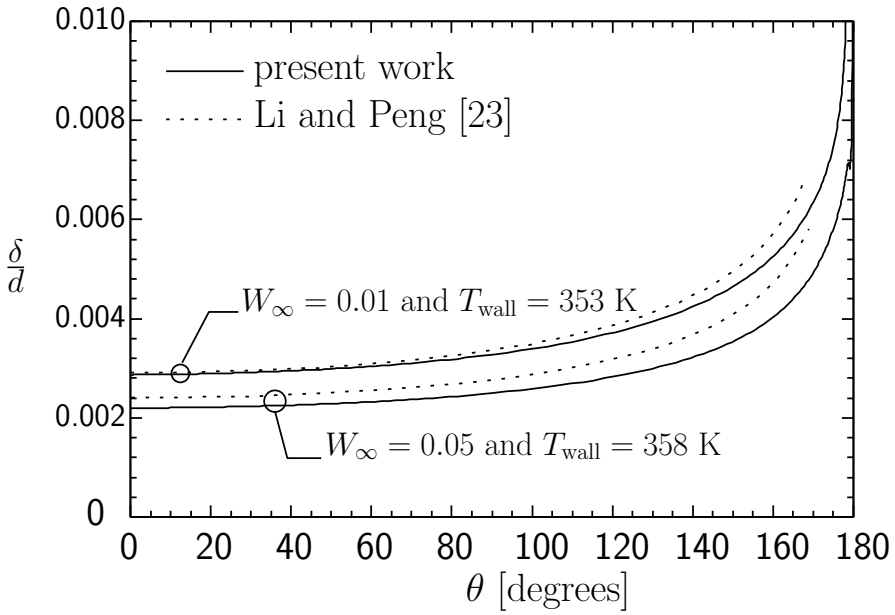

Figure 6.21: Condensate film thickness along the tube: comparison with [23] for $\text{Re}_d = 68.5$.

The comparison for the local Nusselt number, Nu_s, along the tube surface is presented in Figure 6.22. Both models predicted a similar trend for Nu_s variation with θ in which Nu_s value is maximum at the top of the tube, $\theta = 0°$, and decreases toward the bottom of the tube as a result of thickening film. In both cases, the present work values for Nu_s are substantially lower than those of [23] for the whole range of θ. In terms of quantitative comparison, the current values of Nu_s for the first case are 33.3% and 51.8% less than those of [23] at respectively $\theta = 0°$ and 160°. These differences increased to 45.2% and 70.5% for the second case at the same locations. Differences in $\overline{\text{Nu}}$ are expected to be to be within the same range. The considerable differences in Nu_s values reflect on the condensate mass flux distribution along the tube surface as shown in Figure 6.23.

The reason for the larger differences in Nu_s profiles between the two models in Figure 6.22 compared to the relatively smaller differences in δ profiles in Figure 6.21 can be explained with the aid of Figure 6.24 that shows the variation of the interfacial temperature, T_{int}, with θ for both models. According to the results of [23], the value of T_{int} is approximately constant

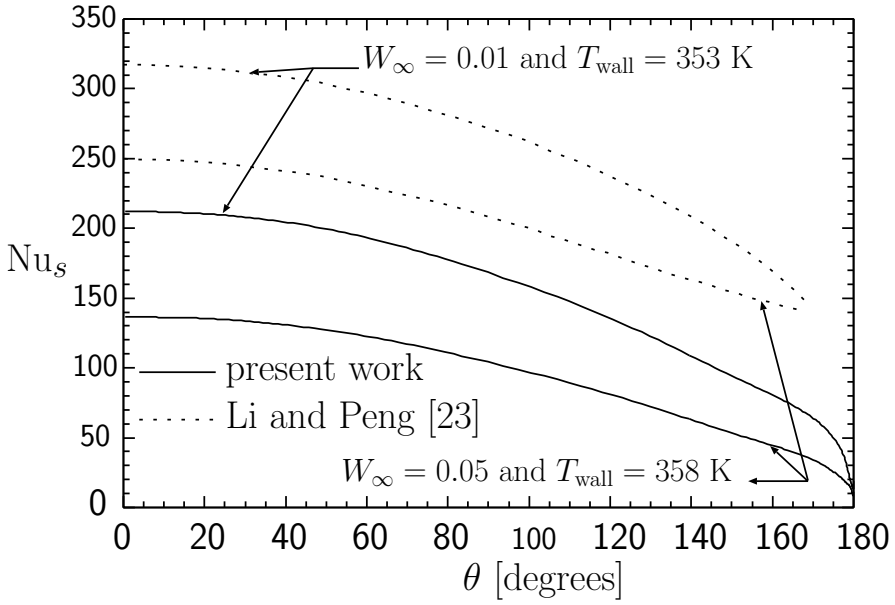

Figure 6.22: Local Nusselt number along the tube surface: comparison with [23] for $\text{Re}_d = 68.5$.

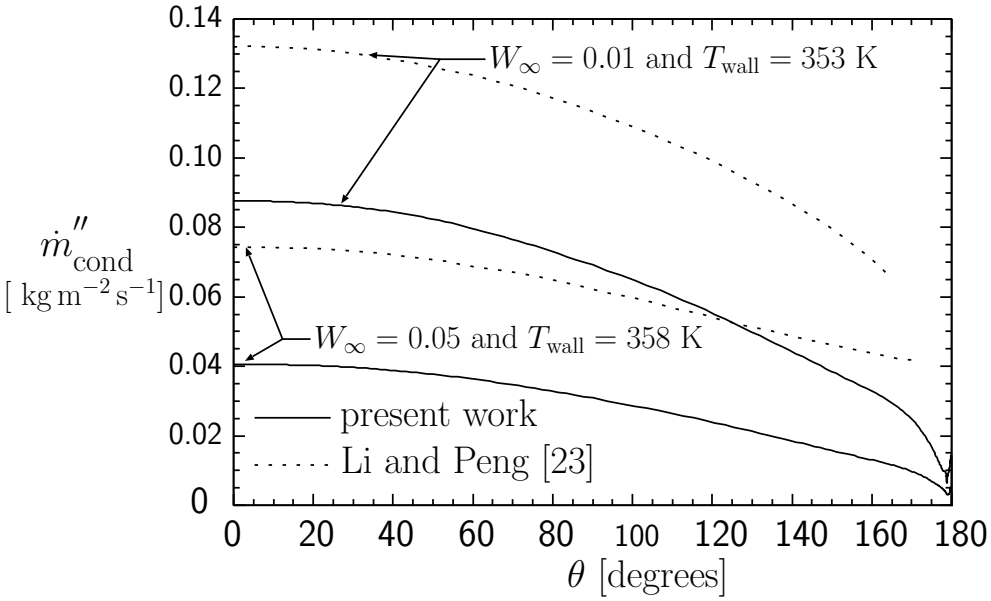

Figure 6.23: Condensate mass flux along the tube surface: comparison with [23] for $\text{Re}_d = 68.5$.

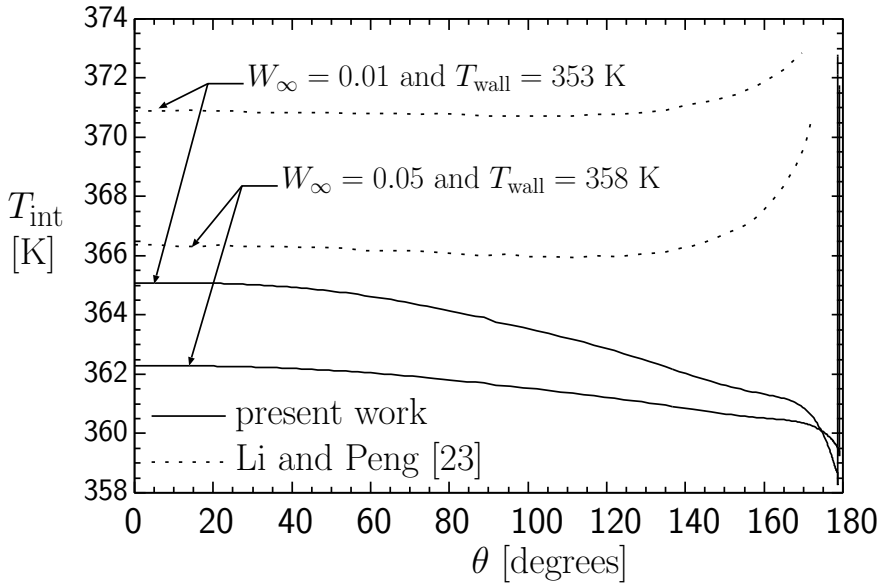

Figure 6.24: Interface temperature T_{int} along the tube surface: comparison with [23] for $\text{Re}_d = 68.5$.

up to $\theta = 120°$. Then, T_{int} starts to increase indicating that W_{int} is decreasing with θ at this portion of the tube surface. The results of the present work, however, show a different trend for T_{int} in which the value of T_{int} is maximum at $\theta = 0°$ and decreases gradually with θ up to $\theta \approx 170°$. Further along the tube surface, T_{int} decreases rapidly, relatively speaking, indicating that the value of W_{int} is increasing at higher rate with θ at this portion of the tube surface. In both test cases, the difference in T_{int} values between the results of the two models is 5 to 6 K at $\theta = 0°$. This difference increases along the tube surface to reach 9.5 to 12 K at $\theta = 168°$. The discrepancy in T_{int} profiles in Figure 6.24 reveals that there is a corresponding significant discrepancy in predicting the interfacial gas mass fraction value, W_{int}, between the two models.

To explain the possible reasons for this discrepancy, it is worthwhile to highlight the major differences in model equations and solution method between the current approach and those of [23]. As mentioned in Section 1.3.2, the mathematical two-phase model of Li and Peng [23] is based on the boundary layer theory. Therefore, both diffusion and advection

in the transverse direction were omitted in both phases. More over, the advection term in the normal direction in the liquid film was neglected. Thus, the actual elliptical nature of the partial differential equations was converted to parabolic one and made it possible to be solved by following a marching technique around the tube. An equation for a so-called induced velocity at the interface based on the thickness of the mixture boundary layer and the limiting values of W at the interface at each axial location and in the free stream was derived and used to calculate the condensate mass flux. The thickness of the momentum and temperature boundary layers in the mixture were expressed in terms of the mixture boundary layer using analogy theory. On the other hand, the current model uses the full elliptic set of Navier-Stokes governing equations. The condensate mass flow rate was calculated using local energy balance at the interface. No estimation was involved to determine the thickness of momentum, temperature, and mixture boundary layers. It is believed that those major differences in model equations and solution method between the current approach and those of [23] contributed mainly to the discrepancy between the results of the two models. Other assumptions that were used in [23] such as constant properties, constant mixture density, linear temperature profile in the liquid, and potential flow outside the mixture boundary layer might have also contributed to the discrepancy between the results of the two models.

Comparison with Chen and Lin [19]

In the second comparison, the variation of the film thickness and the local Nusselt number for $\mathrm{Pr}_L/(\mathrm{Fr}\,\mathrm{Ja}) = 100$, $\mathrm{Re}_d = 100$, and $W_\infty = 0.1$ are compared with the numerical results of Chen and Lin [19]. The given value of $\mathrm{Pr}_L/(\mathrm{Fr}\,\mathrm{Ja})$ could not be achieved with water properties at 1 atm, standard gravitational acceleration, and a tube diameter of of 14 mm. Therefore, a tube diameter of 10 mm and g of 7.34 $\mathrm{m\,s^{-2}}$ were used in this comparison.

The comparison for the dimensionless film thickness is shown in Figure 6.25. Noticeable differences in predicting the shape and the thickness of the liquid film can be seen between

the two results. The present model result of δ profile is similar to those in Figure 6.21 in

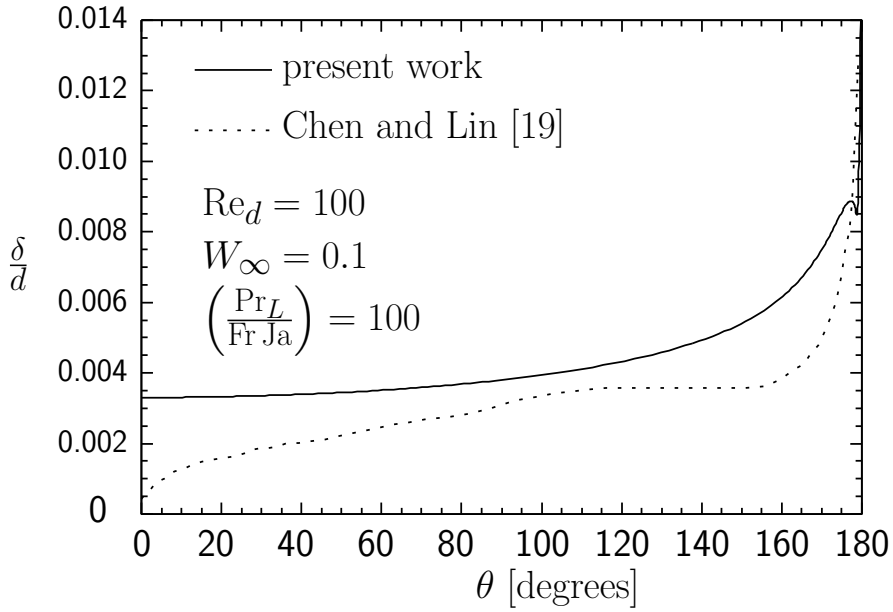

Figure 6.25: Condensate film thickness along the tube: comparison with [19] for $P_\infty = 1$ atm.

terms of the shape with thicker film over most of θ range compared to the result of [19], especially at $\theta = 0°$. In the present results, the film thickness increases slowly at the upper part of the tube $0° \leq \theta \leq 90°$. For the lower part of the tube $90° < \theta \leq 180°$, both δ and the rate of increase of δ with θ are increasing until the film thickness reaches a maximum value at $\theta = 177°$ before $\delta \to \infty$ for values of θ corresponding to the falling film region at the bottom of the tube. By contrast, a maximum film thickness near $\theta \approx 115°$ was predicted for this case in [19]. Example differences in δ in [19] relative to the present work are -85%, -18%, and -37% at angles of 0°, 100°, and 160°, respectively.

For most of the tube surface $0° \leq \theta < 175°$, the shape of the normalised film thickness is unique for the same values of $\mathrm{Pr}_L/(\mathrm{Fr\,Ja})$ and Re_d with any selected combinations of P_∞, g, ΔT, and d. It is believed that individual selection of the variables appearing in the parameter $\mathrm{Pr}_L/(\mathrm{Fr\,Ja})$ has a slight impact on the film profile near the bottom of the tube. Experience in this work makes the author believe that another separate dimensionless group (perhaps

Fr) should be specified to determine uniquely the shape of the interface every where along the tube surface. Determining this dimensionless group is, however, beyond the scope of this work.

The comparison with [19] for the local Nusselt number along the tube surface is shown in Figure 6.26. The current results showed a similar trend for Nu_s variation with θ as

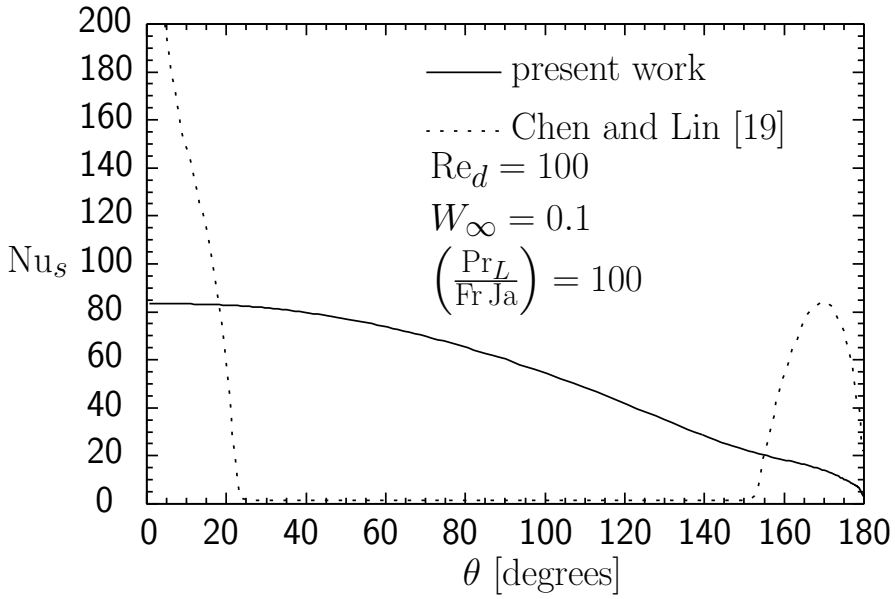

Figure 6.26: Local Nusselt number along the tube surface: comparison with [19] for $P_\infty = 1$ atm.

those in Figure 6.22. That is, the Nu_s value is a maximum at the top of the tube and decreases gradually toward the bottom of the tube due to thickening film and decreasing local temperature difference across the film ($T_{\mathrm{int}} - T_{\mathrm{wall}}$). The results of [19] showed a much different profile for Nu_s where heat transfer occurs mainly over two small portions of the tube surface at $0° \leq \theta \leq 25°$ and $155° \leq \theta \leq 180°$. Over the rest of the tube surface, the Nu_s value is very small ($\mathrm{Nu}_s = 1.44$). This can only happen if $T_{\mathrm{int}} \approx T_{\mathrm{wall}}$. In other words, the gas concentration builds up very quickly between $0° \leq \theta \leq 25°$ and reaches a value of W_{int} corresponding to $T_{\mathrm{int}} \approx T_{\mathrm{wall}}$ and remains constant up to $\theta = 155°$ before decreasing

over $155^\circ \leq \theta \leq 180^\circ$; it is difficult to think of a physical reason for this type of behaviour.

To infer the possible sources for the noticeable discrepancy between the results of the two models, a summary for the key features of Chen and Lin [19] model that are different than the present model is given below. As discussed in Section 1.3.2, the numerical 2D and two-phase model of Chen and Lin [19] is based on the boundary layer assumptions. Therefore, only the momentum equation in the transverse direction was used. The continuity equation was used as an equation for the velocity component in the normal direction to the tube surface. Diffusion terms in the transverse direction in all equations were omitted in both phases including in the gas conservation equation in the mixture. Constant physical properties were used. At each location around the tube, the pressure gradient at the corresponding boundary of the mixture boundary layer was evaluated using a potential flow assumption. This pressure gradient was used through both liquid and mixture regions. Moreover, the effect of gravity in the mixture was neglected. The resulting parabolic set of equations was solved by following a marching technique around the tube. A Newton-Raphson linearization was used to handle non-linearity and inter-equation coupling. On the other hand, the current model uses the full elliptic set of Navier-Stokes governing equations. This enables better prediction for the full viscous flow around the tube. No assumption of potential flow was used. Instead, the pressure field is calculated indirectly from the continuity equation as presented in Chapter 5. It is believed that all those major differences in model equations and solution method contributed to the noticeable discrepancy between the results of the present model and those of [19]. Ignoring the transverse diffusion term in the W equation and the effect of gravity in the mixture momentum equation in the Chen and Lin model might have a main role in the prediction of W_{int} and hence the different profiles of Nu_s in Figure 6.26.

Chapter 7

Results and Discussion

In this chapter, new numerical results for two parametric studies are presented in detail. Both studies dealt with condensation over an isothermal horizontal tube. The first study dealt with pure steam while the second study used mixtures of steam and air with different values of gas mass fraction. The studies demonstrated the effects of free stream-to-tube surface temperature difference, ΔT, free stream mass flow rate as indicated by Re_d, free stream gas mass fraction, W_∞, and free stream pressure, P_∞, on the condensation process. A single tube with 14mm O.D. was used. Also, detailed results for a selected case are presented first for each study. The presented results cover the steam or steam-air mixture around the tube and the entire liquid film from the top of the tube to the falling film below the tube. Analysis of heat transfer at the tube surface and the definitions of local and average Nusselt number are given as well in a separate section.

7.1 Heat Transfer at the Tube wall

The heat flux toward the tube at any location along the tube wall is calculated using:

$$q''_{\text{wall}} = k_L \left.\frac{\partial T_L}{\partial n}\right|_{\text{wall}} \tag{7.1}$$

where n is the outward normal to the tube surface.

The average heat flux that crosses the tube wall is obtained by integrating Equation (7.1) over half of the circumference of the tube s, where $(s = \pi\, d/2)$.

$$\overline{q} = \frac{2}{\pi\ d} \int_0^{\frac{\pi}{2}d} q''_{\text{wall}}\ ds \tag{7.2}$$

The local Nusselt number, Nu_s, is defined as follows:

$$\mathrm{Nu}_s = \frac{h_s\ d}{k_L} = \frac{q''_{\text{wall}}\ d}{k_L\ \left(T_\infty - T_{\text{wall}}\right)} \tag{7.3}$$

The average Nusselt number, the average dimensionless heat transfer coefficient, is obtained by as follows:

$$\overline{\mathrm{Nu}} = \frac{\overline{h}\ d}{k_{_L}} = \frac{2}{\pi\ d}\int_0^{\frac{\pi}{2}d} \mathrm{Nu}_s\ ds = \frac{2}{\pi}\frac{1}{(T_\infty - T_{\mathrm{wall}})}\int_0^{\frac{\pi}{2}d} \left.\frac{\partial T}{\partial n}\right|_{\mathrm{wall}} ds \tag{7.4}$$

7.2 Pure Vapour Condensation

New results were produced using the present model to study the effects of ΔT, Re_d and P_∞ on film condensation from a vertically downward uniform laminar flow of steam over an isothermal horizontal tube. For $P_\infty = 1$ atm, three different steam flow rates were chosen that correspond to $\mathrm{Re}_d = 20$, 50, and 100. The range of Re_d used in this study was constrained to ensure steady and laminar flow in the steam region. For single phase flow, Re_d greater than 49 leads to vortex shedding. In this case, however, the reduction in mass flow due to condensation reduces the effective Re_d and steady flow is expected for $\mathrm{Re}_d = 100$. Flow with values of Re_d above 100 were expected to lead to unsteady steam flow with vortex shedding. The effect of inlet-to-tube-wall temperature difference was studied using values of $\Delta T = 5$, 10 and 20 K. This range of ΔT was chosen to keep Re_L within the smooth laminar flow regime. To examine the effect of inlet pressure on the condensation process, additional values of $P_\infty = 0.5$ and 2 atm were considered for $\mathrm{Re}_d = 50$ and $\Delta T = 5$ and 20 K. The results obtained in this study have been reported in [70]. In this parametric study, a small region of reverse flow was predicted at the domain outlet at $y/d \approx 1.6$ for the case of $\mathrm{Re}_d = 20$ and $\Delta T = 20$ K. In that case, the maximum value of the reverse flow velocity had a magnitude of about 1.6% of the inlet velocity. The extent of the reverse flow region was about 2.8% of the domain width. This small pocket of reverse flow had a mass flow rate of 0.06% of the total condensation rate and negligible effect on the solution fields near

the tube. Detailed results for a selected case are presented in the next section followed by analysis of the effects of different flow parameters on the condensation process.

7.2.1 Detailed Examination of Sample Results

The operating parameters for the selected case are $\mathrm{Re}_d = 100$ and $\Delta T = 20$ K. Figure 7.1 shows the normalised film thickness $\frac{\delta}{d}$ versus a normalised distance, $\frac{L_s}{d}$, that goes along the tube surface and then along x below the tube. Along the tube, the film thickness is measured in the normal direction to the tube surface. According to this definition of δ, $\delta \rightarrow \infty$ at the bottom of the tube. Plots of the shape of the phase interface below the tube were presented in Section 6.4. To show the film thickness beyond the tube, the film height measured in the y direction in the falling film region ($\frac{L_s}{d} > 1.57$) is shown by dashed line in Figure 7.1. The film thickness increases gradually up to $\frac{L_s}{d} \approx 1$ or $\theta \approx 115°$. For ($1 < \frac{L_s}{d} \leq 1.57$), the film thickness increases with greater rate to become 3.5 times thicker than the film thickness at the top of the tube at ($\frac{L_s}{d} = 1.562$) which corresponds to $\theta = 179°$. After $\theta = 179°$, the film transitions rapidly to a falling film so δ normal to the tube is no longer a meaningful quantity. Therefore, its value is not shown for ($\frac{L_s}{d} > 1.562$). For larger L_s values, the y height of the film is plotted as mentioned above. In the transition to the falling film region the film height decreases rapidly over a short distance due to gravitational force. For greater values of L_s (farther in the x direction), the film height decreases with very slow rate toward an equilibrium height.

In Figure 7.2, the dimensionless U velocity profiles in the liquid film are plotted versus $y_L^\star$ at different axial locations. At $\frac{x}{d} = 0$ ($\theta = 90°$), the U profile has a parabolic shape and the normalised film thickness is $\frac{\delta}{d} = 3.7 \times 10^{-3}$. As the liquid reaches the falling film region, it accelerates due to gravity and the velocity profiles become essentially uniform because of the zero shear condition at $y = 0$. As a result, the film thickness decreases substantially over a short distance. For example, the normalised film thickness drops from 3.95×10^{-3}

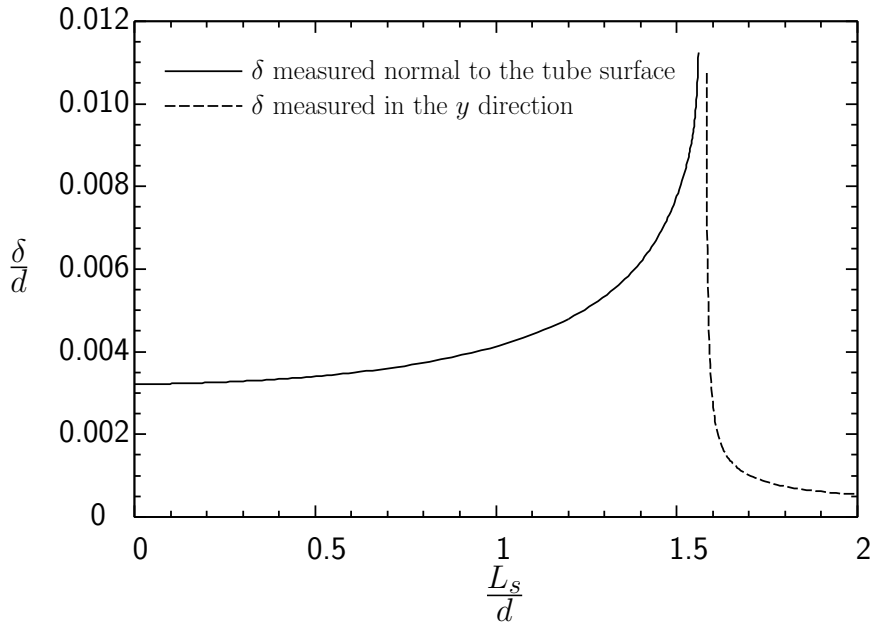

Figure 7.1: The condensate film thickness for $P_\infty = 1$ atm, $\mathrm{Re}_d = 100$, and $\Delta T = 20$ K.

at $\frac{x}{d} = 0.52$ to reach 1.8×10^{-3} at $\frac{x}{d} = 0.55$. Farther in the x direction, the film thickness keeps decreasing to become $\frac{\delta}{d} = 5.2 \times 10^{-4}$ at $\frac{x}{d} = 2.5$. Both the film thickness and the velocity stay approximately constant through out the rest of the domain indicating that an equilibrium height was reached.

The dimensionless U velocity profiles in the vapour region are given in Figure 7.3 for the same case. For $\frac{x}{d} = 0$, the velocity is minimum at the interface and reaches a maximum value not far from the interface. Close to the bottom of the tube, $\frac{x}{d} = 0.52$, and 0.55, the U velocity profiles first decreases in the y direction and becomes negative indicating occurrence of flow reversal. Then, not far from the interface, the profiles reach minimum value of -0.6 compared to U_∞. Farther in the x direction, the relatively fast falling film drags the vapour that is in contact with it. Therefore, for $\frac{x}{d} = 2.5$ and 12, the maximum value of U occurs at the interface. At all shown axial locations, the profiles become more uniform farther in the y direction and they approach a value of 1 as $\frac{y}{d} = 16$.

The isobars around the tube are shown in Figure 7.4. The shown values of the pressure

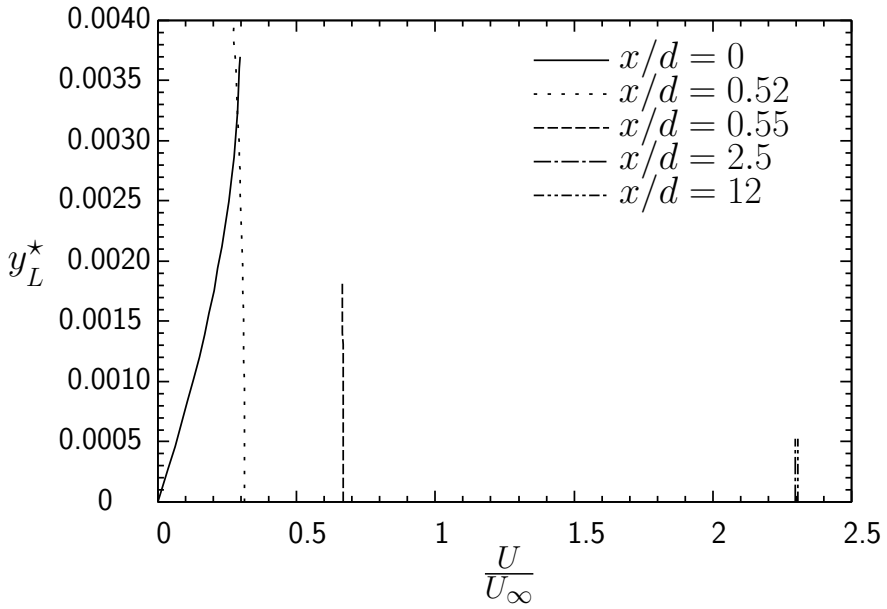

Figure 7.2: U velocity profiles in the liquid film at different locations for $P_\infty = 1$ atm, $\mathrm{Re}_d = 100$, and $\Delta T = 20$ K.

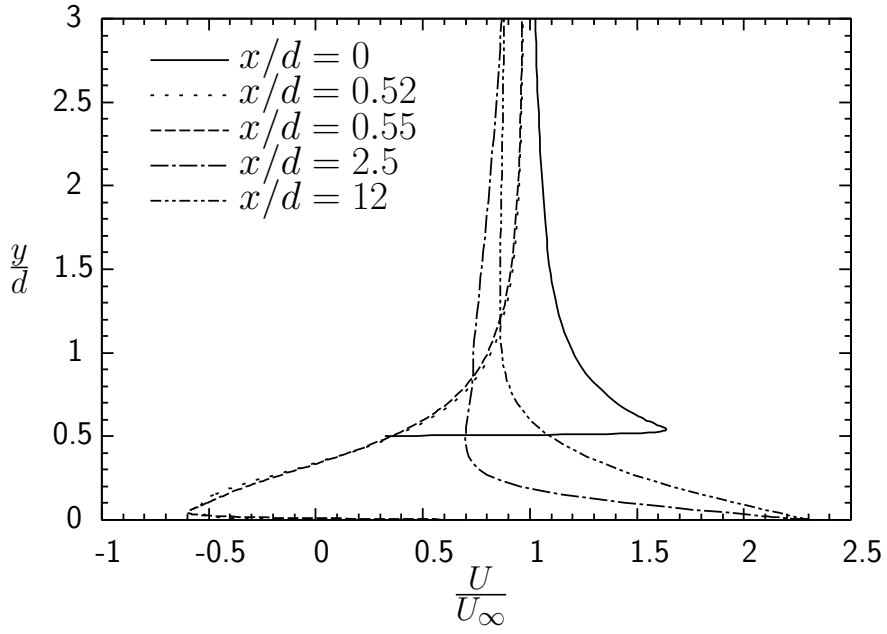

Figure 7.3: U velocity profiles in the vapour at different locations for $P_\infty = 1$ atm, $\mathrm{Re}_d = 100$, and $\Delta T = 20$ K.

are the relative to the outlet pressure and are in Pa. In general, the differences in the pressure

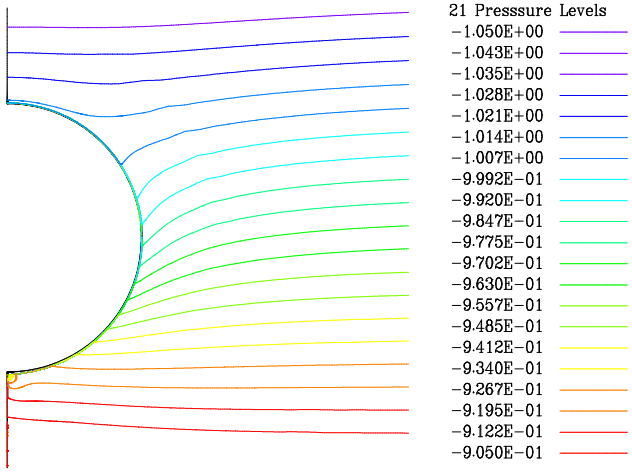

Figure 7.4: Relative pressure distribution around the tube for $P_\infty = 1$ atm, $\mathrm{Re}_d = 100$, and $\Delta T = 20$ K.

correspond to the differences in the hydrostatic pressure. As the vapour flows around the tube, it accelerates resulting in minor changes in the pressure near the tube. These changes have no sensible impact on the properties. Farther in y direction, the pressure profiles are essentially uniform.

In Figure 7.5, the dimensionless temperature profiles in both regions versus $y_L^\star$ are shown at different axial locations. At $\frac{x}{d} = 0$, the T profile varies linearly with $T = T_{\text{wall}}$ at the tube surface. After the tube ($\frac{x}{d} > 0.5$), the falling film is still colder than the vapour because it was in contact with the tube wall. In the falling film region, there is a small amount of condensation to the cooler film. The film warms up quickly because no energy leaves at $y = 0$. This can be noticed from the significant change in T profile between $\frac{x}{d} = 0.52$ and 0.55. The film temperature keeps increasing and becomes uniform before $\frac{x}{d} = 2.5$. As a result, the T profiles at $\frac{x}{d} = 2.5$ and 12 in Figure 7.5 lay on each other. The condensate mass flow rate that is added to the film after the tube is 1.45% of the total condensate mass flow rate. At all axial locations, the value of the dimensionless temperature at the interface

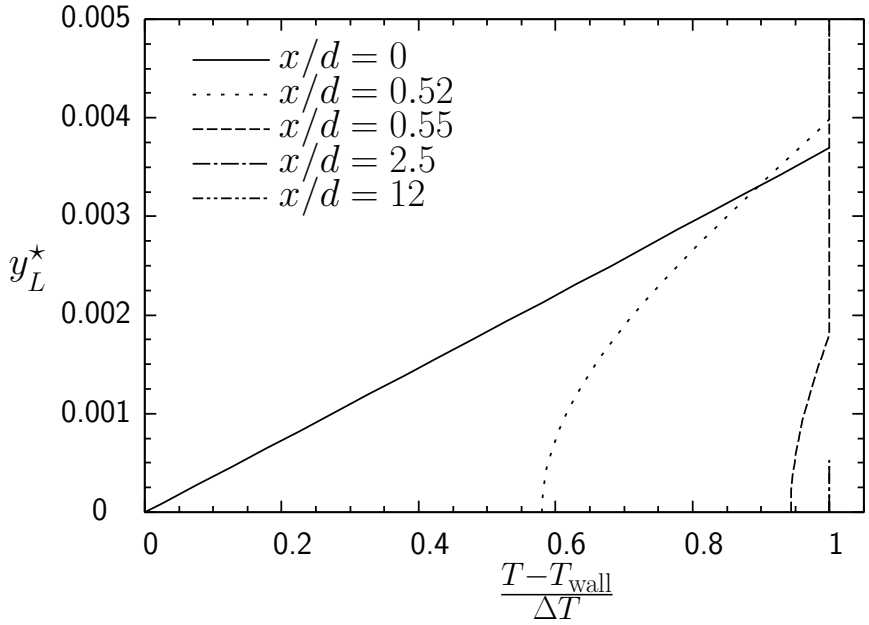

Figure 7.5: Temperature profiles in the liquid film at different locations for $P_\infty = 1$ atm, $\text{Re}_d = 100$, and $\Delta T = 20$ K.

is always equal to 1 referring to $T = T_\infty$. In the vapour region, the temperature is always constant at T_∞.

To illustrate flow pattern in two-dimensions often streamlines plots are used. In this work, however, streamlines plots are not used because there is mass loss in the vapour and mass gain in the liquid. These mass transfers cause variations in the streamlines which make them much less informative than vectors. Because of the density difference of a factor of approximately 1650 in this case, the magnitude of the velocity in the vapour is much larger than the velocity in the liquid. To enable visualization of the two sets of vectors in the same figure, different scales are used for the two vector fields plotted in Figure 7.6. The red vectors are in the vapour while the blue vectors, not visible in Figure 7.6(a), are in the liquid. Figure 7.6(b) shows the velocity vectors in the vapour as the vapour flow approaches the interface at the top of the tube. The much smaller liquid vectors are covered by the vapour vectors. Figure 7.6(c) shows the details of the flow pattern in both fluids as the liquid film

leaves the tube surface and starts descending in the falling film region. The velocity in the liquid increases near the interface and accelerates in the falling film.

7.2.2 Effect of Changing ΔT

The effect of changing ΔT on the variation of the film thickness around the tube is shown in Figure 7.7 for $P_\infty = 1$ atm and $\mathrm{Re}_d = 50$. Increasing ΔT increases the condensation rate and the film thickness over the entire range of θ.

Figure 7.8 shows the effect of ΔT on the local Nusselt number, Nu_s, along the tube circumference for $P_\infty = 1$ atm and $\mathrm{Re}_d = 50$.

It is clear that Nu_s decreases along the tube surface as ΔT increases. This trend can be explained by the increase in the thermal resistance across the condensate as the film thickness increases with increasing ΔT. The sudden drop in Nu_s as θ approaches 180° is due to the rapid thickening of the film at the bottom of the tube as it transitions to a vertical falling film.

Table 7.1 shows the increasing mass flow rate of liquid with increased ΔT through the increase in film Reynolds number, Re_L, with increased ΔT. The dynamic viscosity in the

Table 7.1: Average Nusselt number and film Reynolds number variation with ΔT and Re_d for $P_\infty = 1$ atm.

	$\mathrm{Re}_d = 20$		$\mathrm{Re}_d = 50$		$\mathrm{Re}_d = 100$	
ΔT [K]	$\overline{\mathrm{Nu}}$	Re_L	$\overline{\mathrm{Nu}}$	Re_L	$\overline{\mathrm{Nu}}$	Re_L
5	360.13	12.01	361.28	12.25	363.14	12.31
10	301.12	20.35	302.46	20.44	304.65	20.59
20	250.32	33.54	251.80	33.74	254.28	34.07

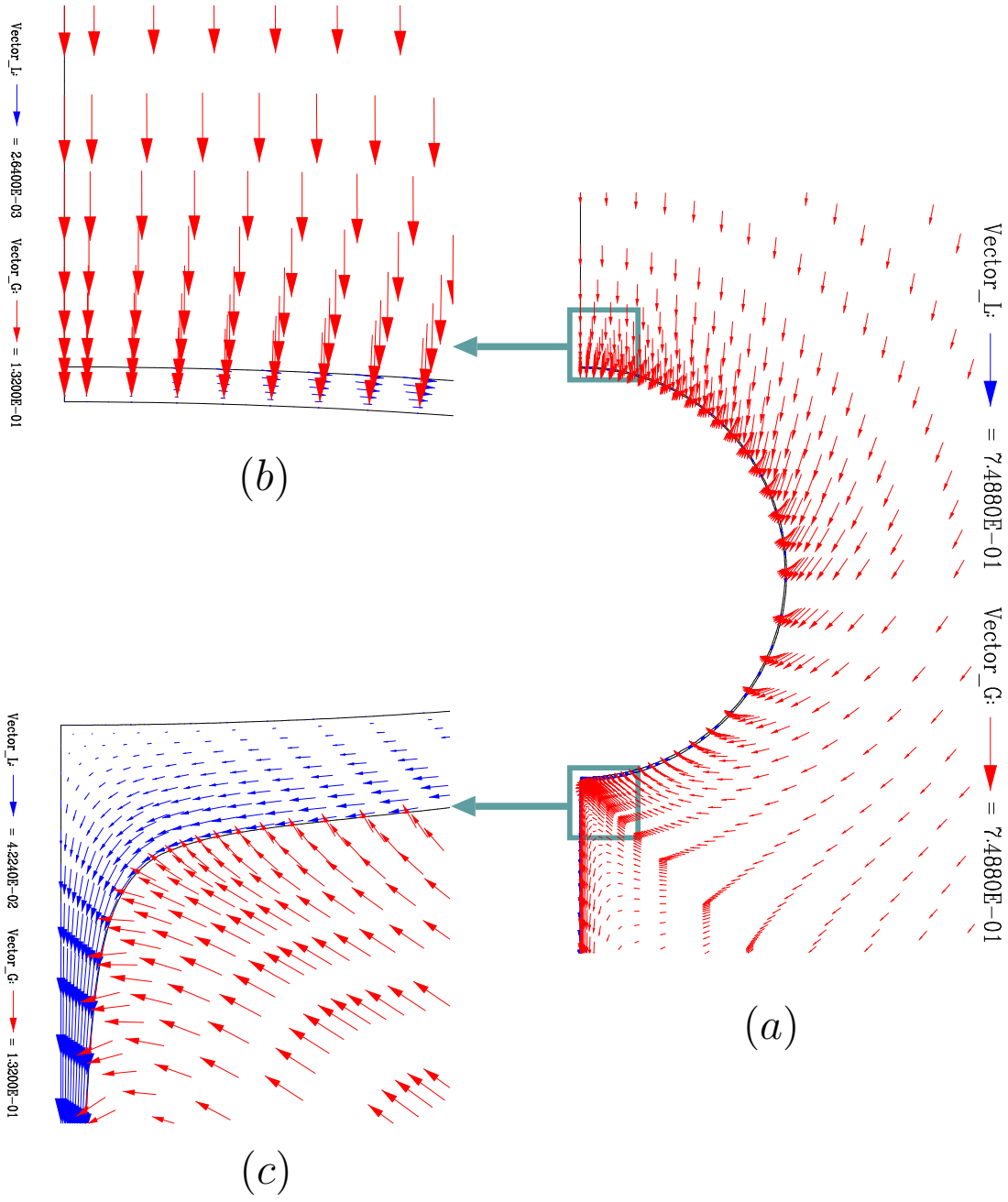

Figure 7.6: Details of the flow pattern for $\mathrm{Re}_d = 100$ and $\Delta T = 20$ K at: (a) around the tube, (b) at the top of the tube, and (c) at the bottom of the tube.

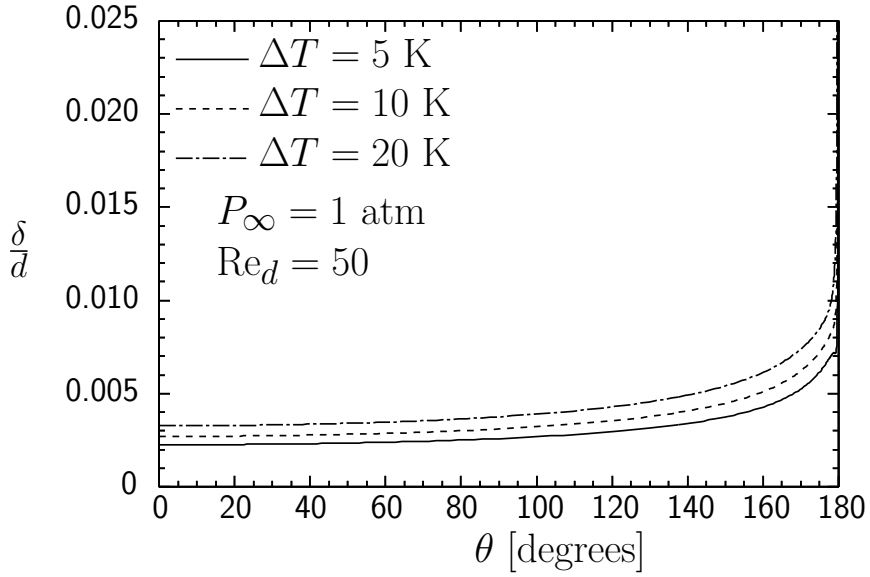

Figure 7.7: Effect of temperature difference for $\mathrm{Re}_d = 50$ and $P_\infty = 1$ atm.

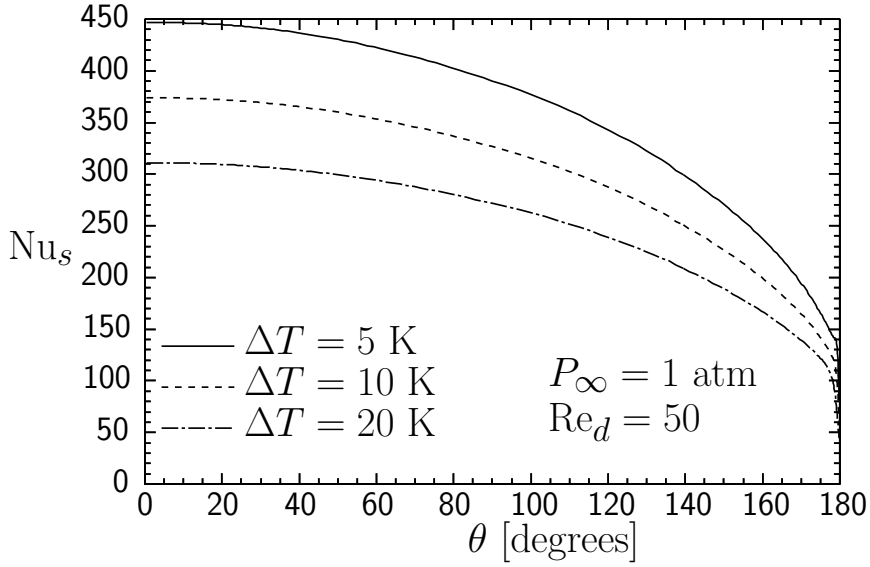

Figure 7.8: Effect of temperature difference on Nu_s for $\mathrm{Re}_d = 50$ and $P_\infty = 1$ atm.

film Reynolds number was evaluated at T_∞ corresponding to the free stream pressure. Also, Table 7.1 shows the average Nusselt number values corresponding to the cases presented in Figure 7.8.

It was found that a reverse flow region forms near the bottom of the tube in the vapour. To examine the effect of ΔT on this phenomenon, the U velocity contours for $U < 0$ are plotted in Figure 7.9 for $\mathrm{Re}_d = 50$. Both the intensity and the extent of the reverse flow increase with ΔT. For $\Delta T = 20$ K, the reverse flow region extends to $0.91d$ beyond the tube.

7.2.3 Effect of Changing Re_d

The effect of changing Re_d on the condensate film thickness is presented in Figure 7.10 for $\Delta T = 5$ and 20 K. Taking into account the relatively narrow range of Re_d, Re_d has a generally slight effect on δ for both $\Delta T = 5$ and 20 K. The results demonstrated that, for the same value of ΔT, the film in the upper part of the tube becomes slightly thinner as Re_d increases due to increasing interfacial shear stress caused by increased steam velocity. However, differences in film profiles for a fixed value of ΔT vanish gradually in the lower part of the tube. The effect of Re_d on local heat transfer coefficient is shown in Figure 7.11. For each value of ΔT, Nu_s in the upper part of the tube increases slightly as Re_d increases as a direct impact of thinner films associated with increasing Re_d. As θ increases, Nu_s profiles for a fixed ΔT collapse on each other. The effect of changing Re_d on the average Nusselt number, as shown in Table 7.1, is consistent with the trends for the local Nusselt number. The film Reynolds numbers in Table 7.1 indicate a slight increase in condensate mass flow rate with increasing Re_d.

The increased inertia force with increased Re_d noticeably reduces the extent of the reverse flow region as seen in Figure 7.12 for $\Delta T = 20$ K. For $\mathrm{Re}_d = 20$, the reverse flow region extends to $5.15d$ beyond the tube. For $\mathrm{Re}_d = 50$ and 100, the extent of the reverse flow region reduces to $0.91d$ and $0.33d$, respectively. The intensity of the reverse flow, however, remains

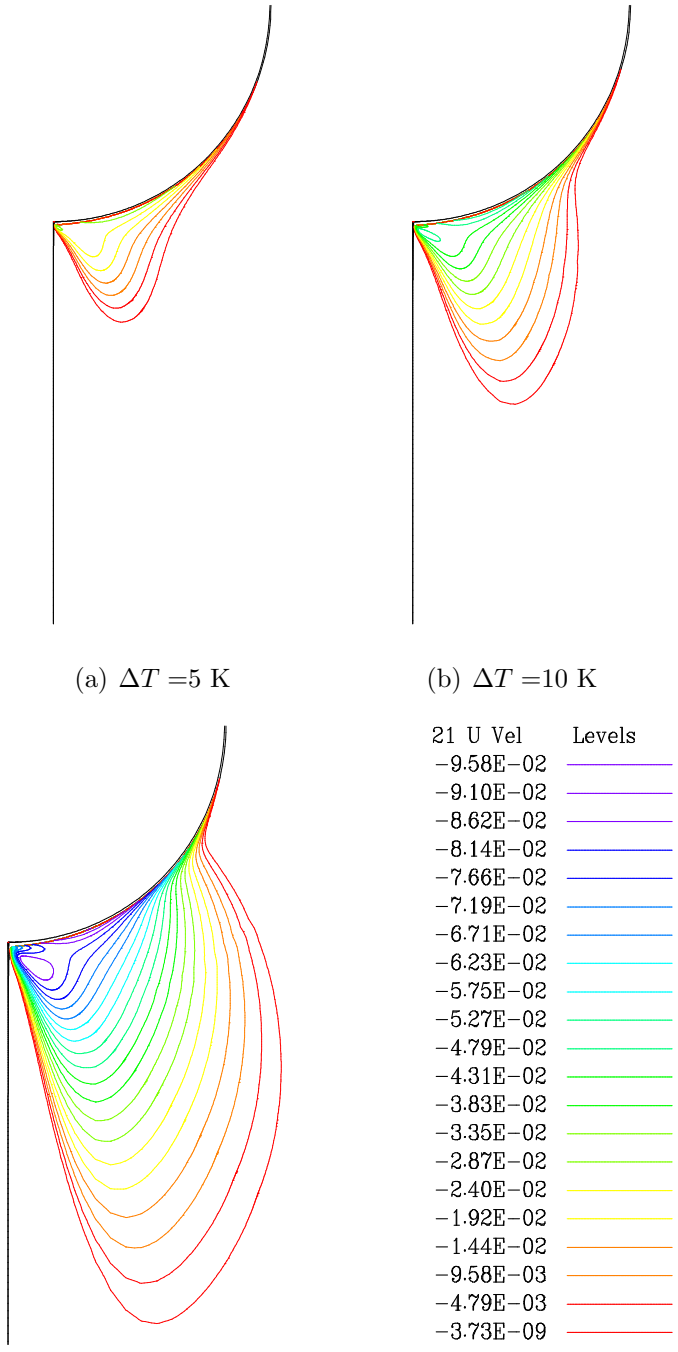

(a) ΔT =5 K

(b) ΔT =10 K

(c) ΔT =20 K

Figure 7.9: Effect of ΔT on the reverse flow region for $\mathrm{Re}_d = 50$ ($U_\infty = 7.3 \times 10^{-2}$ m/s).

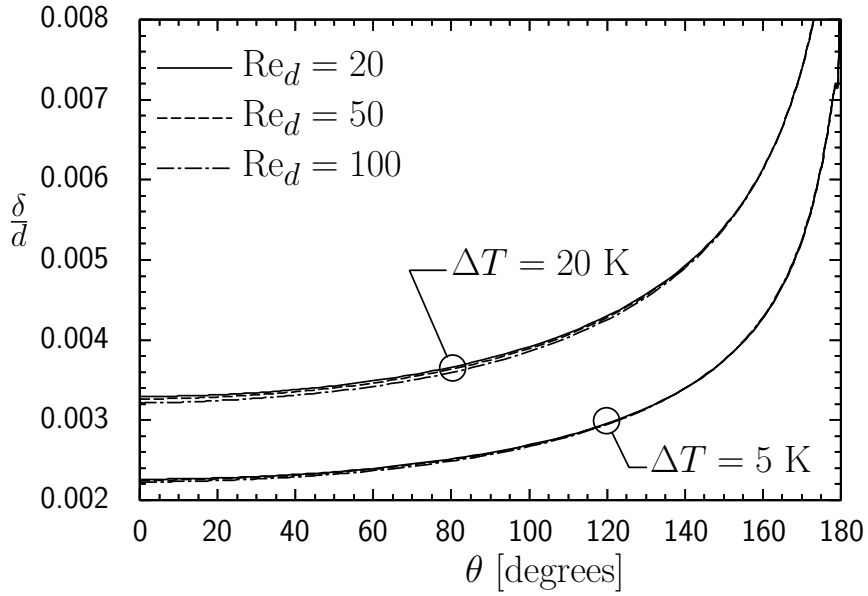

Figure 7.10: Effect of Re_d on the condensate thickness for $P_\infty = 1$ atm.

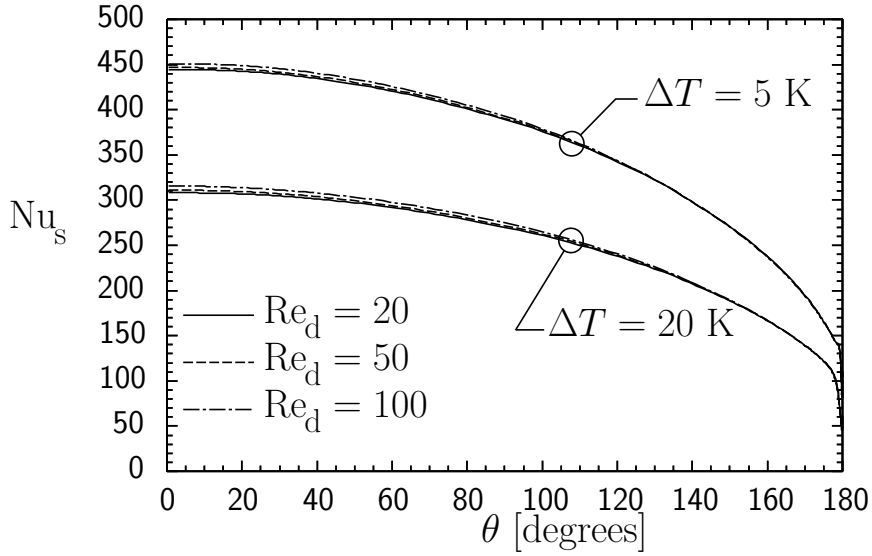

Figure 7.11: Effect of Re_d on the local Nusselt number for $P_\infty = 1$ atm.

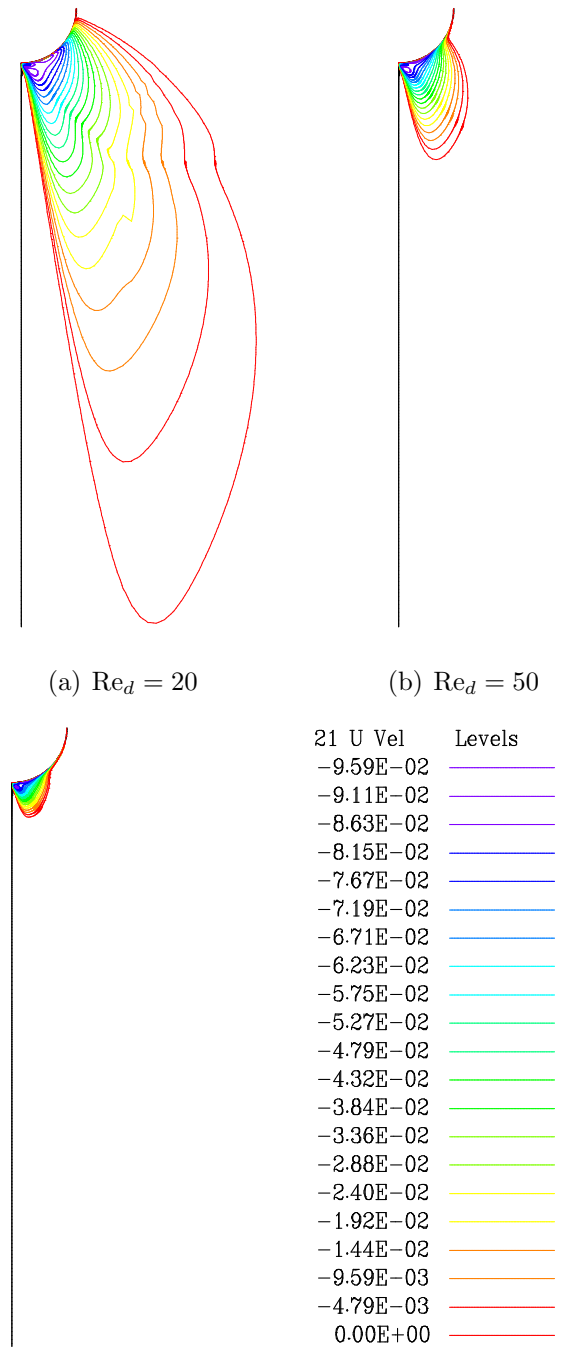

(a) $\mathrm{Re}_d = 20$ (b) $\mathrm{Re}_d = 50$

(c) $\mathrm{Re}_d = 100$

Figure 7.12: Effect of Re_d on the reverse flow region for $\Delta T = 20$ K.

approximately constant for these cases. For example, the minimum value of U changed from -9.59×10^{-2}m/s (-3.27 U_∞) for $\mathrm{Re}_d = 20$ ($U_\infty = 2.92\times10^{-2}$m/s) to -9.57×10^{-2}m/s (-0.66 U_∞) for $\mathrm{Re}_d = 100$ ($U_\infty = 1.46\times10^{-1}$m/s).

7.2.4 Effect of Changing P_∞

The effect of changing the free stream pressure P_∞ on the condensation process was investigated for $\mathrm{Re}_d = 50$ and $\Delta T = 5$, and 20 K. Changing the free stream pressure while keeping ΔT and Re_d fixed allowed studying the impact of changing the thermophysical and transport properties on the condensation process.

The effect of changing P_∞ on the development of δ is shown in Figure 7.13. The results show that decreasing P_∞ results in an increase in δ for the two values of ΔT. The differences in the film thickness are relatively small. For $\Delta T = 20$ K, the difference in the film thickness between pressures of 0.5 atm and 1 atm is less than 4.5% up to $\theta = 179°$. The difference between the film thickness for pressures of 1 atm and 2 atm over the same range is less than 4.7%.

This increase in film thickness with decreased free stream pressure is believed to be related mainly to the increase in the dynamic viscosity of the liquid as T_∞ decreases with P_∞ decreasing. A more viscous film will be thicker because it is less effected by interfacial shear. The viscosity increases approximately 23% for the temperature change corresponding to the pressure change from 1 atm to 0.5 atm. There is an increase of approximately 21% in the dynamic viscosity for the temperature change corresponding to a pressure change from 2 atm to 1 atm. As ΔT increases, differences in δ profiles for the different pressures become larger, indicating that the effect of a more viscous film is more noticeable for a greater liquid mass flow rates.

The influence of changing P_∞ on local Nusselt number, shown in Figure 7.14, is consistent with previous results. The decrease in Nu_s is related to an increase in δ as discussed earlier.

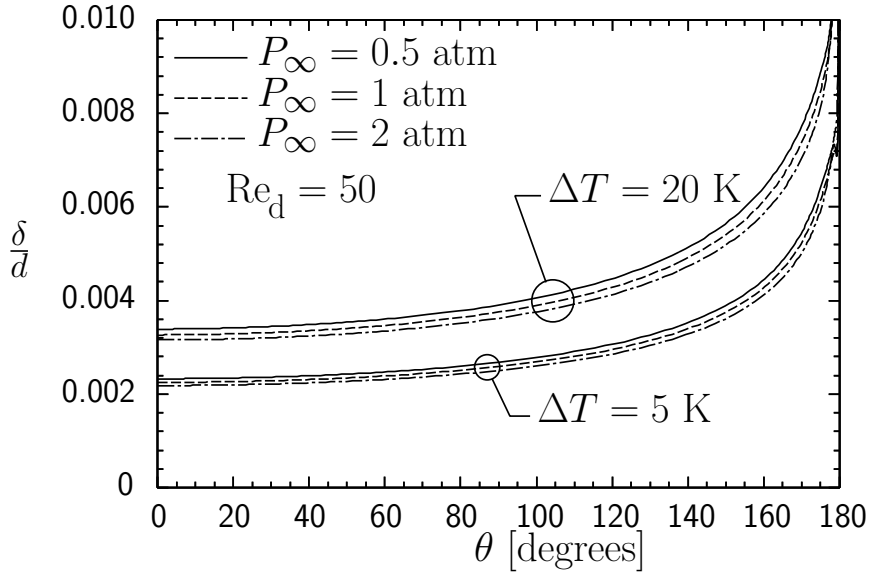

Figure 7.13: Effect of pressure on the condensate thickness for $\mathrm{Re}_d = 50$.

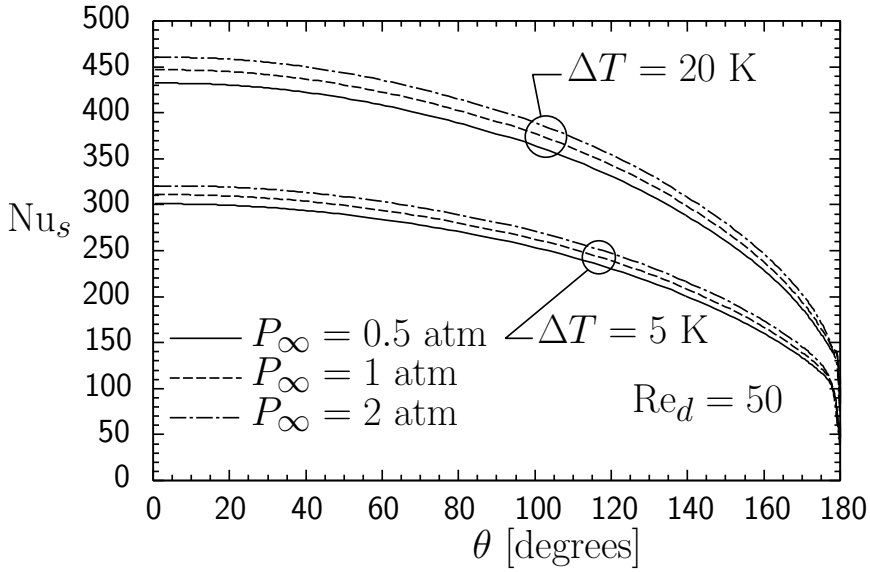

Figure 7.14: Effect of pressure on the local Nusselt number for $\mathrm{Re}_d = 50$.

Values of $\overline{\mathrm{Nu}}$ for $P_\infty = 0.5$ and 2 atm, $\Delta T = 5$ and 20 K, and $\mathrm{Re}_d = 50$ are given in Table 7.2; also shown in the table are values of Re_L. Comparing with Table 7.1, Re_L decreases by about 24% to 25% for the pressure change from 1 atm to 0.5 atm. The reduction in Re_L for the pressure change from 2 atm to 1 atm is about 23% to 24%. Most, but not all, of these changes are due to the change in dynamic viscosity. Because of the definition of Re_L, these results indicate that the condensate mass flow itself is not changed significantly by the change in pressure. There is an approximately 7% decrease in liquid mass flow rate with each of the pressure changes. This reduction is expected to be related to the increase in h_{fg} and decrease in k_L as the pressure decreases, plus combined effects of other property changes. Overall, the property change effects are smaller than the effect of changing ΔT.

Table 7.2: Average Nusselt number and film Reynolds number variation with P_∞ and ΔT for $\mathrm{Re}_d = 50$.

		$\mathrm{Re}_d = 50$	
P_∞ [atm]	ΔT [K]	$\overline{\mathrm{Nu}}$	Re_L
0.5	5	348.98	9.26
0.5	20	243.11	25.35
2	5	372.68	15.93
2	20	260.09	44.15

7.3 Mixture of Vapour and Non-condensable Gas Condensation

A detailed study was conducted to examine the effect of changing independently the values of W_∞, ΔT, Re_d, and P_∞ on condensation of steam from a downward flow of steam-air mixture on a horizontal tube. The effect of P_∞ on the condensation process was investigated using P_∞ = 0.5, 1, and 2 atm. For P_∞ = 1 atm, three flow rates corresponding to Re_d =20, 50, and 100 were used. The effect of non-condensing gas was examined using W_∞ = 0.001, 0.005, 0.01, and 0.05. For each value of W_∞, the effect of inlet-to-tube wall temperature difference ΔT was investigated using ΔT = 5, 10, and 20 K. For the additional values of P_∞, the effect of P_∞ was studied for Re_d = 50 , W_∞ = 0.001 and 0.05, and ΔT = 5 and 20 K. Detailed results for a selected case are presented first followed by analysis of the effects of different flow parameters on the condensation process.

7.3.1 Detailed Examination of Sample Results

The operating parameters for the selected case are Re_d = 100 , W_∞ =0.05 and ΔT = 20 K. Figure 7.15 shows the normalised film thickness $\frac{\delta}{d}$ versus $\frac{L_s}{d}$. The solid line is the film thickness measured in the direction normal to the tube surface. According to this definition of δ, $\delta \rightarrow \infty$ at the bottom of the tube as mentioned in Section 7.2.1. The dashed line in Figure 7.15 is the film height measured in the y direction. The film thickness increases gradually up to $\frac{L_s}{d} \approx 1$ or $\theta \approx 115°$. For ($1 < \frac{L_s}{d} \leq 1.57$), the film thickness increases with greater rate to become 3.94 times thicker than the film thickness at the top of the tube at ($\frac{L_s}{d} = 1.562$) which corresponds to $\theta = 179°$. Once the film transitions to a falling film below the tube, the film thickness decreases rapidly over a short distance due to gravitational force. Farther along the x direction, the film height decreases with very slow rate towards an equilibrium height.

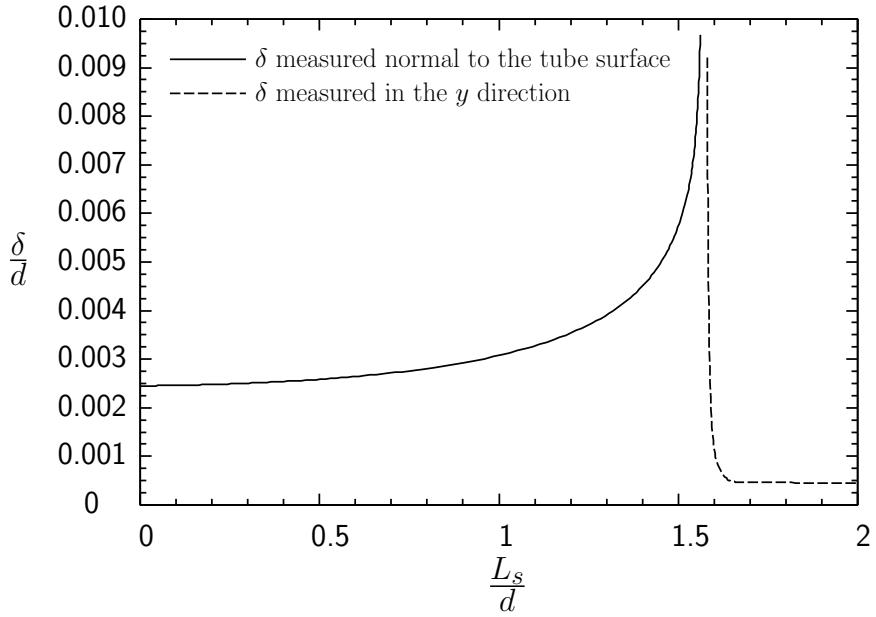

Figure 7.15: The condensate film thickness for $P_\infty = 1$ atm, $\mathrm{Re}_d = 100$, $W_\infty = 0.05$, and $\Delta T = 20$ K.

In Figure 7.16, the dimensionless U velocity profiles in the liquid film are plotted versus $y_L^\star$ at different axial locations. At $\frac{x}{d} = 0$ ($\theta = 90°$), the U profile has a parabolic shape and the normalised film thickness is $\frac{\delta}{d} = 2.8\times10^{-3}$. As the liquid reaches the falling film region, it accelerates due to gravity and the velocity profiles become essentially uniform because of the zero shear condition at $y = 0$. As a result, the film thickness decreases substantially over a short distance to reach $\frac{\delta}{d} = 6.69\times10^{-4}$ at $\frac{x}{d} = 0.55$. Farther in the x direction, the film thickness keeps decreasing to become $\frac{\delta}{d} = 4.5\times10^{-4}$ at $\frac{x}{d} = 2.5$. The film keeps accelerating and reaches an equilibrium height farther in the x direction. At the domain outlet, the dimensionless film thickness is $\frac{\delta}{d} = 4.16\times10^{-4}$.

The dimensionless U velocity profiles in the mixture region are given in Figure 7.17 for the same case. For $\frac{x}{d} = 0$, 2.5, and 12, the velocity is minimum at the interface and reaches a maximum value not far from the interface. Close to the bottom of the tube at $\frac{x}{d} = 0.52$ and 0.55, the U velocity profiles first decreases in the y direction and becomes negative indicating

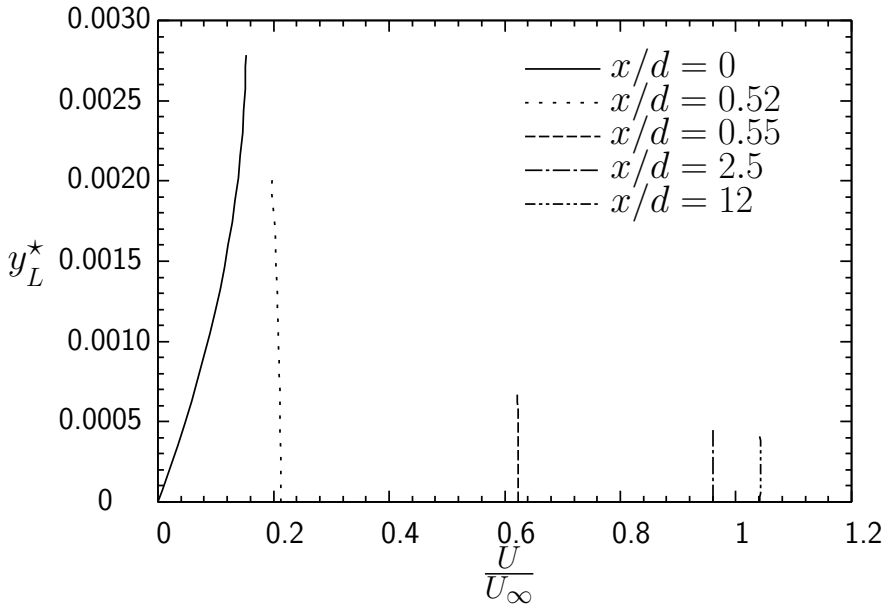

Figure 7.16: U velocity profiles in the liquid film at different locations for $P_\infty = 1$ atm, $\mathrm{Re}_d = 100$, $W_\infty = 0.05$, and $\Delta T = 20$ K.

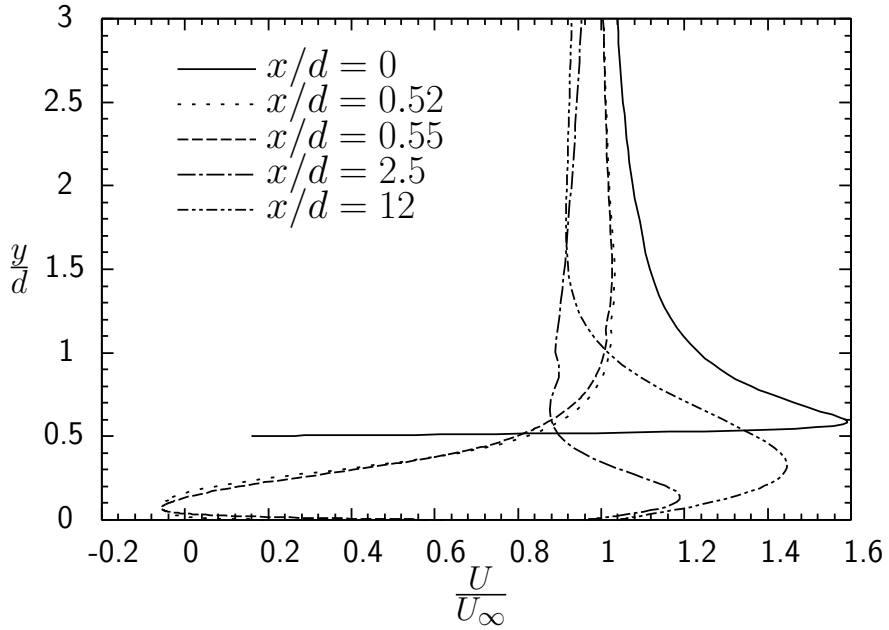

Figure 7.17: U velocity profiles in the mixture at different locations for $P_\infty = 1$ atm, $\mathrm{Re}_d = 100$, $W_\infty = 0.05$, and $\Delta T = 20$ K.

the occurrence of flow reversal. Then, the profiles reach minimum value not far from the interface. At all shown axial locations, the profiles become more uniform farther in the y direction and they approach a value of 1 as $\frac{y}{d} = 16$.

The isobars around the tube are shown in Figure 7.18. The shown values of the pressure are the relative to the outlet pressure and are in Pa. In general, the differences in the pressure

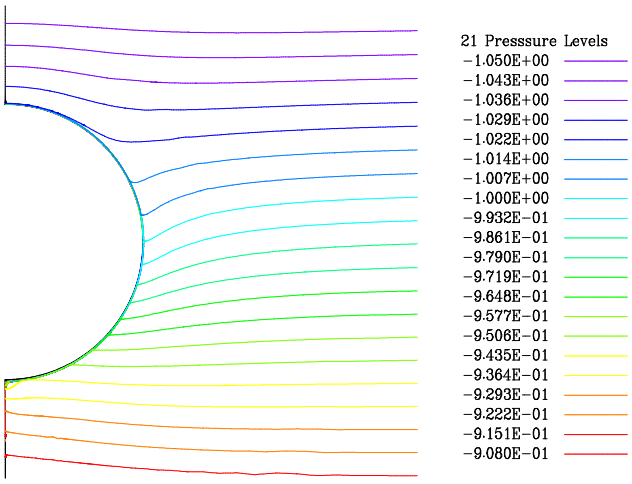

Figure 7.18: Relative pressure distribution arount the tube for $P_\infty = 1$ atm, $\mathrm{Re}_d = 100$, $W_\infty = 0.05$, and $\Delta T = 20$ K.

correspond to the differences in the hydrostatic pressure. In the mixture, the pressure profiles are uniform except near the interface where minor changes in P values occur. These changes result from accelerating mixture flow as it moves around the tube. Also, these changes have no sensible impact on the properties nor on W_{int} values.

In Figure 7.19, the dimensionless temperature profiles in the liquid versus $y_L^\star$ are shown at different axial locations. At $\frac{x}{d} = 0$, the T profile variation is linear with $T = T_{\text{wall}}$ at the tube surface. After the tube ($\frac{x}{d} > 0.5$), the falling film is still colder than the mixture because it was in contact with the tube wall. In the falling film region, there is a small amount of condensation to the cooler film, but the film warms up quickly because no energy leaves at $y = 0$. The condensate mass flow rate that is added to the film after the tube is

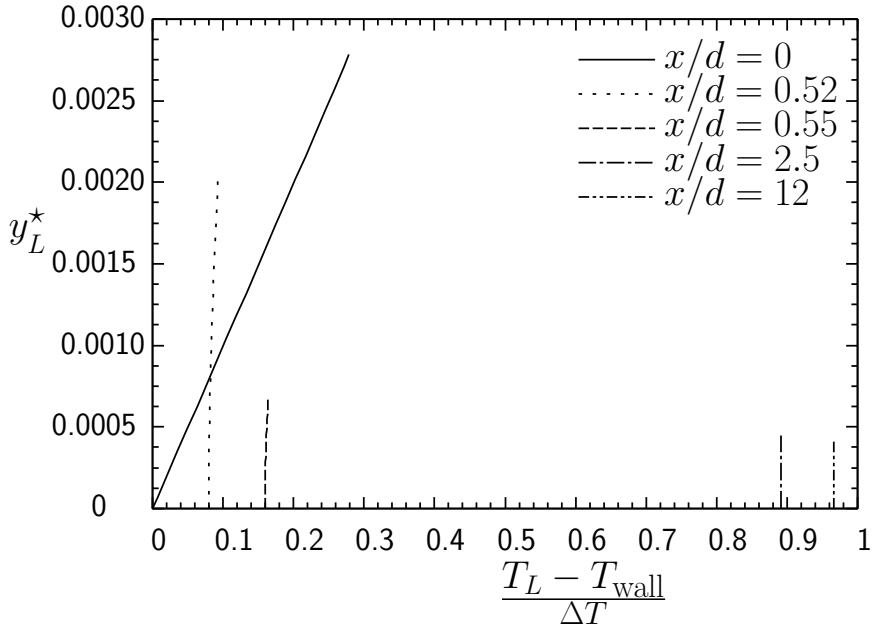

Figure 7.19: Temperature profiles in the liquid film at different locations for $P_\infty = 1$ atm, $\text{Re}_d = 100$, $W_\infty = 0.05$, and $\Delta T = 20$ K.

2.7% of the total condensate mass flow rate. The film temperature increases and develops to a uniform as it approaches the outlet.

Figure 7.20 shows the dimensionless temperature profiles in the mixture at $\frac{x}{d} = 0$, 0.52, 0.55, 2.5, and 12. At $\theta = 90°$, $\frac{x}{d} = 0$, T reaches a minimum value at the interface corresponding to W_{int} and local value of the vapour partial pressure $P_{\text{v,int}}$. The same trend can be seen in the falling film region with T_{int} increasing in the downstream direction. In all locations, T increases in the y direction and reaches the upstream value at a distance not far from the interface.

Figure 7.21 shows W versus $\frac{y}{d}$ at different x locations. The W value is substantially higher around the tube where most of the condensation occurs. At $\frac{x}{d} = 0$, the W value decreases rapidly in the y direction and reaches the free stream value, W_∞, at $\frac{y}{d} \approx 0.725$. Close to the bottom of the tube, $\frac{x}{d} = 0.52$ and 0.55, the W value decreases with a moderate rate in the y direction and reaches W_∞ value at about the same height as the profile at

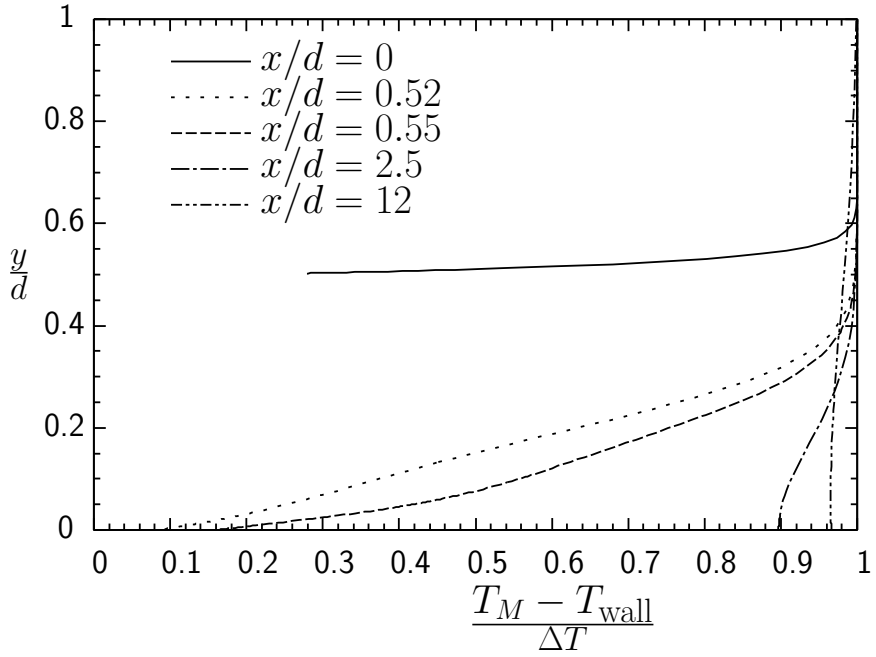

Figure 7.20: Temperature profiles in the mixture at different locations for $P_\infty = 1$ atm, $\text{Re}_d = 100$, $W_\infty = 0.05$, and $\Delta T = 20$ K.

$\frac{x}{d} = 0$. For $\frac{x}{d} = 2.5$ and 12, W value decreases gradually in the y direction. Also, it can be seen that W profile becomes more uniform towards the outlet.

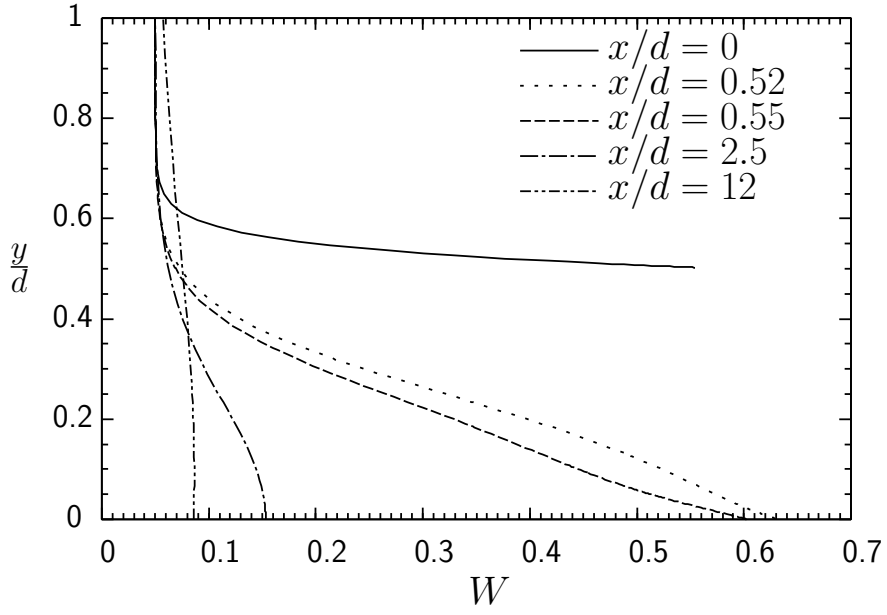

Figure 7.21: Gas mass fraction profiles in the mixture at different locations for $P_\infty = 1$ atm, $\mathrm{Re}_d = 100$, $W_\infty = 0.05$, and $\Delta T = 20$ K.

Because of the density difference of a factor of approximately 1270 in this case, the magnitude of the velocity in the mixture is much larger than the velocity in the liquid. Therefore, the velocity vector fields for both phases are plotted in Figure 7.22 with different scales to enable visualization in the same figure. The red vectors are in the mixture and the blue vectors, not visible in Figure 7.22(a), are in the liquid. Figure 7.22(b) shows the velocity vectors in the mixture as the mixture flow approaches the interface at the top of the tube. The much smaller liquid vectors are covered partially by the mixture vectors. Figure 7.22(c) shows the details of the flow pattern in both fluids as the liquid film leaves the tube surface and starts descending in the falling film region. The velocity in the liquid increases near the interface and accelerates in the falling film.

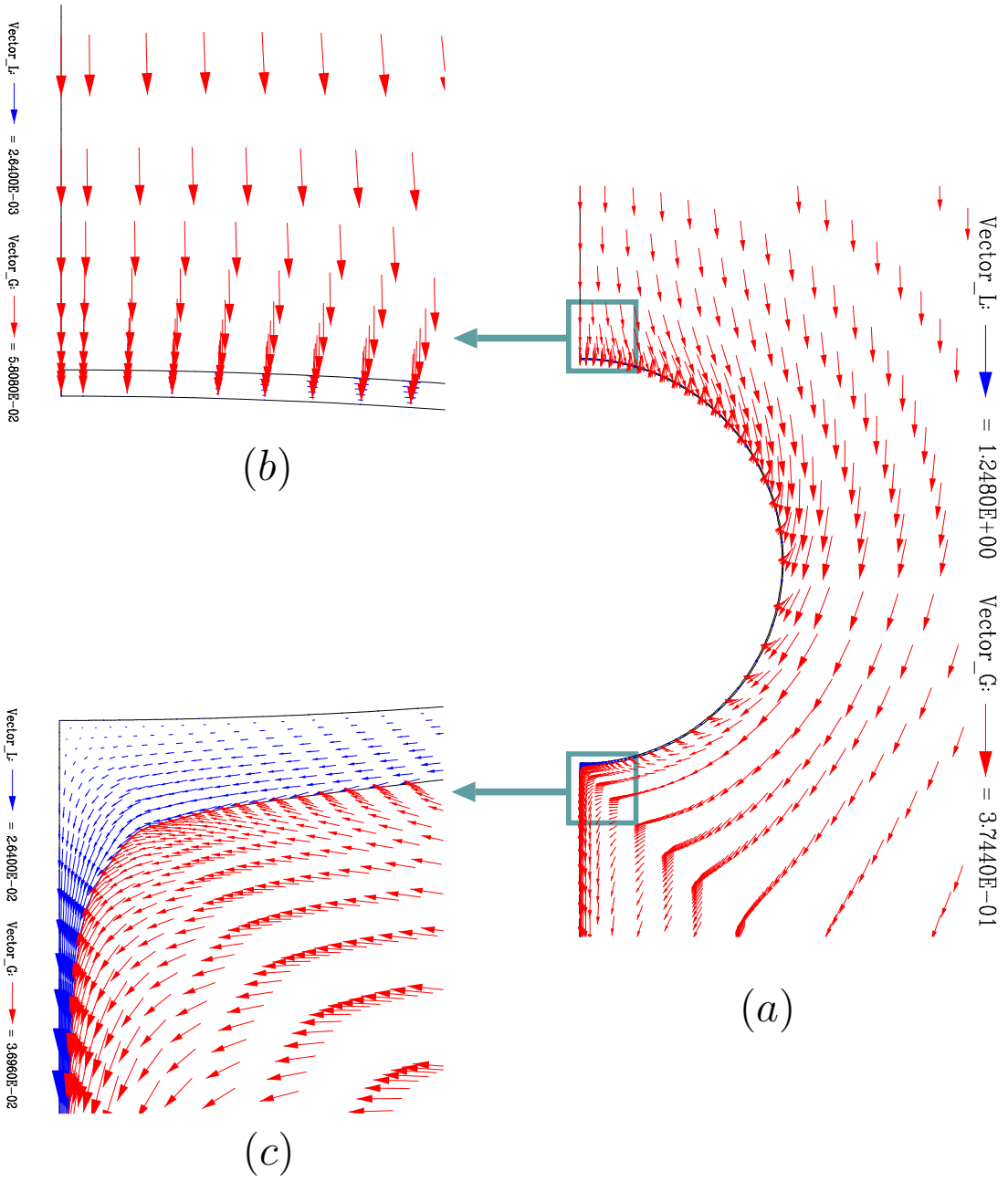

Figure 7.22: Details of the flow pattern for $\mathrm{Re}_d = 100$, W_∞ =0.05 and $\Delta T = 20$ K at: (a) around the tube, (b) at the top of the tube, and (c) at the bottom of the tube.

7.3.2 Effect of Changing W_∞

Effect of changing W_∞ on the film thickness around the tube is shown in Figure 7.23 for $P_\infty = 1$ atm, $\mathrm{Re}_d = 50$, and $\Delta T = 5$ K. Increasing the content of non-condensing gas in the mixture leads to a noticeable decrease in the film thickness around the tube. The same

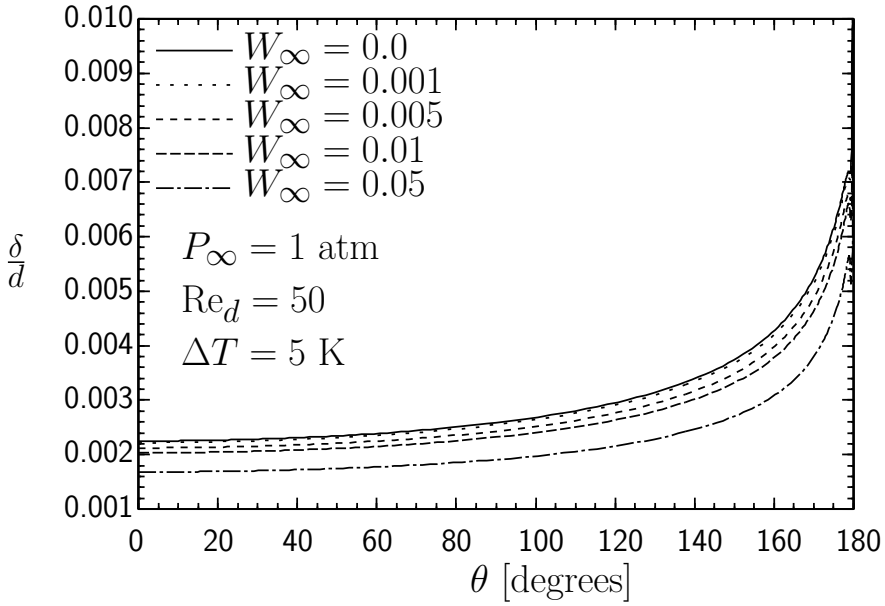

Figure 7.23: Effect of W_∞ on condensate height for $\mathrm{Re}_d = 50$, $P_\infty = 1$ atm and $\Delta T = 5$K.

trend can be seen in Figures 7.24 and 7.25 for $\Delta T = 10$ and 20 K, respectively. At the top of the tube ($\theta = 0°$), the film thickness for $\Delta T = 5$ K and $W_\infty = 0.05$ is 25.4% smaller than the film thickness for $W_\infty = 0$ at the same ΔT. The percentage difference between any two δ profiles remains approximately constant for the most of θ range. For $\Delta T = 10$ and 20 K, the percentage difference in δ at ($\theta = 0°$) between the $W_\infty = 0.05$ and 0 cases is 27% and 30%, respectively. These differences stay approximately constant along the tube circumference. The sharp change in δ profiles in Figure 7.23 at $177° < \theta < 180°$ is due to the concave shape of the interface that forms at this region. This will be shown later in the discussion of changing ΔT.

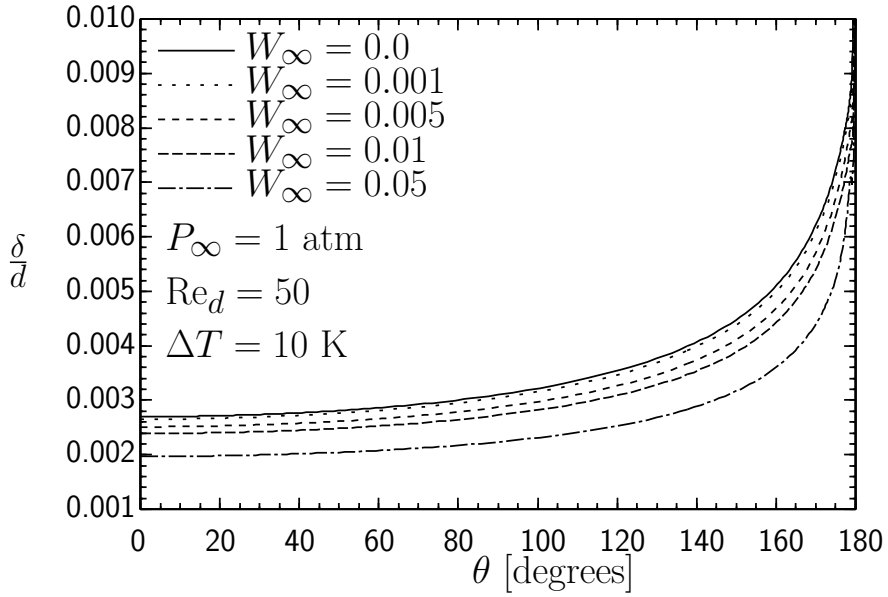

Figure 7.24: Effect of W_∞ on condensate height for $\mathrm{Re}_d = 50$, $P_\infty = 1$ atm and $\Delta T = 10$K.

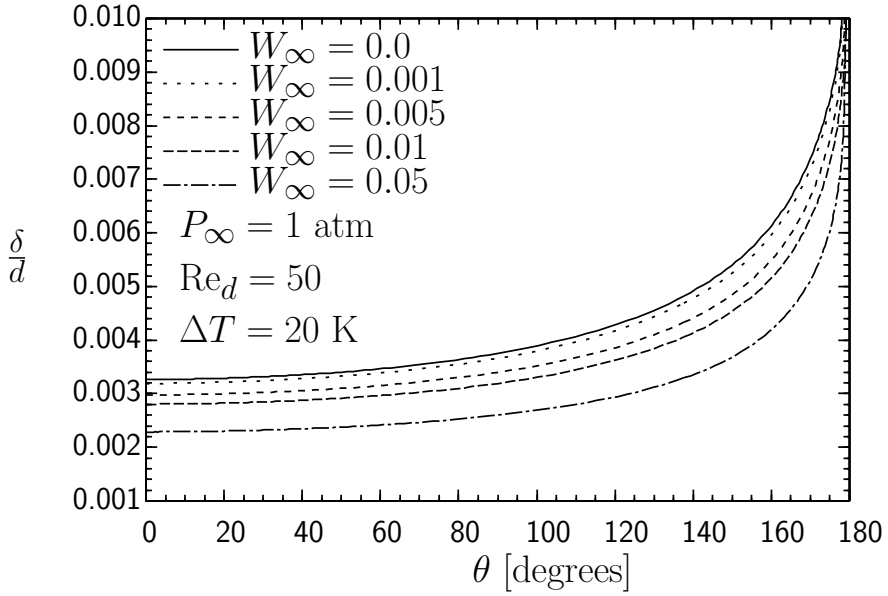

Figure 7.25: Effect of W_∞ on condensate height for $\mathrm{Re}_d = 50$, $P_\infty = 1$ atm and $\Delta T = 20$K.

Figures 7.26 to 7.28 show the effect of W_∞ on Nu_s for $\Delta T = 5$, 10, and 20 K, respectively. The presence of the non-condensing gas in the mixture, even with very small concentration, decreases Nu_s around the tube for all values of ΔT presented. As the content of the gas in

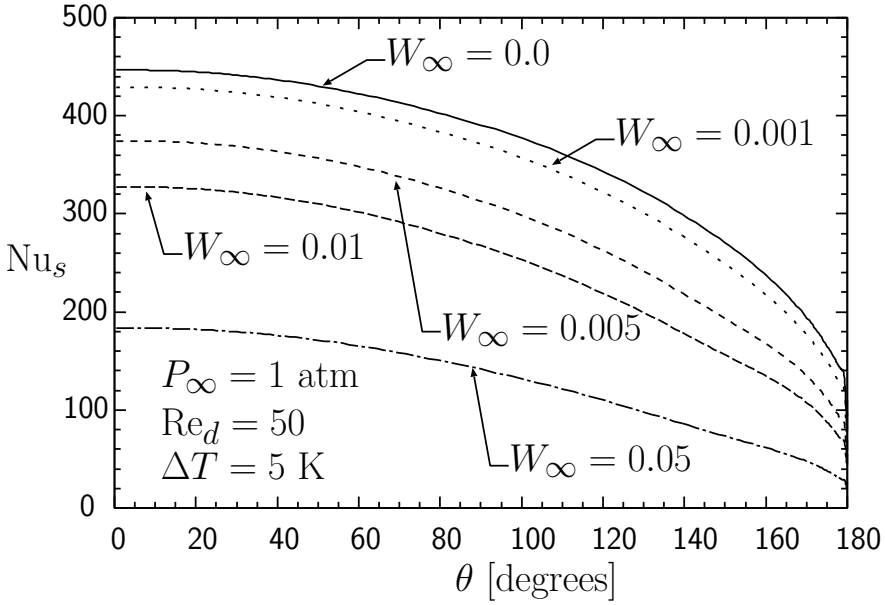

Figure 7.26: Effect of W_∞ on Nu_s for $\mathrm{Re}_d = 50$, $P_\infty = 1$ atm and $\Delta T = 5$K.

the mixture increases, Nu_s, and hence the condensation rate, decreases. For $\Delta T = 5$ K, the maximum value of Nu_s, at $\theta = 0°$, drops by 3.9%, 16.2%, 26.6%, and 58.9% for $W_\infty = 0.001$, 0.005, 0.01, and 0.05, respectively compared to the case of pure steam. In comparison with corresponding pure steam case, the reduction in Nu_s at $\theta = 0°$ increases with ΔT to reach 62% and 66.5% for $W_\infty = 0.05$ at $\Delta T = 10$ and 20 K, respectively. The decrease in Nu_s with ΔT is related to the increase in the thermal resistance across the condensate as the film thickness increases with increasing ΔT. The sharp reduction in Nu_s as θ approaches 180° is due to the rapid thickening of the film at the bottom of the tube as it transitions to a vertical falling film.

Figure 7.29 shows the variation of W_{int}, the interface gas mass fraction, with θ for $P_\infty = 1$ atm, $\mathrm{Re}_d = 50$, and $\Delta T = 5$ K. For all values of W_∞, W_{int} increases slightly with θ up to

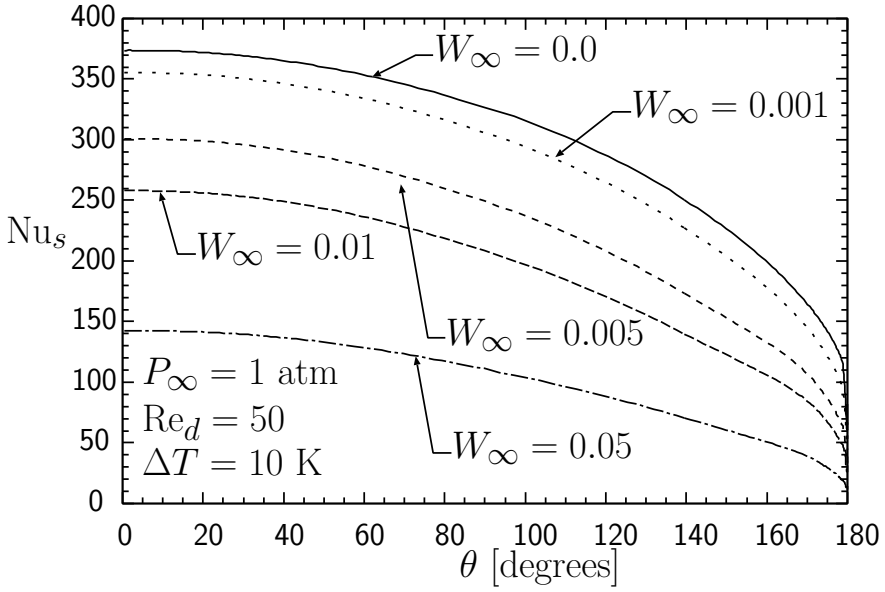

Figure 7.27: Effect of W_∞ on Nu_s for $\mathrm{Re}_d = 50$, $P_\infty = 1$ atm and $\Delta T = 10$K.

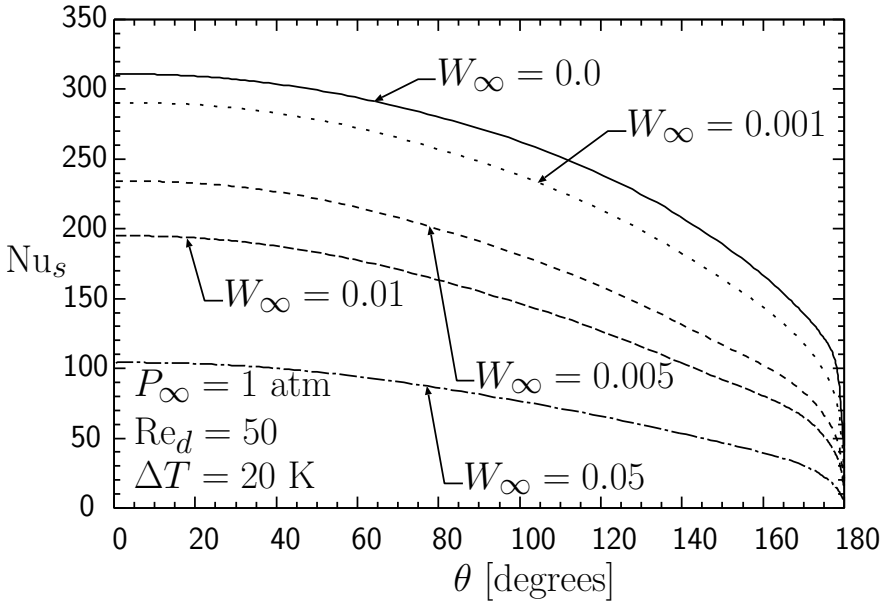

Figure 7.28: Effect of W_∞ on Nu_s for $\mathrm{Re}_d = 50$, $P_\infty = 1$ atm and $\Delta T = 20$K.

$\theta \approx 170°$. Afterward, W_{int} increases with θ at a relatively higher rate, especially for the lowest value of W_∞, to reach a maximum value at $\theta \approx 179°$. This can be explained by relatively lower flow rate of steam from the free stream to the mixture zone just behind the tube in the down stream direction. To clearly examine the interface gas mass fraction

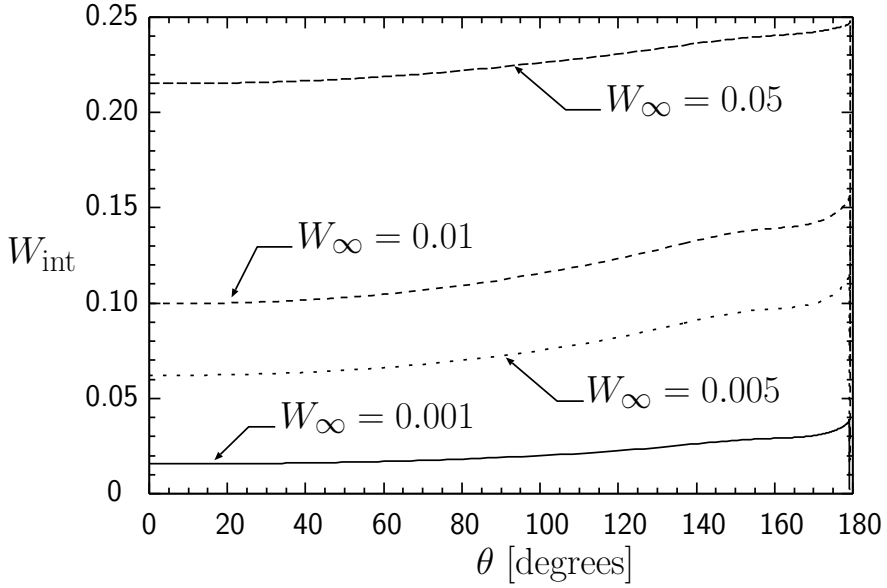

Figure 7.29: Effect of W_∞ on W_{int} at the interface for $\text{Re}_d = 50$, $P_\infty = 1$ atm and $\Delta T = 5$K.

in the falling film region after the tube, Figure 7.30 shows W_{int} for $\Delta T = 5$ K versus the normalised distance $(\frac{L_s}{d})$ measured from the top of the tube ($\theta = 0°$). The vertical solid line at $(\frac{L_s}{d} = 1.57)$ indicates the end of the tube circumference. The value of W_{int} decreases sharply in the down stream direction to reach an equilibrium value farther downstream.

As ΔT increases, the rapid increase in W_{int} for $170° < \theta < 179°$ becomes more recognizable specifically for the lower values of W_∞ as shown in Figures 7.31 and 7.32. The maximum value of W_{int} increases with ΔT. For example, the maximum value of W_{int} increases from 0.248 for $W_\infty = 0.05$ and $\Delta T = 5$ K to reach 0.408 and 0.631 for $\Delta T = 10$ and 20 K, respectively. This is attributed to greater condensation rate associated with increasing ΔT. As a result, more air accumulates in the mixture layer that is adjacent to the condensate

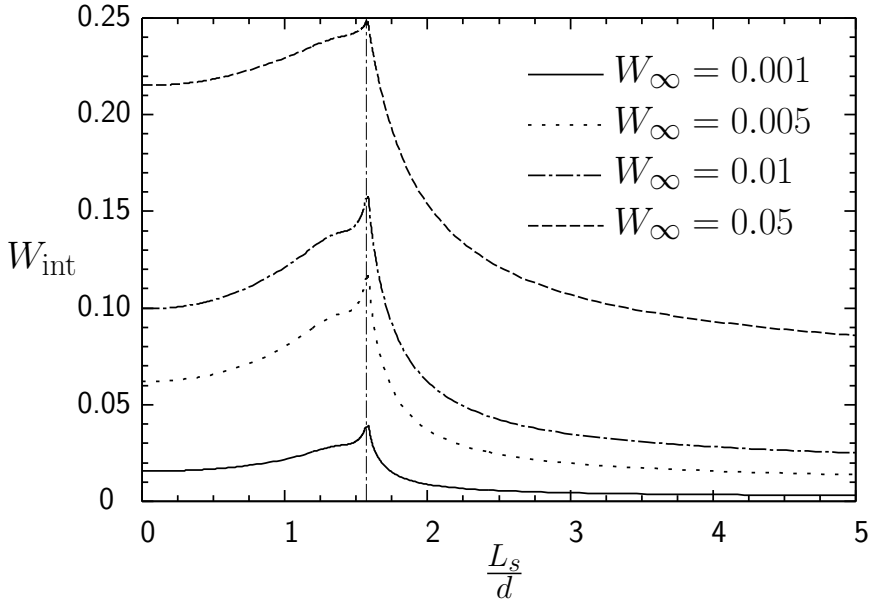

Figure 7.30: Effect of W_∞ on W_{int} at the interface for $\text{Re}_d = 50$, $P_\infty = 1$ atm and $\Delta T = 5$K.

film because the interface is impermeable to non-condensing gas.

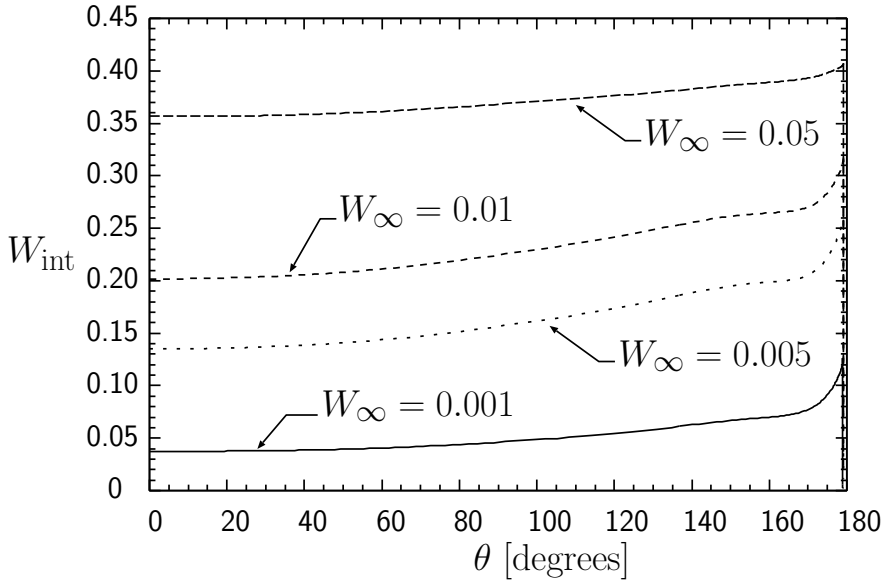

Figure 7.31: Effect of W_∞ on W_{int} at the interface for $\text{Re}_d = 50$, $P_\infty = 1$ atm and $\Delta T = 10$K.

Values of the average Nusselt number and the film Reynolds number for all performed

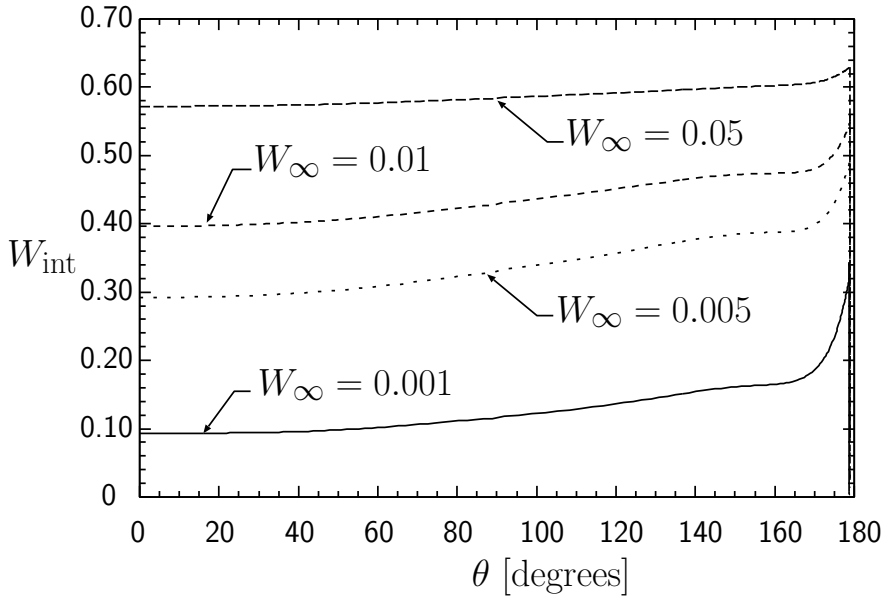

Figure 7.32: Effect of W_∞ on W_{int} at the interface for $\text{Re}_d = 50$, $P_\infty = 1$ atm and $\Delta T = 20$K.

tests at $P_\infty = 1$ atm are summarised in Table 7.3. The table shows the decreasing mass flow rate of liquid with increased W_∞ through the decrease in Re_L with increased W_∞. The dynamic viscosity in the film Reynolds number was evaluated at T_∞ that corresponds to the upstream pressure. At $W_\infty = 0.001$, $\text{Re}_d = 50$ and $\Delta T = 20$ K, the condensate mass flow rate drops by 9.1% compared to the corresponding pure vapour case value. The magnitude of the reduction in Re_L increases with W_∞ to reach 30.1%, 43.2% and 70.6% for W_∞ =0.005, 0.01, and 0.05, respectively. A similar argument can be made for changes in $\overline{\text{Nu}}$. The effect of W_∞ on Re_L and $\overline{\text{Nu}}$ is also shown graphically in Figures 7.33 and 7.34 for $P_\infty = 1$ atm, $\text{Re}_d = 50$, and $\Delta T = 5$, 10, and 20 K.

To examine the effect of W_∞ on the reverse flow, the U velocity contours for $U < 0$ are plotted in Figure 7.35 for $\text{Re}_d = 50$ and $\Delta T = 20$ K. Both the intensity and the extent of the reverse flow decrease as W_∞ increases. This trend is due to increased W_{int} and decreased condensation rate. With decreased condensation rate there is less suction of vapour towards the interface below the tube. Note that the larger negative value of U contours plotted in

Table 7.3: Average Nusselt number and Re_L variation with W_∞, ΔT, and Re_d for $P_\infty = 1$ atm.

W_∞	ΔT [K]	$\mathrm{Re}_d = 20$		$\mathrm{Re}_d = 50$		$\mathrm{Re}_d = 100$	
		$\overline{\mathrm{Nu}}$	Re_L	$\overline{\mathrm{Nu}}$	Re_L	$\overline{\mathrm{Nu}}$	Re_L
0	5	360.13	12.01	361.28	12.25	363.14	12.31
	10	301.12	20.35	302.46	20.44	304.65	20.59
	20	250.32	33.54	251.80	33.74	254.28	34.07
0.001	5	326.48	11.06	342.16	11.59	350.52	11.88
	10	264.43	17.86	281.95	19.04	291.52	19.69
	20	209.09	27.98	228.96	30.66	240.07	32.15
0.005	5	249.81	8.45	287.16	9.72	310.10	10.50
	10	194.47	13.12	228.90	15.44	252.45	17.03
	20	146.81	19.61	176.42	23.57	200.63	26.82
0.01	5	205.91	6.96	244.71	8.27	273.53	9.25
	10	160.28	10.79	191.52	12.90	219.97	14.82
	20	117.22	15.63	143.74	19.17	169.69	22.64
0.05	5	108.97	3.64	129.49	4.33	152.35	5.10
	10	85.11	5.66	101.85	6.77	122.48	8.15
	20	62.48	8.23	75.27	9.91	91.74	12.07

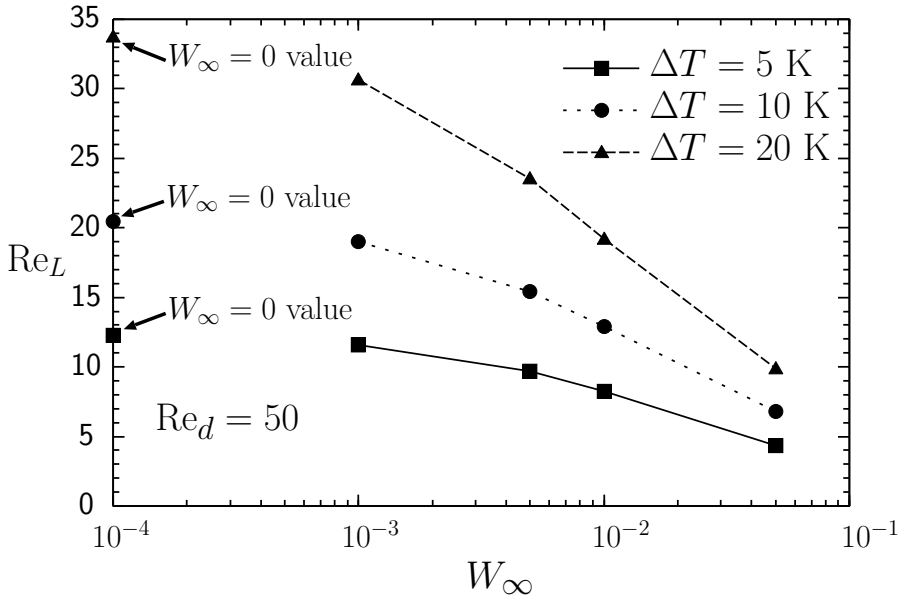

Figure 7.33: Effect of W_∞ on condensate mass flow rate, Re_L, for $P_\infty = 1$ atm and $\mathrm{Re}_d = 50$.

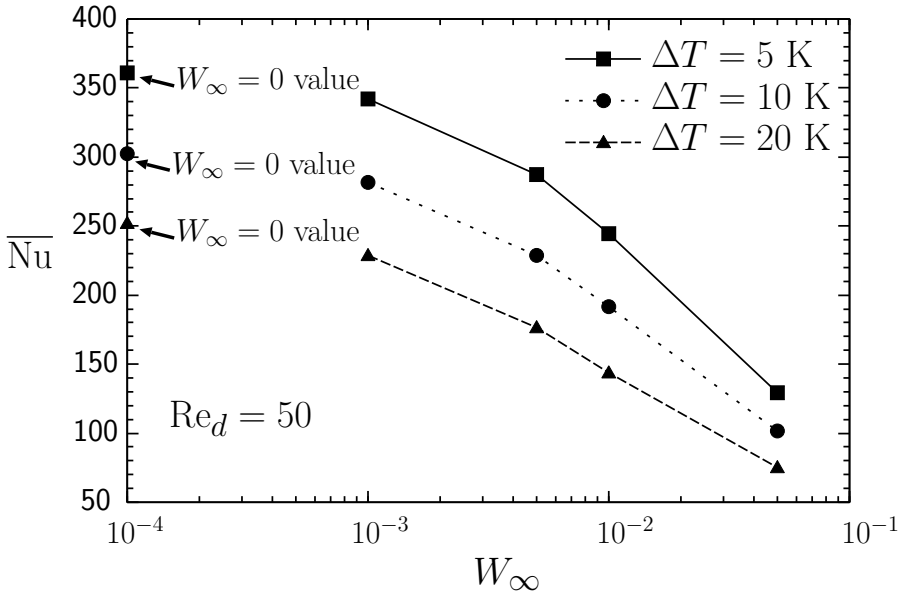

Figure 7.34: Effect of W_∞ on the average Nusselt number, $\overline{\mathrm{Nu}}$, for $P_\infty = 1$ atm and $\mathrm{Re}_d = 50$.

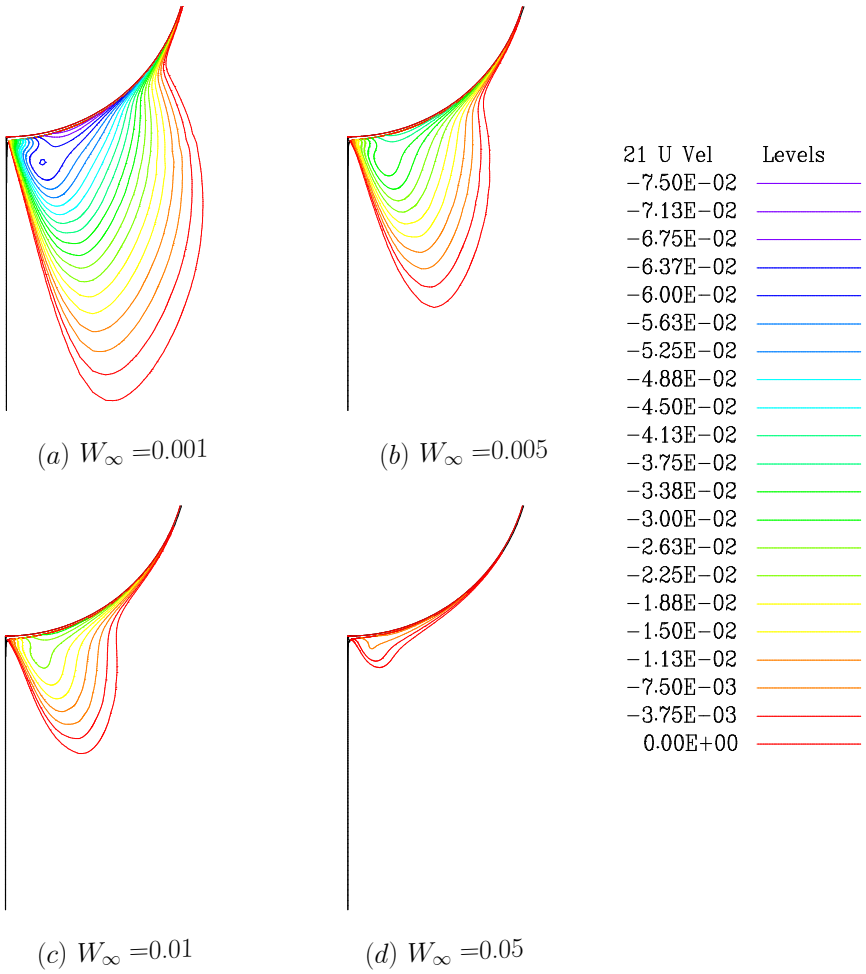

(*a*) W_∞ =0.001 (*b*) W_∞ =0.005

(*c*) W_∞ =0.01 (*d*) W_∞ =0.05

Figure 7.35: Effect of W_∞ on the reverse flow region below the tube for $\mathrm{Re}_d = 50$ ($U_\infty = 7.3\times10^{-2}$ m/s) and $\Delta T = 20$ K.

Figure 7.35 is 7.5×10^{-2}m/s which is about 102.7% of U_∞.

7.3.3 Effect of Changing ΔT

Figure 7.36 shows the variation of the film thickness with ΔT along θ for $P_\infty = 1$ atm, $\mathrm{Re}_d = 50$, and $W_\infty = 0.001$ and 0.05. Similar to the case of pure vapour, the condensate film thickens as ΔT increases for all values of W_∞. Differences between δ profiles for the same gas content and different values of ΔT remain approximately consistent for the whole range of θ. These differences, however, decrease as W_∞ increases from 0.001 to 0.05. The

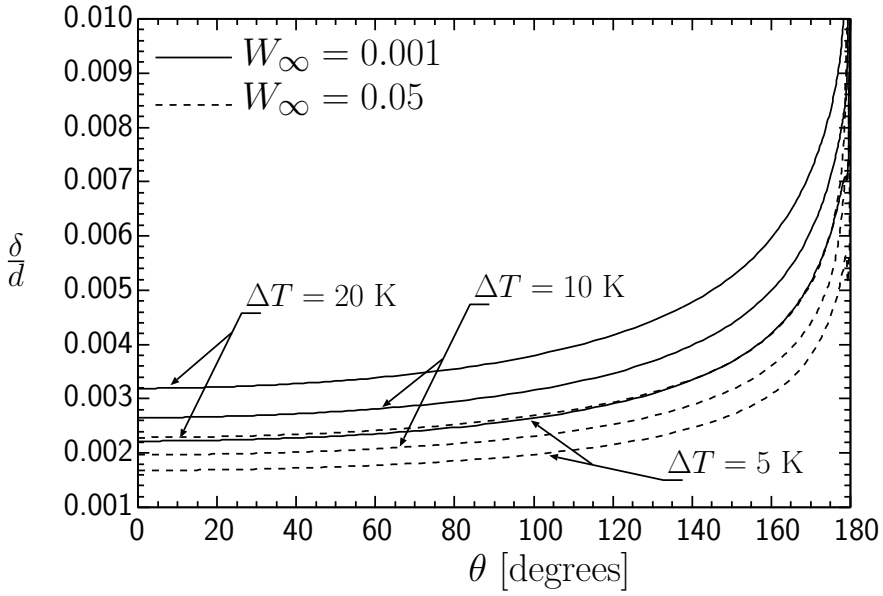

Figure 7.36: Effect of ΔT on condensate height for $\mathrm{Re}_d = 50$ and $P_\infty = 1$ atm.

same trend can be noticed for Nu_s as shown in Figure 7.37. In Figure 7.38, a region at the bottom of the tube for $\mathrm{Re}_d = 50$ and $W_\infty = 0.01$ is enlarged to show the variation of the interface shape with ΔT. For $\Delta T = 5$ K, the interface thins as it approaches the falling film zone forming a concave surface over a narrow range of θ. The concave shape appears as a sharp change in δ profiles for $\Delta T = 5$ K as seen in Figures 7.23 and 7.36. As ΔT increases,

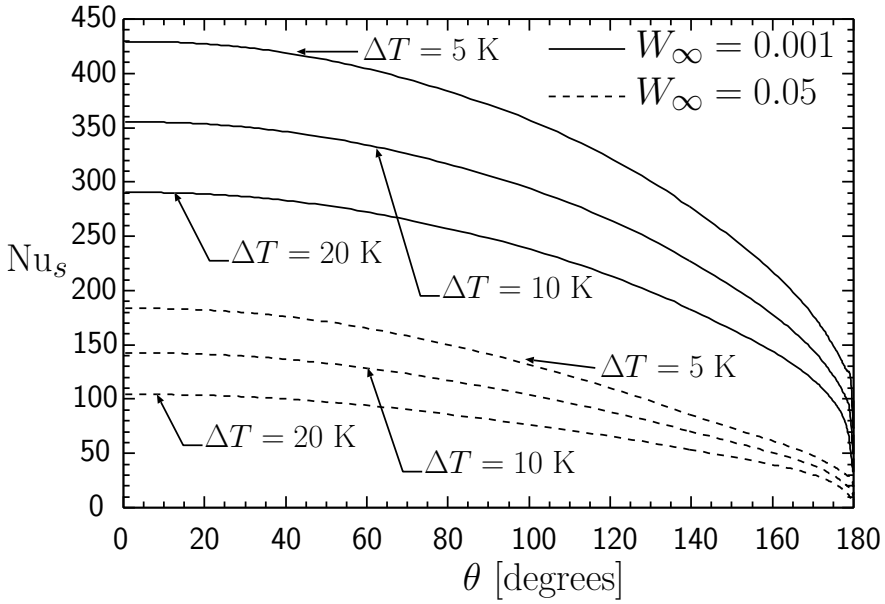

Figure 7.37: Effect of ΔT on Nu_s for $\mathrm{Re}_d = 50$ and $P_\infty = 1$ atm.

the transition to the falling film becomes smoother.

Table 7.3 shows that the magnitude of the reduction in Re_L value compared to the pure steam case increases with ΔT for all values of W_∞ considered. For example, at $W_\infty = 0.05$ and $\mathrm{Re}_d = 50$, the reduction in Re_L increases from 64.7% at $\Delta T = 5$ K to reach 66.9% and 70.6% for ΔT =10 K and 20 K, respectively. The same trends are observed for $\overline{\mathrm{Nu}}$.

Figure 7.39 illustrates the effect of changing ΔT on the reverse flow for $\mathrm{Re}_d = 50$ and $W_\infty = 0.001$. Both the intensity and the extent of the reverse flow increase with ΔT. For $\Delta T = 20$ K, the reverse flow region extends to $0.75d$ beyond the tube.

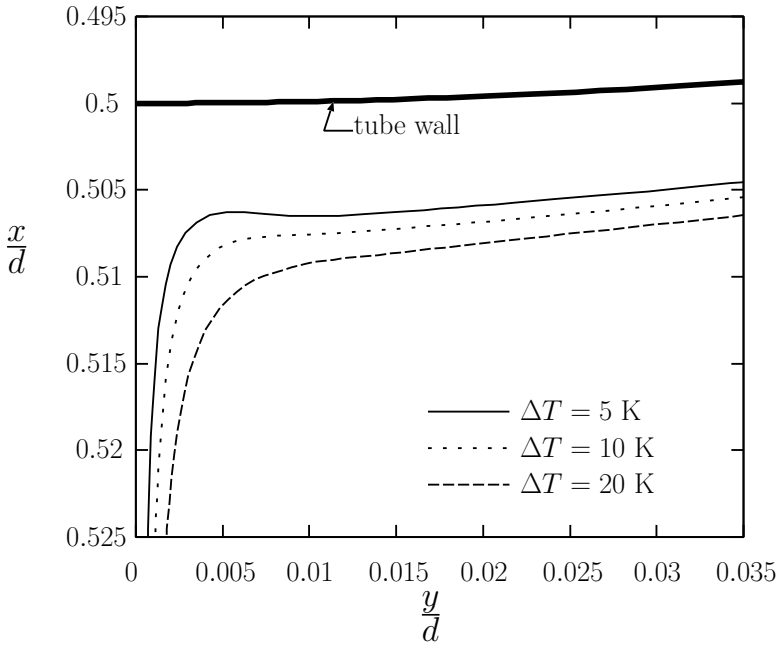

Figure 7.38: Change of interface shape with ΔT at the tube bottom for $P_\infty = 1$ atm, $\mathrm{Re}_d = 50$, and $W_\infty = 0.01$.

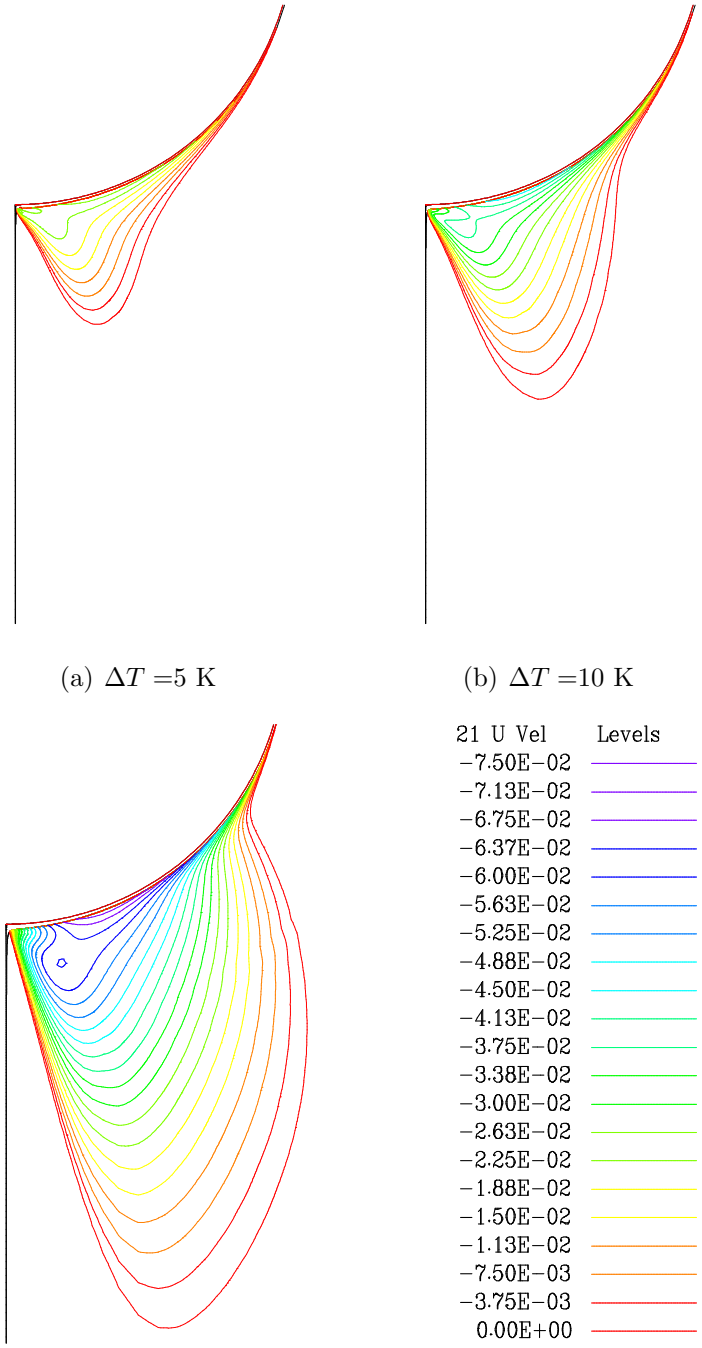

(a) ΔT =5 K

(b) ΔT =10 K

(c) ΔT =20 K

Figure 7.39: Effect of ΔT on the reverse flow region for $\mathrm{Re}_d = 50$ ($U_\infty = 7.3{\times}10^{-2}$ m/s) and W_∞ =0.001.

7.3.4 Effect of Changing Re_d

Effect of Re_d on the condensate film thickness is demonstrated in Figure 7.40 for $P_\infty = 1$ atm, $\Delta T = 5$ K , and $W_\infty = 0.001$ and 0.05. Similar to the cases of pure vapour shown in

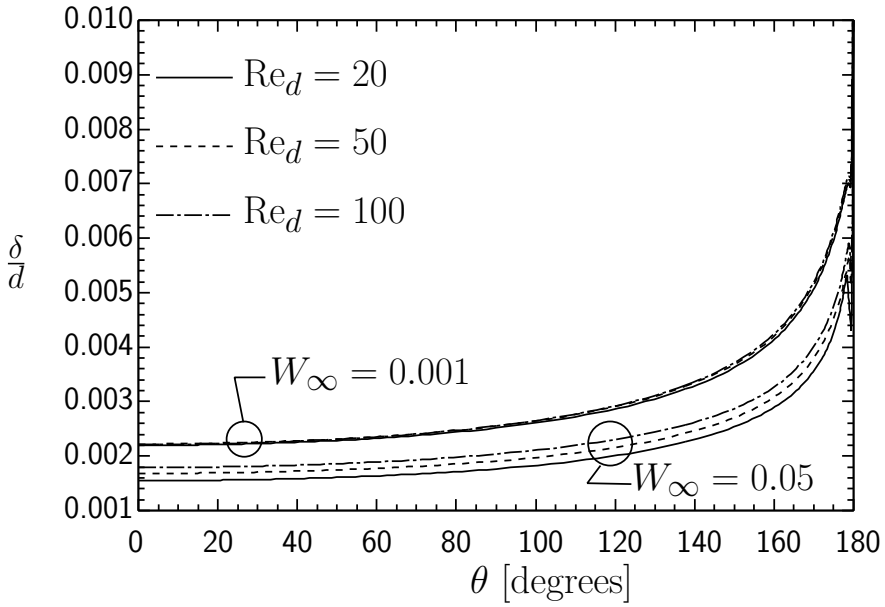

Figure 7.40: Effect of Re_d on condensate height for $\Delta T = 5$ K and $P_\infty = 1$ atm.

Figure 7.10, Re_d has small effect on δ profiles for the lower value of W_∞. As W_∞ increases, the influence of Re_d on the film thickness becomes more noticeable. In these cases the film thickness increases with Re_d, which is the opposite of the trend found for pure vapour. The same trend can also be seen in Figure 7.41 for both values of W_∞. This behaviour can be explained with the aid of Figure 7.42 that shows the effect of Re_d on W_{int} for $P_\infty = 1$ atm, $W_\infty = 0.05$ and $\Delta T = 5$ and 20 K. Increasing the value of Re_d for a fixed value of ΔT has two effects on the film thickness. The first effect is that increasing Re_d leads to an increase in the interfacial shear stress. The increasing interfacial shear stress thins the film, especially for the upper part of the tube ($\theta \leq 90°$) that is exposed to the free stream. On the other hand, increasing Re_d improves mixing in the mixture region adjacent to the liquid film

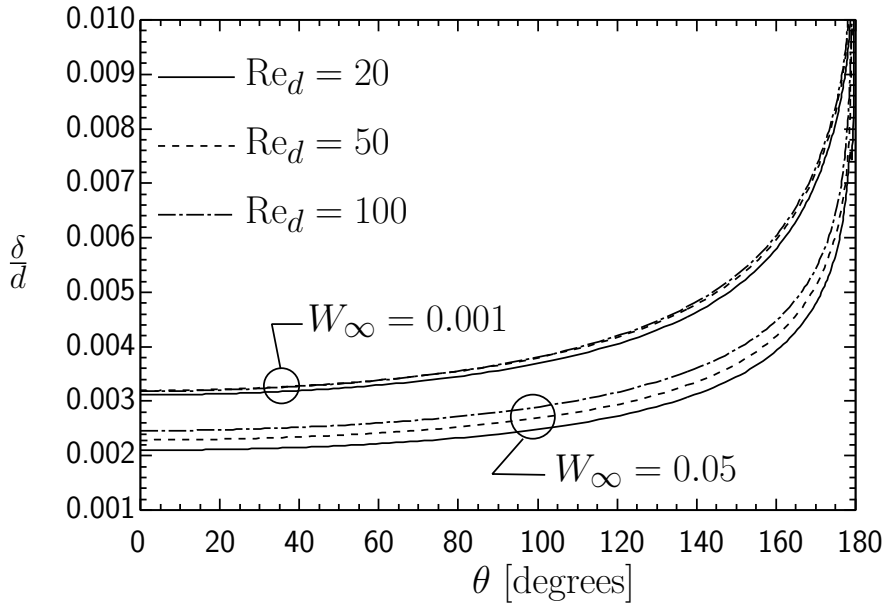

Figure 7.41: Effect of Re_d on condensate height for $\Delta T = 20$ K and $P_\infty = 1$ atm.

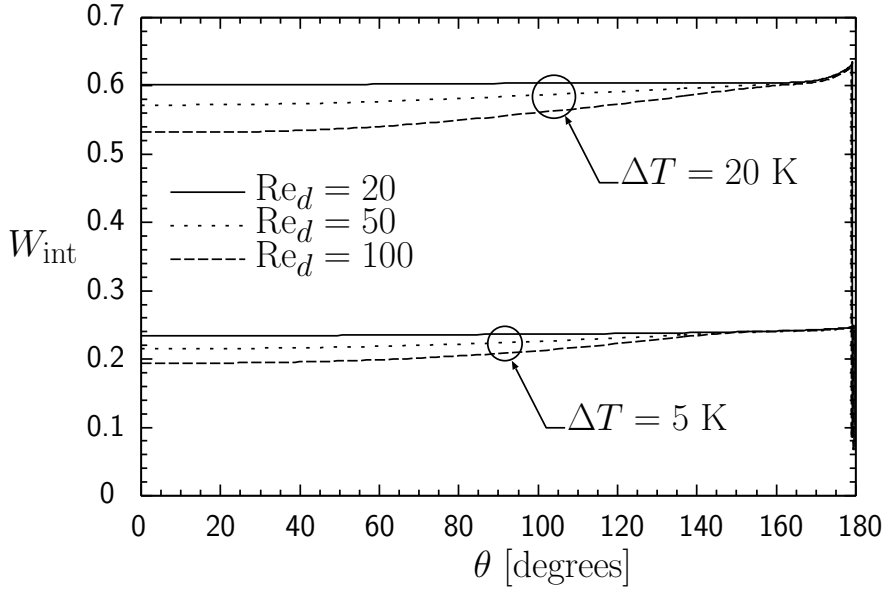

Figure 7.42: Effect of Re_d on W_{int} for $W_\infty = 0.05$, $P_\infty = 1$ atm, and $\Delta T = 5$ and 20 K.

where variations in W occur. As a result, the content of steam in that region increases and W_{int} decreases as shown in Figure 7.42. As W_{int} decreases, the interfacial temperature, T_{int}, increases and the local temperature difference across the liquid film, $(T_{\text{int}} - T_{\text{wall}})$, increases. This increase in the local temperature difference increases the condensation rate and the film thickness. Differences in W_{int} and consequently in T_{int} for different Re_d start to diminish gradually for $\theta > 60°$ and disappear at $\theta \approx 140°$ and $160°$ for $\Delta T = 5$ and 20 K, respectively. Also from Figure 7.42, it can be seen that the value of W_{int} remains almost constant with θ for $\text{Re}_d = 20$ for both values of ΔT. This trend can be explained by increasing role of the diffusion mechanism in gas transportation over advection mechanism as Re_d decreases.

The increase in the condensation rate due to increasing Re_d leads to thicker liquid films, as shown in Figures 7.40 and 7.41, and greater thermal resistance across the film. This explains the slight decrease in Nu_s with Re_d for $W_\infty = 0.05$ in Figures 7.43 and 7.44 at the regions where W_{int} remains approximately constant for all values of used Re_d (i.e. $\theta > 137°$ for $\Delta T = 5$K and $\theta > 152°$ for $\Delta T = 20$).

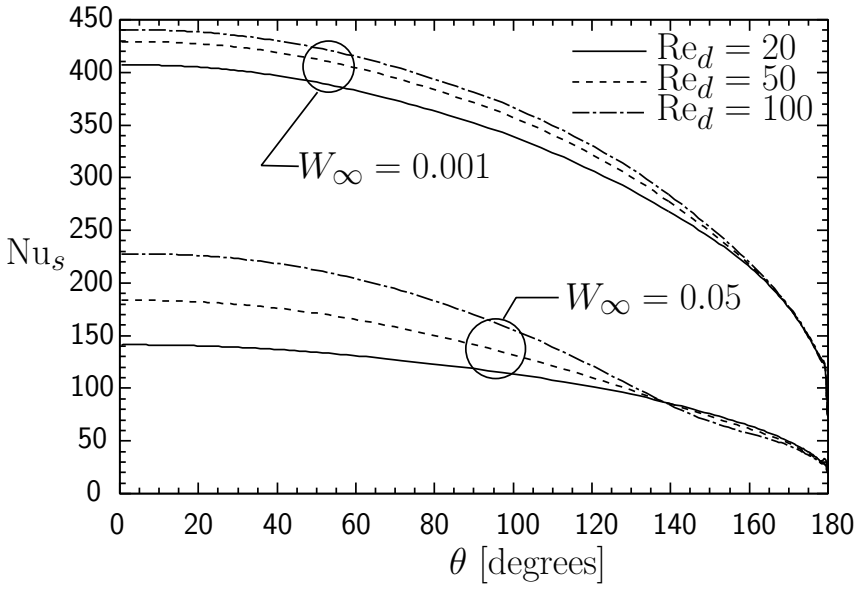

Figure 7.43: Effect of Re_d on Nu_s for $\Delta T = 5$ K and $P_\infty = 1$ atm.

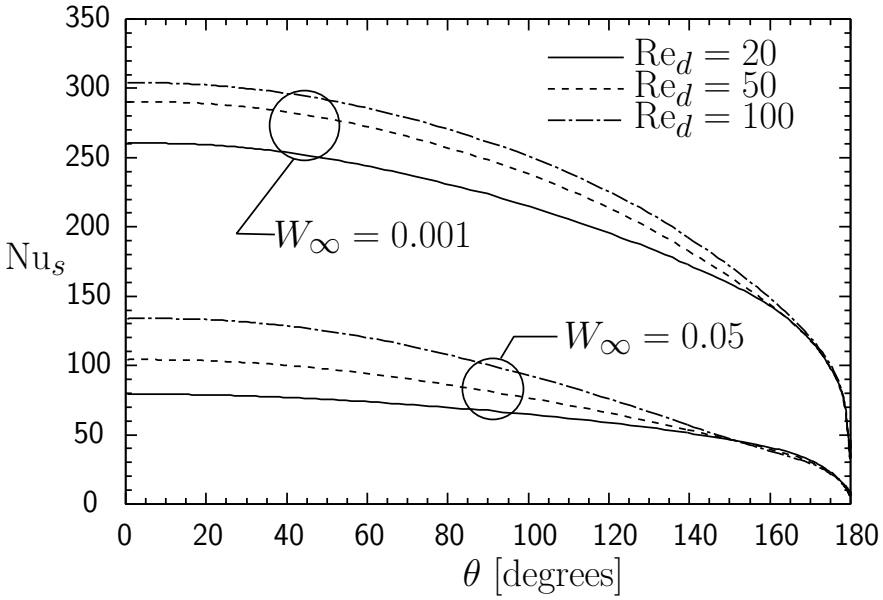

Figure 7.44: Effect of Re_d on Nu_s for $\Delta T = 20$ K and $P_\infty = 1$ atm.

The favorable effect of increasing Re_d on the condensation process for $W_\infty > 0$ can be noticed also in Table 7.3. For example, at $W_\infty = 0.05$ and ΔT =20 K, the magnitude of the reduction in Re_L compared to the pure vapour case decreases from 75.5% at $\mathrm{Re}_d = 20$ to reach 70.6% and 64.6% for $\mathrm{Re}_d = 50$ and 100, respectively. For $W_\infty < 0.05$, the positive influence of increasing Re_d is more recognizable. For example, at $W_\infty = 0.01$ and ΔT =20 K, the magnitude of the reduction in Re_L decreases from 53.4% at $\mathrm{Re}_d = 20$ to reach 43.2% and 33.6% for $\mathrm{Re}_d = 50$ and 100, respectively. The effect of changing Re_d on Re_L and $\overline{\mathrm{Nu}}$ is also shown graphically in Figures 7.45 and 7.46 for $P_\infty = 1$ atm and $\Delta T = 20$ K.

Figure 7.47 shows the influence of Re_d on the gas mass fraction distribution around the tube for W_∞ =0.05 and $\Delta T = 20$ K. The gas mass fraction boundary layer becomes slightly thinner as Re_d increases. The thickness of the W boundary layer at the top of the tube reduces from $0.5d$ for $\mathrm{Re}_d = 20$ to reach $0.31d$ and $0.22d$ for $\mathrm{Re}_d = 50$ and 100, respectively. The value of $W_{\max}$ at the interface decreases by 0.9 % for $\mathrm{Re}_d = 100$ compared to the case of $\mathrm{Re}_d = 20$.

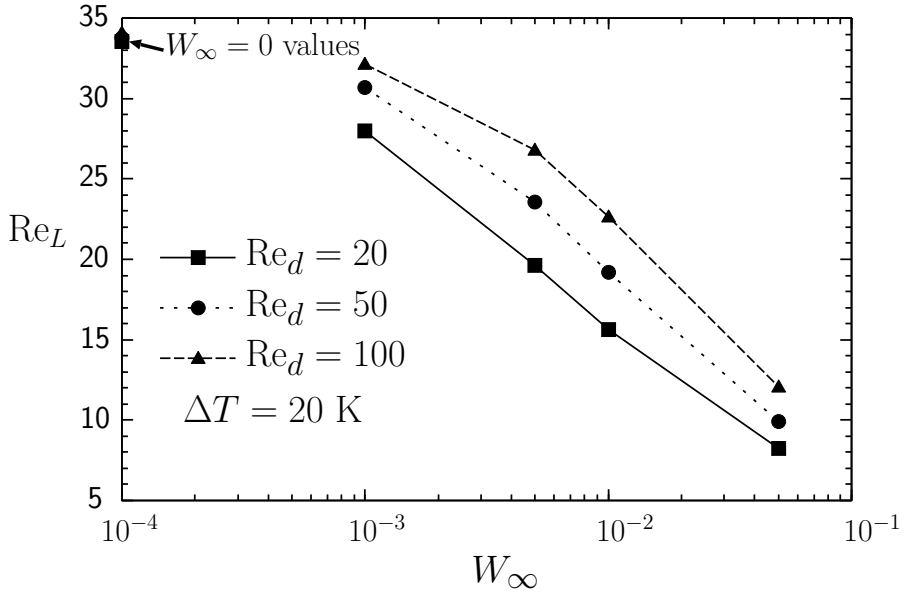

Figure 7.45: Effect of Re_d on condensate mass flow rate, Re_L, at $\Delta T = 20$K.

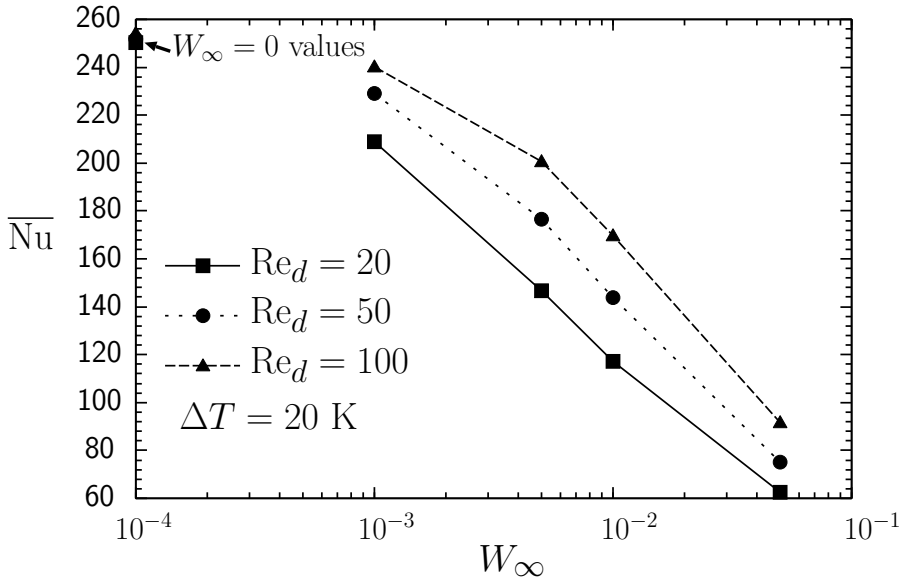

Figure 7.46: Effect of Re_d on $\overline{\mathrm{Nu}}$ for $P_\infty = 1$ atm and $\Delta T = 20$ K.

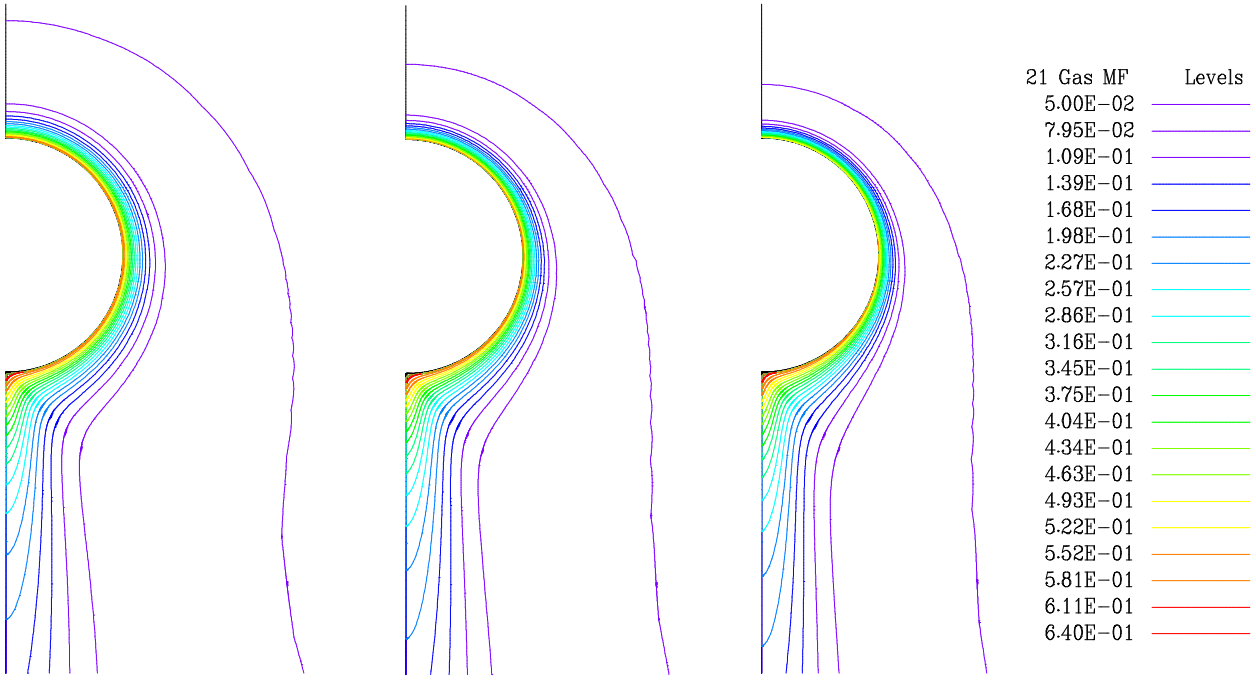

(*a*) $\mathrm{Re}_d = 20$ (*b*) $\mathrm{Re}_d = 50$ (*c*) $\mathrm{Re}_d = 100$

Figure 7.47: Effect of Re_d on the gas mass fraction boundary layer for W_∞ =0.05 and $\Delta T = 20$ K.

The increased inertia force with increased Re_d distinctly reduces the extent of the reverse flow region as seen in Figure 7.48 for W_∞ =0.001 and $\Delta T = 20$ K. For $\mathrm{Re}_d = 20$, the reverse flow region extends to $3.5\,d$ beyond the tube. For $\mathrm{Re}_d = 50$ and 100, the extent of the reverse flow region reduces to $0.75\,d$ and $0.31\,d$, respectively. The intensity of the reverse flow, however, remains approximately constant for these particular cases. For example, the minimum value of U changed from -7.46×10^{-2}m/s for $\mathrm{Re}_d = 20$ to -7.77×10^{-2}m/s for $\mathrm{Re}_d = 100$.

7.3.5 Effect of Changing P_∞

The influence of changing P_∞ on the condensation process was investigated for $\mathrm{Re}_d = 50$, $\Delta T = 20$ K, and $W_\infty = 0.001$ and 0.05. The purpose behind this test is to study the impact of changing the properties on the condensation process.

The effect of P_∞ on the condensate film thickness is presented in Figure 7.49 for $\Delta T =$ 20 K and $W_\infty = 0.001$ and 0.05. For each value of W_∞, decreasing P_∞ leads to an increase in δ along the tube. The differences in the film thickness are consistent with those for pure vapour cases in Section 7.2.4. Taking the case of $W_\infty = 0.05$ as an example, the film thickness at $\theta = 0°$ decreases by 5.1% and 3.8% as the pressure increases from 0.5 atm to 1 atm and from 1 atm to 2 atm, respectively. These differences in δ profiles remain approximately constant for the most of the tube circumference. The increase in δ due to decreasing T_∞ (because of decreasing P_∞) is related to the increase in the liquid dynamic viscosity which was discussed in Section 7.2.4.

The influence of changing P_∞ on local Nusselt number is shown in Figure 7.50 for the same cases in Figure 7.49. The increase in Nu_s with increasing P_∞ is linked to a decrease in δ associated with increasing P_∞. Values of $\overline{\mathrm{Nu}}$ and Re_L for $P_\infty = 0.5$ and 2 atm, $\Delta T =$ 5 and 20 K, $\mathrm{Re}_d = 50$, and $W_\infty = 0$, 0.001, 0.005, 0.01, and 0.05, are given in Table 7.4. The influence of changing P_∞ on the value of Re_L in the presence of air is similar to the

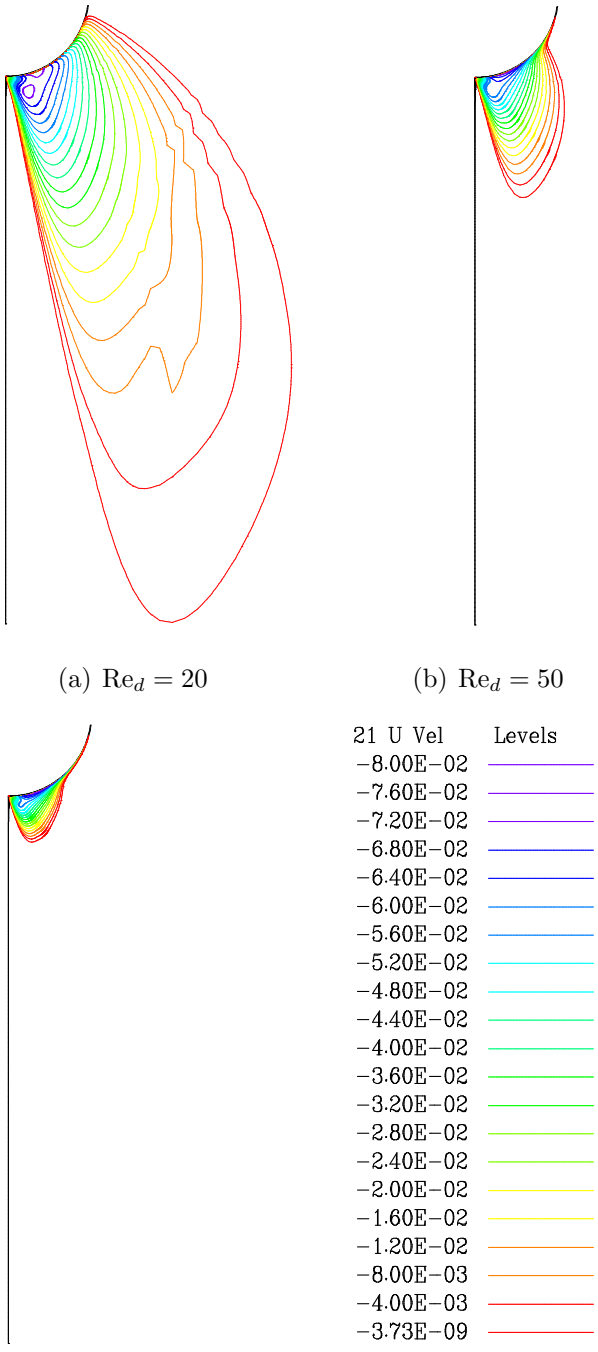

(a) $\mathrm{Re}_d = 20$

(b) $\mathrm{Re}_d = 50$

(c) $\mathrm{Re}_d = 100$

Figure 7.48: Effect of Re_d on the reverse flow region for $\Delta T = 20$ K and W_∞ =0.001.

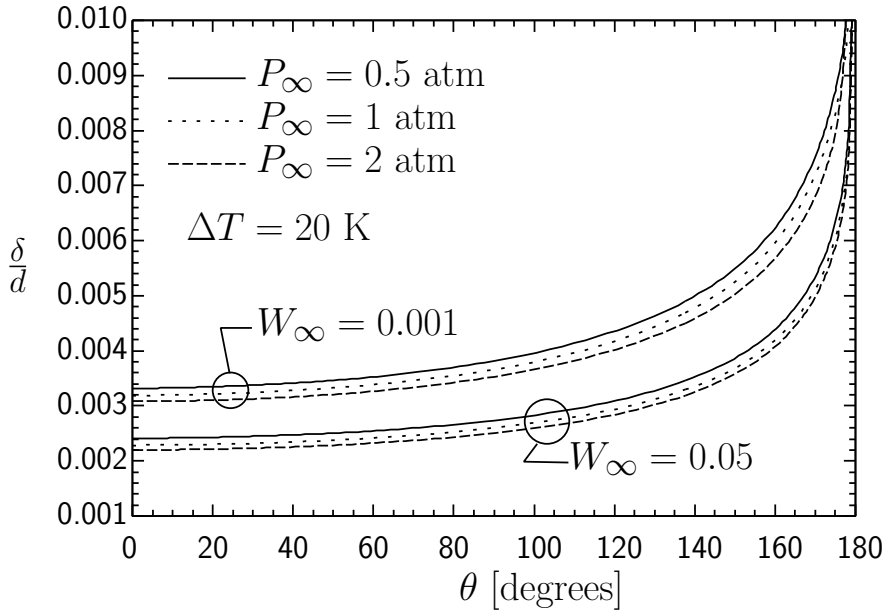

Figure 7.49: Effect of pressure on the condensate thickness for $\mathrm{Re}_d = 50$ and $W_\infty = 0.001$ and 0.05.

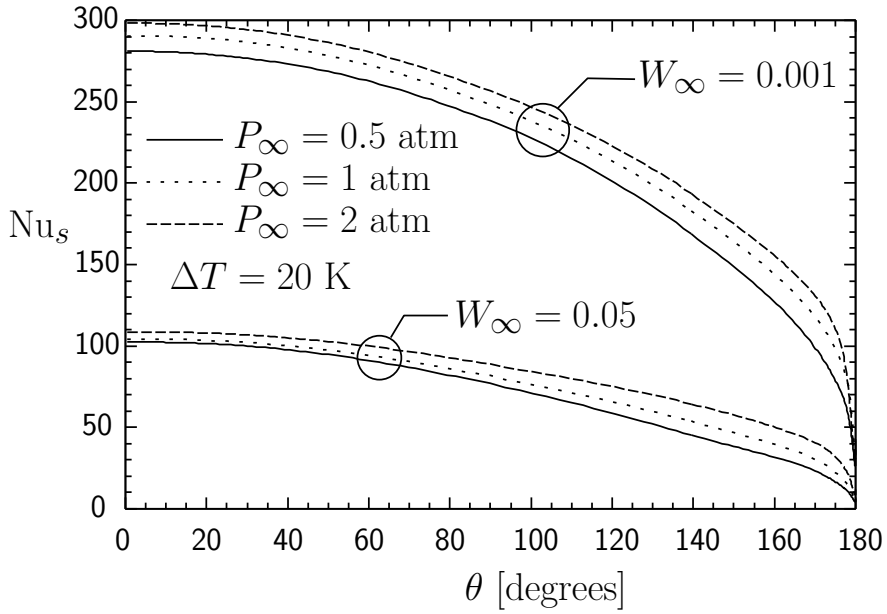

Figure 7.50: Effect of pressure on the local Nusselt number for $\mathrm{Re}_d = 50$ and $W_\infty = 0.001$ and 0.05.

Table 7.4: Average Nusselt number and Re_L variation with W_∞ and ΔT for $P_\infty = 0.5$ and 2 atm and $\mathrm{Re}_d = 50$.

W_∞	ΔT [K]	$P_\infty = 0.5$ [atm]		$P_\infty = 2.0$ [atm]	
		$\overline{\mathrm{Nu}}$	Re_L	$\overline{\mathrm{Nu}}$	Re_L
0	5	348.98	9.26	372.68	15.93
	20	243.11	25.35	260.09	44.15
0.001	5	329.40	8.73	352.46	15.06
	20	216.96	22.60	237.84	40.33
0.005	5	276.66	7.33	297.21	12.68
	20	164.86	17.14	185.16	31.32
0.01	5	234.97	6.21	253.44	10.80
	20	133.76	13.88	153.27	25.88
0.05	5	124.33	3.25	136.70	5.77
	20	70.36	7.21	136.70	13.82

pure vapour case that was discussed in Section 7.2.4. At $W_\infty = 0.05$, the magnitude of the reduction in Re_L for the pressure change from 1 atm to 0.5 atm is about 27%. The pressure change from 2 atm to 1 atm results in decrease in Re_L by about 28% for $W_\infty = 0.05$. This trend is attributed mainly to the change in the dynamic viscosity. The condensate mass flow rate increases with increasing P_∞. For $W_\infty = 0.05$ and ΔT =20 K, the condensation rate increased from 6.254×10^{-4} kg/s for $P_\infty = 0.5$ atm to reach 6.98×10^{-4} kg/s and 7.985×10^{-4} kg/s for $P_\infty = 1$ and 2 atm, respectively. In other words, the condensation rate increased by respectively 11.6% and 14.4% as P_∞ increased from 0.5 atm to 1 atm and from 1 atm to 2 atm.

Chapter 8

Summary, Conclusions, and Recommendations

8.1 Summary and Conclusions

A complete two-phase numerical model for steady state laminar flows was developed. The model solves the full 2D Navier-Stokes equations using a structured non-orthogonal computational grid. The computational grid moves dynamically to match precisely the interface between the two phases by using an adaptive-grid Eulerian method. In this method, the grid is moved at the end of each time step in the computation using a mass conservation based approach in the liquid phase at all locations along the solution domain referred to as the integral liquid mass balance method. Fundamental mass and force balances are implemented at the phase interface. The current model was validated against various experimental and theoretical works in the literature for different two-phase flow tests. The validation tests involved stratified flow of liquid and gas in a horizontal channel, falling thin liquid film over a vertical wall, film condensation in a vertical channel, and condensation of steam from pure steam and steam-air mixture over a horizontal tube. The elliptic solution method successfully computed flow around the tube with reverse flow in the gas phase. It also predicted the film thickness from the top of the tube all the way around the tube and in the falling film region below the tube.

Two parametric studies were performed to investigate condensation of steam from a downward flow over a horizontal isothermal tube. The first study dealt with pure steam while the second study used mixtures of steam and air with different values of the gas mass fraction. The studies demonstrated the effects of free stream-to-tube surface temperature difference, ΔT, free stream gas mass fraction, W_∞, free stream velocity in terms of Re_d, and free

stream pressure, P_∞ on the condensation process. The numerical results presented included predictions of the condensate film thickness profile, δ, and local heat transfer coefficient, Nu_s, for the whole range of the angle, θ; average heat transfer coefficient, $\overline{\mathrm{Nu}}$; condensate film Reynolds number, Re_L; and fields of flow variables. From these results, the following conclusions may be drawn:

1. The free stream-to-tube surface temperature difference ΔT has a strong effect on the condensation and film thickness for both pure steam and steam-air mixture cases. For the case of pure steam, ΔT is the dominant parameter in the condensation process.

2. For a constant value of Re_d, condensate mass flow rate and film thickness increase with ΔT for all values of W_∞ used, including $W_\infty = 0$.

3. For the case of pure steam, moderate changes in the free stream Reynolds number Re_d showed a slight increase in the condensate mass flow rate with increased Re_d.

4. Even small concentrations of air in the steam-air mixture cause a reduction in the condensation rate and film thickness.

5. For the case of steam-air mixture, a moderate increase in Re_d caused an increase in the condensate rate and in $\overline{\mathrm{Nu}}$. This trend was more noticeable as W_∞ increased.

6. Changing the properties through changing the free stream pressure has a relatively smaller effect than the effect of changing the temperature difference or the free stream gas mass fraction.

8.2 Recommendations for Further work

The following recommendations taking into account the results of the present work, the current code development stage, and the potential of the present numerical model. These

recommendations might add advancement to this work and overcome the current limitations of the code.

1. It is recommended to develop an algorithm in which the surface tension can be included. Depending on the curvature of the tube and interface surface, surface tension could play an important rule in determining the shape of the interface at the bottom of the tube. Considerable efforts were made during this work to include the effect of surface tension to the model but attempts to achieve a stable algorithm were not successful.

2. It is recommended to develop a robust linear equation solver that is less sensitive to aspect ratio and skewness of the control volumes and large variations in the sizes of the control volumes.

3. It is recommended to explore the effect of gas mass fraction in the mixture for $W_\infty > 0.05$. In the present work, numerical instability at the bottom of the tube made it difficult to obtain converged results for $W_\infty > 0.05$. Coupling the T and W equations at the interface might be beneficial in this regard.

4. It is recommended that the future projects consider extending the current model to be applied to falling film applications with evaporation or absorption.

5. It is recommended to develop an improved meshing scheme and consider unstructured grid so that the current model can be applied to condensation in tube bundles with various arrangements.

6. It is recommended to explore thoroughly the effect of strong suction at the interface due to condensation on the stability of the mixture flow around the tube. This could help in establishing limits of flow modes in the presence of condensation.

7. It is recommended that the current model could be extended to include turbulence effects in both phases.

Bibliography

[1] S. Ghiaasiaan, *Two-Phase Flow, Boiling and Condensation: In Conventional and Miniature Systems*, pp. 1–614, Cambridge Univ Press, England, 2008.

[2] W. Nusselt, The surface condensation of steam., *Zeitschrift des Vereines Deutscher Ingenieure*, vol. 60, pp. 569–575, 1916.

[3] D. Butterworth and G. . Hewitt, *Two-Phase Flow and Heat Transfer*, pp. 447–450, Oxford University Press, 1977.

[4] Shekrila.IG and Gomelaur.VI, Theoretical Study of Laminar Film Condensation of Flowing Vapour, *International Journal of Heat and Mass Transfer*, vol. 9, pp. 581–591, 1966.

[5] V. Denny and A. Mills, Laminar Film Condensation of a Flowing Vapor on a Horizontal Cylinder at Normal Gravity, *Journal of Heat Transfer*, vol. 91, pp. 495–501, 1969.

[6] T. Fujii, H. Uehara, and C. Kurata, Laminar Filmwise Condensation of Flowing Vapor on a Horizontal Cylinder, *International Journal of Heat and Mass Transfer*, vol. 15, pp. 235–246, 1972.

[7] V. Denny and V. South, Effects of Forced Flow, Noncondensables, and Variable Properties on Film Condensation of Pure and Binary Vapors at Forward Stagnation Point of a Horizontal Cylinder, *International Journal of Heat and Mass Transfer*, vol. 15, pp. 2133–2142, 1972.

[8] E. Gaddis, Solution of The Two Phase Boundary-Layer Equations for Laminar-Film Condensation of Vapor Flowing Perpendicular to a Horizontal Cylinder, *International Journal of Heat and Mass Transfer*, vol. 22, pp. 371–382, 1979.

[9] H. Honda, S. Nozu, and T. Fujii, Vapour-to-Coolant Heat Transfer During Condensation of Flowing Vapour on a Horizontal Tube, *Proc. Seventh Int. Heat Transfer Conf., München*, pp. 77–82, 1982.

[10] A. A. Roshko, A New Hodograph for Free-Stream-Line Theory, *NACA*, vol. TN 8168, 1954.

[11] J. Rose, Effect of Pressure-Gradient in Forced-Convection Film Condensation on a Horizontal Tube, *International Journal of Heat and Mass Transfer*, vol. 27, pp. 39–47, 1984.

[12] R. Krupiczka, Effect of surface-tension on laminar-film condensation on a horizontal cylinder, *Chemical Engineering and Processing*, vol. 19, pp. 199–203, 1985.

[13] A. M. Jacobi and V. W. Goldschmidt, The Effect of Surface Tension Variation on Filmwise Condensation and Heat Transfer on a Cylinder in Cross Flow, *International Journal of Heat and Mass Transfer*, vol. 32, pp. 1483–1490, 1989.

[14] S. Yang, Superheated laminar film condensation on a nonisothermal horizontal tube, *Journal of Thermophysics and Heat Transfer*, vol. 11, pp. 526–532, Oct-Dec 1997.

[15] C. H. Hsu and S. A. Yang, Pressure gradient and variable wall temperature effects during filmwise condensation from downward flowing vapors onto a horizontal tube, *International Journal of Heat and Mass Transfer*, vol. 42, pp. 2419–2426, Jul. 1999.

[16] M. Mosaad, Forced convection film condensation of flowing vapour on an inclined circular tube, *Heat and Mass Transfer*, vol. 36, pp. 1–6, Mar. 2000.

[17] M. Asbik, A. Daïf, P. K. Panday, and A. Khmou, Numerical Study of Laminar Condensation of Downward Flowing Vapour on a Single Horizontal Cylinder or a Bank of Tubes, *Canadian Journal of Chemical Engineering*, vol. 77, pp. 54–61, 1999.

[18] M. Asbik, D. O. Hadda, A. Il Idrissi, B. Zeghmati, and A. Khmou, Forced Convection Laminar Film Condensation of Downward Flowing Vapror on a Single Horizontal Elliptic Cylinder or a Bank of Elliptical Tubes, *Numerical Heat Transfer, Part A (Applications)*, vol. 37, pp. 511–544, 2000.

[19] C.-K. Chen and Y.-T. Lin, Laminar film condensation from a downward-flowing steam-air mixture onto a horizontal circular tube, *Applied Mathematical Modelling*, vol. 33, pp. 1944 – 1956, 2009.

[20] G. H. Tang, H. W. Hu, Z. N. Zhuang, and W. Q. Tao, Film condensation heat transfer on a horizontal tube in presence of a noncondensable gas, *Applied Thermal Engineering*, vol. 36, pp. 414–425, Apr 2012.

[21] D. Othmer, The Condensation of Steam, *Industrial and Engineering Chemistry*, vol. 21, pp. 576–583, 1929.

[22] C. X. Zhu and Y. M. Zhang, Experimental Research on External Film Condensation Heat Transfer of Horizontally Coiled Tubes in the Presence of Air, *Power Eng. 4*, pp. 10–16, 1991.

[23] H. Li and W. Peng, A Study on Gas-Liquid Film Thicknesses and Heat Transfer Characteristics of Vapor-Gas Condensation Outside a Horizontal Tube, *Journal of Heat Transfer-Transactions of the ASME*, vol. 136, Feb 2014.

[24] P. Sarma, B. Vijayalakshmi, F. Mayinger, and S. Kakac, Turbulent film condensation on a horizontal tube with external flow of pure vapors, *International Journal of Heat and Mass Transfer*, vol. 41, pp. 537–545, Feb 1998.

[25] H. Kato, Nishiwak.N, and M. Hirata, On Turbulent Heat Transfer by Free Convection from a Vertical Plate, *International Journal of Heat and Mass Transfer*, vol. 11, pp. 1117–&, 1968.

[26] D. Homescu and P. K. Panday, Forced convection condensation on a horizontal tube: Influence of turbulence in the vapor and liquid phases, *Journal of Heat Transfer*, vol. 121, pp. 874–885, Nov. 1999.

[27] Y. Lin and S. Yang, Turbulent film condensation on a nonisothermal horizontal tube, *Journal of Mechanics*, vol. 21, pp. 235–242, ” Dec ” 2005.

[28] S. Yang and Y. Lin, Turbulent film condensation on a non-isothermal horizontal tube-effect of eddy diffusivity, *Applied Mathematical Modelling*, vol. 29, pp. 1149–1163, Dec 2005.

[29] C.-K. Chen and Y.-T. Lin, Turbulent film condensation in the presence of non-condensable gases over a horizontal tube, *International Journal of Thermal Sciences*, vol. 48, pp. 1777 – 1785, 2009.

[30] J. Min and D. Choi, Analysis of the absorption process on a horizontal tube using Navier-Stokes equations with surface-tension effects, *International Journal of Heat and Mass Transfer*, vol. 42, pp. 4567–4578, Dec 1999.

[31] J. Rauscher, A. Mills, and V. Denny, Experimental Study of Film Condensation from Steam-air Mixtures Flowing Downward over a Horizontal Tube, *Jornal of Heat Transfer-Transactions of the ASME*, vol. 96, pp. 83–88, 1974.

[32] T. Fujii, H. Honda, and K. Oda, Condensation of Steam on a Horizontal Tube-The Influence of Oncoming Velocity and Thermal Condition at the Tube Wall, *Proc. 18th National Heat Transfer Conference, San Diego, CA, USA*, pp. 35–43, 1979.

[33] A. A. Nicol, A. Bryce, and A. S. A. Ahmed, Condensation of a Horizontally Flowing Vapour on a Horizontal Cylinder Normal to the Vapour Stream, *Proc. 6th Int. Heat Transfer Conference*, vol. 2, pp. 401–406, 1978.

[34] A. A. Nicol and D. J. Wallace, Condensation with Appreciable Vapour Velocity and Variable Wall Temperature, *Steam Turbine Condenser, NEL Report No. 619* , pp. 27–38, 1976.

[35] D. W. Nobbs and Y. R. Mayhew, Effect of Downward Vapour Velocity and Inundation on Condensation Rates on Horizontal Tube Banks, *Steam Turbine Condenser, NEL Report No. 619* , pp. 39–52, 1976.

[36] T. Fujii, *Vapour Shear and Condensate Inundation, in Power Condenser Heat Transfer Technology, ed*, pp. 193–223, McGraw-Hill, 1981.

[37] W. Lee and J. Rose, Forced-Convection Film Condensation on a Horizontal Tube with and without Non-Condensing Gases, *International Journal of Heat and Mass Transfer*, vol. 27, pp. 519–528, 1984.

[38] S. B. Memory and J. W. Rose, Film Condensation of Ethylene Glycol on a Horizontal Tube at High Vapour Velocity, *Proc. 8th Int. Heat Transfer Conference, San Francisco, CA, USA*, pp. 1607–1612, 1986.

[39] A. G. Michael, J. W. Rose, and L. C. Daniels, Forced Convection Condensation on a Horizontal Tube-Experiments With Vertical Downflow of Steam, *Journal of Heat Transfer-Transactions of the ASME*, vol. 111, pp. 792–797, Feb 1989.

[40] H. Honda and T. Fujii, Condensation of Flowing Vapor on a Horizontal Tube Numerical-Analysis as a Conjugate Heat-Transfer Problem, *Journal of Heat Transfer Transactions of the ASME*, vol. 106, pp. 841–848, 1984.

[41] A. Briggs and S. Sabaratnam, Condensation of steam in the presence of air on a single tube and a tube bank, *International Journal of Energy Research*, vol. 27, pp. 301–314, 2003, 12th International Symposium on Transport Phenomena, Istanbul, Turkey, JUL 16-20, 2000.

[42] J. H. Ferziger and M. Peric, *Computational Methods for Fluid Dynamics*, 3rd ed., Springer, Verlag Berlin Heidelberg, 2002.

[43] J. M. Floryan and H. Rasmussen, Numerical Methods for Viscous Flows with Moving Boundaries, *American Society of Mechanical Engineers*, vol. 42, pp. 323–341, 1989.

[44] A. Prosperetti and G. Tryggvason, *Computational Methods for Multiphase Flow*, 1st ed., Cambridge, 2007.

[45] E. C. Siow, Numerical Solution of a Two-Phase Model for Laminar Film Condensation of Vapour-Gas Mixtures in Channels, Master thesis, University of Manitoba, Manitoba, 2001.

[46] F. P. Incropera and D. P. DeWitt, *Fundamentals of Heat and Mass Transfer*, 4th ed., John Wiley and Sons, New York, 1996.

[47] T. F. Irvine and P. E. Liley, *Steam and Gas Tables with Computer Equations*, 1st ed., Academic Press, INC., 1984.

[48] R. C. Reid, J. M. Prausnitz, and T. K. Sherwood, *The properties of Gases and Liquids*, 3rd ed., McGraw-Hill, 1977.

[49] P. Knupp and S. Steinberg, *Fundamentals of Grid Generation*, CRC Press, Boca Raton, 1993.

[50] L. A. Penner, Two-Dimensional Flow Predictions in a Tube Bundle Using Orthogonal and Non-Orthogonal Grids, Master thesis, University of Manitoba, Manitoba, 1996.

[51] S. V. Patankar, *Numerical Heat Transfer and Fluid Flow*, Hemisphere Publishing Corporation, 1980.

[52] G. Raithby, P. F. Galpin, and J. Van Doormaal, Prediction of Heat and Fluid flow in Complex Geometries Using General Orthogonal Coordinates, *Numerical Heat Transfer*, vol. 9, pp. 125–142, 1986.

[53] G. Raithby and K. Torrance, Upstream-Weighted differencing Schemes and Their Application to Elliptical Problems Involving Fluid Flow, *Conput. Fluids*, vol. 2, pp. 191–206, 1974.

[54] J. Van Doormaal and C. Raithby, Enhancements of the SIMPLE Method for Predicting Incompressible Fluid Flows, *Numerical Heat Transfer*, vol. 7, pp. 147–163, 1984.

[55] G. Raithby and G. E. Schneider, Numerical Solution of Problems in Incompressible Fluid Flow; Treatment of the Velocity-Pressure Coupling, *Numerical Heat Transfer*, vol. 2, pp. 417–440, 1979.

[56] S. Patankar and D. Spalding, A Calculation Procedure for Heat, Mass and Momentum Transfer in Three-dimensional Parabolic Flows., *International Journal of Heat and Mass Transfer*, vol. 15, pp. 1787–1806, 1972.

[57] T. Miller and F. Schmidt, Use of a Pressure-Weighted Interpolation Method for the Solution of the Incompressible Navier-Stokes Equations on a Nonstaggared Grid System, *Numerical Heat Transfer*, vol. 14, pp. 213–233, 1988.

[58] C. Rhie and W. Chow, Numerical Study of The Turbulent Flow Past an Airfoil with Trailing Edge Separation, *AIAA Journal*, vol. 21, pp. 1525–1532, 1983.

[59] S. Zhang, X. Zhao, and S. Bayyuk, Generalized Formulations for the Rhie-Chow Interpolation, *Journal of Computational Physics*, vol. 258, pp. 880–914, 2014.

[60] S. Majumdar, Role of Underrelaxation in Momentum Interpolation for Calculation of Flow with Nonstaggered Grids, *Numerical Heat Transfer*, vol. 13, pp. 125–132, 1988.

[61] M. Peric, Efficient Semi-Implicit Solving Algorithm for nine-Diagonal Coefficient Matrix, *Numerical Heat Transfer*, vol. 11, pp. 251–279, 1987.

[62] Y. Saad and M. Schultz, GMRES - A Generalized Minimal Residual Algorithm for Solving Nonsymmetric Linear-Systems, *Journal of the Society of Industrial and Applied Mathematics*, vol. 7, pp. 856–869, Jul 1986.

[63] G. E. Schneider and M. Zedan, A modified Strongly Implicit Procedure for the Numerical Solution of Field Problem , *Numerical Heat Transfer*, vol. 4, pp. 1–19, 1981.

[64] H. Soliman, personal communication.

[65] M. M. Rahman, A. Faghri, W. L. Hankey, and T. D. Swanson, Computation of the Free-Surface Flow of a Thin Liquid-Film at Zero and Normal Gravity, *Numerical Heat Transfer, Part A (Applications)*, vol. 17, pp. 53–71, Jan 1990.

[66] R. A. Cook and R. H. Clark, Experimental Determination of Velocity Profiles in Smooth Falling Liquid Films, *Canadian Journal of Chemical Engineering*, vol. 49, pp. 412–416, 1971.

[67] K. J. Ruschak and S. J. Weinstein, Thin-film flow at moderate Reynolds number, *Journal of Fluids Engineering*, vol. 122, pp. 774–778, Dec 2000.

[68] E. A. Saleh and S. J. Ormiston, A Sharp-Interface Elliptic Numerical Model of Laminar Two-Phase Gas-Liquid Downward Flow in a Vertical Parallel Plate Channel, *Canadian Journal of Chemical Engineering*, in press.

[69] J. W. Rose, Fundamentals of Condensation Heat-Transfer - Laminar-Film Condensation, *JSME International Journal*, vol. 31, pp. 357–375, Aug. 1988.

[70] E. A. Saleh and S. J. Ormiston, A Sharp-Interface Elliptic Two-Phase Numerical Model of Laminar Film Condensation on a Horizontal Tube, *International Journal of Heat and Mass Transfer*, vol. 102, pp. 1169–1179, 2016.

[71] G. Schneider and M. Raw, A Skewed, Positive Influence Coefficient Upwinding Procedure for Control-Volume-Based Finite-Element Convection-Diffusion Computation, *Numerical Heat Transfer*, vol. 9, pp. 1–26, 1986.

[72] H. Saabas and B. Baliga, Co-Located Equal-Order Control-Volume Finite-Element Method for Multidimensional, Incompressible, Fluid-Flow .1. Formulation, *Numerical Heat Transfer, Part B (Fundamentals)*, vol. 26, pp. 381–407, Dec 1994.

[73] C. Masson, H. Saabas, and B. Baliga, Co-Located Equal-Order Control-Volume Finite-Element Method for 2-Dimensional Axisymmetrical Incompressible Fluid-Flow, *International Journal for Numerical Methods in Fluids*, vol. 18, pp. 1–26, Jan 15 1994.

[74] L. Tran, C. Masson, and A. Smaili, A stable second-order mass-weighted upwind scheme for unstructured meshes, *International Journal for Numerical Methods in Fluids*, vol. 51, pp. 749–771, Jul 10 2006.

Appendix A

The Mass-Weighted Upwind Scheme (MAW)

A.1 Introduction

In discretisation of convective-diffusion transport equations, it is important to implement an advection scheme that guarantees generating positive coefficients. Otherwise, negative coefficients can cause divergence of the numerical procedure or could lead to unrealistic results. While the central differencing scheme, CDS, generates negative coefficients, the EDS scheme is guaranteed to generate positive coefficients. Unfortunately, the EDS scheme suffers from false diffusion. Therefore, the EDS scheme might not be adequate to handle complex flows patterns where main flow is not parallel to the grid lines. Schneider and Raw [71] presented an advection scheme known as the Mass-Weighted Upwind Scheme (MAW) that accounts for the grid skewness. The MAW scheme uses ratio of mass fluxes to convect the transported property. The first order scheme was first applied to quadrilateral control volumes using control-volume based finite element method. Then, the MAW scheme was applied to tetrahedral and triangular elements by [72] and [73] respectively. Later, Tran et. al [74] presented a second order version of the MAW scheme. In this section, the detailed description and implementation of the first order MAW scheme are provided.

A.2 Discretisation of the Advection Term

A typical control volume is shown in Figure A.1. The nodes are represented with solid circles. Another control volume, I, is defined so that its centre is located at the north east corner, ne, of control volume P and it is marked by a solid square. This vortex-centered control volume will be referred to as a control element in this section. The values of variable Φ are known

at the centre nodes of all control volumes. For the control element being considered, the values of Φ at NE, N, P and E are known. For simplicity, compass notation is replaced with numbers. Face segments or portions that are included in the element numbered from 1 to 4 in counter-clockwise direction starting from NE. Each segment has one integration point, ip, at the middle. The arrows in Figure A.1 shows the conventional direction of mass flow and convected variable ϕ at the four face segments. The MAW scheme suggests evaluating the convected variable based on the mass flow rate at the faces as follows:

$$\phi_1^{ip} = R_1 \left[\left(1-\lambda_1\right) \Phi_1 + \lambda_1 \phi_2^{ip} \right] + \left(1-R_1\right) \left[\left(1-\lambda_1\right) \Phi_4 + \lambda_1 \phi_4^{ip} \right] \tag{A.1}$$

$$\phi_2^{ip} = R_2 \left[\left(1-\lambda_2\right) \Phi_2 + \lambda_2 \phi_3^{ip} \right] + \left(1-R_2\right) \left[\left(1-\lambda_2\right) \Phi_1 + \lambda_2 \phi_1^{ip} \right] \tag{A.2}$$

$$\phi_3^{ip} = R_3 \left[\left(1-\lambda_3\right) \Phi_3 + \lambda_3 \phi_4^{ip} \right] + \left(1-R_3\right) \left[\left(1-\lambda_3\right) \Phi_2 + \lambda_3 \phi_2^{ip} \right] \tag{A.3}$$

$$\phi_4^{ip} = R_4 \left[\left(1-\lambda_4\right) \Phi_4 + \lambda_4 \phi_1^{ip} \right] + \left(1-R_4\right) \left[\left(1-\lambda_4\right) \Phi_3 + \lambda_4 \phi_3^{ip} \right] \tag{A.4}$$

Values of parameters R_1 to R_4 are evaluated at face segment f based on mass flow ratio ω_f and direction of mass flow as follows:

$$\omega_1 = \frac{\dot{m}_2}{\dot{m}_1} \text{ and } R_1 = 1 \text{ for } \dot{m}_1 > 0 \quad \text{or} \quad \omega_1 = \frac{\dot{m}_4}{\dot{m}_1} \text{ and } R_1 = 0 \text{ for } \dot{m}_1 < 0 \tag{A.5}$$

$$\omega_2 = \frac{\dot{m}_3}{\dot{m}_2} \text{ and } R_2 = 1 \text{ for } \dot{m}_2 > 0 \quad \text{or} \quad \omega_2 = \frac{\dot{m}_1}{\dot{m}_2} \text{ and } R_2 = 0 \text{ for } \dot{m}_2 < 0 \tag{A.6}$$

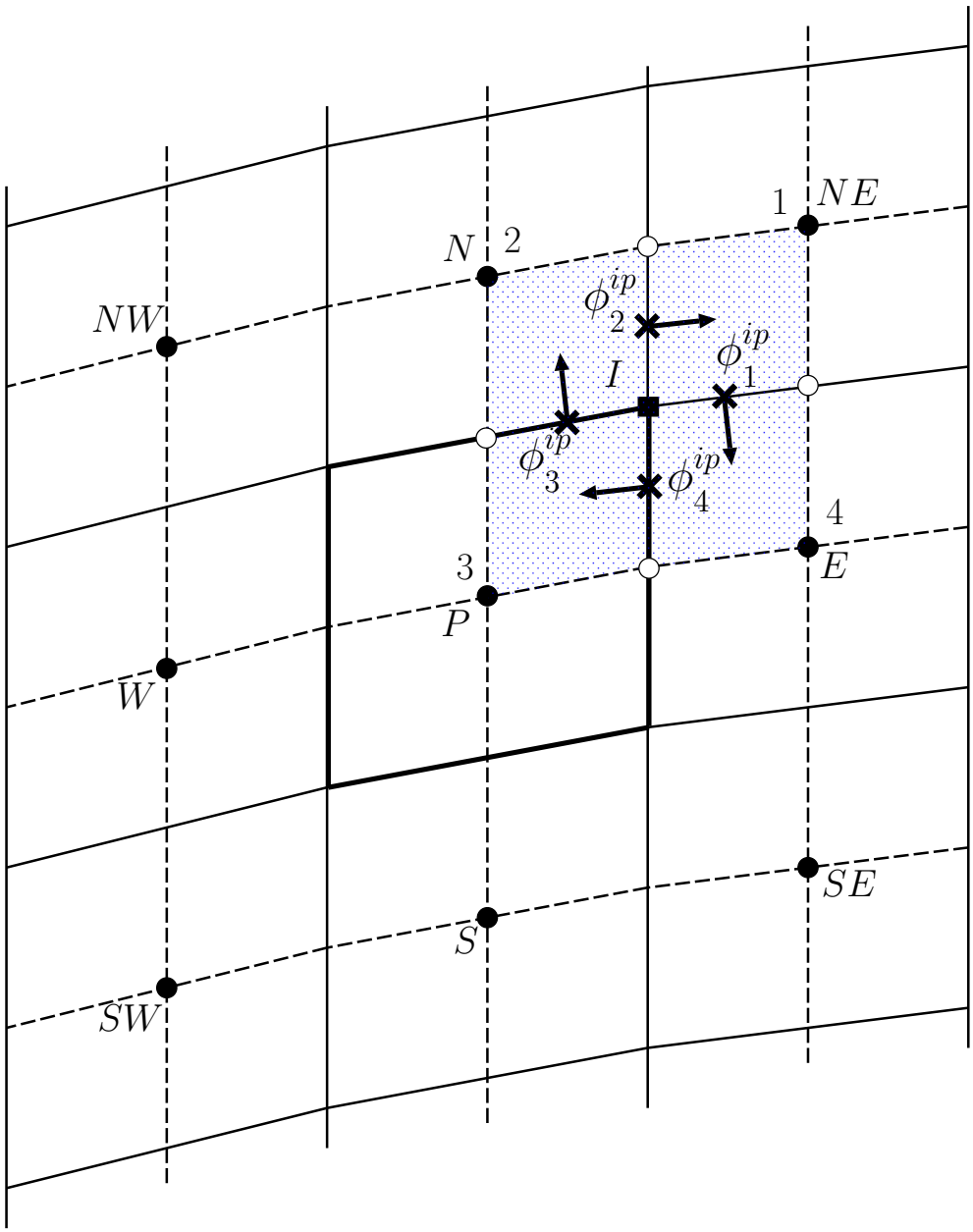

Figure A.1: Typical control element and control volume.

$$\omega_3 = \frac{\dot{m}_4}{\dot{m}_3} \text{ and } R_3 = 1 \text{ for } \dot{m}_3 > 0 \quad \text{or} \quad \omega_3 = \frac{\dot{m}_2}{\dot{m}_2} \text{ and } R_3 = 0 \text{ for } \dot{m}_3 < 0 \tag{A.7}$$

$$\omega_4 = \frac{\dot{m}_1}{\dot{m}_4} \text{ and } R_4 = 1 \text{ for } \dot{m}_4 > 0 \quad \text{or} \quad \omega_4 = \frac{\dot{m}_3}{\dot{m}_4} \text{ and } R_4 = 0 \text{ for } \dot{m}_4 < 0 \tag{A.8}$$

The parameter λ_f is evaluated based on ratio of mass flow rates as follows:

$$\lambda_f = \min\left[\max\left(\omega_f, 0\right), 1\right] \tag{A.9}$$

Considering all possible flow configurations in Equations (A.5 to A.8) and after rearrangement, the following equations are written for the convected variables:

$$\phi_1^{ip} - R_1\,\lambda_1\,\phi_2^{ip} - \left(1 - R_1\right)\,\lambda_1\,\phi_4^{ip} = R_1\left(1 - \lambda_1\right)\Phi_1 + \left(1 - R_1\right)\left(1 - \lambda_1\right)\Phi_4 \tag{A.10}$$

$$-\left(1 - R_2\right)\,\lambda_2\,\phi_1^{ip} + \phi_2^{ip} - R_2\,\lambda_2\,\phi_3^{ip} = R_2\left(1 - \lambda_2\right)\Phi_2 + \left(1 - R_2\right)\left(1 - \lambda_2\right)\Phi_1 \tag{A.11}$$

$$-\left(1 - R_3\right)\,\lambda_3\,\phi_2^{ip} + \phi_3^{ip} - R_3\,\lambda_3\,\phi_4^{ip} = R_3\left(1 - \lambda_3\right)\Phi_3 + \left(1 - R_3\right)\left(1 - \lambda_3\right)\Phi_2 \tag{A.12}$$

$$-R_4\,\lambda_4\,\phi_1^{ip} - \left(1 - R_4\right)\,\lambda_4\,\phi_3^{ip} + \phi_4^{ip} = R_4\left(1 - \lambda_4\right)\Phi_4 + \left(1 - R_4\right)\left(1 - \lambda_4\right)\Phi_3 \tag{A.13}$$

This linear system can be written in the compact form $\mathcal{A}\,\boldsymbol{\phi} = \boldsymbol{b}$. Let $\mathcal{C} = \mathcal{A}^{-1}$. Then, the solution of this algebraic system is $\boldsymbol{\phi} = \mathcal{C}\,\boldsymbol{b}$. The convected variable at the four integration points can be given in terms of the right hand side vector $\boldsymbol{b}$ as follows:

$$\begin{aligned}
\phi_1^{ip} &= b_1\, C_{11} + b_2\, C_{12} + b_3\, C_{13} + b_4\, C_{14} \\
\phi_2^{ip} &= b_1\, C_{21} + b_2\, C_{22} + b_3\, C_{23} + b_4\, C_{24} \\
\phi_3^{ip} &= b_1\, C_{31} + b_2\, C_{32} + b_3\, C_{33} + b_4\, C_{34} \\
\phi_4^{ip} &= b_1\, C_{41} + b_2\, C_{42} + b_3\, C_{43} + b_4\, C_{44}
\end{aligned} \tag{A.14}$$

The solution can be expressed in terms of the associated four nodal values, Φ, as follows:

$$\begin{aligned}
\phi_1^{ip} &= C_1^{\phi_1^{ip}}\, \Phi_1 + C_2^{\phi_1^{ip}}\, \Phi_2 + C_3^{\phi_1^{ip}}\, \Phi_3 + C_4^{\phi_1^{ip}}\, \Phi_4 \\
\phi_2^{ip} &= C_1^{\phi_2^{ip}}\, \Phi_1 + C_2^{\phi_2^{ip}}\, \Phi_2 + C_3^{\phi_2^{ip}}\, \Phi_3 + C_4^{\phi_2^{ip}}\, \Phi_4 \\
\phi_3^{ip} &= C_1^{\phi_3^{ip}}\, \Phi_1 + C_2^{\phi_3^{ip}}\, \Phi_2 + C_3^{\phi_3^{ip}}\, \Phi_3 + C_4^{\phi_3^{ip}}\, \Phi_4 \\
\phi_4^{ip} &= C_1^{\phi_4^{ip}}\, \Phi_1 + C_2^{\phi_4^{ip}}\, \Phi_2 + C_3^{\phi_4^{ip}}\, \Phi_3 + C_4^{\phi_4^{ip}}\, \Phi_4
\end{aligned} \tag{A.15}$$

where the details of the coefficients in Equations (A.15) are

$$\begin{aligned}
C_1^{\phi_1^{ip}} &= C_{11}\, R_1\, \left(1-\lambda_1\right) + C_{12}\, \left(1-R_2\right)\, \left(1-\lambda_2\right) \\
C_2^{\phi_1^{ip}} &= C_{12}\, R_2\, \left(1-\lambda_2\right) + C_{13}\, \left(1-R_3\right)\, \left(1-\lambda_3\right) \\
C_3^{\phi_1^{ip}} &= C_{13}\, R_3\, \left(1-\lambda_3\right) + C_{14}\, \left(1-R_4\right)\, \left(1-\lambda_4\right) \\
C_4^{\phi_1^{ip}} &= C_{14}\, R_4\, \left(1-\lambda_4\right) + C_{11}\, \left(1-R_1\right)\, \left(1-\lambda_1\right)
\end{aligned} \tag{A.16}$$

,

$$
\begin{aligned}
C_1^{\phi_2^{ip}} &= C_{21}\, R_1\, \left(1-\lambda_1\right) + C_{22}\, \left(1-R_2\right)\, \left(1-\lambda_2\right) \\
C_2^{\phi_2^{ip}} &= C_{22}\, R_2\, \left(1-\lambda_2\right) + C_{23}\, \left(1-R_3\right)\, \left(1-\lambda_3\right) \\
C_3^{\phi_2^{ip}} &= C_{23}\, R_3\, \left(1-\lambda_3\right) + C_{24}\, \left(1-R_4\right)\, \left(1-\lambda_4\right) \\
C_4^{\phi_2^{ip}} &= C_{24}\, R_4\, \left(1-\lambda_4\right) + C_{21}\, \left(1-R_1\right)\, \left(1-\lambda_1\right)
\end{aligned}
\tag{A.17}
$$

,

$$
\begin{aligned}
C_1^{\phi_3^{ip}} &= C_{31}\, R_1\, \left(1-\lambda_1\right) + C_{32}\, \left(1-R_2\right)\, \left(1-\lambda_2\right) \\
C_2^{\phi_3^{ip}} &= C_{32}\, R_2\, \left(1-\lambda_2\right) + C_{33}\, \left(1-R_3\right)\, \left(1-\lambda_3\right) \\
C_3^{\phi_3^{ip}} &= C_{33}\, R_3\, \left(1-\lambda_3\right) + C_{34}\, \left(1-R_4\right)\, \left(1-\lambda_4\right) \\
C_4^{\phi_3^{ip}} &= C_{34}\, R_4\, \left(1-\lambda_4\right) + C_{31}\, \left(1-R_1\right)\, \left(1-\lambda_1\right)
\end{aligned}
\tag{A.18}
$$

and

$$
\begin{aligned}
C_1^{\phi_4^{ip}} &= C_{41}\, R_1\, \left(1-\lambda_1\right) + C_{42}\, \left(1-R_2\right)\, \left(1-\lambda_2\right) \\
C_2^{\phi_4^{ip}} &= C_{42}\, R_2\, \left(1-\lambda_2\right) + C_{43}\, \left(1-R_3\right)\, \left(1-\lambda_3\right) \\
C_3^{\phi_4^{ip}} &= C_{43}\, R_3\, \left(1-\lambda_3\right) + C_{44}\, \left(1-R_4\right)\, \left(1-\lambda_4\right) \\
C_4^{\phi_4^{ip}} &= C_{44}\, R_4\, \left(1-\lambda_4\right) + C_{41}\, \left(1-R_1\right)\, \left(1-\lambda_1\right)
\end{aligned}
\tag{A.19}
$$

For control volume P in Figure A.2, there are four faces. Each face consists of two segments. Thus, two integration points are used in each face. To evaluated ϕ at all four faces of control volume P, all eight faces segments must be considered. This can be done by considering control elements II, III and IV in addition to I.

For each face segment, the mass-weighted average of ϕ_{f}^{ip} is assumed to prevail through the entire segment. The convection terms for both face segments that consist a complete

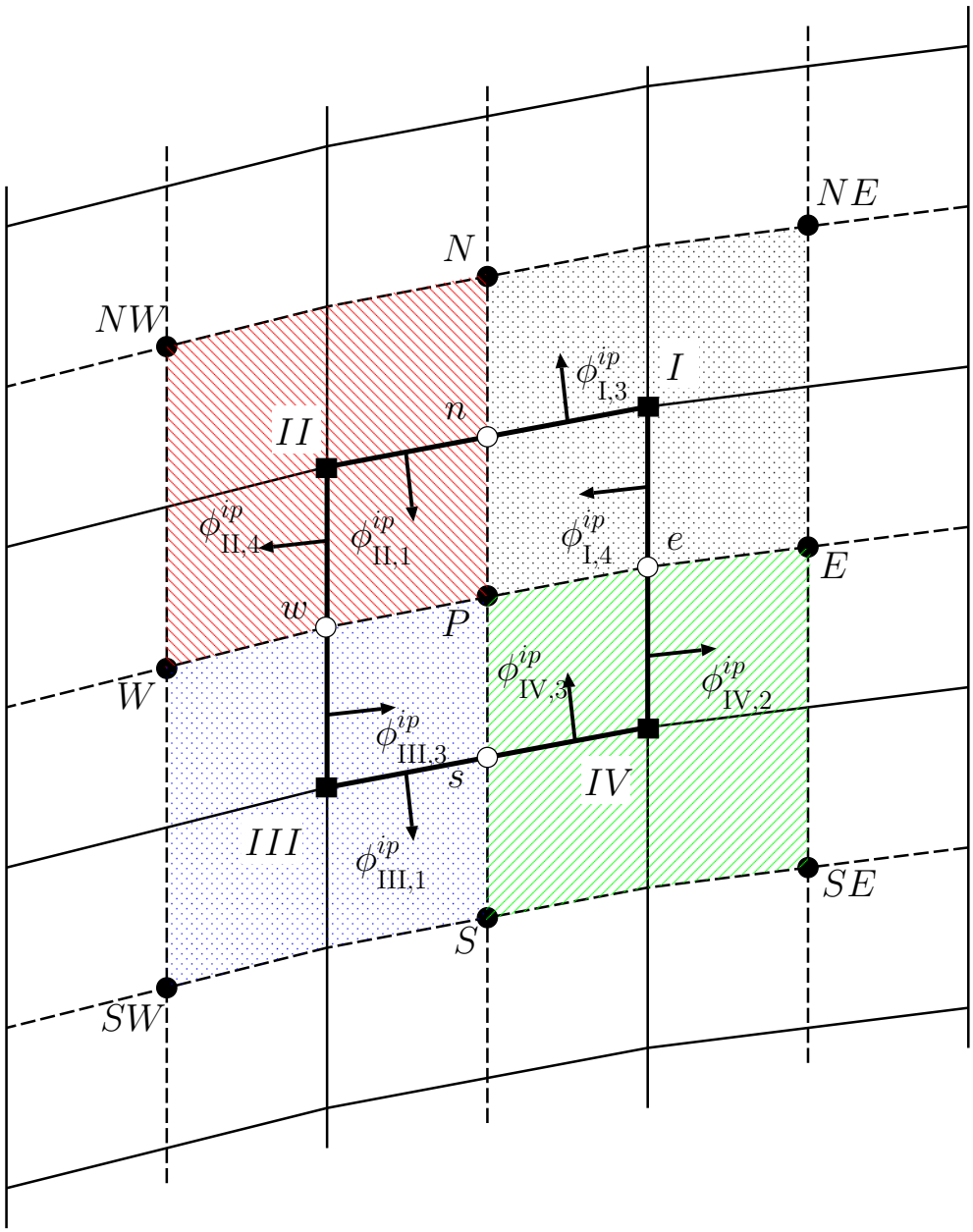

Figure A.2: Associated control elements with control volume P.

face of control volume P are added together. This step produces the following equations for the components of the advection term:

$$
\begin{aligned}
\dot{m}_e\ \phi_{\mathrm{e}} &= \frac{\dot{m}_e}{2}\ \left(\phi^{ip}_{\mathrm{IV},2}\ +\ \phi^{ip}_{\mathrm{I},4}\right)\\
\dot{m}_w\ \phi_{\mathrm{w}} &= \frac{\dot{m}_w}{2}\ \left(\phi^{ip}_{\mathrm{III},2}\ +\ \phi^{ip}_{\mathrm{II},4}\right)\\
\dot{m}_n\ \phi_{\mathrm{n}} &= \frac{\dot{m}_n}{2}\ \left(\phi^{ip}_{\mathrm{II},1}\ +\ \phi^{ip}_{\mathrm{I},3}\right)\\
\dot{m}_s\ \phi_{\mathrm{s}} &= \frac{\dot{m}_s}{2}\ \left(\phi^{ip}_{\mathrm{III},1}\ +\ \phi^{ip}_{\mathrm{IV},3}\right)
\end{aligned}
\tag{A.20}
$$

The advection term for the transport equation of the variable Φ is evaluated as follows:

$$
\begin{aligned}
\dot{m}_e\phi_{\mathrm{e}} - \dot{m}_w\phi_{\mathrm{w}} + \dot{m}_n\phi_{\mathrm{n}} - \dot{m}_s\phi_{\mathrm{s}} = \frac{\dot{m}_e}{2}\ &\left[\left(C^{\phi^{ip}_2}_{\mathrm{IV},1}\,\Phi_{\mathrm{IV},1} + C^{\phi^{ip}_2}_{\mathrm{IV},2}\,\Phi_{\mathrm{IV},2} + C^{\phi^{ip}_2}_{\mathrm{IV},3}\,\Phi_{\mathrm{IV},3} + C^{\phi^{ip}_2}_{\mathrm{IV},4}\,\Phi_{\mathrm{IV},4}\right)\right.\\
&\left.+\left(C^{\phi^{ip}_4}_{\mathrm{I},1}\,\Phi_{\mathrm{I},1} + C^{\phi^{ip}_4}_{\mathrm{I},2}\,\Phi_{\mathrm{I},2} + C^{\phi^{ip}_4}_{\mathrm{I},3}\,\Phi_{\mathrm{I},3} + C^{\phi^{ip}_4}_{\mathrm{I},4}\,\Phi_{\mathrm{I},4}\right)\right]\\
-\frac{\dot{m}_w}{2}\ &\left[\left(C^{\phi^{ip}_2}_{\mathrm{III},1}\,\Phi_{\mathrm{III},1} + C^{\phi^{ip}_2}_{\mathrm{III},2}\,\Phi_{\mathrm{III},2} + C^{\phi^{ip}_2}_{\mathrm{III},3}\,\Phi_{\mathrm{III},3} + C^{\phi^{ip}_2}_{\mathrm{III},4}\,\Phi_{\mathrm{III},4}\right)\right.\\
&\left.+\left(C^{\phi^{ip}_4}_{\mathrm{II},1}\,\Phi_{\mathrm{II},1} + C^{\phi^{ip}_4}_{\mathrm{II},2}\,\Phi_{\mathrm{II},2} + C^{\phi^{ip}_4}_{\mathrm{II},3}\,\Phi_{\mathrm{II},3} + C^{\phi^{ip}_4}_{\mathrm{II},4}\,\Phi_{\mathrm{II},4}\right)\right]\\
+\frac{\dot{m}_n}{2}\ &\left[\left(C^{\phi^{ip}_1}_{\mathrm{II},1}\,\Phi_{\mathrm{II},1} + C^{\phi^{ip}_1}_{\mathrm{II},2}\,\Phi_{\mathrm{II},2} + C^{\phi^{ip}_1}_{\mathrm{II},3}\,\Phi_{\mathrm{II},3} + C^{\phi^{ip}_1}_{\mathrm{II},4}\,\Phi_{\mathrm{II},4}\right)\right.\\
&\left.+\left(C^{\phi^{ip}_3}_{\mathrm{I},1}\,\Phi_{\mathrm{I},1} + C^{\phi^{ip}_3}_{\mathrm{I},2}\,\Phi_{\mathrm{I},2} + C^{\phi^{ip}_3}_{\mathrm{I},3}\,\Phi_{\mathrm{I},3} + C^{\phi^{ip}_3}_{\mathrm{I},4}\,\Phi_{\mathrm{I},4}\right)\right]\\
-\frac{\dot{m}_s}{2}\ &\left[\left(C^{\phi^{ip}_1}_{\mathrm{III},1}\,\Phi_{\mathrm{III},1} + C^{\phi^{ip}_1}_{\mathrm{III},2}\,\Phi_{\mathrm{III},2} + C^{\phi^{ip}_1}_{\mathrm{III},3}\,\Phi_{\mathrm{III},3} + C^{\phi^{ip}_1}_{\mathrm{III},4}\,\Phi_{\mathrm{III},4}\right)\right.\\
&\left.+\left(C^{\phi^{ip}_3}_{\mathrm{IV},1}\,\Phi_{\mathrm{IV},1} + C^{\phi^{ip}_3}_{\mathrm{IV},2}\,\Phi_{\mathrm{IV},2} + C^{\phi^{ip}_3}_{\mathrm{IV},3}\,\Phi_{\mathrm{IV},3} + C^{\phi^{ip}_3}_{\mathrm{IV},4}\,\Phi_{\mathrm{IV},4}\right)\right]
\end{aligned}
\tag{A.21}
$$

Now, using the regular control volume notation, i.e. P, E, W, N, S , NE, NW, SE and SW, to replace the local notation,i.e. I, II, III, IV, 1, 2, 3, and 4, yields.

$$\begin{aligned}
\dot{m}_e\,\phi_{\mathrm{e}} \;-\; \dot{m}_w\,\phi_{\mathrm{w}} \;+\; \dot{m}_n\,\phi_{\mathrm{n}} \;-\; \dot{m}_s\,\phi_{\mathrm{s}} \;=\; & \frac{\dot{m}_e}{2}\;\left[\left(C^{\phi^{ip}_2}_{\mathrm{IV},1}\,\Phi_{\mathrm{E}} + C^{\phi^{ip}_2}_{\mathrm{IV},2}\,\Phi_{\mathrm{P}} + C^{\phi^{ip}_2}_{\mathrm{IV},3}\,\Phi_{\mathrm{S}} + C^{\phi^{ip}_2}_{\mathrm{IV},4}\,\Phi_{\mathrm{SE}}\right)\right. \\
& \left. + \left(C^{\phi^{ip}_4}_{\mathrm{I},1}\,\Phi_{\mathrm{NE}} + C^{\phi^{ip}_4}_{\mathrm{I},2}\,\Phi_{\mathrm{N}} + C^{\phi^{ip}_4}_{\mathrm{I},3}\,\Phi_{\mathrm{P}} + C^{\phi^{ip}_4}_{\mathrm{I},4}\,\Phi_{\mathrm{E}}\right)\right] \\
& - \frac{\dot{m}_w}{2}\;\left[\left(C^{\phi^{ip}_2}_{\mathrm{III},1}\,\Phi_{\mathrm{P}} + C^{\phi^{ip}_2}_{\mathrm{III},2}\,\Phi_{\mathrm{W}} + C^{\phi^{ip}_2}_{\mathrm{III},3}\,\Phi_{\mathrm{SW}} + C^{\phi^{ip}_2}_{\mathrm{III},4}\,\Phi_{\mathrm{S}}\right)\right. \\
& \left. + \left(C^{\phi^{ip}_4}_{\mathrm{II},1}\,\Phi_{\mathrm{N}} + C^{\phi^{ip}_4}_{\mathrm{II},2}\,\Phi_{\mathrm{NW}} + C^{\phi^{ip}_4}_{\mathrm{II},3}\,\Phi_{\mathrm{W}} + C^{\phi^{ip}_4}_{\mathrm{II},4}\,\Phi_{\mathrm{P}}\right)\right] \\
& + \frac{\dot{m}_n}{2}\;\left[\left(C^{\phi^{ip}_1}_{\mathrm{II},1}\,\Phi_{\mathrm{N}} + C^{\phi^{ip}_1}_{\mathrm{II},2}\,\Phi_{\mathrm{NW}} + C^{\phi^{ip}_1}_{\mathrm{II},3}\,\Phi_{\mathrm{W}} + C^{\phi^{ip}_1}_{\mathrm{II},4}\,\Phi_{\mathrm{P}}\right)\right. \\
& \left. + \left(C^{\phi^{ip}_3}_{\mathrm{I},1}\,\Phi_{\mathrm{NE}} + C^{\phi^{ip}_3}_{\mathrm{I},2}\,\Phi_{\mathrm{N}} + C^{\phi^{ip}_3}_{\mathrm{I},3}\,\Phi_{\mathrm{P}} + C^{\phi^{ip}_3}_{\mathrm{I},4}\,\Phi_{\mathrm{E}}\right)\right] \\
& - \frac{\dot{m}_s}{2}\;\left[\left(C^{\phi^{ip}_1}_{\mathrm{III},1}\,\Phi_{\mathrm{P}} + C^{\phi^{ip}_1}_{\mathrm{III},2}\,\Phi_{\mathrm{W}} + C^{\phi^{ip}_1}_{\mathrm{III},3}\,\Phi_{\mathrm{SW}} + C^{\phi^{ip}_1}_{\mathrm{III},4}\,\Phi_{\mathrm{S}}\right)\right. \\
& \left. + \left(C^{\phi^{ip}_3}_{\mathrm{IV},1}\,\Phi_{\mathrm{E}} + C^{\phi^{ip}_3}_{\mathrm{IV},2}\,\Phi_{\mathrm{P}} + C^{\phi^{ip}_3}_{\mathrm{IV},3}\,\Phi_{\mathrm{S}} + C^{\phi^{ip}_3}_{\mathrm{IV},4}\,\Phi_{\mathrm{SE}}\right)\right] \qquad \text{(A.22)}
\end{aligned}$$

The contributions of the advection term to each coefficient using RHS notation are:

$$\begin{aligned}
ADV^{\phi}_{\mathrm{P}} = & \frac{\dot{m}_e}{2}\left(C^{\phi^{ip}_2}_{\mathrm{IV},2} + C^{\phi^{ip}_4}_{\mathrm{I},3}\right) - \frac{\dot{m}_w}{2}\left(C^{\phi^{ip}_2}_{\mathrm{III},1} + C^{\phi^{ip}_4}_{\mathrm{II},4}\right) \\
& + \frac{\dot{m}_n}{2}\left(C^{\phi^{ip}_1}_{\mathrm{II},4} + C^{\phi^{ip}_3}_{\mathrm{I},3}\right) - \frac{\dot{m}_s}{2}\left(C^{\phi^{ip}_1}_{\mathrm{III},1} + C^{\phi^{ip}_3}_{\mathrm{IV},2}\right) \qquad \text{(A.23)}
\end{aligned}$$

$$ADV^{\phi}_{\mathrm{E}} = -\frac{\dot{m}_e}{2}\left(C^{\phi^{ip}_2}_{\mathrm{IV},1} + C^{\phi^{ip}_4}_{\mathrm{I},4}\right) - \frac{\dot{m}_n}{2}\,C^{\phi^{ip}_3}_{\mathrm{I},4} + \frac{\dot{m}_s}{2}\,C^{\phi^{ip}_3}_{\mathrm{IV},1} \qquad \text{(A.24)}$$

$$ADV^{\phi}_{\mathrm{W}} = +\frac{\dot{m}_w}{2}\left(C^{\phi^{ip}_2}_{\mathrm{III},2} + C^{\phi^{ip}_4}_{\mathrm{II},3}\right) - \frac{\dot{m}_n}{2}\,C^{\phi^{ip}_1}_{\mathrm{II},3} + \frac{\dot{m}_s}{2}\,C^{\phi^{ip}_1}_{\mathrm{III},2} \qquad \text{(A.25)}$$

$$ADV^{\phi}_{\mathrm{N}} = -\frac{\dot{m}_n}{2}\left(C^{\phi^{ip}_1}_{\mathrm{II,1}} + C^{\phi^{ip}_3}_{\mathrm{I,2}}\right) - \frac{\dot{m}_e}{2}C^{\phi^{ip}_4}_{\mathrm{I,2}} + \frac{\dot{m}_w}{2}C^{\phi^{ip}_4}_{\mathrm{II,1}} \tag{A.26}$$

$$ADV^{\phi}_{\mathrm{S}} = +\frac{\dot{m}_s}{2}\left(C^{\phi^{ip}_1}_{\mathrm{III,4}} + C^{\phi^{ip}_3}_{\mathrm{IV,3}}\right) - \frac{\dot{m}_e}{2}C^{\phi^{ip}_2}_{\mathrm{IV,3}} + \frac{\dot{m}_w}{2}C^{\phi^{ip}_2}_{\mathrm{III,4}} \tag{A.27}$$

$$ADV^{\phi}_{\mathrm{NE}} = -\frac{\dot{m}_e}{2}C^{\phi^{ip}_4}_{\mathrm{I,1}} - \frac{\dot{m}_n}{2}C^{\phi^{ip}_3}_{\mathrm{I,1}} \tag{A.28}$$

$$ADV^{\phi}_{\mathrm{NW}} = -\frac{\dot{m}_n}{2}C^{\phi^{ip}_1}_{\mathrm{II,2}} + \frac{\dot{m}_w}{2}C^{\phi^{ip}_4}_{\mathrm{II,2}} \tag{A.29}$$

$$ADV^{\phi}_{\mathrm{SE}} = -\frac{\dot{m}_e}{2}C^{\phi^{ip}_2}_{\mathrm{IV,4}} + \frac{\dot{m}_n}{2}C^{\phi^{ip}_3}_{\mathrm{IV,4}} \tag{A.30}$$

$$ADV^{\phi}_{\mathrm{SW}} = +\frac{\dot{m}_w}{2}C^{\phi^{ip}_2}_{\mathrm{III,3}} + \frac{\dot{m}_s}{2}C^{\phi^{ip}_1}_{\mathrm{III,3}} \tag{A.31}$$